The University Of Sheffield.

Development of new ceramic nano-composites for the next generation prosthetic devices

Samira Bostanchi

A thesis submitted in partial fulfilment of the requirements for the degree of Doctor of Philosophy

The University of Sheffield
Faculty of Materials Science and Engineering

November 2017

عشق ما را پی کاری به جهان آورده است

ادب این است که مشغول تماشا نشویم

تقدیم به حسین و سارای عزیزم

“Dedicated to my life’s treasures, Hossein and Sara”

Acknowledgements

A wise man once said, “A PhD is like a child”. From a helpless loud little baby in its first year, to a not entirely independent toddler in its second year, and almost an adult by the time of submission. And at whatever stage it is, you love your research with motherly (fatherly) passion even with all the frustration, and exhaustion you might go through.

First and foremost, I would like to say a million thanks to my PhD supervisor, Professor Mark Rainforth who gave me the opportunity to shape and grow my professional life. Words can neither qualify nor quantify how helpful your advice was during these years. Your patience and encouragement always inspired me to overcome the difficulties. You were the one who gave me the opportunity to experience the yell and scream of joy after each success. Thank you for being the greatest supervisor and a wonderful role model!

I would like to pass my gratitude to members of staff in the Department of Materials Science and Engineering; to Akemi for valuable constant advice on specimens’ preparation without which I would have had much more difficulties to find my way on this project; to Andrew Mould for his training and friendly help during the sintering process; to Amit for training me on the Tribometer and his non-stop helpful guidance; to Micheal Bell for his valuable comments during countless hours of annoying grinding and polishing; to Ben Palmer for doing TGA/DTA and training me for the density measurements; to Nik Reeves for helping me quantify peaks; to Dawn Bussey for her grateful willingness to help and her endless tips on the AFM analysis. My deepest appreciation goes to the Sorby staff; to Cheryl Shaw for teaching me how to use the SEM and cheer me up with her words; to Peng Zeng for her kind help in imaging with HRTEM; to Peng Gong for her admiring willingness to help me use Tecnai; to Le Ma for spending long hours with me, sharing the breathtaking moments of FIB lift-outs and laughter of success. I wish to thank the people who made my time in the department enjoyable; Peng, Mozart, Moe, Dawai, Amir Khesro, Itzel, Carl, Righdan, Neda, Navid and equally the people that I shared office H6 with.

Finally, I wish to show my profound gratitude to my parents and beloved siblings Hossein, and Sara for your love and support during these years. More importantly, massive thanks to Navid Manai for his professional advice on my research, friendship, inspiration and being there for me, every single time. And to all of you that I might have forgotten, THANK YOU!!

Abstract

The international market for hip and knee joint arthroplasty is expected to continue to grow into the foreseeable future as people live longer and expect a higher quality of life. Therefore, designing and production of a material with higher mechanical reliability is targeted by the international market. Ceramics are the latest materials in this regard, which offer the potential for the lowest wear rate and therefore the longest lifespan. The strength and toughness of ceramic prostheses have been greatly enhanced through the emergence of a zirconia toughened alumina (ZTA) composite. However, there remains a clear drive to reduce fracture rates through yet more reliable mechanical properties.

This research focuses on processing of a new ceramic composite with fine, well dispersed and high-density microstructure and also evaluating the effect of grain refinement on wear resistance. Furthermore, it seeks to further investigate the contribution of ternary and quaternary metal oxides, namely SrO and Cr_2O_3, to wear behaviour of this nano-composite. Therefore, nano-ceramic composites of zirconia toughened alumina (ZTA) and ZTA containing SrO and Cr_2O_3 additives (ZTA-additives) were formed using Spark Plasma Sintering (SPS) and were optimised, in terms of mechanical properties and grain size. The prepared specimens were almost the same, in terms of grain size, but differed in constituent components. In addition to these specimens, a commercial sample called BIOLOX® delta (with the same composition, but coarser grain size) was also investigated.

All materials were subjected to lubricated reciprocating sliding wear testing. To define the operative lubrication regime for each load, the Stribeck curve was plotted for each individual specimen. The results obtained from this curve, along with AFM and SEM images, revealed the operation of full fluid film and mixed lubrication in the ZTA composite and the operation of mixed lubrication in the ZTA-additives and commercial specimens. Upon applying a load of 32 N, the specific wear rate of ZTA presented an abrupt increase of two orders of magnitude, but for the other two specimens, only a small change was observed. This highlighted the effect of the ternary oxide, Cr_2O_3, on changing the chemistry of the material and therefore the behaviour of the surface. The addition clearly had a beneficial effect on the transition point from mild to severe wear, which was shifted to higher loads.

The specific wear rates, SEM and AFM images of the worn surfaces revealed that the commercial specimen was mid transition to severe wear at 32 N load, while the ZTA-additives composite did not show any sign of transition. This was probably due to the smaller grain size

of the ZTA-additives, compared to the commercial specimen. The grain size refinement would decrease the thermal mismatch stresses and slip length and therefore dislocation accumulation. In all three materials tested at 8N, TEM results exhibited limited dislocation activity in the surface alumina grains. This was in line with the specific wear rate and the features of the worn surfaces. The polymorphic phase transformation in zirconia grains was observed only in the commercial specimen, which was consistent with the results obtained from Raman spectroscopy. This was probably due to the smaller grain size of zirconia in the ZTA and the ZTA-additives compared to the commercial specimen. The SEM and AFM images presented contradictory results about the effect of platelet grains on the wear resistance of the composite. However, the constructive effect of these grains on the fracture toughness was observed in this study, as it was demonstrated by other researchers. The AFM, SEM and TEM results suggested that the dominant wear mechanism pre-transition was tribochemical wear for all materials. This led to the presence of a thin (nm) tribo-layer which may have affected the coefficient of friction (COF) and the specific wear rate.

Table of contents

1 Introduction

Hip joint replacement, as a great achievement in orthopaedic surgery, is mainly undertaken in older people, although newly published health data has exposed that the number of surgeries in young people has increased by up to ~76% [1]. The same source suggests that this increase in hip replacements belongs to patients aged 59 and under in years between 2004 -2015. They correlate this increase to the improvements in hip replacement surgery. The main limitation in total hip replacement (THR) is related to its life span, lasting for about 15 years, which is not acceptable for patients under 60, while their life expectancy ranges for much longer times. Therefore, this necessitates the introduction of more wear resistant and long-lasting biomaterials to cope with the higher activity level of younger people.

The emergence of hip joint orthopaedics dates back to the early 1900's when a narrow knowledge and limited facilities in this area were available. Extensive work was performed by Charnely in 1961 in which many materials from metals to Teflon coatings, to polyethylene were tried out during his research [2]. Among his trials, a polymer-based material called polyethylene was found to be a significant improvement which led to the development of ultra-high molecular weight polyethylene (UHMWPE) that is still extensively in use. Nowadays the ball on socket (acetabular cup against femoral head) articulations can be composed of metals such as CoCr, ultra-high molecular weight polyethylene (UHMWPE) and ceramics such as alumina and zirconia toughened alumina. Metal-on-metal articulation has been used for over 30 years, although there have been some concerns about implant loosening and also possible toxicity of nano-sized metal particles [3,4]. These concerns are very much to the fore at the moment, with most metal on metal designs now removed from the market. Polymeric acetabular cups assembled against ceramic or metallic femoral heads have demonstrated great biocompatibility, ductility, chemical stability and low coefficient of friction [5,6]. However, polymers wear more than any other material and a survival rate of 75% during 20 years is estimated for this type of joint [7,8]. It has been reported that many of the failures are a result of aseptic loosening which arises from localized osteolysis (bone resorption)[9,10].

Subsequently, hard on hard combinations including monolithic alumina are the most well-known ceramics introduced to the industry. Alumina, as a bio-ceramic, has been used in arthroplasty of hip joints since 1970s and more than 3.5 million joints using this material have been implanted worldwide. However, the application and enhancement of alumina hip joints stumbled due to their poor performance resulting from poor design, inferior mechanical

properties and improper implantation skill by surgeons. The 3rd generation alumina, manufactured by Hot Isostatic Pressing (HIP), represents the greatest improvement in performance compared with 1st and 2nd generation aluminas due to its higher density and finer grain size. However, less *in vitro* data and very sparse *in vivo* data is available about this generation of alumina due to their shorter implantation time in the body compared to the 1st and 2nd generation of alumina grade [11–13].

Despite all the improvements, aseptic loosening is still a clinical issue. The research on retrieved implants that failed due to the aseptic loosening showed that the explanted joints exhibited a localized high wear zone called "stripe wear". Extensive investigations showed that micro separation between the ball and socket during walking results in impact stresses that causes localised high wear. This, in addition to failure of the joints through fracture, necessitated the introduction of a tougher material. A new generation ceramic, called zirconia toughened alumina nano-composite (ZTA), was designed and successfully implanted within the body. It is well documented that the incorporation of zirconia into monolithic alumina introduces a polymorphic phase transformation, which is probably one of the reasons for the improvement of wear resistance. Correspondingly, zirconia inclusion hinders the grain growth of alumina through its pinning effect on grain boundaries and reduces the average grain size of the composite, which predominantly enhances sliding wear resistance of the nano-composite. As corroborated by a few authors [14,15], the grain size effect is directly linked to both the amount of thermal mismatch stresses and slip length. Therefore, grain size refinement will reduce the thermal mismatch stresses and slip length and subsequently the dislocation pile up which results in an increase of the time to transition from mild to severe wear.

Therefore, there exist clear and logical reasons to use a technique that reduces the grain size of the composite. To achieve this goal, spark plasma sintering (SPS) was employed to produce a specimen with high density and a finer grain size. SPS employs simultaneous pressure and temperature to form a specimen in much shorter times compared to conventional pressure-less sintering. Consequently, the first objective of this study was defined as an optimization of material processing to manufacture a well-dispersed composite with superior mechanical properties in terms of hardness, toughness, density and most importantly small grain size.

Currently the best product of the ZTA family called "BIOLOX®delta" is made by CeramTec AG, Plochingen, in Germany, which has the smallest number of failures inside the body. BIOLOX® delta is mainly composed of Al_2O_3, ZrO_2 and a small fraction of SrO and Cr_2O_3. In

addition to the grain size effect, two different batches, with and without these additives were produced to assess the role of these dopants in mechanical reliability of specimens. A newly published paper put this idea forward that these additives change the chemistry of the surface and assist the nano-composite microstructure to resist against hydrothermal degradation and wear in the body. The same author has revealed the attempt of the manufacturer, during consecutive years, to reduce the monoclinic phase of zirconia in the as-received specimens through grain size refinement [16].

Subsequently, the wear resistance of produced composites (ZTA and ZTA-additives) and BIOLOX® delta was examined through lubricated reciprocating sliding wear tests to shed light on the contribution of grain size refinement and the impact of additives on wear resistance of the composite. In other words, the role of these factors namely grain size effect and additives, on the transition point from mild to severe wear, upon increasing the applied load, were assessed and compared.

2 Literature review

2.1 Total hip replacements (THRs)

Various types of joints produce different kinds of motions in a human body. The hip and shoulder joints form a ball-on-socket articulation, other joints such as knee and elbow have a hinged shape. However, the common characteristic of these two different joints is the synovial fluid which flows around them and lubricates the two opposing surfaces. The development of hip joint materials and treatment of deformities in this articulation are the most challenging problems to prosthesis technology in this millennium [17].

Total hip replacement is a surgical procedure to help patients relieve pain, also provides them a chance to regain physical fitness and return them to social function within fairly short period of time after surgery. The emergence of total hip replacement (THR) by Dr. J. Charnley dates back to 1960 and was composed of a metal femoral head fixed to the bone by cement such as PMMA and of the acetabular cup made of Ultra High Molecular Weight Polyethylene (UHMWPE).

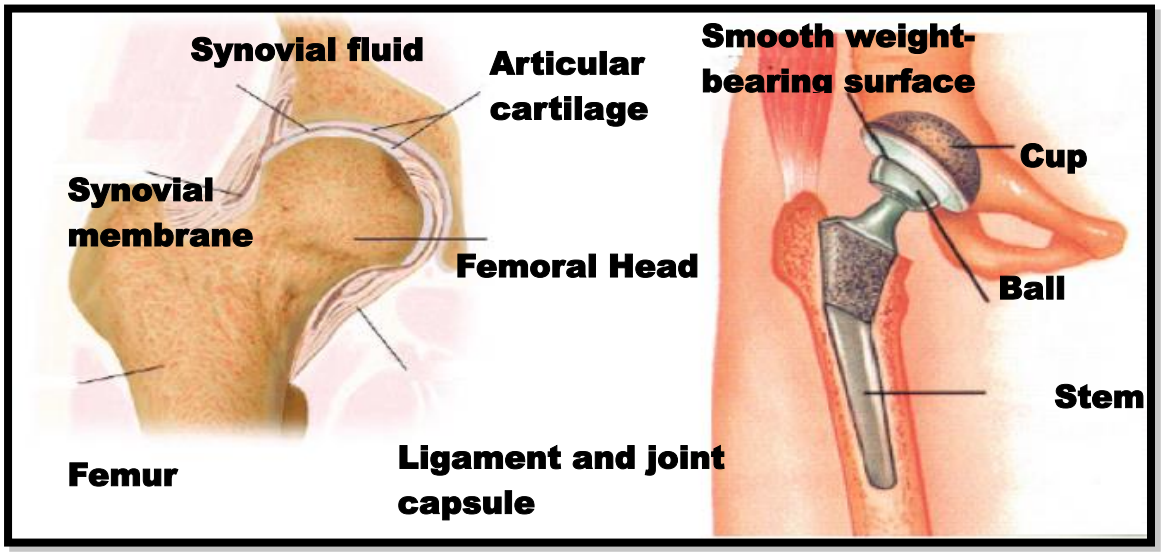

Figure 2.1 (a) Schematic of human hip joint. (b) Schematic of a prosthetic device in total hip arthroplasty [17]**.**

In the late nineteenth, several surgeries with the use of metallic and natural biomaterials and subsequently polymeric biomaterials for treatment of skeletal defects have been reported. Materials to be employed for THR need to fulfil certain requirements including wear resistance,

biocompatibility, low risk of failure *in vivo*, and durability. More specifically, the desired specifications for materials utilized in ball-on-socket articulation should satisfy the following criteria:[17]

(1) High mechanical properties (high fracture toughness, hardness, high strength, high fatigue resistance) with low risk of failure when put through the loads in the body. The loads differ from three times the body weight (~3 kN) for normal daily walking to eight times the body weight (~ 8 kN) for stumbling or jogging
(2) High corrosion resistance and biocompatibility *in vivo*
(3) High hardness and good polished surface for low friction and wear for operation over the long term
(4) Good wetting between articulating surface and the synovial fluids to make a good lubrication *in vivo*

The bearing designs currently in use for the total hip arthroplasty are illustrated in Figure 2.2.

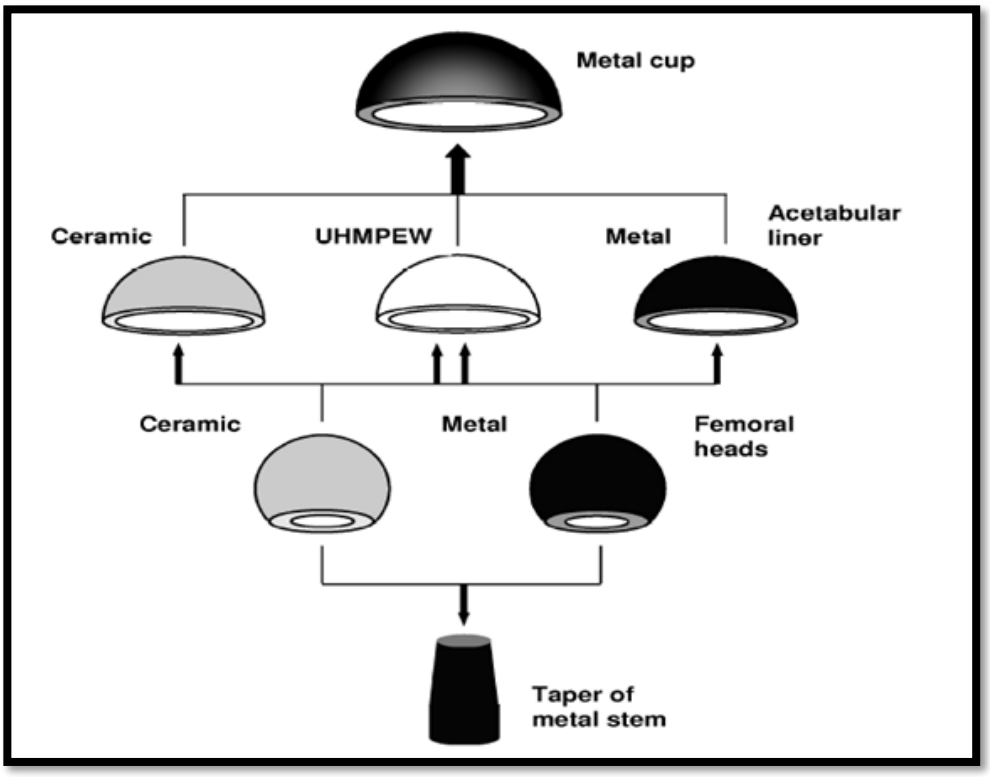

Figure 2.2. Schematic design of bearing currently used in total hip arthroplasty and their classification [17]**.**

The materials that are studied and developed for this application are categorised in three main classes:

(1) Metal alloys (Co-Cr alloys, stainless steel) to be used for femoral heads and acetabular cups
(2) Monolithic oxide ceramics (alumina, zirconia and alumina-zirconia composites) to be utilized in both femoral heads and acetabular cups
(3) Ultra-high molecular weight polyethylene (UHMWP) to be used in acetabular cup to be fixed into a metal cup

2.2 Polyethylene acetabular cups with metallic or ceramic femoral head cups

According to artificial hip joint history, polyethylene acetabular cups coupled with a metal or ceramic femoral head remain the most common bearing combination in the hip [18]. In the long term the polyethylene cups wear and the micron and sub-micron wear particles cause osteolysis and loosening. Osteolysis is due to particle accumulation in peri-prosthetic tissues until a critical volume and concentration is reached. As an example, a polyethylene wear rate of 30 mm^3/million cycles will reach a total wear volume of 500 mm^3 in between 1 and 8 years depending on the level of activity, and this will lead to the osteolysis and failure in some patients. In order to increase the osteolysis-free life-time, the wear rate of polyethylene needs to be be reduced. The introduction of ceramic femoral heads has been demonstrated to decrease polyethylene wear. Cross-linked polyethylene has exhibited 50-80% decrease in wear rates in the laboratory compared to historical polyethylene with further benefit when utilized with ceramic femoral heads [19]. It also produces smaller and more reactive particles. It has been predicted that wear rates of less than 10 mm^3/million cycles give osteolysis-free lifetime of over 20 years and this delivers a good solution for patients over the age of 60, so it is beneficial to consider alternative options for more active and younger people [17].

2.3 Metal-on-metal bearing

In 1951, metal on metal total hip implant was designed by George McKee and John Watson. Metallic prostheses have high strength and toughness though the first generation of metallic prosthesis had high failure rates, due to poor manufacturing and loosening. Furthermore, due to corrosion, wear and adverse tissue reaction rejection rates by the body were high. The soluble metallic salts produced by metallic ions move into the body fluids such as blood and urine. While some metallic salts like those based on nickel are usually removed quickly from the body by urine whereas others such as chromium and cobalt stay longer in the body [20,21]. Up

to now, no direct causal link has been reported in patients with metal on metal implants, though the topic of potential carcinogenesis is still a big concern.

2.4 Ceramic-on-metal bearing

In the case of ceramic on metal bearings, a differential hard on hard bearing was presented recently to decrease wear, compared to metal on metal bearings. This was achieved through design flexibility on the acetabulum by applying a metal insert which allows 36mm heads to be used in patients with size 50mm acetabular sockets and to eliminate ceramic insert chipping. The wear and friction of ceramic on metal bearings has been shown to be less than metal on metal bearings and comparable to ceramic on ceramic bearings [22]. They have also exhibited decreased metal ion levels released in the patient's body compared to metal on metal bearings.

2.5 Ceramic-on-ceramic bearing (COC)

The studies show that alumina on alumina ceramic bearings delivers the lowest friction and wear of all bearing couples, with up to 50 times less than polyethylene, under standard walking situations [18]. So far, the most successful ceramic matrix composite bearings, with increased toughness, reduced risk of fracture and even lower wear rates has been introduced by CeramTec as BIOLOX®Delta [23]. The size of the ceramic femoral head is in the size range of 28-40 mm. These materials perform much better than the most common ceramics Al_2O_3 show high mechanical and acceptable biocompatibility. As COC components exhibit lower wear compared to conventional metal-on-plastic prostheses, the extension in life time of the implant is expected. However, ceramics implants have very low fracture toughness compared to metals or polymer which is not desirable for an implant.

2.6 Monolithic ceramics

2.6.1 Alumina

Aluminum oxide is commonly referred to as alumina (α-alumina), or corundum in its crystalline form reflecting its widespread occurrence in nature and industry. In nature, alumina contains Cr_2O_3 impurities and it is called Ruby and the one including titanium impurities is termed as Sapphire [24]. The crystal structure is often explained as having O^{2-} anions in an approximately hexagonal close packed arrangement with Al^{3+}cations filling two thirds of the octahedral interstices. Figure 2.3 shows the crystal structure of alumina.

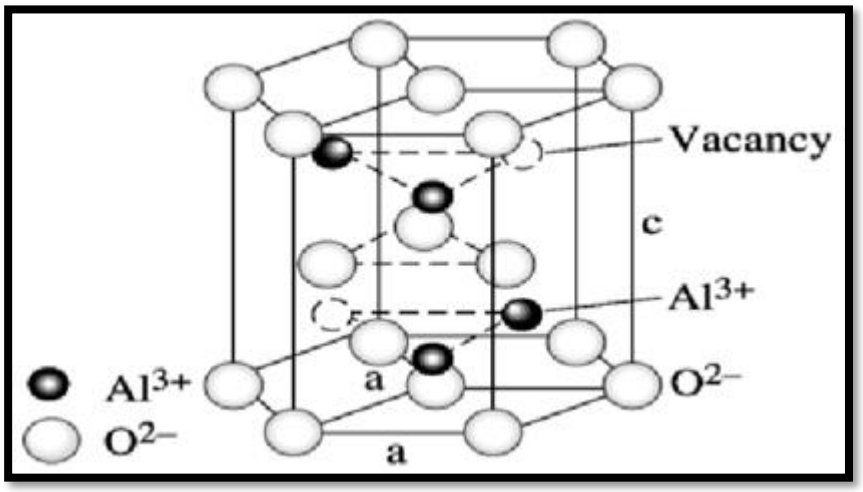

Figure 2.3 Illustration of alumina crystal structure.

In 1930 for the first time alumina was utilized as a biomaterial with a patent by Rock in Germany [25] . In 1970, with the introduction of first generation of alumina hip joint ceramics, the use of ceramic components in joint replacement surgery was initiated and Professor Bautin in France who replaced the traditional metal femoral heads with alumina. However, due to the low density and coarse microstructure these early ceramics were more prone to fracture [25]. With time improvement in the material's quality and processing techniques and a better understanding of ceramic design resulted in the second-generation alumina components that presented better performance than the first generation. Finally, the third generation of alumina continued the trend of increasing density and reducing grain size. Table 2.1 shows the influence of the material characteristics on the mechanical properties.

Table 2.1 Properties of various alumina ceramics [26]**.**

Property	**Alumina Ceramics as specified by ISO 6474**	**1st and 2nd generation Alumina**	**3rd generation HIPed generation**
4-point bending strength	400 MPa	500MPa	580MPa
Mean grain size	< 4.5μ	<3.2 μ	<1.8 μ
Density	3.94 gr/cm^3	3.96 gr/cm^3	3.98 gr/ cm^3
Vickers Hardness	1800 HV	1900 HV	2000 HV

Alumina is one of the most stable oxides [27], and can resist strong acidic or alkaline environment at high temperature [27]. Alumina shows high compressive strength, but as with most ceramics, it has poor tensile strength due to its natural brittleness and once fracture starts

the crack growth is quick (low toughness). The mechanical strength is closely related to density, with an increase in density giving an increase in strength. The mean grain size must be kept small and the presence of a glassy phase at the grain boundaries must be avoided by using high-purity alumina. The high hardness of alumina provides a minimum wear of the femoral heads and of the cups, also because it permits a superior surface quality. Furthermore, the capability of adsorbing polar molecules advances the creation of a liquid film providing the lubrication between the ceramic head and the socket [26].

Despite the aforementioned good mechanical characteristics, alumina suffers from low fracture toughness (~4 MPa $m^{1/2}$) and the vulnerability to fail at stresses below the maximum fracture strength through slow crack growth [28]. Consequently, the application of alumina is limited to particular type of prosthetic design. For example, ball heads made of alumina should be designed to a diameter larger than 28 mm to avoid risk of failure *in vivo* [28].

Alumina was initially introduced to the dental device industry by Dr Sami Sandhaus, who developed the application of polycrystalline alumina in entire medical devices, the CBS dental implant [29]. Besides the excellent benefit of aesthetic and biocompatibility, alumina has exhibited several weaknesses in terms design, stiffness, low flexural strength and fracture toughness in addition to defects appeared through surface grinding have resulted in failures on these devices [29].

2.6.2 Zirconia

2.6.2.1 Structure and properties of zirconia

Zirconia (ZrO_2) can possess good mechanical properties such as high tensile strength, high hardness and corrosion resistance. However, zirconium oxide cannot be found in pure form in nature, but Zircon ($ZrSiO_4$) is the principle precursors. The name of the metal zirconium comes from the Arabic word *Zargon* which is originated from two Persian words Z*ar* (Gold) and *Gun* (colour) [30]. Zirconia is known to have three different polymorphs; monoclinic, tetragonal and cubic which is shown in Figure 2.4.

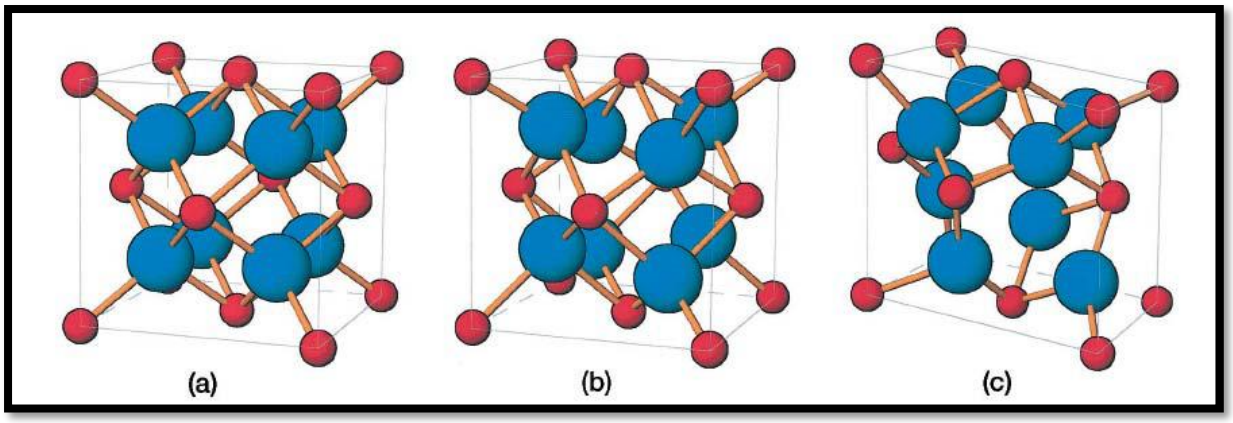

Figure 2.4 Zirconia crystal structure for (a)cubic,(b) tetragonal ,and(c) monoclinic [31]**. The blue circles represent O atoms and red spheres represent Zr atoms.**

The monoclinic structure is stable at room temperature and transforms to tetragonal phase at 1170ºC. As the temperature increases, the tetragonal polymorph transforms to cubic phase at 2370˚C. This phase remains stable up to 2680ºC once it starts melting.

Zirconia can be categorised into three groups; partially stabilized zirconia (PSZ) such as magnesia stabilized zirconia named as (Mg-PSZ) and zirconia toughened dispersed ceramics (ZTC/ZDC) in which zirconia as one of the components is dispersed in ceramics matrix *e.g.* Zirconia Toughened Alumina (ZTA). Finally tetragonal zirconia polycrystals (TZP) in which the tetragonal phase is retained at room temperature in metastable form by the addition of cerium (Ce-TZP) or yttrium oxides (Y-TZP)[32,33]. Although TZP contains predominantly tetragonal phase [34], small amounts of cubic phase are frequently present as well [35]. Another way to stabilise tetragonal phase is to reduce the size of grain to nanoscale which are generally in the range between 0.2-1µm [36–38] . Generally, zirconia stabilized with yttria has better mechanical properties compared with other types namely partially stabilized zirconia (PSZ). The processing parameters and amount of yttria used in the formation of Y-TZP are decisive factors for its mechanical properties [35]. Provided the processing conditions are optimised, metastable zirconia exhibits the highest value of fracture toughness of any ceramic material. Another motivation for application of zirconia in THR is attributed to reduced frictional torque and consequently decreased amount of polyethylene debris formed in zirconia head and polyethylene acetabular cup articulation [39]. In such a system the wear rate is lower than even alumina [40,41] though *in vivo* studies revealed a delayed failure [42]. However, there are major concerns of the application of zirconia is related to its hydrothermal stability that questions the use of zirconia-on-zirconia articulation in body [43].

2.6.2.2 Transformation toughening

The concept of transformation toughening was introduced for the first time by Garvie et al. [44] and afterwards by Gupta et al.[45]. Transformation toughening is a mechanism related to the phase transformation of metastable tetragonal grains to monoclinic t→m in a region of high stress region at the head of a crack and is accompanied by a volume expansion. As a crack propagates [35] and passes through a matrix of metastable tetragonal zirconia grains local stress concentrates in the material. Subsequently, the mechanism of phase transformation is activated in the vicinity ahead of the crack tip (frontal zone) where the highest stress is accumulated. During crack growth the monoclinic transformation in the crack wake acts to close the crack, an effect known as crack shielding. It is this crack-wake effect that results in the increase in toughness, Figure 2.5. Accordingly, the crack resistance force increases as the crack grows into the constrained zone, i.e. the toughness increases as the crack grows up to the critical fracture toughness, K_{1c}. This is called as R-Curve behaviour.

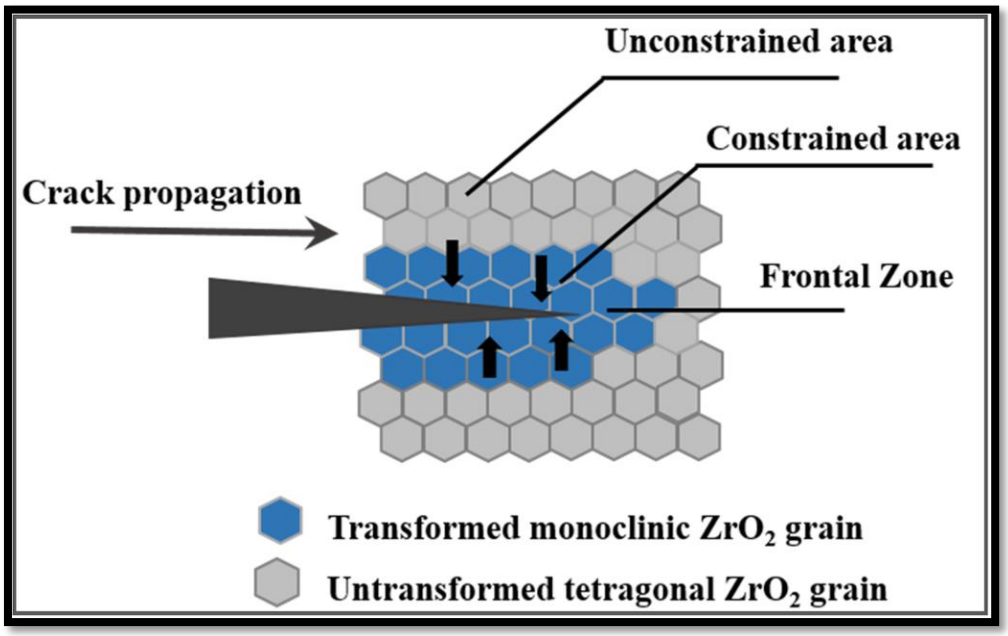

Figure 2.5 Schematic of the stresses arising from crack propagation in a transformation toughened ceramic [46]**.**

2.6.2.3 Subcritical crack growth

It is well known that ceramics materials suffer from subcritical crack growth (SCG) that is defined as a slow propagation of a crack. This phenomenon generally occurs when the stress intensity factor K_I is less than toughnessK_{IC}. The subcritical crack growth is extremely sensitive to applied load and is influenced by environmental factors including temperature and other

external variables [43]. SCG in bio-ceramics is associated with the corrosive action in the stressed zone at the crack tip under constant load or a pre-existing defect in the material [43].

Figure 2.6 illustrates three distinct zones, describing the crack growth velocity (V) against stress intensity factor of the inserted force (V-K_I). Among these three zones, only region I is associated with the low growth velocities and it has attracted the most attention due to the possibility of calculation of the survival of ceramic materials [47].

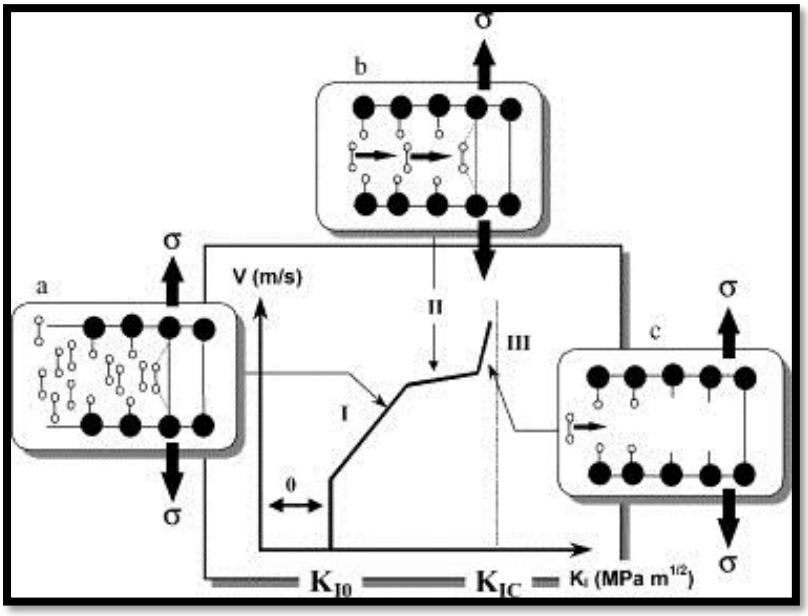

Figure 2.6 Schematic illustration of different crack velocity zones observed in experimental *V-K$_I$* graphs [43]**.**

2.6.3 Zirconia toughened alumina composite (ZTA)

Zirconia toughened alumina composites have been developed for biomedical applications to overcome the low fracture toughness of alumina and aging susceptibility of zirconia. The idea behind development of these novel materials is the belief that they exhibit a combination of the good mechanical properties of alumina, particularly hardness and at the same time enhancing the toughness of the composite through zirconia transformation toughening mechanism, without the major concern of the ageing under steam or body fluid.

Zirconia-alumina composites developed for biomedical applications can be either zirconia rich or alumina rich. The example of alumina rich composite is zirconia toughened alumina that typically contains 60-95 vol% alumina. In June 2000, ZTA femoral head commercialized under the trade name of BIOLOX® delta by a German Company called CeramTec AG. During the last 10 years, about one million of ZTA femoral head and more than 700, 000 inserts under this

brand have been internationally implanted. Bioceram® AZ209 is another product made out of ZTA by KYOCERA Medical in 2011 (Osaka, Japan)[48].

The ZrO_2 particles can have a m-phase structure or t-phase structure (or a mixture of both), but the largest improvements in strength and fracture toughness has been reported when the particles have a t-phase structure [49–52]. The critical factor is that t-ZrO_2 particle size, controlled by the composition and fabrication conditions to optimize the transformation toughening in ZTA [49]. In this composite, the ZrO_2 particles that are constrained by the Al_2O_3 matrix should have sizes below the critical value to avoid any significant transformation from tetragonal to monoclinic phase [25].

When compared with single α- Al_2O_3matrix, ZTA presents the high hardness of the Al_2O_3 matrix, coupled with advantages in strength and fracture toughness. Due to the presence of t-phase ZrO_2 particles in this composite the potential for strength degradation caused by aging in moist environments is not as severe as in Y-TZP. However, the concentration of Y-TZP particles for the application in total hip replacement should be below the percolation limit (about %16. vol) [17]. This is to prevent the formation of contiguous network in Y-TZP which is responsible for aging in material through nucleation and growth mechanism [17, 53]. It has quantitatively demonstrated that aging, as measured by the amount of tetragonal to monoclinic conversion, was almost absent in ZTA for less than %16 volume Y-TPZ particle but it does increase with addition of Y-TZP [54]. In addition, aging of ZTA including 14 vol.% Y_2O_3 stabilized ZrO_2 particles for long periods (19 months) in Ringer's solution was reported to increase the formation of a surface layer of monoclinic ZrO_2 that results in 10% reduction of flexural strength [17]. These results show that despite the improvements in both composition and architecture of ZTA composites, further investigation is required to be performed. Biolox® Delta, a commercialized product by CeramTec AG, is a ZTA but also contains small quantities of SrO and Cr_2O_3[55]. These additives react with alumina and form plate-like alumina grains that produce extra toughening mechanisms through crack deflection and crack bridging [56].

2.6.3.1 Platelet reinforcement ($SrCO_3$)

Alumina as a successful candidate for structural applications, suffers poor fracture toughness or brittleness. To enhance the poor fracture toughness in alumina, alumina-based composites have been produced with the addition of zirconia particles [57,58], SiC whiskers [59] and metallic[60] or ceramics particles [61]. For this study yttria-stabilized tetragonal zirconia (3Y-TZP) was selected as a reinforcement constituent of in alumina matrix. The mechanical

properties of ZTA composites is partially related to the stability of zirconia tetragonal phase. In other words, the environmental conditions such as moisture might lead to the transformation (tetragonal to monoclinic phase) in yttria zirconia grains at low temperature of about 100ºC. Of course, the toughening behaviour of zirconia does not occur above the martensitic start temperature due to the stability of tetragonal phase [62, 63]. While the stable tetragonal phase is present in the composite, the mechanical properties cannot enhance because the zirconia grains exhibit inert behaviour towards cracks propagation due to the lack of sufficient tetragonal- monoclinic transformation. Consequently, the incorporation of other toughening element to maintain the fracture toughness in satisfactory level is of a great interest. One of the main candidates which meets the required conditions to incorporate the Alumina matrix and assists the toughening process is Strontium. The presence of alkali earth oxides such as Sr in the alumina based composite leads to the formation of hexaluminate which develop plate-like or elongated grains if special procedures for preparation are employed, Figure 2.7.

Cutler et al. [64] reported that by small quantity addition of $SrZrO_3$ into Ce-TZP-Al_2O_3 matrices, the plate like crystal structure of strontium hexaluminate can be formed leading to the improvement of flexural strength and fracture toughness. This finding is fully compatible with the results obtained by Masichio et al. [65] which demonstrates higher fracture toughness in Al_2O_3-Cr_2O_3/ZrO_2 matrix. Balmonte et al. [66] and Maity et al. [67] demonstrated the enhancement of mechanical properties in zirconia toughened alumina by incorporation of calcium and strontium hexaluminate. Therefore, reinforcement as well as enhancement of mechanical properties of alumina based composites can be achieved by incorporation of such additives. Figure 2.7 shows how a platelet particle (elongated grain) deflects the pathway of a crack in a composite through which the fracture toughness gets improved.

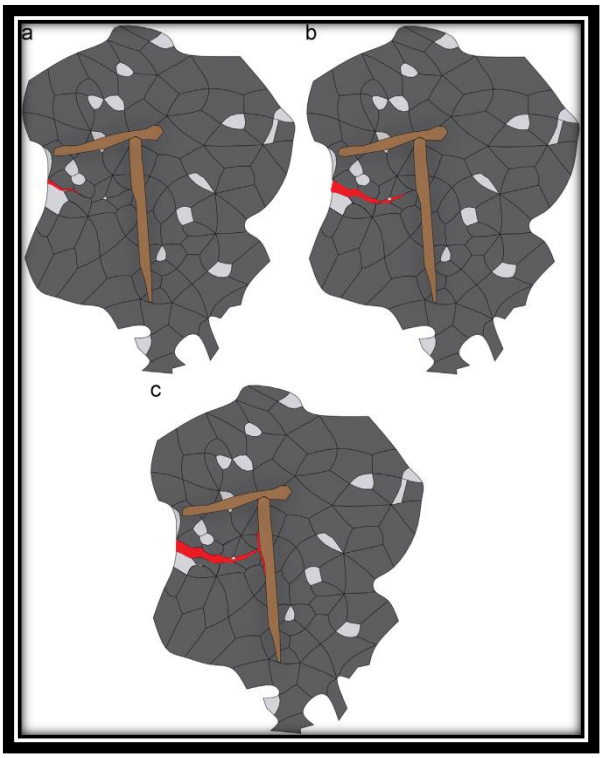

Figure 2.7 Schematic illustration of a crack (red pathway) that reaches a platelet particle (brown particles) in zirconia toughened alumina composite and gets deflected by an elongated grain [48]**.**

2.6.3.2 Solid solution hardening (Cr_2O_3)

Alumina as a well-known ceramic for structural application suffers from low fracture toughness. The inclusion of hard reinforcing particulates in the matrix can improve the fracture toughness. In addition to the incorporation of a second phase such as zirconia, solid solution strengthening has been widely employed. Chromium oxide and alumina have the same hexagonal crystal structure leading to the formation of substitutional solid solution at temperatures between 950ºC and 2100ºC [68]. In addition to enhancing toughness, the addition of chromium oxide in alumina matrix enhances the hardness, the tensile strength and resistance to corrosion and thermal shock [69]. However, the densification of chromia- doped alumina in air is very low due to the vaporization- condensation sintering mechanism. Therefore, chromia doped alumina requires a reducing environment or vacuum to reach high density [70]. In a study conducted by Pezzotti et al. [71], the incorporation of chromia in zirconia toughened alumina (ZTA) leads to the deceleration of hydrothermal degradation in the zirconia. In the same study, the role of alumina was described as a self-sacrificing component which confines moisture on its surface and prevent phase transformation in zirconia. While using chromia in

zirconia toughened alumina, especially yttria with zirconia, due to the strong interaction between chromia and both the alumina and zirconia phases, the diffusion of water into the zirconia phase gets inhibited. Consequently, due to the quick formation of oxygen vacancies in the chromia-alumina matrix, the hydrothermal attack in yttria stabilized zirconia is also inhibited [71].In addition, chromium oxide acts as sintering aid in yttria stabilized zirconia and also prevents the growth of grains in zirconia [72]. In contrast, it is reported that chromium oxide retards the densification process in alumina matrix [73] and also small fraction of this oxide (0.6% weight) in ZTA structure increases grain growth and forms plate-like-shaped grain [74]. Consequently, the requirement of chromia doped alumina to be sintered at high temperature and under reducing environment makes Spark Plasma Sintering (SPS) a good candidate to achieve this goal.

2.7 Powder processing

Synthesis of powder as an initial step of powder processing strongly influences the successive processing stages. The proper selection of processing route is critical to producing a highly dispersed and densified composite with a minimal number of residual flaws in the microstructure. The mechanical properties of the ZTA composite depend strongly on the grain size of the two phases and the degree of dispersion of the zirconia in the alumina. This calls for a precise control over the powder processing parameters to gain a homogenous dispersion of both alumina and zirconia.

Up to now, various techniques have been applied to produce zirconia toughened alumina composites. Among those traditional mixing [75–77] and wet chemical processing including sol gel [78–80], co-precipitation[81,82] and hydrothermal routes [83] are of a great importance. As expressed in the literature, traditional milling-mixing is the most commonly employed routes to form bi and tri phase composites out of common oxide powders. This procedure requires a careful control of raw powder characteristics such as size, size distribution, surface area, agglomeration and the morphology of particles to produce high stabilized suspension [28]. It is well documented that a large range of size distribution results in high packing density in green bodies though under these circumstances the growth of larger grains can take place at the detriment of smaller grains leading to coarsening. On the other hand the fine staring particles enhance densification rate due to their higher specific surface area if their tendency for agglomeration to be monitored [84]. Extensive research [85] shows that agglomeration of

powder causes heterogeneity of particle packing in green body and intensifies both differential sintering rates and inhomogeneous composite microstructures [86].

During wet powder mixing, an instability of the suspension can result in microstructure defects, aggregates and non-uniform dispersion of second phase in the composite. Therefore, the degree of dispersion and the rheological behavior of the suspension must be controlled through a careful selection of dispersant type and amount, pH, and milling time [76].

Due to the Brownian motion, gravity and Coulombic forces, particles are easily attracted to each other leading to agglomeration and destabilization of the suspension. If two colloidal particles are brought to close vicinity, they are attracted to each other due to van der Waals forces. When the dominant force is attraction, the particles stick to each other and eventually coalescence takes place in the colloid. On the other hand, the domination of repulsive force results in a stable and dispersed system [43]. In fact, the stability of the colloid arises from balancing between attractive and repulsive forces.

In general, there are three different types of stabilization in a colloidal system:

(1) Electrostatic stability

(2) Steric stability

(3) Electrosteric stability

2.7.1 Colloidal method to synthesize zirconia toughened alumina composite powder

2.7.1.1 DLVO theory

DLVO theory is a classical explanation of the stability of colloids in suspension and named in 1940s by Derjaguin , Landau, Verwey and Overbeek [87]. Based on DLVO theory [88], the colloidal stability of a system is determined by total potential energy of particles (V_T) Figure 2.8 Total potential energy is the sum of the attractive potential due to the van der Waals force (V_A) and potential energy due to the repulsive electrostatic interaction (V_R).

$$V_T = V_A + V_R \qquad \text{Eq. 2.1}$$

For the spherical particles with radius a at a distance h, V_T is defined as,

$$V_T = -\frac{A}{6}\left(\frac{2a^2}{H^2-4a^2} + \frac{2a^2}{H^2} + Ln\,\frac{H^2-4a^2}{H^2}\right) \qquad \text{Eq. 2.2}$$

where is $H = h + 2a$, A is the Hamkar constant. On the other hand V_R is expressed as;

$$V_R = 2\pi\varepsilon\varepsilon_\circ\emptyset_\circ^2 \, ln(1 + e^{-kh}) \qquad \text{Eq. 2.3}$$

where ε is the dielectric constant of liquid dispersion medium, $\varepsilon_\circ$ is the permittivity of the vacuum $\emptyset$ is the surface potential of particles, K is the Debye parameter.

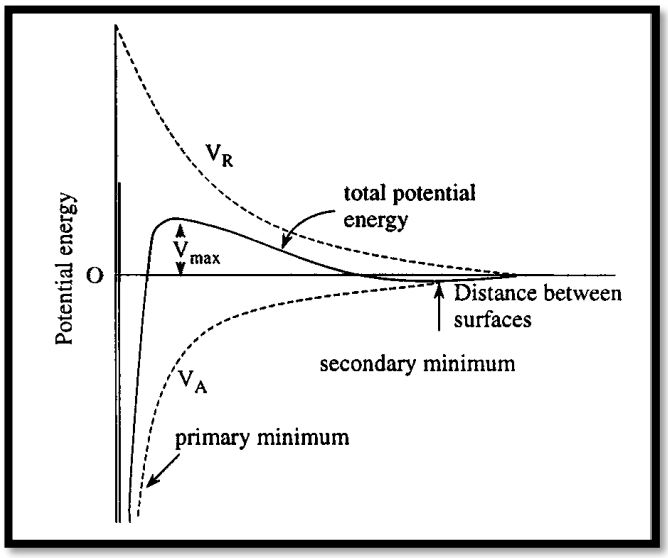

Figure 2.8 Schematic of typical energy barrier for two plates charged based on DLVO theory [88]**.**

2.7.1.2 Electrostatic stabilization

In liquid media, the adsorption of ionic species to the surface of a colloidal particle forms a charged film around the particle. Subsequently, an equal number of oppositely charged ions surround the colloidal particles to retain electro neutrality and raise the total charge-neutral double layers.

The interfacial layer around a dispersed particle that contains both adsorbed ions on the particle surface and the plane of the counter charged dispersion medium (Stern plane) is called the Electric Double Layer. The electric double layer is electrically neutral, and it is composed of three parts; surface charge, stern layer and diffuse layer as shown in Figure 2.9. The maximum value of electrical potential inside the electric double layer belongs to the surface of the particle or Stern layer. However, the electrical potential reduces while moving towards boundary of the electric double layer. One of the parameters that plays a key role in determining the stability of colloidal system is called the zeta potential (ζ). Theoretically, the amount of zeta potential has originated from the value of electric potential at the slipping plane [88]. The greater magnitude

of zeta potential results in more stable suspension. When this value is around isoelectric point (IEP), the potential is small and the attractive forces may exceed repulsive force leading to flocculation or coagulation in suspension [26]. In general, electrostatic stabilization is due to the mutual repulsion between similar electrical charges. In any system including ions, electrostatic interactions are present. In water or any other media with high dielectric constant, the natural surface charges of the particles can repulse each other. In addition, other mechanisms such as ionization or disconnection of surface group, adsorption or attachment of ions to a particle surface, or exchange mechanisms like acid base type interaction are sources for existence of ion in the suspension [89].

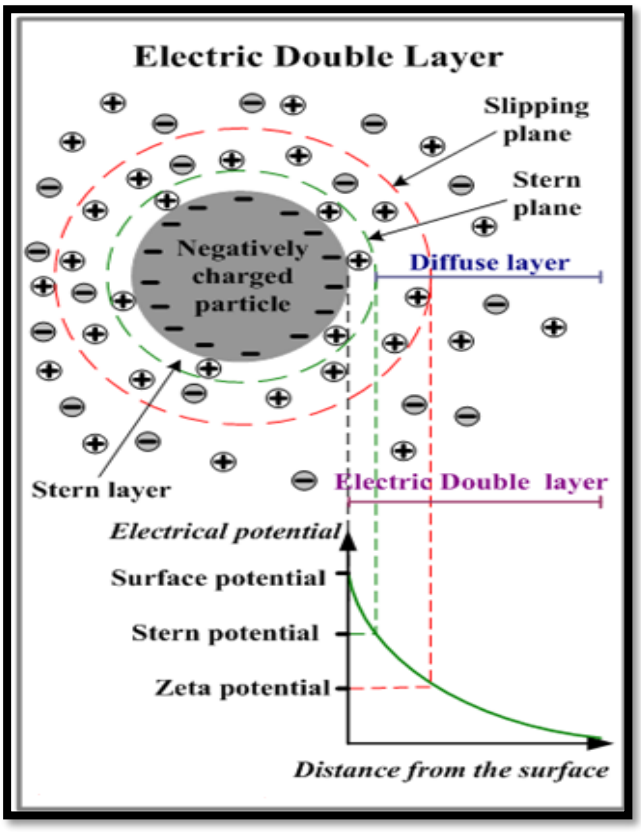

Figure 2.9. Schematic of electric double layer [88].

2.7.1.3 Steric stabilization

An alternative way to stabilize a colloidal system is called steric stabilisation. In this type of stabilization, the macromolecules attach (graft or chemisorb) to the surface of colloidal particles and produce a barrier between surface of the particle and other particles surrounding, as illustrated in Figure 2.10. To obtain pure steric stabilization, two conditions need to be satisfied; firstly, the dispersant molecules should strongly anchor to the surface of colloidal

particle; and secondly, sufficiently long chain of dispersant in solution is required to prevent close vicinity of neighboring particles [89].

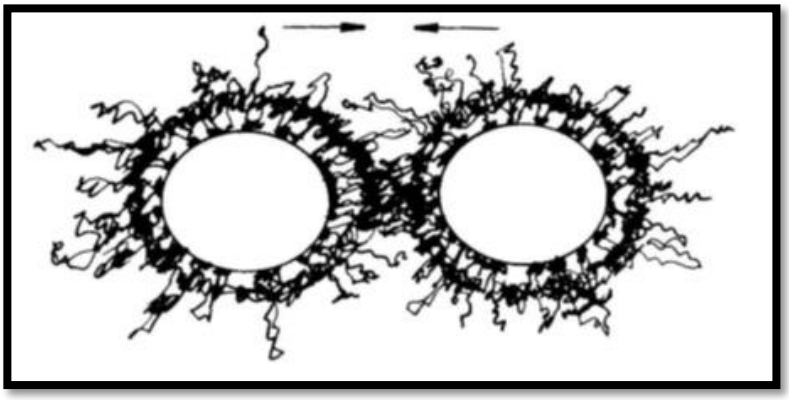

Figure 2.10 Schematic of Steric Stabilization[90]**.**

2.7.1.4 Electrosteric or semi-steric stabilization

The combination of steric and electrostatic stabilization forms a new type of stabilization, which is called electrosteric or semi steric. Small molecules such as oleic acid or stearic acid are known to be effective in stabilization in organic media though, as these molecules are not sufficiently long to produce pure steric stabilization (shown in Figure 2.11). After adsorption, such molecules modify the Hamakar constant of the particles and therefore the attractive van der Waals force between particles drops. It is well documented that dispersion of many ceramics [91] takes place through this type of stabilization.

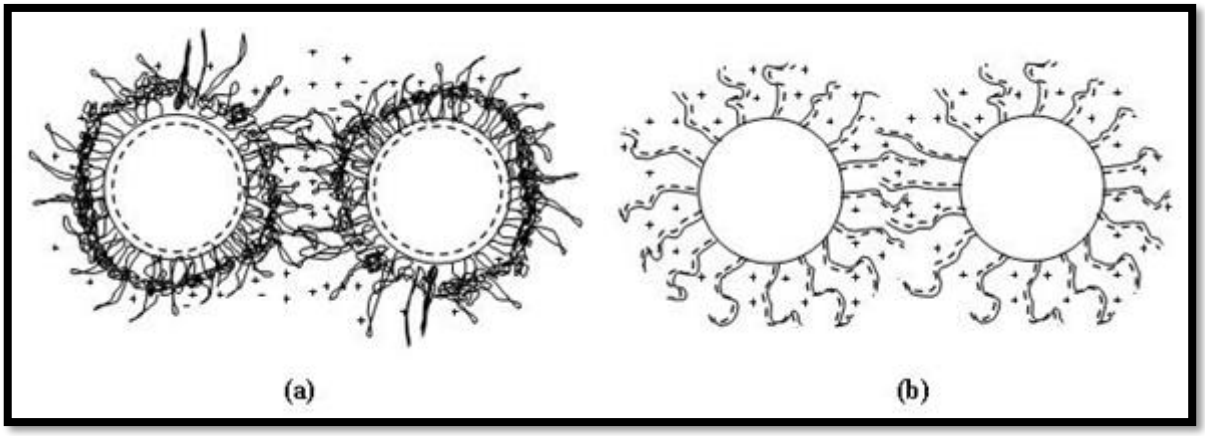

Figure 2.11 Schematic of electrosteric stabilization (a).Two charged particles with non-ionic polymers (b).Polyelectrolytes linked to uncharged particles [90]**.**

Based on the conditions and properties of colloidal particles, the right selection among the three aforementioned methods leads to well dispersion of suspension. Ramakrishnan et al. [92]

reported that improper selection of pH range causes heterocoagulation in a mixed Al_2O_3 and ZrO_2 suspension. The experimental results showed that this suspension is unstable in a pH range between 7 and 9 where the surface is highly charged to oppose van der Waals' attractions.

Novak et al. [93] noticed that species such as CO_3^{2-} and Cl^- in Al_2O_3 and ZrO_2 suspension shifts the isoelectric point of each powder as well as their mixed suspension due to the adsorption of ions on particle surfaces. They also reported that washing of the ceramic particles before production of suspension optimize both dispersion and density. Leriche et al. [94,95] developed a well dispersed microstructure of zirconia and alumina through electrostatic stabilization. They tried different pH ranges and mixed Al_2O_3, ZrO_2 and Y_2O_3 slurries after individually deflocculation process to reach satisfactory dispersion.

2.7.2 Chemical methods to synthesize zirconia toughened alumina composite powder

In addition to the conventional method of ZTA powder synthesis, the chemical methods are developed with the purpose of careful control over size and dispersion of alumina and zirconia particles to inhibit aggregation of particles. Among these routes co precipitation and sol gel are well known and mainly utilized. A good review and role of different wet chemical methods to produce ZTA composites are compiled by Rana et al. [82].

2.8 Spark plasma sintering (SPS)

Spark Plasma Sintering (SPS) or field assisted sintering technique (FAST) is a new technique to consolidate powder by applying both uniaxial mechanical force and pulsed direct electrical current (DC). This method benefits from direct transmission of energy within the sample if the green body is electrically conductive. However, for electrically non-conductive powder, an electrically conductive part needs to be employed and the produced heat by Joule heating can be transferred to the powder [96]. Spark plasma sintering is a fast sintering method allowing the dissipation of heating power in both macroscopic and microscopic scale where energy needs to be acquired to weld the contact points of sintering powder. This behavior leads to the quick densification with less grain growth. Compared with other sintering techniques such as hot isostatic pressing (HIP), hot pressing (HP) or atmospheric furnaces, SPS has many advantages including rapid heating rate, precise conduction of sintering energy as well as easy, reliable and safe operation [97].

The heating rate in SPS depends on geometry, electrical and thermal properties of tooling parts (punch and die) as well as the supplier producing electric power source. Considering of these parameters, SPS is able to reach a rate as high as 1000º C/min. It is known that SPS efficiently employs the heat input due to the use of pulsed electric current [98]. In order to achieve homogenous temperature dissipation, the problem of sufficient electrical conductivity of powder needs to be considered. To obtain a homogeneous sintering performance, the temperature gradients within the sample need to be reduced. Temperature distribution within the sample is strongly influenced by some parameters including electrical conductivity of the specimen, the thickness of die wall and the presence of graphite papers between sintering body and graphite tooling components. These graphite papers can avoid the direct connection of the specimen with other graphite parts and also certify that all parts are electrically linked.

2.8.1 Configuration of SPS

The primary configuration design of FAST/SPS is illustrated in Figure 2.12 [98] which shows various components of the sintering system with vertical uniaxial press, water cooled vacuum chamber, atmosphere controls, special sintering pulsed direct current supplier and SPS controller.

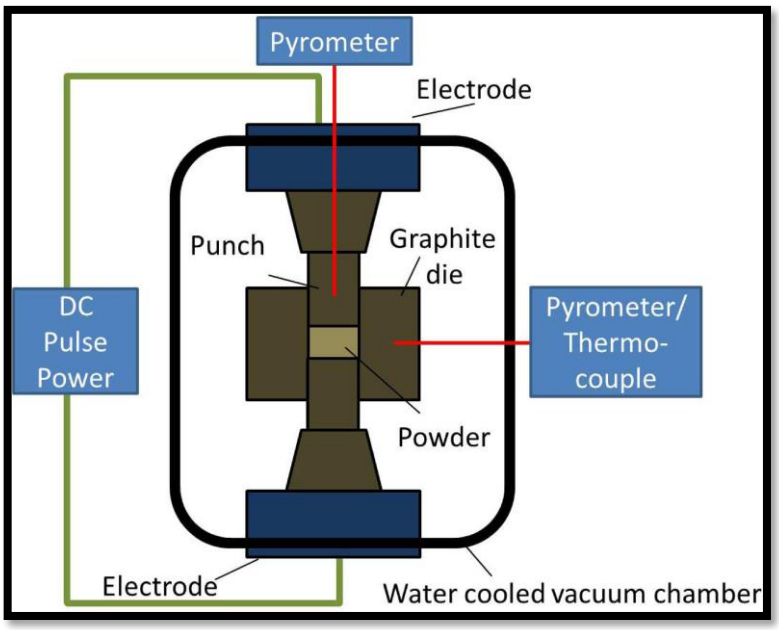

Figure 2.12 Schematic of SPS configuration [98]**.**

The sintering process can be performed under vacuum or inert gas at atmospheric pressure. Monitoring of the sintering cycle is carried out by measuring of temperature using either axial/radial pyrometers or thermocouples [98]. The green body is piled up between the die and

punch and held between two electrodes while sintering is taking place. Using the standard graphite papers, the maximum temperature that can be reached is around 2400ºC.

2.8.2 The sintering mechanisms in SPS

2.8.2.1 Mechanical effect

SPS employs the quasi-static compressive mechanical pressure resulting in more contact between particles. This pressure leads to improving the densification mechanisms already existed in free sintering such as grain boundary diffusion, lattice diffusion and viscose flow. Alternatively it can activate new densification mechanisms such as plastic flow or grain boundary sliding [17]. During the sintering process in the SPS apparatus, the pressure can raise up to several hundreds of MPa leading to possible break of powder agglomerates. This rearrangement of particles while the temperature is low gives rise to the packing and homogenous densification and lessens the pore size and grain growth. Munir and co-workers [96] reported that in cubic zirconia, in order to reach %95 density, the required temperature reduces linearly with the logarithm of inserted mechanical pressure. Furthermore, while the applied pressure at constant temperature does not affect the grain size, it drastically influences the density of zirconia at 1200ºC for 5 min.

2.8.2.2 Thermal effect

In addition to pressure, the high heating rates in SPS is of great importance. When the activation energy of densification mechanism such as grain boundary diffusion surpasses the activation energy in coarsening mechanism such as surface diffusion, it is quite favorable to rapidly reach the maximum sintering temperature to improve densification rate and delay coarsening. Regardless of the sintering approach, for all heating rates fully or nearly dense samples can be obtained and those were rapidly thermally heated form a smaller grain size compared to the samples gone through slow heating rates [99,100]. It is reported [101] that significant grain size reduction can take place in the final alumina microstructures heated with the rates of 50ºC min^{-1} to 700º C min^{-1} compared to that have gone through slower heating rates.

Being diffusion controlled, grain growth requires time at high temperature in order to increase the mobility of grain boundary. If the green body is held at high temperature for short time, the coarsening will be reduced. Furthermore, higher heating rates reduce interaction between the sample and graphite parts and also in some nano structured materials such as zinc oxide and hydroxyapatite [102,103] produces higher density specimen. Based on the study performed by

Munir et al. and Zhou at al. [104,105], the heating rate ranging from 50-300ºC/min has no significant effect on the final density of fully stabilized cubic zirconia and alumina while it significantly influences the grain size.

Another thermal effect in SPS is associated with high local temperature gradient or inhomogeneous distribution of heating plus macroscopic temperature fields forming thermal stresses[106]. Extra driving force for diffusion mechanism produced by microscopic temperature gradients is recognized as Ludwig-Sorret thermal diffusion or it might even activate local melting. On the other hand, depending on the physical properties as well as range of particle size and grain boundary, these local gradients can get greater [107]. However, it appears that for ceramics which are either mixed or ionically conducting and also range of grain size is in scale of sub- micrometre or micrometre, the achievable (possible) local temperature gradients can be ignored.

2.8.2.3 Electrical effect

In SPS if the green body is electrically conductive, the majority of electric current passes directly through the powder rather than neighbouring graphite tool. In these circumstances, there are three possible interactions between electric current and powder bed while going through sintering process, (i) percolation effects of the current while the sintering powder is porous [108,109], (ii) the Peltier effect at the boundary between powder bed and punches [110], (iii) electro migration and electrochemical reaction [96].

Electrical fields are found to influence defect migration of grain boundary and transport of matter[111,112]. Nevertheless, the voltages employed in SPS are quite low and that is why some possible aforementioned effects have not been observed. For instance, in terms of alumina and stabilized zirconia the obtained results in SPS were the same as hot pressing considering the processing parameters were similar. Makino et al. [113] showed that a current as small as ~100 mA flows through the alumina sample at 1000ºC. In another study carried out by Tommino et al. [114], no flowing current within the alumina samples was observed.

2.8.2.4 Effect of atmosphere

In general, defect structure and diffusivity in the materials during sintering are affected by the composition of the sintering atmosphere plus the amount of pressure resulting from constituting elements. Principally, the adsorption of particular types of gas, water or organics reduces the surface energy of particles since this adsorption leads to the modification of thermodynamical

driving force to surface reduction and sintering. Furthermore, in some cases gases are captured in closed pores that results in disinterring due to the accumulation of pressure [115].

If the gas pressure in the sintering chamber reduces, the surface contamination of particles in sintering body will decrease. On the other hand, some experimental tests should be run in vacuum to prevent the possible reaction of specimen with the flowing gas such as nitrogen, hydrogen or oxygen in chamber. As the temperature rises above 600ºC, the graphite sections (punch and die) initiate to react with oxygen entrapped in samples leading to the continuous reduction of oxygen partial pressure in the furnace and particularly in the pressing compartment.

During sintering process, the reaction of adsorbed moisture, oxygen, or entrapped oxides in powder bed with graphite produces a reducing atmosphere by the formation of CO. Subsequently powerful gas phase transport can be formed between the specimen and the graphite die during the time that open pores are existed. This causes the reduction of oxides. The results of reducing atmosphere on some oxides such as $BaTiO_3$ and yttria- magnesia composite have already been published [116,117].

2.9 Definition of bio-tribology

The term tribology is originated from the Greek words *tribos*=rubbing/friction and *logos* =science [118]. Tribology can be defined as a science of interaction between surfaces in relative motion and includes the concept such as friction, wear and lubrication. While the aspects of study is associated with human body or animals, including both natural and artificial joints (e.g hip joint), the term “bio tribology” is employed.

2.10 Ceramic-on-ceramic THRs *in vivo*

Amanatullah et al. [119] ran a short term study (60 months) of 125 ceramic-on-ceramic hip joints and compared the results with 95 ceramic-on-UHMWPE bearings. The clinical outcomes revealed that both materials are statistically similar though in 3.1% of ceramic-on-ceramic bearing audible noise of “squeaking “took place.

Another follow up study performed by Stafford et al. [120] during 59 months in which 6 out of 250 ceramic-on-ceramic went through revision. The results showed that two were revised due to the recurrent dislocation secondary to impingement, two of them for severe infection, one due to fracture of the femoral head and one for recurrent dislocation [121]. These patients did not experience “squeaking” though they confirmed that they experienced a grinding or

crunching noise chiefly during flexion position. One of these "squeaking joints" belonged to a BIOLOX®delta which did not go through a revision surgery. The follow up studies confirm that "squeaking joints" do not necessarily go through revision process.

There are many follow up studies (*in vivo*) that certify the exceptionally good performance of ceramic-on-ceramic hip joints. However, early dislocation did occur with the occurrence possibility of 0%-2.3% [120,122–127]. Component fracture 0%-2.3% [119,128–134],mal-positioning of joint during surgery [134] and loosening are the main concerns that may lead to the failure of hip joint prosthesis.

2.10.1 Lubrication *in vivo*

In the natural joint in a body, the femoral head and acetabular cup are lubricated with synovial fluid which covers them up with a thin layer called cartilage and protect them from direct contact. Normal synovial fluid shows a non-Newtonian shear thinning behaviour with a medium to high range of viscosity. The reason behind low frictional resistance to joint motion is attributed to a mixture of mechanisms. Each of the involved mechanism acts as a supplement for the other and also relies upon the tissue engaged and the load transferred to the joint. Surfaces that are in contact during sliding motion against each other give rise to the frictional resistance that have been specified at the outset as a soft tissue interface synovium on synovium and additionally as cartilage on cartilage type [135].

Synovial fluid lubricates synovial surfaces through hyaluronate which is based on the boundary mechanism. During boundary lubrication each sliding surface is covered with a thin layer of lubricant that separates the moving surfaces and eases the sliding with a low coefficient of friction. The mechanism involved in cartilage on cartilage lubrication is related to boundary effect and existence of fluid layer. The boundary effect of synovial fluid in cartilage on cartilage system is the same as soft tissue system however the boundary of synovial fluid is due to the glycoprotein content of synovial fluid [135].

Synovial fluid is able to lubricate the natural joint in body, but it has not been designed to lubricate other type of materials such as ceramic or metal. Although the surface of ceramic joint is hydrophilic due to its nature, it cannot be lubricated by synovial fluid when wear damage occurs so wear rate and friction rise.

2.10.2 Friction of ceramic-on-ceramic *in vivo*

It is well recorded [136] that *in vivo* artificial hip implant goes through higher rate of friction since more localised friction heat is produced compared to normal hip joint. There are several *in vivo* studies that demonstrate that the contact force during normal walking and the loads acting on hip implant ranges between 240% and 480% of the bodyweight [121]. However, no precise results are available stating the accurate value of friction coefficient *in vivo*.

2.10.3 Wear of ceramic-on-ceramic THRs *in vivo*

The growing demand to treat younger people has encouraged researchers to introduce a novel hard-on-hard bearing articulation of ceramic-on-ceramic in total hip replacement. The earliest example of this group belongs to alumina femoral head which moves within an alumina acetabular cup. Wear rates of the first generation alumina-on-alumina bearing is reported to be low *in vivo* varing between 1 to 5 mm^3 /year [137]. The vast majority of research on retrieved ceramic artificial hip joints exhibit a common type of wear called "stripe wear". The stripe wear as a distinctive localized elliptical area is known to be the key reseaon for asepectic loosening and squeaking shown in Figure 2.13. The emergence of stripe wear in the first and second generation alumina ceramics is attributed to inferrior quality of ceramic material, poor fixation and stability of acetabular shell to the bone[138,139]. However, the fluoroscopic images obtained from patients walking on a treadmill revealed that the acetabular head and socket detach slighly throughout the swing phase.

Figure 2.13.Stripe wear in third generation alumina[140]**.**

During the micro-seperation of the femoral head and cup, the cup keeps in contact with the rim and subsequently the high contact pressure at this point during heel-stike phase takes place and leads to the surface damage in the shape of wear strip Figure 2.14. Consequently, they demonstrated that stripe wear originates from the edge loading when the hip is bent.

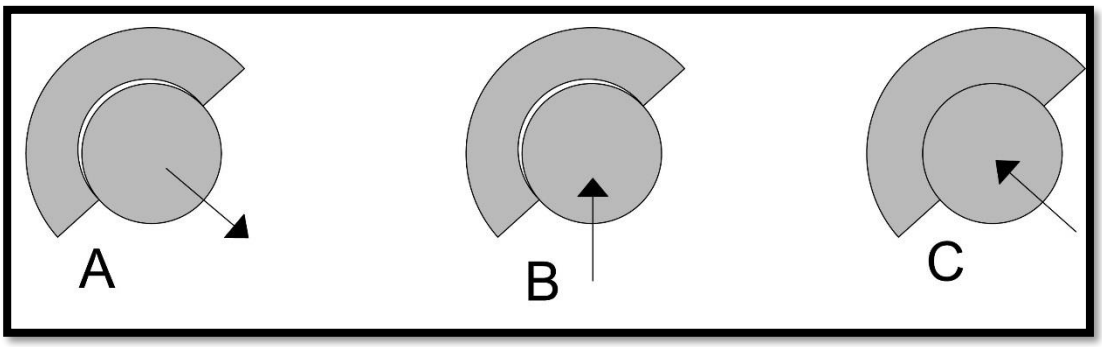

Figure 2.14. (a) Microsparation, swing phase (b) Rim contact, Heel strike phase (c) Relocation, stance phase.

Alumina particles are known to be biocompatible and non-toxic however the accumulation of alumina wear debris *in vivo* can activate osteoclast and leads to a bone resorption [141]. However, due to the insufficient data it is still controversial that alumina wear debris have direct relation with osteolysis. The size range of ceramic wear particle depending on the method of visualization is different. For instance, studies using SEMs show that ceramic wear debris ranges from 0.05µm to 3.2 µm, though TEMs reveal smaller particle size range from 5 nm to 90 nm [142].

Finally, a new failure mechanism in C-on-C introduced by Bonnaig et al. [143] indicates that fretting corrosion and failure of Morse taper generates metal debris acting as a third body and leading to a dramatic wear.

2.11 Ceramic-on-ceramic THRs *in vitro*

In vivo studies of ceramic on ceramic are the most satisfactory and authentic way of collecting data during long term behaviour and failure of hip joint replacement. However, no matter how much information is obtained from wear rates measurement in hip implant or from retrieved hip components, the process of analysing *in vivo* data only gives limited understanding. The success of each individual joint depends on the success of the operation, the patient's body and the activity of the patient.

On the other hand, *in vitro* studies of artificial hip joint are known to be the only way for systematic experimentation and elucidation of plausible modes of failure. A new orthopaedics

biomaterial needs to be assessed under the load and motion anticipated during normal walking cycle in terms of friction, lubrication and wear [144].

2.11.1 Friction on ceramic-on-ceramic *in vitro*

Friction is defined as a force resists against the motion of an object. The coefficient of friction is a dimensionless parameter that represents the relationship between the friction force and the normal force. The friction coefficient is defined as [145]:

$$\mu = \frac{F}{N} \qquad \text{Eq. 2.4}$$

Where μ is the friction coefficient, F is the friction force and N is the normal force. Friction factor f is a dimensionless value used rather than friction coefficient for the specific bearing surface of hip joint and is defined as [145]:

$$f = \frac{T}{R_1 N} \qquad \text{Eq. 2.5}$$

where T is the friction torque and R_1 is the radius of femoral head, Figure 2.15.

Depending on the roughness of contact surface, motion and lubrication the friction coefficient factor varies. In general, certain parameters influence the bearing system that their combination introduces a dimensionless parameter called Sommerfeld number Z:

$$Z = \frac{\eta v}{N} \quad [146] \qquad \text{or} \qquad \text{Eq.2.6}$$

$$Z = \frac{\eta v R_1}{N} \quad [145] \qquad \text{Eq.2.7}$$

where, η is lubricant viscosity, v is the entraining speed of the bearing surfaces, N is the applied force and R_1 is the radius of joint (femoral head). Depending on the geometry of the articulating surfaces either former equation (plane surfaces) or latter one (ball-on-socket) may be used.

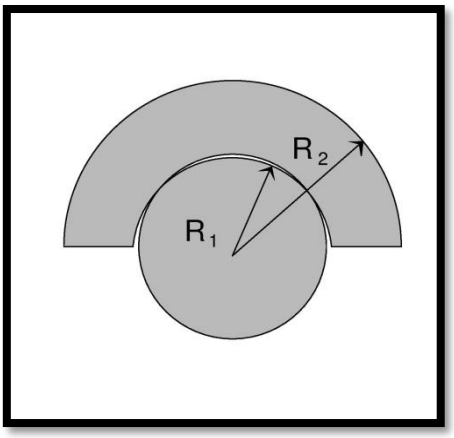

Figure 2.15 Schematic of hip joint articulation.

2.11.2 Lubrication on ceramic-on-ceramic *in vitro*

An upward trend of friction factor with rising Summerfield number demonstrates full fluid film lubrication regime. In this regime, the surfaces are completely separated by the lubricant and the friction only depends on the shear of the lubricant film. In the mixed lubrication regime, the load is partly transferred between the surfaces by the contact between high surface points and also through the pressure within the lubricant. In the boundary lubrication regime, continuous contact occurs between asperities of the sliding surfaces takes place and the fluid film is negligible shown in Figure 2.16. The generated friction during sliding of surfaces against each other results in energy dissipation and produces heating and surface deformation. To study *in vitro* performance of prosthetic hip joint it is important to select the appropriate lubricant which provides similar behaviour to synovial fluid in body.

Bovine serum and calf serum are the most widespread lubricants used in hip joint simulation due to the amount of protein that they contain. As studied by Fisher and Dowson [147], the wear surface formed by bovine serum is similar to the one obtained from retrieved orthopaedic UHMWPE components[148,149]. Since the protein content in synovial fluid is not always constant, various concentration of bovine serum have been tested.

In general, the protein content in synovial fluids of normal joints is much less than diseased ones. Furthermore, the viscosity of the lubricant is another key factor to assess the behaviour of lubrication system in *in vitro* study. Bovine serum exhibits shear thinning which means the viscosity of the lubricant depends on the shear rate [150]. During the testing the composition of a biological lubricant such as bovine serum may change and accordingly influence the viscosity and mainly the wear process [147]. Thereby, test parameters including frictional

heating, fluid degeneration and calcium phosphorus that may influence the composition of serum need to be controlled [151].

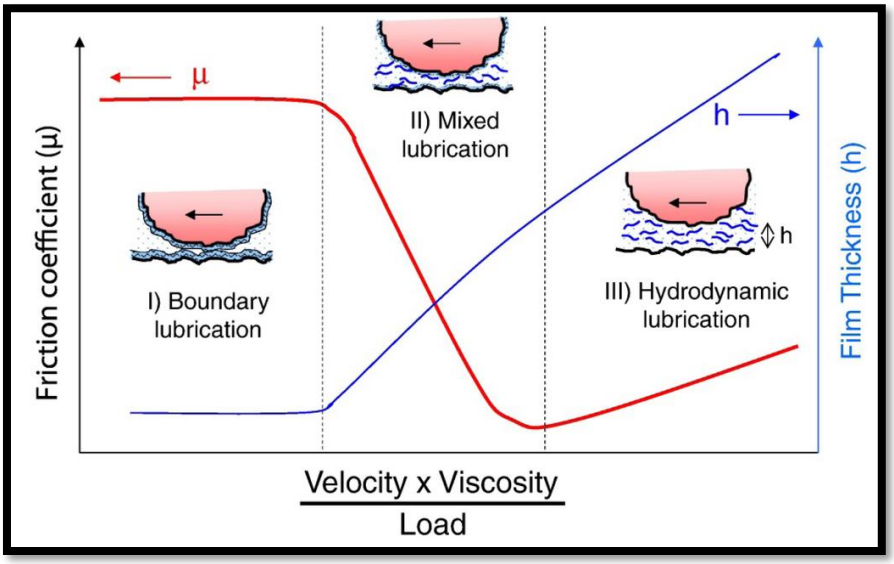

Figure 2.16 Schematic of Stribeck curve and lubrication regimes [152]**.**

Recently, hyaluronic and the combination of hyaluronic acid with albumin solution have been employed as testing lubricants. The studies [153] show that both of these lubricants are the most significant parts in the determining tribological behaviour of synovial fluid [154]. Hyaluronic acid provides high viscosity while albumin is adsorbed on the surface of the biomaterial protecting them against wear.

2.11.3 Wear *in vitro*

In general, there are two types of equipment used to investigate the tribology of hip joints in the laboratory; wear screening devices (quick tests) and wear joint devices (slow tests) [155]. In wear screening devices both simulator and sample are simplified. They can only investigate a specific wear mechanism rather than complex ones which results in insufficient data to anticipate worn surface morphology and wear rates in prosthetic joints. A few common types of screening devices contain; pin on disc [156], ring on flat [6,157], reciprocating [5] and crossed cylinder Figure 2.17.

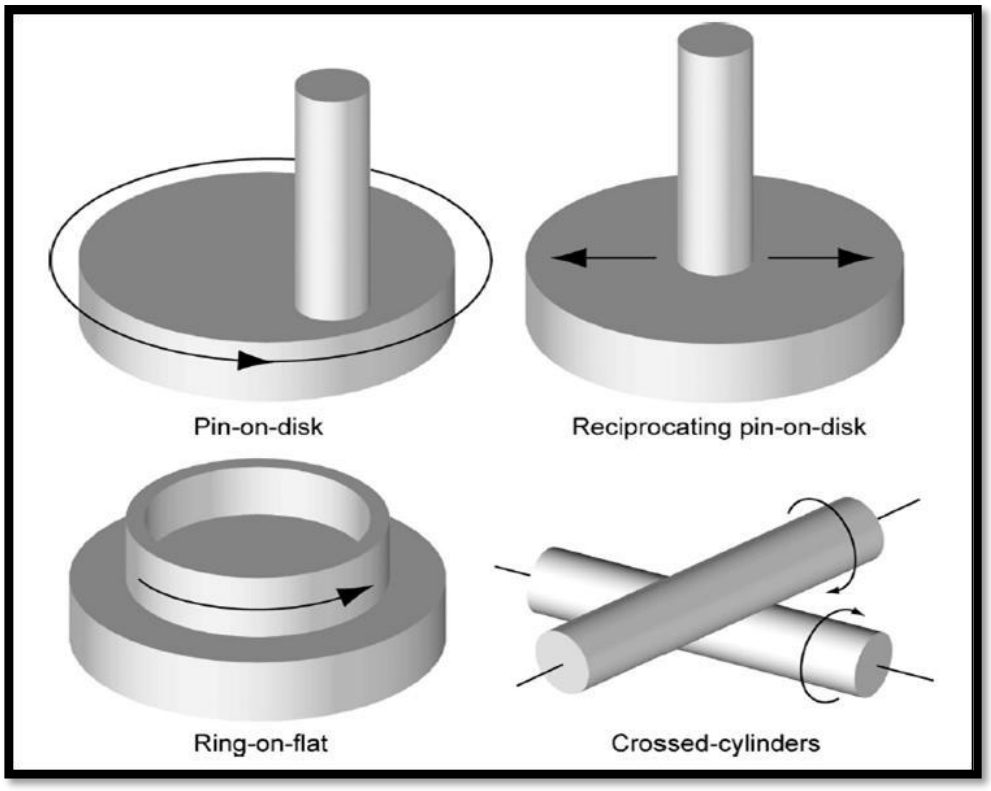

Figure 2.17. The most common wear screening devices[155]**.**

Wear joint devices provide more accurate information by simulation of both the environmental condition and physiological behaviour of actual hip joint. These devices are designed to replicate the *in vivo* wear model on the joint combinations and consequently anticipate some clinical behaviour of biomaterial. A very well-designed simulator is the Leeds Mark ll which includes micro-separation in the articulation, which is observed in *in vivo* study Figure 2.18.

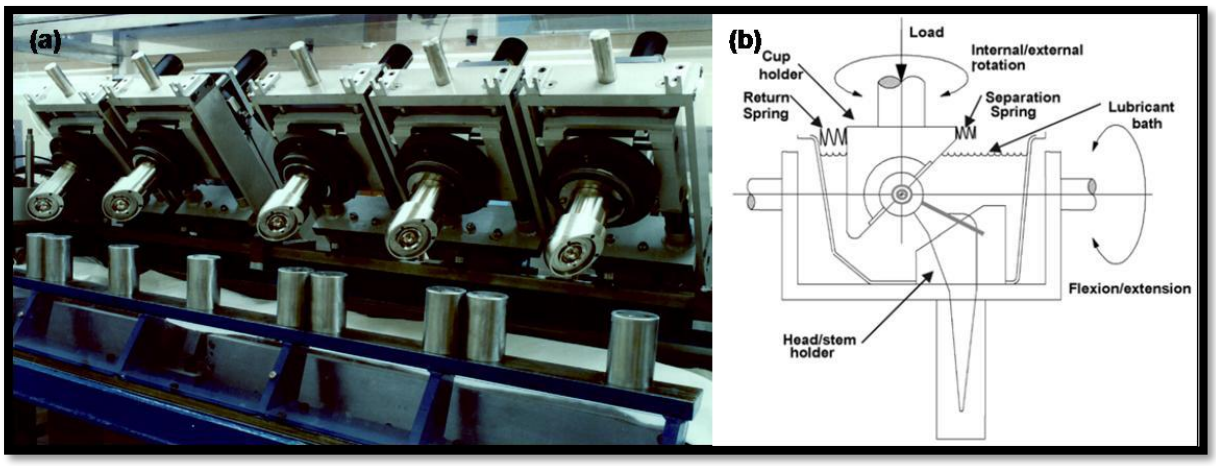

Figure 2.18. (a) Hip joint simulator (Leeds Mark ll). (b)Schematic of the simulator including concept of micro separation (reproduced from[158]**).**

The most severe wear damage is so called stripe wear and assumed to be the direct consequence of micro-separation. Stripe wear is primary revealed at both pole and periphery location on hip bearing. The wear pattern observed on retrieved hip implants is generally in the location as the stripe wear observed in simulation tests that include micro-separation [12,159–161]. However, due to the variation of motion and wear duration the width of stripe wear is not always comparable with retrieved joints. The most recent work performed by Al-Hajjar et al. on BIOLOX®delta bearing shows that micro-separation set up results in a higher wear rate than observed *in vivo*, although this wear rate is still very low compared with conventional joints [144]. Although the wear debris produced in *in vitro* tests is smaller than that observed *in vivo*, the size difference is not large.

It is still controversial as to whether the stripe wear detected in retrieved implants originates from micro-separation or alternatively by edge loading of head on the socket by an unknown process. High wear rate which may be revealed in the form of strip wear can be attributed to either steep angle implantation of acetabular shell or repeated dislocation [162]. As clarified by Fisher et al. [163], the combination of small reactivity and low wear propose that "the ceramic on ceramic bearings satisfy the tribological lifespan requirement of highly active patients".

2.12 Wear mechanisms

The main wear mechanisms that have been proposed by many researchers over the last 50 years include adhesive/abrasive/corrosive or fatigue of the surface [164], corrosion/ delamination/ fretting [165,166], tribochemical and cavitational wear [167,168]. However, the most predominant wear mechanisms in structural ceramic materials such as alumina and zirconia toughened alumina are known to be plastic deformation, micro cracking and chemical interactions[165,169,170]. The detailed review of involving mechanism in alumina and zirconia toughened alumina is reviewed in part 2.13.

2.12.1 Sliding wear

2.12.1.1 Type of wear

Sliding wear occurs when two surfaces, usually solids, slide over one another and can often involve multiple wear mechanisms that the greatest of which is called rubbing wear mechanism. Adhesive wear is sometimes used to describe the mechanism involved in sliding wear. However, it is more common in metals where localised plastic flow occurs at the surface,

where interactions with soft or weak particle are pulled off due to strong adhesive forces of the contact surfaces. For metal materials, adhesion, abrasion and chemical wear are more prevalent. Therefore, these descriptions may be better suited to metal-on-metal THR applications.

Ceramics exhibit different wear behaviour compared to metal due to their interatomic bonding which results in restricted capacity for plastic flow at room temperature. Therefore, they are more likely to experience brittle fracture under stress. Tangential forces caused by sliding wear between two ceramic surfaces may lead to fracture rather than plastic flow [171]. Their brittle nature means that they are more likely to suffer from abrasion, tribo-chemical wear or cracking and chipping. When the applied normal force reaches a critical value, a crack just outside the circular contact area starts off and rapidly grow to shape a Hertzian cone crack Figure 2.19. The typical characteristics of a Hertzian cone crack are as follows [172]:

(1) The crack begins just outside the contact circle
(2) The crack propagates upright towards the surface above it and then propagates downwards and outward away from loading axis
(3) It is almost symmetric with respect to the axis

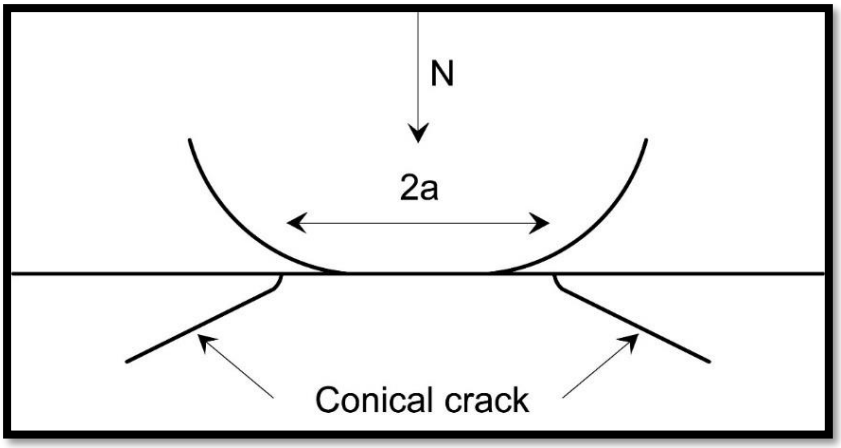

Figure 2.19 Schematic illustration of a crack produced by a normal load inserted by a sphere on to the surface of a brittle material.

In sliding wear due to the tangential force, the stress distribution is improved, and the normal load required to initiate fracture is significantly reduced. In addition, the tangential force increases the formation of partial cone fracture due to the modification of the stress distribution under the indenter and consequently gives rise to the tensile stresses in the wake of the indenter as illustrated in Figure 2.20.

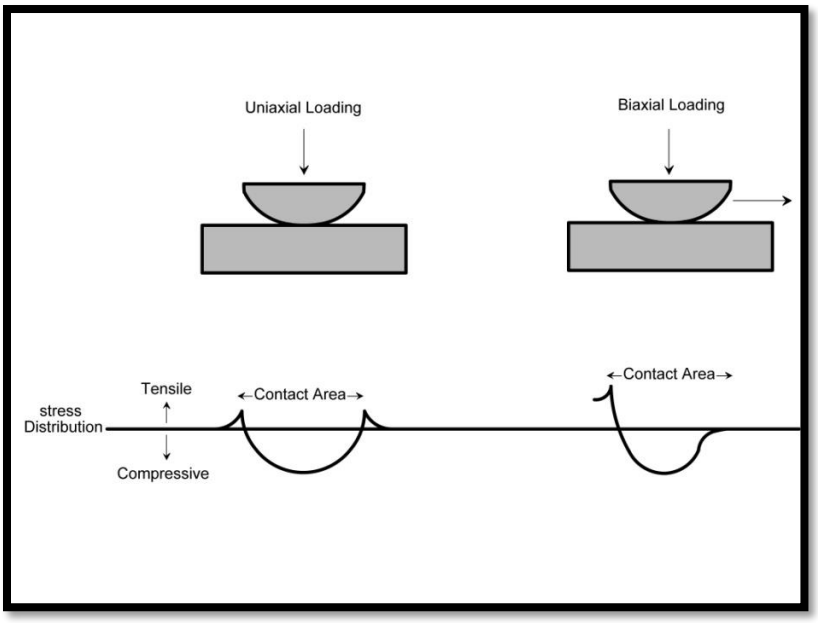

Figure 2.20. Graphical illustration of stress distribution under uniaxial and biaxial loading on the contact surface.

2.12.1.2 Wear rate based on Archard theory

A simple theoretical analysis that explains the wear of two sliding surfaces was originally given by Archard and modified by Hutchings[146]. This simplified theory is based on a single asperity deformation and emphasises the principal variables that affect sliding wear. In addition, it provides a method to assess the grades of wear through a parameter called wear coefficient, *K*.

The initial assumption for this model is that the contact between two bodies takes place when the asperities meet and therefore the true contact area will be given by sum of the individual asperity contact areas. This area is approximately proportional to the normal load and it is postulated that under most circumstances, mainly for metals, the localised deformation of the asperities is plastic.

Figure 2.21 gives a schematic of a single asperity contact, which are presumed to be circular in this view with radius a. In Figure 2.21 (c), they reach to the maximum contact and the normal load supported by it, δW, is given by:

$$\delta W = P\pi a^2 \qquad \text{Eq. 2.8}$$

in which P is the yield pressure during plastic deformation of asperity and is close to the indentation hardness H.

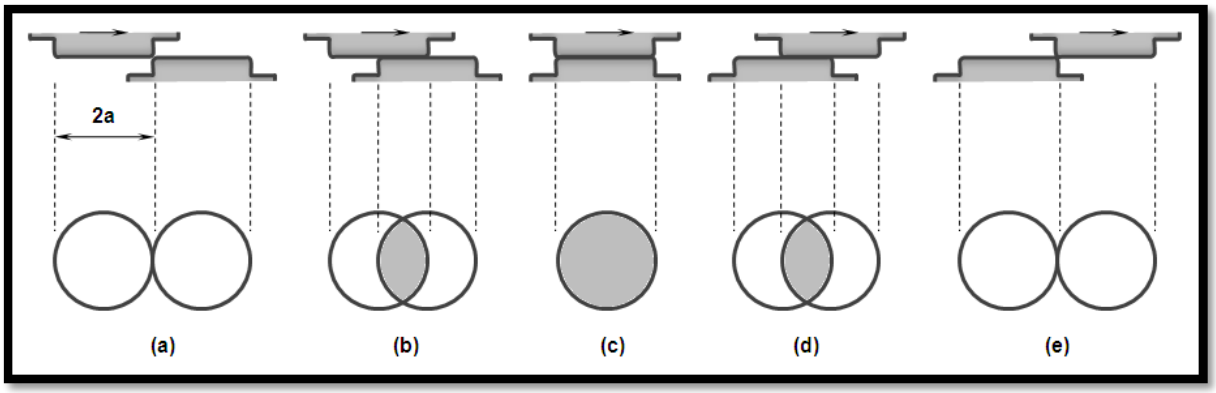

Figure 2.21. Schematic illustration of a single contact patch when two asperities slide over each other [146] **(a) Asperities before sliding contact (b) Partial contact as sliding (c) Maximum contact (d) Partially contact after sliding over (e) Asperities completion of sliding.**

During constant sliding motion, continuous formation and destruction of individual asperity contact occurs. In general, wear is correlated to the separation of fragments of material from the asperities. It is assumed that removed fragments through the wear process possess hemisphere shape and therefore the volume of each fragment, δV, is given by:

$$\delta V = \frac{2\pi a^3}{3} \qquad \text{Eq. 2.9}$$

Considering the fact that just a portion of asperity contacts (k) increases the wear particles, the average volume of material δQ worn away per unit distance during sliding of two asperities over each other along a distance, $2a$, is given by:

$$\delta Q = \frac{k\delta V}{2a} = \frac{k\pi a^2}{3} \qquad \text{Eq. 2.10}$$

So, the total wear rate,Q, originating from entire asperity contacts can be obtained from:

$$Q = \sum Q = \frac{k}{3}\sum \pi a^2 \qquad \text{Eq.2.11}$$

And the overall normal load W can be calculated by:

$$W = \sum W = P\sum \pi a^2 \qquad \text{Eq.2.12}$$

And therefore:

$$Q = \frac{kW}{3P} \qquad \text{Eq. 2.13}$$

To achieve more simplified equation, the factor of $\frac{1}{3}$ can be incorporated into the constant of proportionality. By considering $K = \frac{k}{3}$ and this assumption that $P = H$ (the indentation Hardness), the aforementioned equation can be rewritten as:

$$Q = \frac{KW}{H} \qquad \text{Eq. 2.14}$$

where Q is the volume worn per unit sliding distance, W is the normal load, H is the hardness of the softer surface. Additionally, constant K is labelled as a wear coefficient and is dimensionless and always less than unity [146].

2.12.1.3 Mild and severe wear

The mechanism in which the material removed from the surface in ceramics through the mild wear regime is poorly understood. The main mechanisms in the sliding wear of ceramics are fracture, tribo-chemical and plastic flow. Transition from mild to severe wear can occur through dominance of each of these mechanisms and results in an abrupt change in wear rate. The investigation shows that in most ceramics, the transition is dependent on the load, sliding speed and environmental condition as well as material parameters such as grain size.

Mild wear has been defined as a type of a wear resulting in a smooth surface, a low wear rate (typically below 10^{-6} mm^3/Nm) and stable friction in ceramics. In this regime the dominant mechanism is generally tribo-chemical wear. The wear debris in this regime may be chemically different from the substrate, and may have gone through oxidation, hydration and mixing with the lubricant. On the other hand, severe wear leads to a rough surface as a result of surface fracture, a high wear rate, and an unstable friction force. In contrast to mild wear, this regime is dominated by brittle fracture of the surface grains. The angular wear debris is chemically the same as the bulk sliding material.

The ceramics materials follow the Archard equation and exhibit a linear relation between wear on sliding motion and load to provide a useful wear coefficient (K). The typical values of wear coefficient for mild, severe and ultra-severe wear are respectfully lower than 10^{-6}, 10^{-4}, and 10^{-2} $\frac{mm^3}{Nm}$. As illustrated in Figure 2.22 Shishido et al. presented a wear map for each wear scar of the alumina microstructure using their measured grading scale. For instance, a round region of wear was observed at the top of the ball head expanding to the super anterior aspect, and the scale of wear was rated as grade IV. Wear scars, in the form of stripes, were also evident in the

superoposterior and inferoanterior regions in which the extent of wear was rated as grade V. Figures 2.22 (A-C) show the severity of wear in three different stages of grading system. They are described as grade III: mild wear as characterised by total removal of the initial machine tracks and relief–polishing revealing the grain structure (Figure 2.2.A); grade IV: progressive wear as illustrated by grain pull out and intergranular fracture accompanied by the formation of craters localized regions in an otherwise intact surface (Figure 2.2.B); and grade V: disruptive wear as evidenced by intergranular fracture with loss of surface integrity (Figure 2.2.C)[12,13].

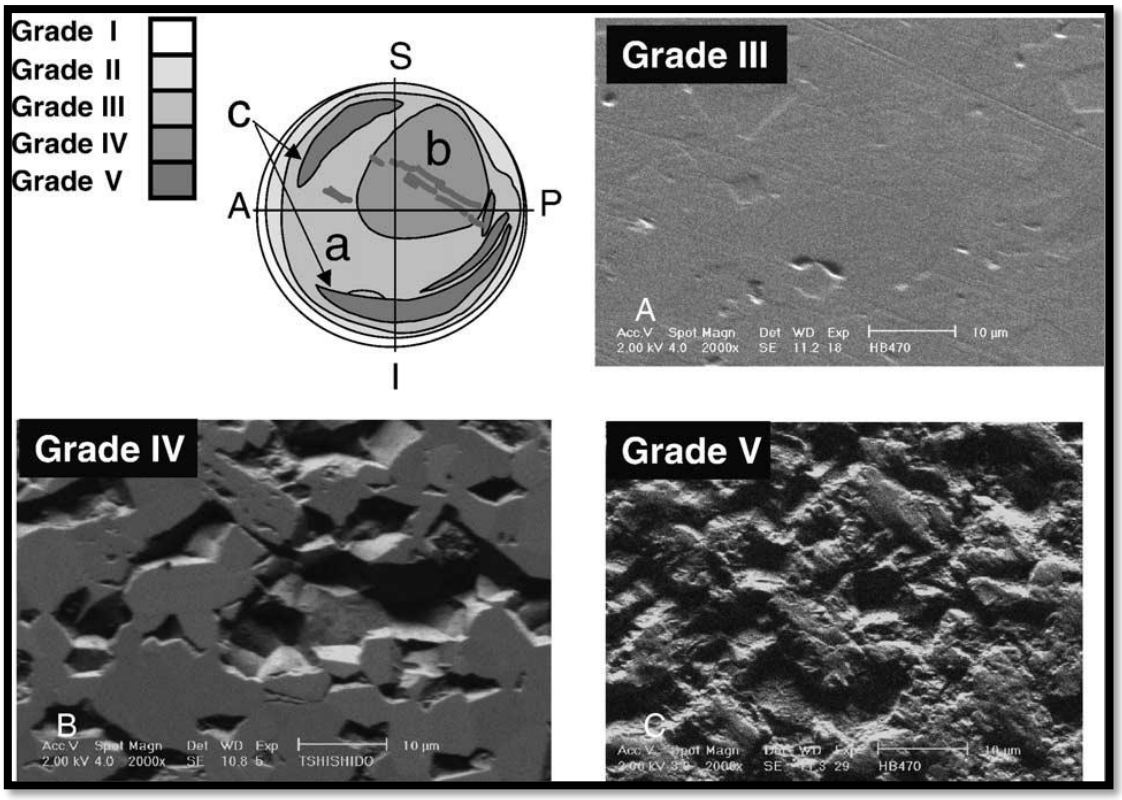

Figure 2.22 wear map and SEM images of alumina microstructures illustrating the severity of wear in different grades[13]**.**

2.12.2 Abrasive wear

Abrasive wear is defined as the loss of material due to the passage of hard particles over the surface. In this type of wear, both in dry and lubricated sliding wear, the existence of hard particles is inevitable either as a separate element between surfaces or as a detached component of one or both surfaces. The movement of these hard particles will eventually produce a groove along the displacement direction. The groove forms due to the plastic deformation of materials under strong contact pressure applied by the hard body on the counter face.

2.12.2.1Abrasive wear modes

Abrasive wear is commonly classified into three different groups, based on the type of the contact and contact environment [173]. Two- body abrasive wear occurs when the hard particle or rough edges are embedded in the counter surface leading to the material removal. In three body abrasive wear the hard abrasive particle is confined between two sliding surfaces and is free to roll and slide over counter faces shown in Figure 2.23.

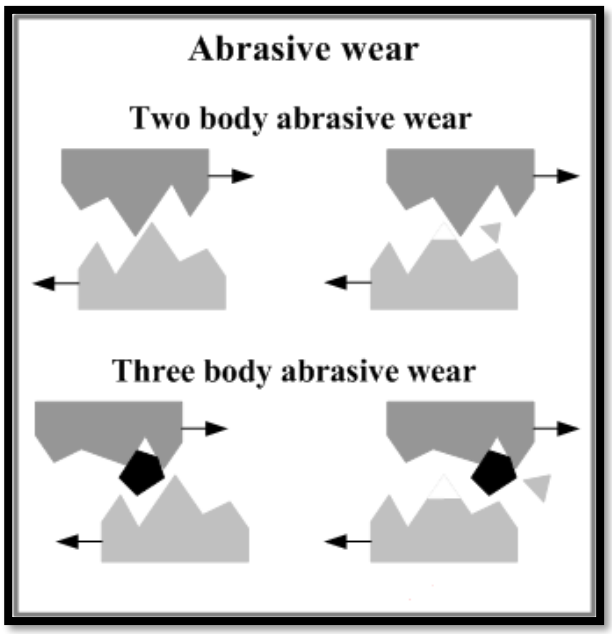

Figure 2.23 Schematic of two body and three body abrasive wear [174]**.**

In some situations, particulates in gases or liquid strike a surface and cause damage on the surface. This type of the wear is classified as erosive wear which involves the continuous loss of original materials from the surface caused by the interaction between surface and a fluid or impinging liquid or solid particles [175].

2.12.2.2 Mechanisms of abrasive wear

In abrasive wear two main involved mechanisms are plastic flow and brittle fracture. It is likely that plastic flow occurs under some conditions, though both can happen simultaneously even in materials conventionally thought of as ideally brittle. Abrasive wear of brittle materials such as ceramics mainly depends on the shape of the abrasive particles. This is why the contact stresses vary in different situations and this leads to various types of cracking.

For instance if the abrasive particle shaped angular, both local plastic deformation and cracks of a different geometry from which wear might immediately occurs can be formed at the point

of contact [146]. Figure 2.24 illustrates how cracks shape in a brittle solid material subjected to a point load. The point of initial contact is accompanied by a very high stress. These intense stresses (shear and hydrostatic compression) are alleviated through local plastic deformation or densification around the tip of the indenter. The deformed area is indicated by letter D in Figure 2.24.

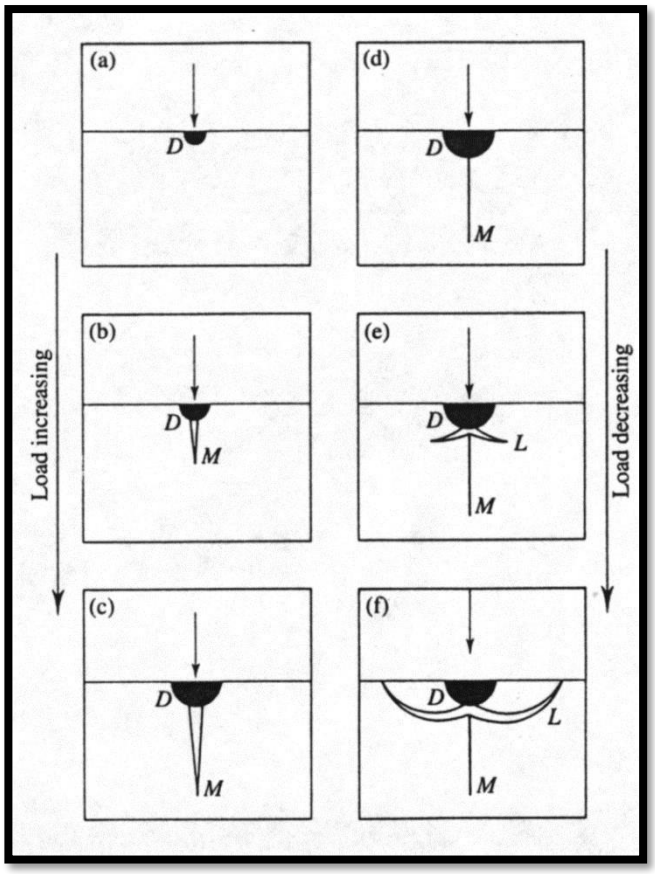

Figure 2.24 Schematic of crack formation in a brittle material under point indentation[176]**.**

Tensile stresses across the vertical mid-plane set off a median crack, labelled M, while the load on the indenter (sharp abrasive particle) reach a critical value. On the other hand, unloading is accompanied by the formation and growth of lateral cracks. The formation of lateral cracks is caused by residual elastic stresses. This type of stress is formed due to relaxation of the deformed material around the zone of contact. Once a blunt particle rolls over the surface, the plastic groove forms. This process is accompanied by the growth of lateral cracks upwards to the free surface from the base of subsurface deformed area Figure 2.25. It is well documented that these types of cracks (lateral) contribute in material removal [177].

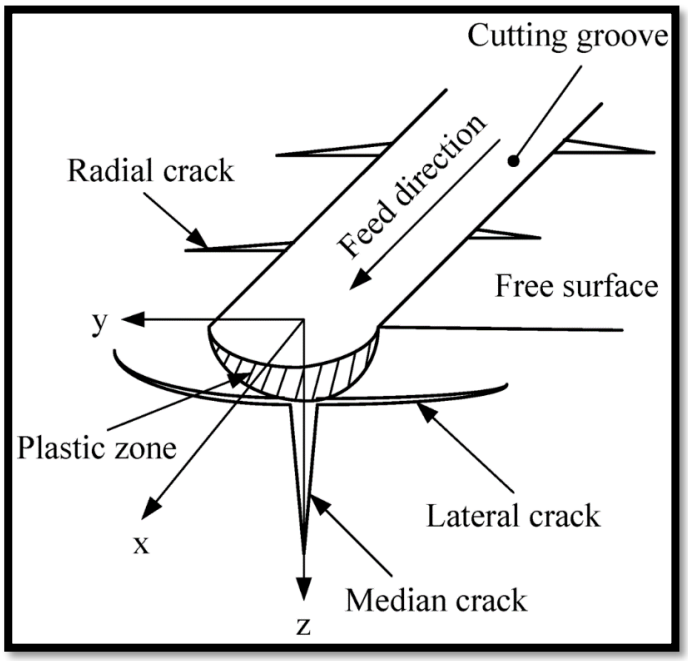

Figure 2.25 Schematic of material removal in a brittle material. Typical illustration of crack induced from beneath a plastic groove [178]**.**

2.13 Wear of alumina

At room temperature, Al_2O_3 and ZrO_2 show high friction (μ~ 0.5-0.9) and a wide range of specific wear rates (k ~10^{-10}- 10^{-4} $mm^3N^{-1}m^{-1}$) depending on the applied normal load and sliding velocity [178–182]. Among oxides ceramics alumina exhibits little wear at moderate pressure. The main mechanisms involved in the wear of alumina are plastic deformation, cracking and tribo-chemical wear[184]. There is a direct relationship between the first two mechanisms indicating that the plastic deformation in alumina is formed by both twinning and slip wear processes due to abrasion [185]. The coefficient of sliding friction for many ceramics under dry conditions is rarely less than 0.5 and in some cases is even higher than this value. The high value of coefficient of friction in an engineering application causes unacceptably high frictional energy losses. Therefore, for most engineering applications lubricants are applied to decrease the frictional force between counter faces. By the introduction of lubricant in wear process another important involved wear mechanism occurs, which is tribo chemical wear. Tribo-chemical wear occurs due to the chemical reactions at the contacting area of two sliding surfaces. The formation of tribo-chemical layers is associated with many factors such as chemistry and physics of counter-faces, environment and shear. The formed tribo-chemical layers function as load bearing surfaces and may have low shearing strength leading to both low wear and friction [186]. The studies performed in this area suggest that wear of

polycrystalline alumina is highly influenced by microstructure of material, environmental condition and the wear test operation parameters.

2.13.1 Role of microstructure in wear mechanism of alumina

2.13.1.1 Grain size

It is generally acknowledged by researchers that the wear of polycrystalline alumina is strongly determined by its microstructure, particularly the grain size. As presented by Miranda-Martines at al. [187] among various polycrystalline alumina microstructures with similar hardness and fracture toughness the one with smaller grain size exhibits higher wear resistance. They also recognized that the wear mechanisms of alumina is influenced by grain size shown in Figure 2.26. In single pass sliding experiment, the wear mechanism was plastic deformation at low loads (<10 N) for small grain-sized alumina however it switched to a mixed mechanism of plastic deformation and intergranular fracture at high loads (>10 N).

In contrast, coarse grain sized alumina mostly exhibited intergranular fracture and some transgranular fracture at all load ranges. As the energy of grain boundary fracture (intergranular) is almost one half of that for crystalline fracture (transgranular) the former process requires less energy. Therefore if the wear particles and thus contact area are large compared with microstructure feature, the grain boundary fracture is likely to be the main wear mechanism [188]. It is well known that alumina suffers a time dependent transition from mild to catastrophic wear in which the time to the transition associated with the grain size of the material [189].

.

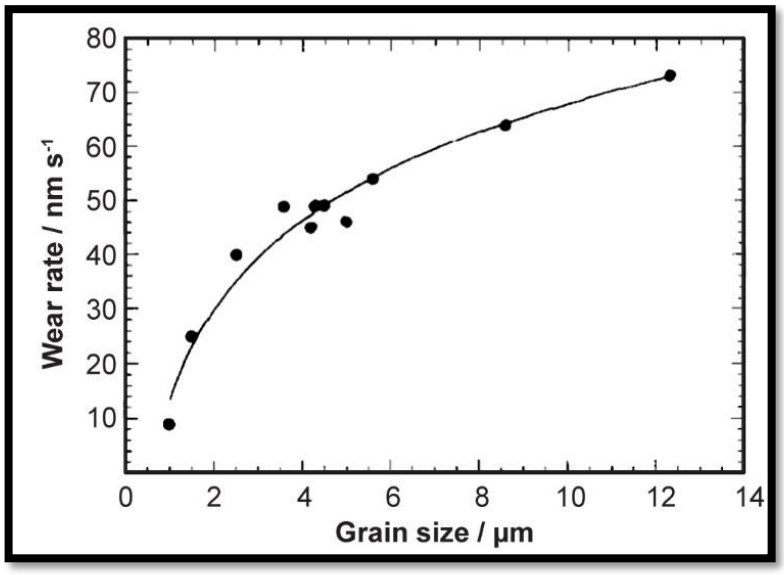

Figure 2.26 .Wear rate-grain size dependence in the wet erosive wear of pure polycrystalline alumina [188]**.**

Figure 2.27 shows the wear scar diameter as a function of sliding time for a range of abraded alumina grain sizes. A transition in wear rate from mild to catastrophic wear is completely obvious in all three aluminas though this transition first occurred in the coarse grain alumina and last in the fine grain alumina. The coarser grain size alumina comprised anisotropic grains which was accompanied by higher toughness based on R curve behaviour[24].

According to Rainforth's [189] research the grain boundary micro-cracking directly initiates from dislocation pile-ups at grain boundaries. Increasing the grain size increases slip length and accordingly the accumulation of dislocation in grain boundary augment the tensile residual stresses in some grains leading to the initiation of cracks at these grain boundaries [189]. The formation of cracks in grain boundary liberates a wear particle which behaves as a third-body abrasive. The onset of abrasive grooves was found to be at the grain boundary. This is commonly due to the differential wear between grains leads to the separation of particles from the grains standing proud of the surface.

In general, three body abrasives cause a variety of damage and it is responsible for the majority of dislocation accumulation. On the other hand, the dislocation activity produces stress concentrations at boundaries that eventually initiate the intergranular fracture and the time dependent wear transition. The localized plastic deformation caused by dislocation activity can occur below microscopic abrasive grooves that is not believed to be rate limiting in mild wear. However, according to Barceinas-Sanchez and Rainforth's research, tribo-chemical is found to be the principal wear mechanism in the mild wear regime and results in the formation of amorphous layer at the surface.

Principally, the time dependent wear transition arises from a mixture of applied stress, residual thermal mismatch stresses and stresses originated from accumulation of dislocation at grain boundaries [14]. Liu and Fine [190] indicated that thermal mismatch during cooling in sintering and the contact stresses are responsible for the critical damage stress arises from residual tensile stresses. On the other hand, the residual thermal mismatch stresses are constant throughout the test and therefore cannot provide the time dependent aspect. A reduction in grain size results in a reduction in slip length, and therefore postponing the critical transition point and increasing the time to wear transition.

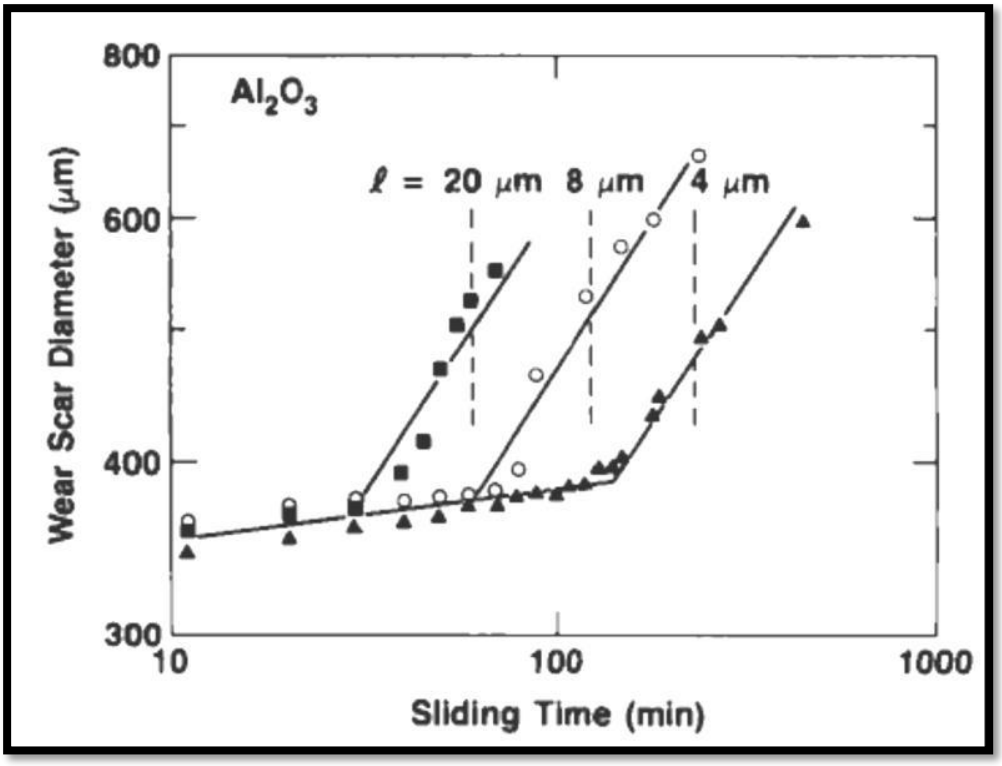

Figure 2.27 Illustration of wear data in pure alumina polycrystalline with three different grain sizes. Silicon nitride sphere with 12 mm in diameter rotating on flat surface, at room temperature and lubrication of paraffin oil. Note initial slow, steady rise of scar diameter in accordance to sliding time followed by abrupt transition to severe wear at critical sliding time. Sliding time for initiation of transition considerably diminishes for the bigger grain size materials. Vertical dashes lines are theoretical predications of the transition times [191]**.**

2.13.1.2 Porosity

The pores in materials results in increasing wear due to the reduction in hardness and because they provide initiation points for cracking. While the microstructure contains pores, the real area of contact between counter surfaces decrease and subsequently the contact pressure increases [192]. Rice has performed comprehensive investigation about the effect of porosity with respect to ceramic wear [170]. The main parameters involved are categorized in three groups; shape, size and location. Intergranular pores with approximately spherical or polyhedral shape are fairly well isolated, play little or no role on cracking while the transgranular crack might be originated from intragranular pores. The pores at grain boundaries cause the easier crack onset. These pores tend to form lenticular or triangular shape if at a junction triple-point and thereby are likely to concentrate high stresses and initiate cracks. Pores with larger size form greater cracks. Additionally, these large pores located near the surface can lead to ploughing, gouging of surface during wear [158].

2.13.2 Environmental Effect

The wear of alumina based ceramics is found to be a multistage process, which is highly influenced by environmental effect such as formation of tribo-films[169, 192,193]. Although ceramic materials are well known for their chemical inertness, alumina has a strong sensitivity to water. For instance, lubrication using water increases the wear rate of aluminas compared to dry sliding. The reason is related to the formation of aluminium hydroxide on the alumina surface at such a rate at which removal speeds up though surface stresses from friction decreased. In oxide ceramics, growth of a crack partially depends on environmental factors that influence the mobility of wear surface dislocations and thereby affect plastic deformation [195].

Two theories about tribochemical wear have been demonstrated and published by various authors. Gate et al. [196] noticed that during the wear of α-alumina transition phase such as δ and γ-alumina could be produced. Chemical reaction between different alumina phases and water/water vapour can form bayerite ($Al(OH)_3$) at ~100ºC or bohemite ((AlO(OH)) at ~200ºC. Jahanmire [197] demonstrated that at low temperatures, T< 200ºC, tribochemical reactions between alumina surface and water vapour in the environment is the dominant tribological mechanism.

Kalin et al. [198] has clearly demonstrated the significance of the pH of an aqueous solution in regard to wear of alumina. In terms of alumina, high wear rate occurs while the pH values are very high or low. This is due to the material removal by chemical solution [198].Studies presented by Rainforth [169] showed that the wear rates of alumina on alumina wear depend on the hydration rate of the surface, removal of the hydrated layer and damage due to the third body abrasive.

2.13.3 Effect of test parameters

Wear test process is influenced by a variety of parameters. Part of these parameters can be determined by the selection of appropriate wear test apparatus. The set of factors are inherent to the apparatus parameters including test geometry, vibration characteristics and the alignment specifications for the experiment [171]. The second group of parameters are called operator controlled parameters depending on the type of selections that an operator can make such as, sliding velocity, normal load, bulk temperature and duration. Transitions between different wear mechanisms generally dominated by fracture, tribochemical effect and plastic

deformation and thereby results in abrupt changes in wear rate with sliding speed, load or environmental conditions.

Dong et al. [199] showed the wear transition diagram for high purity alumina sliding on unlubricated alumina counter face, Figure 2.28 and shows the wear transition in four distinct parts under the effect of applied load and temperature at low sliding speed. At low temperatures in region I (T<200ºC), the dominant wear mechanism is tribochemical reaction between alumina and water vapour in the environment. In region II, at moderate temperatures (200ºC <T < 800º C), the wear mechanism is associated with contact load. At low loads, wear regime is controlled by plastic deformation and ploughing. At the same range of temperature, at loads above 20 N, in region IV, severe wear through intergranular fracture occurs. In region III, at temperatures higher than 800º C, the wear coefficient is low due to the thin surface layer formed. Woydt et al. investigated the sensitivity of pure alumina to sliding speed under constant load [200]. Based on their research, the wear rate of 99.7 percent pure alumina increases by more than two orders of magnitude once the speed is raised from 0.003 to 0.3 m/s under constant applied load of 10 N. The third group of parameters impact the result of tests are denoted as materials effects. The main examples of this group contain the obvious material and type of lubrication, surface preparation and cleaning processes [171].

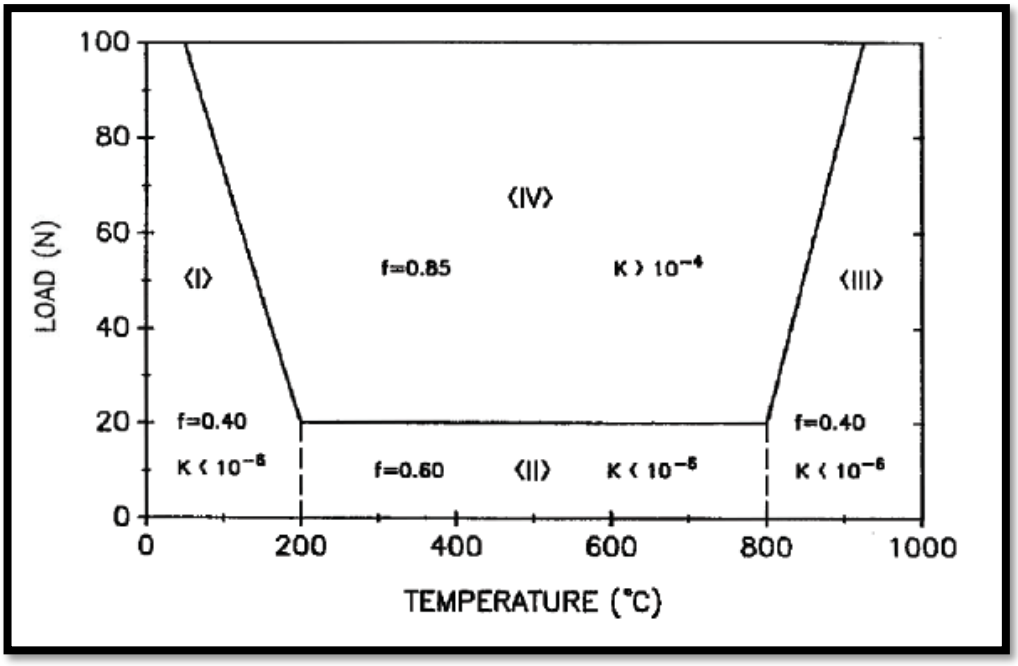

Figure 2.28. Wear transition diagram illustrating four individual regions. *f* and *K* in each region are representative of friction coefficient and wear coefficient respectively [199].

2.13.4 Wear mechanisms in zirconia toughened alumina (ZTA)

A brief summary of main research performed towards understanding the mechanisms in wear of ZTA composite is provided as below:

Author	Material	Contact Configuration	Counter face materials	Environment	Load	Velocity
[201]	Alumina 10 vol. % zirconia	Ball on disc-Reciprocating	3Y-TZP-10mm diameter	At room temperature-humidity %50-70	20 N	17 mm/s
Mechanism	➢ The lower sintering temperature results in the higher wear resistance. ➢ Homogeneity and grain size of the micro- structure are significant parameters in controlling the wear rate.					
[202]	Alumina with %15-25 zirconia ceria stabilized 14 mol.%	Fretting wear test ball on flat	Tungsten carbide (WC)	Dry condition	20 N, 35 N, 50 N	10 Hz frequency of oscillation
Mechanism	➢ Partial cone crack is formed during the sliding of the ball under applied stress results in intergranular fracture at final step of wear. This leads to the spalling or grain pull out causing the wear of materials ➢ The dominant wear mechanism is the asperity scale cracking that piles up at higher load while the number of fretting cycles rises. This mechanism occurs due to the fact that the critical flaw size is much bigger in size than surface asperities. ➢ Furthermore, small surface cracks resulting from the accumulation of surface damage at larger load (50 N) are formed. Nevertheless, these micro cracks need long time (~ 1million cycles) to reach to the critical crack length to fracture.					
[203]	Zirconia toughened alumina with different addition of metal oxide (~8-11wt. %)	Sliding	SiC abrasive grinding paper	Dry sliding wear	50 N	
Mechanism	➢ Abrasion, grain pull-out and removal of secondary phases					
[204]	Alumina with 1.7 vol. % zirconia	Oscillation friction	Mgo-stabilized zirconia -5mm	Room temperature	20 N to 150 N	0.15 m/s
Mechanism	➢ Two main toughening mechanisms in zirconia toughened alumina; (1). Due to the high thermal expansion mismatch between Al_2O_3 and ZrO_2 particles, a compressive residual stress field inside the matrix around the intragranular ZrO_2 particles forms. ➢ Formation of local compressive stresses on neighbouring Al_2O_3/Al_2O_3 grain boundaries because of the existence of intergranular nanoparticles thereby making the boundaries stronger. ➢ The intergranular grains create extra compressive stress component formed on the alumina/alumina grain boundary leading to lower wear rate in zirconia toughened alumina than monolithic alumina.					
Author	Material	Contact Configuration	Counter face materials	Environment	Load	Velocity

[205]	Al_2O_3 with 7,14 and 22 vol. % 3Y-ZrO_2	Oscillating friction machine	5 mm MgO-ZrO_2 ball	Room temperature	20 N to 150 N	0.15 m/s
Mechanism	➢ The most dominant wear mechanism for ZTA composite containing zirconia above percolation threshold (%16.vol) was provocative mechanism that stimulated micro cracking. ➢ The principle wear mechanism for the composite composed of zirconia less than percolation threshold at low load around 20 N is abrasive wear, however at high load above 100 N the pivotal mechanism is distinguished as chipping by intergranular and transgranular crack.					
[15]	Al_2O_3 with 15 wt.% ZrO_2 by both colloidal processing and dry pressing	Pin on disc	10 mm Al_2O_3 ball	Dry-sliding	15.5 N	0.5 m/s
Mechanism	➢ The specific wear rate of ZTA composite manufactured by colloidal processing is around 5.10^{-8} mm^3/ Nm and the main wear mechanism represented by polishing and deformation. ➢ However, the specific wear rate of ZTA made by dry pressing is about 2.10^{-6} mm^3/Nm and the leading wear mechanism is grain pull-out. ➢ The difference of wear mechanism and wear rate is originated from difference in microstructure.					
[206]	Al_2O_3 with 15 wt.% 5Y-ZrO_2	Ball on plate	4 mm SiC Ball	Dry N_2 with humidity <1%	8 N	0.08 m/s
Mechanism	➢ The ruling wear mechanism is polishing, and grain pull out however micros cracks turn up at the turning points. ➢ The grain boundaries can be strengthened by forge sintering which reduces wear rate by 2-3 times					
[207]	Al_2O_3 with 5,10,15 and 20 vol. % ZrO_2	Ball on three flats modified to accommodate ball on four flats configuration	Si_3N_4 ball of 12.7 mm	Purified paraffin oil in room temperature	Different load	0.23 m/s
Mechanism	➢ During wear transition, an abrupt change of wear rate and friction occurs, and micro fracture or grain pull out are controlling wear mechanism. ➢ The wear transition resistance of ZTA rises as the zirconia content increases up to 20%. The improvement in wear transition resistance is due to the small and homogenous microstructure, phase transformation introduced surface compressive stress and low elastic modulus. These parameters lead to a larger Hertezian contact and lower tensile stress. ➢ It is observed that the dense dislocation clouds and twins in fine grain ZTA composite can absorb energy and liberate stress through mechanical contact and assist to the rise in wear transition resistance of ZTA microstructure. In summary, introduction of internal compressive stresses, reduction of grain size and inhibition of internal tensile stresses notably contribute in modification of wear transition resistance.					

3 Experimental procedure

3.1 Powder characterization

Two main metal oxides have been used for this study. The first one was high purity alumina (Al_2O_3, KTP-50, Sumitomo Chemical Co.) which was produced by the hydrolysis method and was composed of uniform and homogenous fine powder.

The second one was biomedical grade 3 mol. % yittria stabilized tetragonal zirconia (ZrO_2, TZ-3Y-E, Tosoh Corporation) and is selected for this study due to its high purity and quality. Based on the supplier report, this product shows superior sintering properties and sintered bodies manufactured by this type of zirconia exhibit a fine crystal grain structure.

In addition to these powders, high purity ternary and quaternary additives were used including chromium (III) oxide (Cr_2O_3, Aldrich) and strontium carbonate ($SrCO_3$, Aldrich).

3.2. Colloidal dispersion of powder

Mixtures of alumina and zirconia, with two oxide additions were processed by the colloidal dispersion method, Table 3.1.

Table 3.1. Compositions and nomenclature of the materials studied.

Nomenclature	***Composition***
ZTA	~ 83 vol. % Al_2O_3, ~ 17 vol.% ZrO_2
ZTA-Additives	~ 82 vol. % Al_2O_3, ~ 17 vol.% ZrO_2,0.3 vol.% Cr_2O_3, 0.7 vol.% $SrCO_3$
Biolox® delta (Commercial)	~ 82 vol. % Al_2O_3, ~ 17 vol.% ZrO_2,0.5 vol.% Cr_2O_3, 0.5 vol.% SrO

Mixture of alumina, chromium (III) oxide and strontium carbonate was attrition milled in a Teflon lined jar with 2 mm alumina balls and milled at ~ 450 rpm for 4 hours. The slurries were filtered to separate the milling media and then dried in freeze dryer for two days at a temperature of -40ºC and a pressure of ~0.1 Mbar (~10 Pa). The fluffy dried powder was crushed in an agate mortar and sieved through a 45 µm stainless steel mesh. The sieved powders were then calcined at 1050ºC for 6 hrs to decompose strontium carbonate, which resulted in the production of CO_2, and completed the reaction between alumina (Al_2O_3) and strontium carbonate ($SrCO_3$) to produce strontium hexa-aluminate ($SrAl_{12}O_{19}$) and also form Al_2O_3-Cr_2O_3 solid solution. Subsequently the calcined powder was mixed with zirconium oxide

(ZrO_2). To form a homogenous ZTA-additives microstructure, stabilization of the colloidal suspension was performed through the following sequential steps.

About 160 ml distilled water, ~0.2 g citric acid as a dispersant and a few drops of ammonium hydroxide as a pH adjuster were added to a batch of ~65 g mixture of powder. Due to the high stability of suspension in alkaline environment, pH ~9.5 was chosen in this study. A constant mixture of the suspension was ensured using a magnetic stirrer, during the experiment, to avoid sedimentation of powder. Subsequently, the prepared suspension was placed in a Teflon lined jar with alumina balls and milled again at ~ 450 rpm for 4 hrs. The slurries were then filtered to remove the milling media, dried in freeze dryer for two days at a temperature of -40ºC and a pressure of ~0.1 Mbar (~10 Pa). The fluffy dried powder was crushed and sieved through a 45 µm stainless steel mesh. The final powder was calcined again at 600ºC for 2 hrs to remove citric acid and ammonium hydroxide.

Similar procedures were used to make the ZTA composite, although a few steps were excluded due to the absence of additives. The slurry was made by mixing ~ 65 g of alumina and zirconia together with the same type and amount of the dispersant and the pH adjuster. Subsequently, the powder was milled, freeze dried, crushed, sieved and thermally etched at 600ºC for 2 hrs.

3.3 Thermal analysis of powder- TGA/DTA

Concurrent measurement of both mass (weight) change (TGA) and heat flux (DTA) were carried out using a TA Instruments Q600 SDT, UK. The advantage of this machine was the simultaneous recording of both mass change and energy change which enables the user to analyse the data more quickly and straightforwardly. In this study, TGA/DTA was used to identify the temperature at which $SrCO_3$ decomposes and the temperature at which solid solution between two other metal oxides forms. The as-received alumina was used as a reference and thermally analysed under the same heating profile for comparison.

Powder (alumina-additives) was obtained by attrition milling, followed by freeze drying, crushing and finally sieving to ~ 45 µm. Approximately 45 mg of the sample was weighed and heated up to 1400 ºC at a rate of 10 ºC/min under the flow of air.

3.4 Particle size distribution (PSD)

The particle size analysis was performed in distilled water (wet dispersion) to reduce the amount of agglomeration. A Malvern Mastersizer 3000 was used to measure particle sizes ranging between 0.01µm-2 mm. In this technique, a laser diffraction method was used which measures the angular variation in intensity of the scattered light, after the laser beam hits a dispersed particle. As shown in Figure 3.1, large particles scatter light in smaller angles compared to small particles.

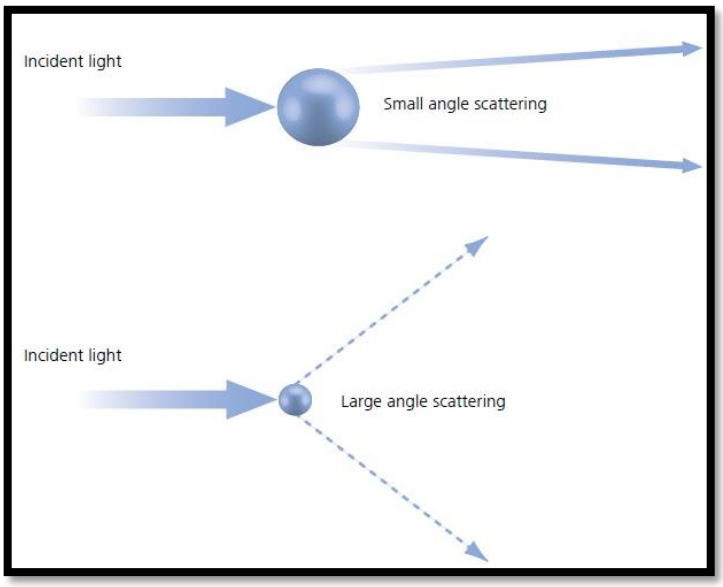

Figure 3.1. Illustration of light scattering upon collision with small and large particles [208]**.**

The angular scattering intensity data creates the scattering pattern, which is then analysed for calculation of particle size distribution. To assist full dispersion of particles, ultrasonic irradiation was used before sampling and three measurements were carried out for each sample to increase the accuracy and consistency of each test.

3.5 Spark plasma sintering (SPS)

Spark Plasma Sintering (SPS) was carried out in a FCT System (GmbH, Germany) apparatus under a vacuum of 10^{-4} bar. For all tests about 3 g of powder was loaded into the cylindrical graphite die of 20 mm internal and 40 mm external diameter. The graphite punch (20 mm in diameter) was mounted at top and bottom of the powder. To protect the powder bed from direct contact with graphite punch and wall of the die, a layer of graphite disc with a thickness of ~ 0.35 mm was used. This layer also helped the release of sample after sintering. Before starting the sintering process, the samples were firstly compacted by uniaxial pressing, using a pressure

of ~20 MPa. The samples were then heated up to 450 ºC in 3 mins and then they were heated to 1200ºC at a heating rate of 100 ºC/min while the pressure was progressively increased from ~16 MPa to ~51 MPa (16 kN). Subsequently, the temperature was increased from 1200ºC to the final sintering temperature at a heating rate of 50 ºC/min. Based on the designed recipe, as summarized in Table 3.2, once the specimen reached the ultimate temperature, it was kept under a pressure of ~51 MPa, for a specific dwell time.

Table 3.2. Summary of prepared specimen under various temperatures and dwell time.

Composite	***ZTA***	***ZTA-Additives***
(Max Temperature (ºC), Dwell Time (min))	(1350,1),(1350,5),(1350,10) (1400,1),(1400,3),(1400,5),(1400,10) (1450,1),(1450,3),(1450,5),(1450,10) (1470,5),(1470,8) (1500,1),(1500,3),(1500,5),(1500,10) (1550,1),(1550,5),(1550,10)	(1400,5),(1400,10) (1450,5),(1450,10) (1500,5),(1500,10) (1550,5),(1550,10)
Max Pressure (kN)	16	16

3.6 Grinding and polishing

Grinding and polishing of ZTA-based composites were found to be one of the tricky steps. This is due to the high hardness of the specimens and also the rough surface of samples, which stems from the graphite adhesion to the top and bottom surfaces of the samples occurring during the spark plasma sintering process. The following stages were proposed to obtain a scratch free surface, Table 3.3. Grinding and polishing was carried out by EcoMet ^{TM} 250 Grinder Polisher-Buehler. Depending on the grinding stage, the head and platen speed changed between 50-60 RPM and 150-250 RPM, respectively. The type of head force used was single and the corresponding force value changed between 10-20 N depending on the level of grinding or polishing.

Table 3.3. Grinding and polishing sequential steps of specimens.

Stage	Abrasive Surface and Abrasives	Pressure N	Time
Grinding Stage	Buehler, ApexDGD color,75µm	15-18	Until the graphite is removed
	Buehler, ApexDGD Color,55 µm	15	Until scratches from previous step were removed
	Buehler, ApexDGD Color,35 µm	15	Until scratches from previous step were removed
	Buehler, SiC Abrasive Paper, P800	15	Until scratches from previous step were removed
	Buehler, ApexDGD Color,15 µm	15	Until scratches from previous step were removed
	Buehler, SiC Abrasive Paper, P1200	15	Until scratches from previous step were removed
	Buehler, SiC Abrasive Paper, P2500	15	Until scratches from previous step were removed
	Buehler, ApexDGD Colour, 8 µm	12-15	Until scratches from previous step were removed
Polishing Stage	Buehler TextMet 1500 cloth, Meta Di™, Monocrystalline Diamond Suspension, 6 µm	12	Until the sample shined
	Buehler TextMet 1500 cloth, Meta Di™ , Monocrystalline Diamond Suspension, 1 µm	12	Until the sample shined
Final Polishing Stage	Metprep, PSA Backed, with Metprep, 0.06 µm Silco® Colloidal Silica Suspension	12-15	Until scratch free

3.7 Thermal etch

Thermal etching is known as a method to expose and characterize grain boundaries and releasing the residual stresses at the specimen surface resulting from grinding and polishing. Over-etching needs to be avoided due to grain growth and formation of an excessively rough surface. The series of experiments were undertaken at different temperatures. It was found that unexpected surface uplift occurred for thermal etching at temperatures higher than 1200ºC. The only explanation for this effect was that during spark plasma sintering, the zirconia was partially reduced and the oxygen deficiency led to a contraction of the unit cell; re-annealing then resulted in the expansion and uplift up of the surface. To avoid the aforementioned problems the thermal etch was carried out at 1200ºC for 0.1hrs at the rate of 10 ºC/min.

3.8 Density measurements

The density of the samples was measured using the Density Kit (Mettler- Toledo AG, Laboratory& Weighing technologies) designed based on the Archimedes' principal. To increase the level of accuracy the measurements were repeated three times. The Density Kit determined the density of the solid sample by the aid of a liquid such as water. The Mettler aperture measured the density of a sample based on the following relationship:

$$\rho = \frac{A}{A-B}\,(\rho_0 - \rho_L) + \rho_L \qquad \text{Eq.3.1}$$

where ρ is the density of a sample, A is the weight of the sample in air, B is the weight of the sample in water, ρ_0 is the density of water and ρ_L is the density of air ($0.0012\ \frac{gr}{cm^3}$).

Measurements were carried out right after the thermal etch when the specimen were at their cleanest state.

3.9 Grain size measurement

For the determination of the grain size in duplex structures, such as zirconia toughened alumina (ZTA), the simultaneous analysis of the volume fraction and grain size of each phase is required. The average grain size of both alumina and zirconia was measured by using the linear intercept method as explained by Higginson and Sellars [209]. The mean linear intercept length for zirconia and alumina are described as follows;

$$\boldsymbol{L}_{\boldsymbol{L(inter)i}=\frac{\overline{\boldsymbol{2P}}\boldsymbol{p}\,\boldsymbol{L}}{\boldsymbol{N}_{\boldsymbol{L(inter)}}}} \qquad \text{Eq. 3.2}$$

where $L_{L(inter)}$ is the linear intercept length of the second phase (zirconia) , $\overline{Pp}$ is the point fraction, L is the length of traverse lines and $N_{L(inter)}$ is the number of interphase boundaries (boundaries between alumina and zirconia).

$$\boldsymbol{L_{L(GB)i}=\frac{(1-\bar{P}_P)L}{(N_{L(GB)}+\frac{N_{L(Inter)}}{2})}} \qquad \text{Eq. 3.3}$$

where $L_{L(GB)}$ is the linear intercept length of matrix (alumina), $\overline{Pp}$ is the point fraction, L is the length of traverse lines, $N_{L(inter)}$ is the number of interphase boundaries (boundaries between alumina and zirconia) and $N_{L(GB)}$ is the number of matrix grain boundaries (boundaries between alumina and alumina).

The relative standard errors in measurements of grain size are given by:

$$\boldsymbol{\frac{S(\overline{L})}{\bar{L}} \approx \frac{0.65}{\sqrt{n}}} \qquad \text{Eq. 3.4}$$

where $\bar{L}$ is the mean linear intercept, $S(\overline{L})$ is the standard error and $\sqrt{n}$ is the number of grains (measurement). For an accurate calculation, more than 1000 grains were counted and measured on each specimen.

3.10 Hardness-Toughness

The fracture toughness (K_c) and hardness (H_V) of the specimens were measured by the macro indentation method. This technique was used in this case because it was the most appropriate given that the focus of the study was on wear behaviour, which is surface specific. To measure the toughness (K_c) and hardness (H_V), the samples were indented using a standard Vickers macro hardness indenter with a load of 10 kg for 10 sec dwell time. About fifteen indentations were made on each sample and the average crack lengths and diagonal lengths were measured by optical microscopy (Nikon Eclipse LV150, Japan).

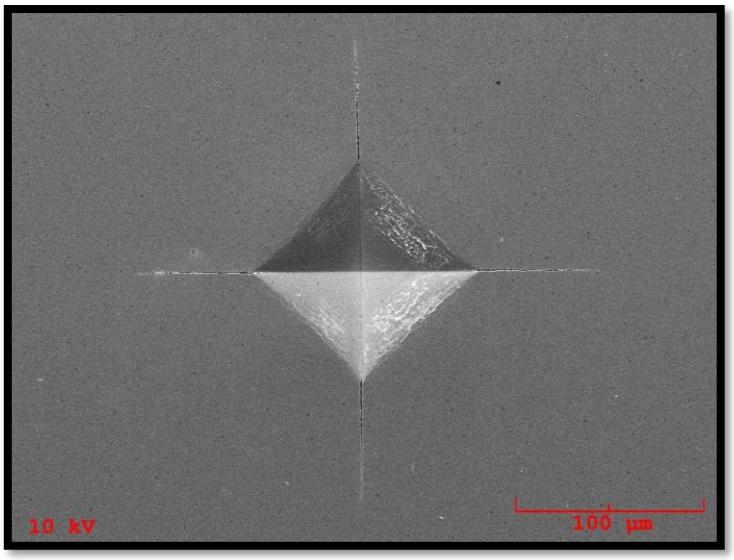

Figure 3.2-Schematic illustration of macro indentation [210]**.**

The average lengths were measured to calculate the fracture toughness by the following equation proposed by Shetty *et al.* [211] and amended by Ponton and Rawlings *et al* [212].

$$\boldsymbol{K_c = \frac{0.0319P}{al^{\frac{1}{2}}}} \qquad \text{Eq. 3.5}$$

where K_c is the indentation toughness, P is the load test, a is the average half diagonal length and l is the average crack length. This equation assumes that the crack is a Palmqvist and not a radial crack, which has experimentally been shown to be the case for this type of material The Vickers hardness was assessed by the equation proposed by the same author.

$$\boldsymbol{H_V = \frac{0.4636P}{a^2}} \qquad \text{Eq.3.6}$$

3.11 Tribological behaviour

3.11.1 Lubricant

Bovine calf serum is one of the common lubricants used in joint simulation tests, although its behaviour in wear test of ceramics is not completely understood. Various research has demonstrated that the composition of the lubricant plays an important role in an *in vitro* wear test. When using this lubricant, it produces debris structures, wear mechanisms, and surface appearances that resemble those of the clinical performances. However various results have been published by researchers, which is due to the different chemical compositions that have been used. The investigation by Doubleton et al. demonstrated that 50 vol.% new born calf

serum solution contains 20 g/L protein that is considered to be within physiological range of synovial fluid [213]. The first important consideration is that the protein concentration can vary based on the joint examined. For example, in diseased joints the synovial fluids include more protein compared to healthy ones. Additionally, in different joints the viscosity of synovial fluid varies [214]. To fulfil the purpose of this study, 25 vol.% sterile new born calf serum was used, supplied by First Link (UK) Ltd. The total protein composition of this product is 63.3 g/L, reported by the corresponding company.

Prior to running the test, the serum solution was diluted with phosphate buffered saline (PBS) 1× (0.01 M). PBS contains sodium chloride, sodium phosphate and potassium phosphate and behaves as a buffer to maintain the pH constant. This salty solution is non-toxic and isotonic to cells. The PBS solution was prepared by dissolving one tablet of Phosphate Buffered Saline (Sigma-Aldrich, UK) in 200 mL ultra-pure water (Fisher Scientific, UK) as per the manufacturer's instructions. In addition to phosphate buffered saline, 0.1 wt. % sodium azide (Fisher Scientific, UK) was added to serum as an antibacterial additive [215,216] to prevent the possibility of bacteria growth and degradation problems at room temperature. The viscosity of the prepared solution as a lubricant was ~ 0.0012 Pa.s.

3.11.2 Wear test equipment

The lubricated sliding wear tests were carried out on a reciprocating ball on flat UMT Tribometer (Centre for Tribology, Inc. USA) at room temperature, using a 25 vol. % new born calf serum as lubricant. A high purity alumina ball, 4 mm in diameter, (Oakwade Ltd, UK) with a constant roughness of about 5-8 nm, was used as a counter body.

As illustrated in Figure 3.3, the alumina ball is set up as a counter body in the upper holder which is linked to a vertical linear motion system. This system can measure to an accuracy of 50 nm. For all the tests, the specimen was mounted in the lower liquid chamber using a thermosetting wax.

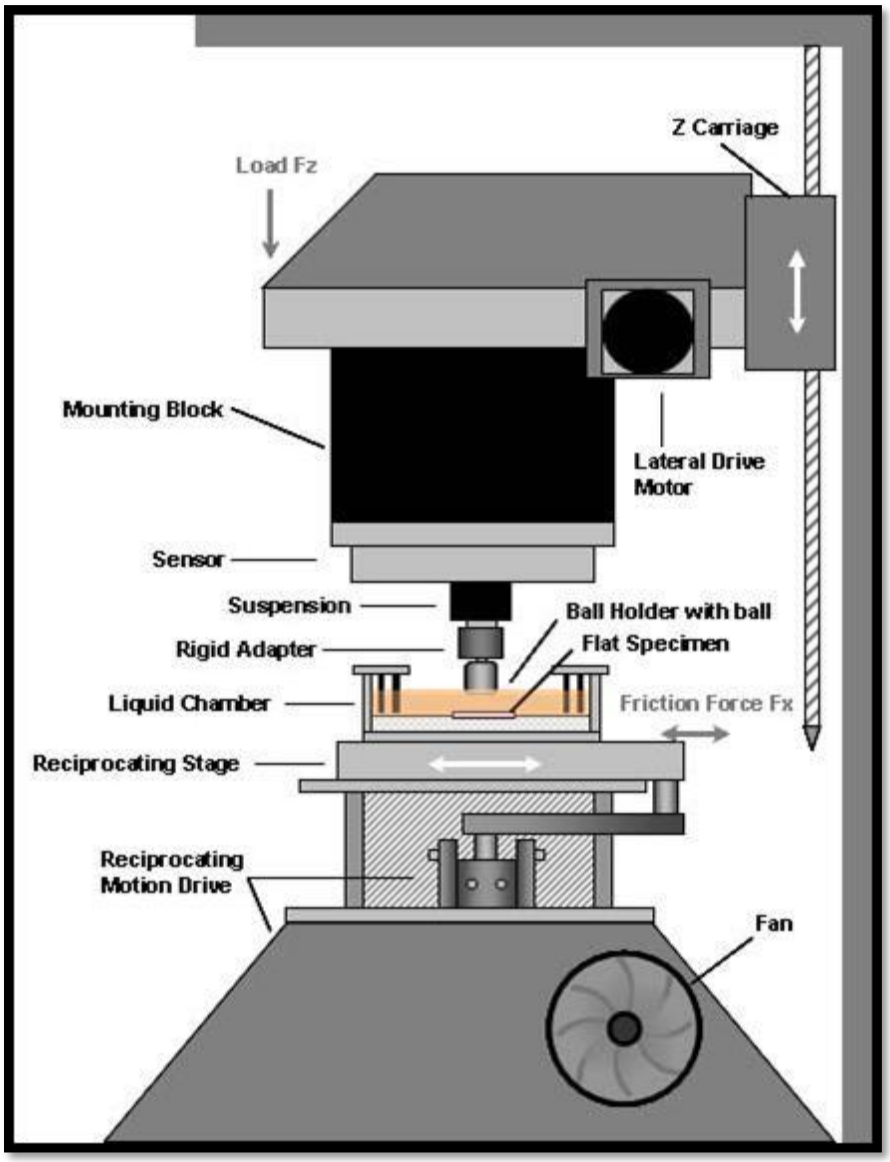

Figure 3.3. Schematic image of the CERT UMT reciprocating tribometer (Image taken from CERT, US).

For the purposes of this study, a range of different force sensors, including DFM-0.5 (0.05-5N) with a resolution of 0.25 mN and DFM-5 (0.5-50 N) with a resolution of 2.5 mN were used. The sensor can make a precise and simultaneous measurement of load and stress in 2D, and subsequently transfer feedback to the vertical motion controller and maintain a constant load through adjustment of the sample position. All data can be obtained, measured and displayed in real time.

Normal loads of 1 N, 2 N, 4 N, 8 N, 16 N and 32 N with a reciprocating motion of 600 rpm and a frequency of 10 Hz (which is equivalent to the velocity of 0.2 m/s) were used. An

identical 10 mm stroke length was pre-set for all tests. The duration of reciprocating motion was set to 10-12 hrs. Prior to running the sliding wear test, the specimens were ultrasonically cleaned with alcohol. Subsequently they were mounted in the clean liquid chamber. Before commencing each test, fresh lubricant was injected into the liquid chamber. The UMT Tribometer is able to record time and coefficient of friction during the test. These data can be then directly used to plot coefficient of friction (COF) Vs time graph to analyse the wear behaviour of specimens under the set up condition.

3.11.3 Lubrication regime

The lubrication regime involved in the wear process can be identified using the conventional Stribeck curve. This curve is the plot of friction coefficient (COF) versus Sommerfeld number (Z), Figure 2.17. The Sommerfeld number is a dimensionless parameter which is important in lubrication analysis and can be calculated by the following equation;

$$Z = \frac{\eta \times v}{N} \qquad \text{Eq. 3.7}$$

where η is the viscosity of the lubricant (Pa.s), v the sliding velocity (m/s) and N is the normal load (N).

3.11.4 Wear rate calculation

The wear rate of a worn sample in a specific lubricant can be calculated from 3D optical profiles using the Contour GT. Initially, the area of about 10 cross-sections along a wear track was measured in order to calculate the average cross-sectional wear loss area (A). Thereby, the total wear loss volume for each wear scar can be assessed by the following equation:

$$V = AD \qquad \text{Eq.3.8}$$

where A (mm^2) is the average area of wear loss and D (mm) is the length of a wear track. Eventually, using the Archard theory [217] [218], the specific wear rate k (mm^3/Nm) was determined;

$$k = \frac{V}{NS} \qquad \text{Eq. 3.9}$$

where V is the volume loss (mm^3), N is the applied load (N) and S is the sliding distance (m).

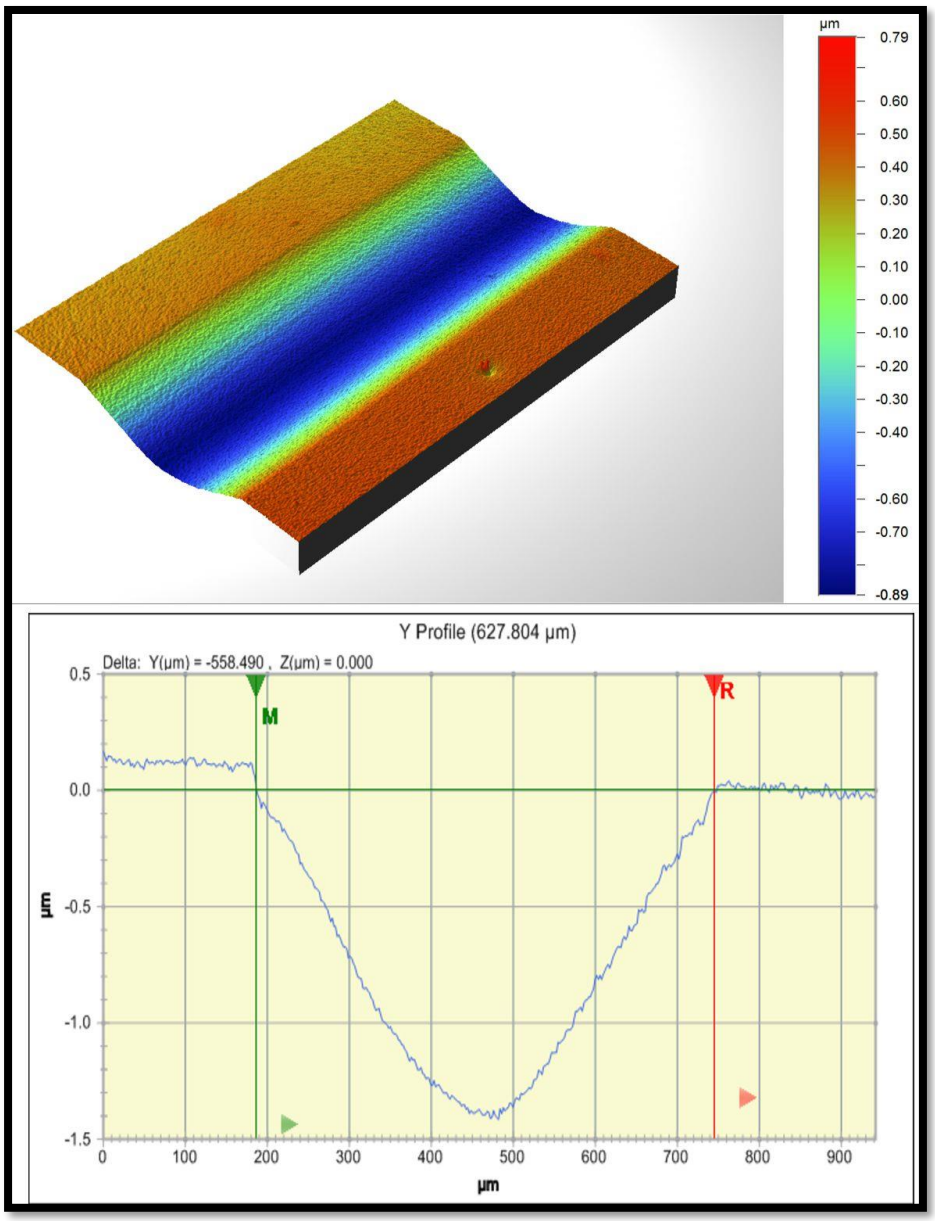

Figure 3.4. Schematic profile of worn surface taken by Contour GT.

3.11.5 Contact pressure

When a sphere of an elastic material such as an alumina ball is pressed by a normal load N over a flat surface, i.e. the zirconia toughened alumina composite, contact will take place. The magnitude of the stress, pressure and contact area can be calculated by Hertzian contact theory [146, 167].

This contact area between the surface and the counter surface forms a circular area of radius a which can be determined by the following equation:

$$a = \left(\frac{3Nr}{4E^*}\right)^{1/3} \qquad \text{Eq.3.10}$$

where r is the radius, N is the load, E^* is an elastic modulus and can be calculated by:

$$\frac{1}{E^*} = \frac{(1-v_1^2)}{E_1} + \frac{(1-v_2^2)}{E_2} \qquad \text{Eq.3.11}$$

where E_1 and E_2 are Young's moduli, v_1 and v_2 are Poisson's ratios and 1 and 2 refer to the contacting surface (1) and the counter surface (2).

The distribution of contact stress over the circular area is not uniform. The value of this stress is maximum at the centre point and decreases to zero at the edges. As a result, the following relation between max pressure P_{max} and mean pressure P_{mean} is as follows;

$$P_{max} = \frac{3}{2}P_{mean} = \frac{N}{A} = \frac{N}{\pi a^2} = \frac{1}{\pi}\left(\frac{6NE^{*2}}{r^2}\right)^{1/3} \qquad \text{Eq.3.12}$$

In initial contact, it was assumed to have a plane strain condition. Therefore, the maximum shear stress τ_{max} was determined by:

$$\tau_{max=\frac{P_{max}}{3.3}} \qquad \text{Eq.3.13}$$

which was formed under the surface at a depth of $0.48a$:

$$h_{max=0.48a} \qquad \text{Eq.3.14}$$

3.12 Wear scar characterization

3.12.1 Contour GT

Wear tracks resulting from reciprocating wear tests were analysed by an optical interferometer, Contour GT-K1 (Veeco Instrument, US). Contour GT is a non-contact, non-destructive method that provides cross sectional profile measurements of the wear scar and facilitates understanding of friction and other wear mechanisms. The Contour GT family is equipped with the software called Vision 64^{TM} which addresses specific and complicated measurements. Through this software, 3D analysis of the surface and the wear scar can be easily achieved, Figure 3.5.

The size of the wear scar changed significantly as a function of applied load and the composition of the specimens. Therefore, the operating parameters of the Contour GT needed to be changed, for example, back scan, length or illumination (white-green) to collect the

required data. In this study mainly white illumination, VSI mode and objective lenses of 2.5x -50 x were used. The back scan and length were correspondingly varied between 10-20 µm. To calculate the wear loss, each wear scar was measured at 10 different points along the track and an average was taken.

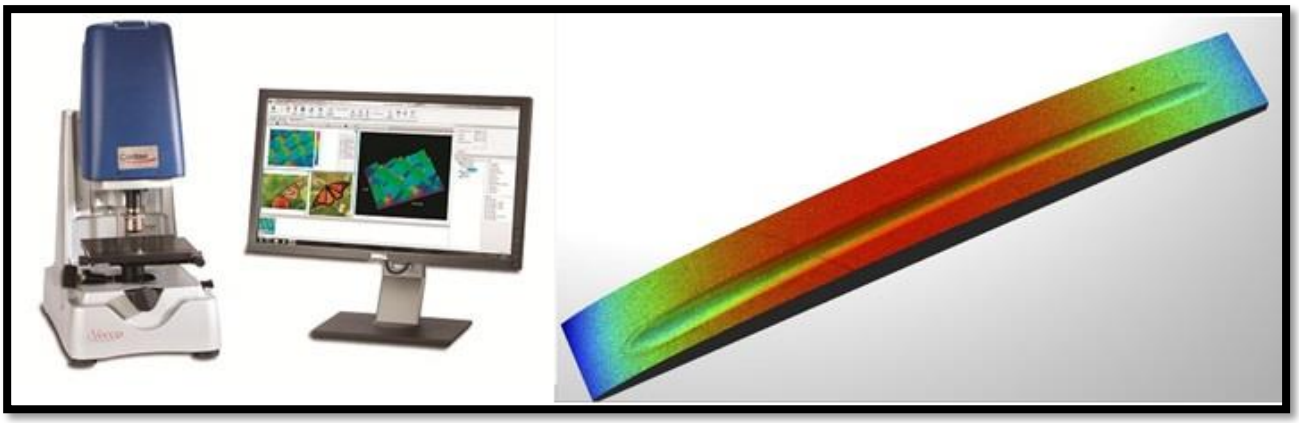

Figure 3.5. Typical schematic of Counter GT [219]**.Stitching profile of wear scar under 8N load in ZTA-additives.**

3.12.2 Atomic force microscopy (AFM)

Atomic force microscopy can provide 3D images of specimens at the nano-scale where standard optical microscopy is not able to operate. In this study, the topographic and friction information of the surface and the wear scar is acquired using Dimension 3100 scanning probe microscope (Veeco Instruments, US) operated in contact mode.

In contact mode, the probe is in permanent contact with the surface while scanning, Figure 3.6. Once the tip comes to the contact with surface, it is deflected which is directly proportional to the normal load on the probe. In this study, a silicon nitride probe with the following specification of cantilevers was employed, Table 3.4.

Silicon nitride cantilevers have a low spring constant which leads to the deflection of the cantilever under small loads. The amount of deflection of the probe can be assessed through laser signal changes in photodiode quadrants that is reflected back to a detector. In order to keep the bending of the cantilever invariable, a Z-feedback circuit is used. The role of this circuit is to change the vertical position (z) of the scanner vertically while the topography of the surface varies during the scanning.

Table 3.4. Specification and schematic of Pyrex Nitride probe for contact mode of AFM [220]**.**

Pyrex Nitride Probe – Silicon Nitride- Triangular Cantilevers		
Cantilever type	Cant. 1	Cant. 2
Thickness (µm)	0.5	0.5
Length (µm)	100	200
Width (µm)	2×13.5	2×28
Resonance Frequency (kHz**)**	67	17
Force constant (N/m)	0.32	0.08

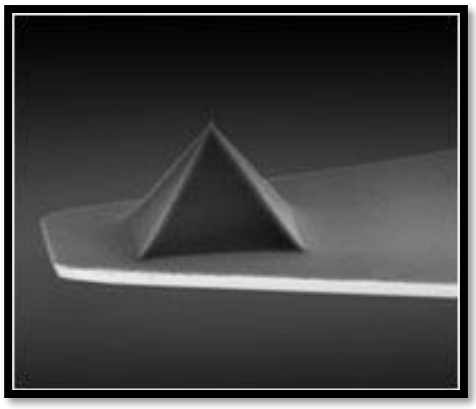

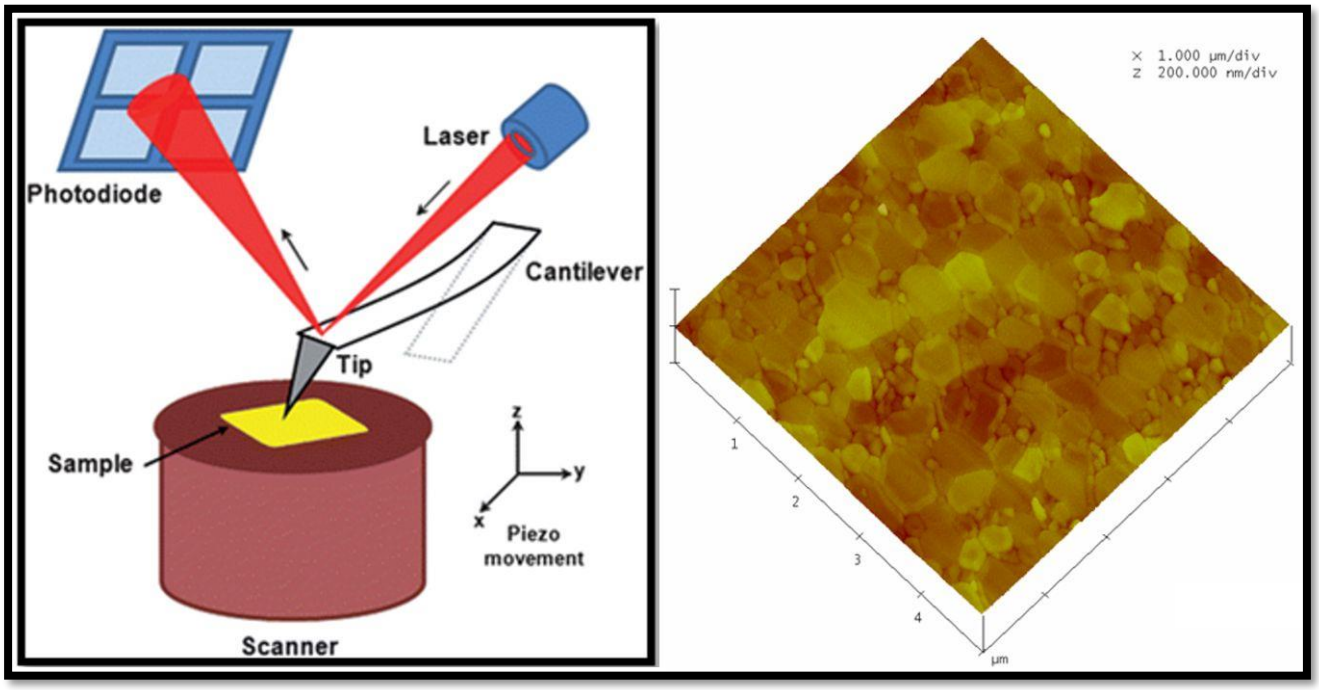

Figure 3.6. Schematic of contact mode in AFM [221]**-3D image of ZTA taken by AFM.**

3.12.3 Raman spectroscopy

In this study, Raman Spectroscopy was used to characterise the wear scar and reveal the possible formation of a carbonaceous layer upon decomposition of the lubricant. This technique also assisted in assessing the phase transformation of zirconia that possibly took place during wear, Figure 3.7.

Raman spectra were obtained through using a Renishaw inVia Raman microscope with a green Ar laser (514.5 nm) passing through the objective lens of 50x. It was powered up to 20 mW and focused on a ~ 3µm spot.

The microscope was connected to a computer controlled stage and was able to record data by the software programme "WiRE 3.4". The collected spectra were in the range 100-1600 cm^{-1} and depending on the specimen, the number of accumulations and exposure time changed between 1-2 and 10-20s, respectively.

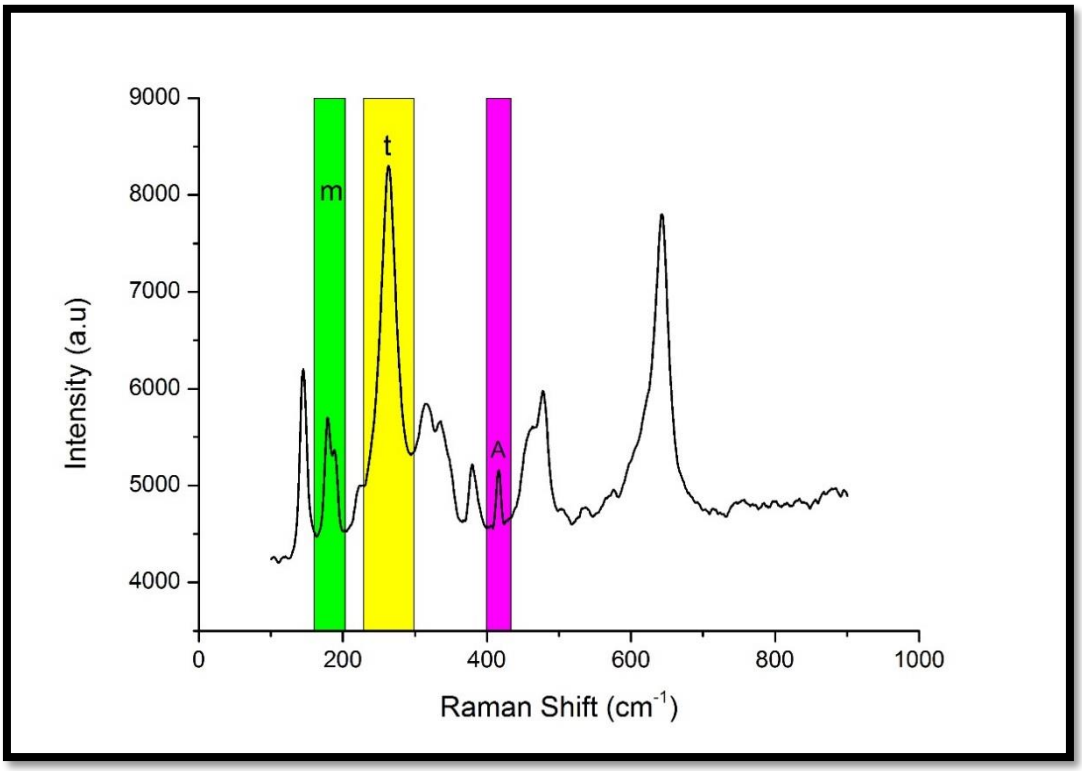

Figure 3.7. Typical Raman spectra of Biolox® delta under 32N load representing monolithic alumina (A), monoclinic (m) and tetragonal (t) phase of zirconia.

3.12.4 Scanning electron microscopy (SEM)

Scanning electron Microscopy (SEM) was used to characterize both the surface and wear scars. To do this, field emission gun scanning electron microscope, Inspect F50 (FEI Company, Netherlands) was used. Prior to the test, the specimens were carbon coated to form a conductive layer on the surface and mounted on an aluminium stub. Subsequently, the specimens were analysed with an accelerating voltage of 5-15 kV, and a working distance of ~10 mm.

3.12.5 Focused ion beam (FIB) microscopy

To examine the sub-surface microstructure of worn surfaces, Focused Ion Beam Microscopy (FIB) was used. In this technique, a focused beam of accelerated Ga^+ ions were employed to impinge the specimen with high energy density and thus directly remove hard material. So, a very thin and electron transparent layer of sample is achievable through this technique. For the purpose of this study, FIB technique was used to prepare site-specific TEM specimens, Figure 3.8.

To protect the section of interest from being damaged by the Ga^+ ions beam, the surface was coated with a layer of gold and carbon respectively. Gold coating covers the worn area and creates a barrier between carbon coating and a possible carbonaceous layer, which might have been left by the lubricant. These layers also provide electrical conductivity and prevent charging. In this study, Helios NanoLab G3 UC (FEI, USA) was employed to prepare the specimens (TEM foil) from the sub-surface of a wear track. In Addition to the protective double layers of gold and carbon, E-deposition and Pt layer deposition was done to protect the area of interest from Ga^+ ions damage.

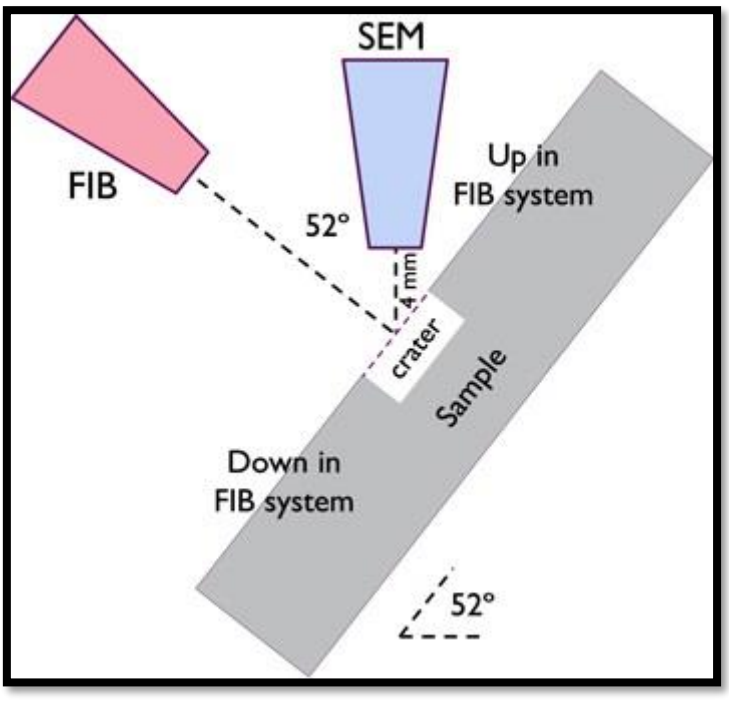

Figure 3.8. Schematic of FIB [222]**.**

Subsequently, in order to make two trenches with a depth of more than 7 µm at each side of the deposition, the sample stage was tilted 52º to be perpendicular to the ion beam, Figure 3.9 (c). To mill the trenches, a high ion current of 5-20 nA followed by a low ion current of 1-3 nA

was used. Once the foil thickness reached ~ 1µm, the stage holder tilted back 7º to cut through the foil and leave a small tab by which the foil was still attached to the bulk specimen, Figure 3.9 (d). Afterwards, the stage holder returned to 0º and an Omni probe micromanipulation tool was inserted and brought into contact with the foil. At this point the Omni probe and right-hand edge of the foil were milled together by carbon deposition (2 µm × 2 µm), Figure 3.9 (e). After milling away the small tab, the Omni probe was retraced and the foil was lifted out. The lifted foil was then attached with carbon deposition to a TEM copper grid which was placed into the FIB chamber. Subsequently the connecting point between the Omni probe and foil was milled away and left the foil attached to the copper grid. Finally, polishing and thinning at each side of the foil was performed with progressively smaller ion beam currents and the final cleaning and polishing was performed with a 30 pA current. After the thinning and polishing step, the thickness of the foil was less than ~100 nm, Figure 3.9 (f).

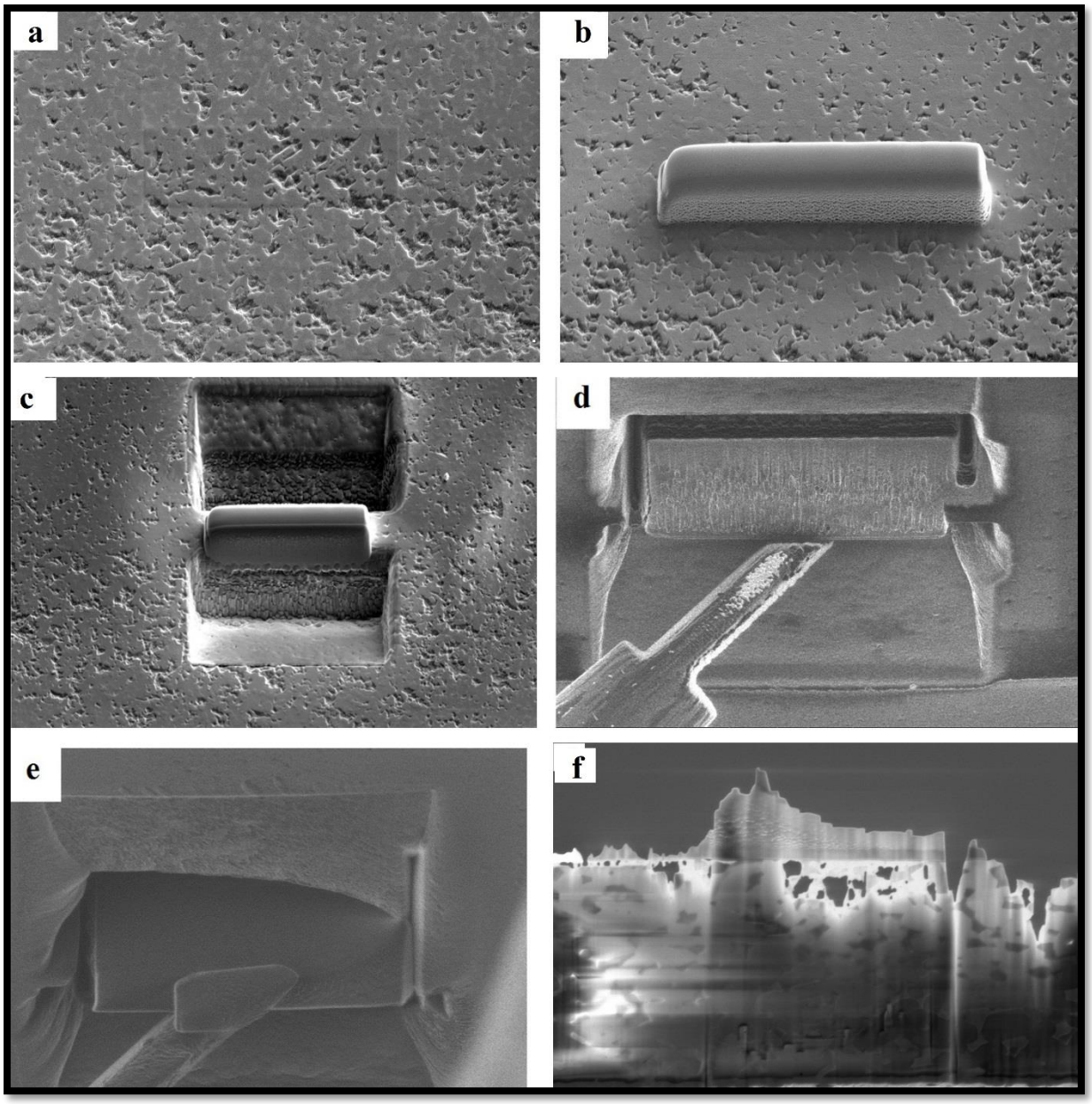

Figure 3.9. a) Pt E-deposition. b) Pt deposition. c) Two trenches at each side of the deposition. d) Omni probe levelled with foil. e) Omniprobe milled to the foil. f) Thinned specimen.

3.12.6 Transmission electron microscopy (TEM)

Transmission electron microscope (TEM) is a technique in which high electron beam is employed through ultra-thin specimens (less than 100 nm) to form an image. This technique is able to reveal the crystal structure, phase, morphology and defects within the specimen with an atomic resolution. In this study, an FEI Tecnai T20 with an accelerating voltage of 200 kV and a Philips EM420 operating at 120 kV were used to characterise the morphology of the worn tracks using FIB specimens.

4 Ceramic processing

4.1. Powder dispersion

In SEM micrographs, Figure 4.1 (a-d), three distinct regions are discernible. The first one was from when the material was distributed and the other two are when there was aggregated zirconia (white regions) and alumina (darker regions). These images represent the dispersion of ZTA under different processing conditions in term of milling time, dispersant and pH environment, Figure 4.1 (a-d).

In Figure 4.1 (a-b), nitric acid (HNO_3), as a dispersant and a pH adjuster, was being used to adjust the pH of the working area to an acidic environment in which the pH is ~ 4.5. In Figure 4.1(c), no dispersant or pH adjuster were used and this batch, similar to the two previous batches (Figure 4.1 a-b), was attrition milled for 7 hrs at 450 rpm. SEM micrograph 4.1 (d), shows a sample that was ball milled for 7 hrs in nitric acid at pH ~4.5. In all processing conditions presented in Figure 4.1(a-d), the slurry solid solution was around ~ 28 wt. % and they were dried by oven, at temperature ~ 80˚C.

In Figure 4.4 (a-b), the optimum condition to obtain a homogenous sample was employed as explained in part 3.2. As illustrated in Figures 4.2 and 4.3, citric acid shifts the isoelectric point (IEP) to the right, for both alumina and zirconia. Thus, zeta potential reached its highest value at a pH range of 8 to 10. As shown by Shen et al. [223] , the addition of 1 wt.% citric acid to zirconia shifted IEP to a pH lower than 2.5, securing a high repulsive negative potential of around 60 mV for a wide range of pH (Figure 4.3). Studart et al. [224] used 0.236 mg/m^2 of citric acid to disperse calcined alumina. With this amount of dispersant, IEP of alumina was effectively shifted from approximately 10 to a pH in the range of 4-6. This consequently resulted in a high negative zeta potential of ~ 40 mV in a pH ranging between 8 to 10. In this study, to determine the required quantity of citric acid, the total surface area of particles was calculated.

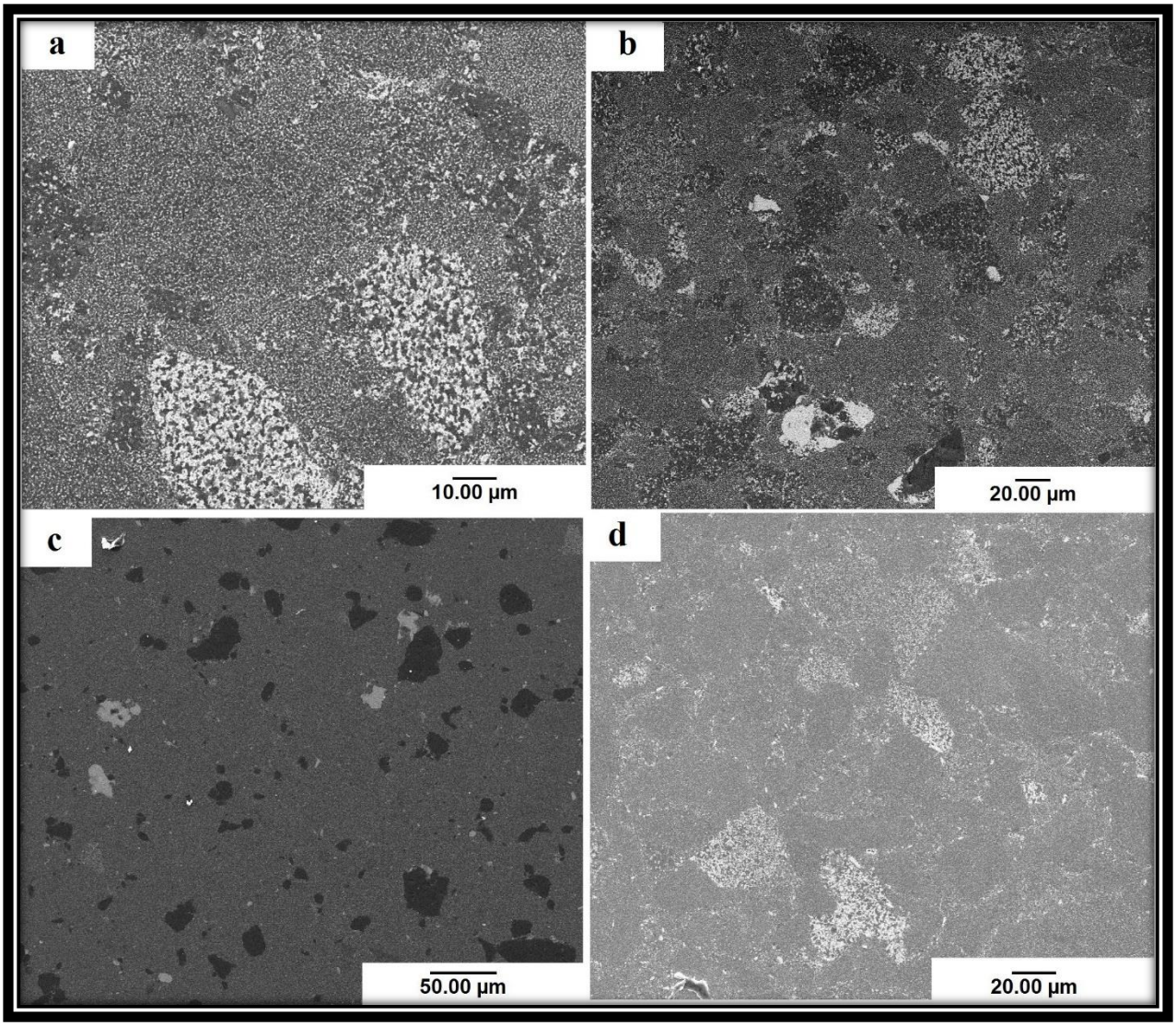

Figure 4.1. a) ZTA additives sintered at 1450ºC-5 min. b) ZTA-additives sintered at 1450ºC-10 min. c) ZTA sintered at 1400ºC-5 min. d) ZTA 1450ºC-5 min.

Subsequently, the amount of citric acid absorption per m^2 in a specific pH was estimated from the literature, for both alumina and zirconia particles [223,225]. The pH of the working environment was adjusted to ~ 9.5 by ammonium hydroxide. About 0.2 g of citric acid, as a dispersant, is believed to cover the entire particle surface area at this pH. Figures 4.2 and 4.3, taken from two different studies, show the behaviour of alumina and zirconia while they are in neutral, acidic and basic environment.

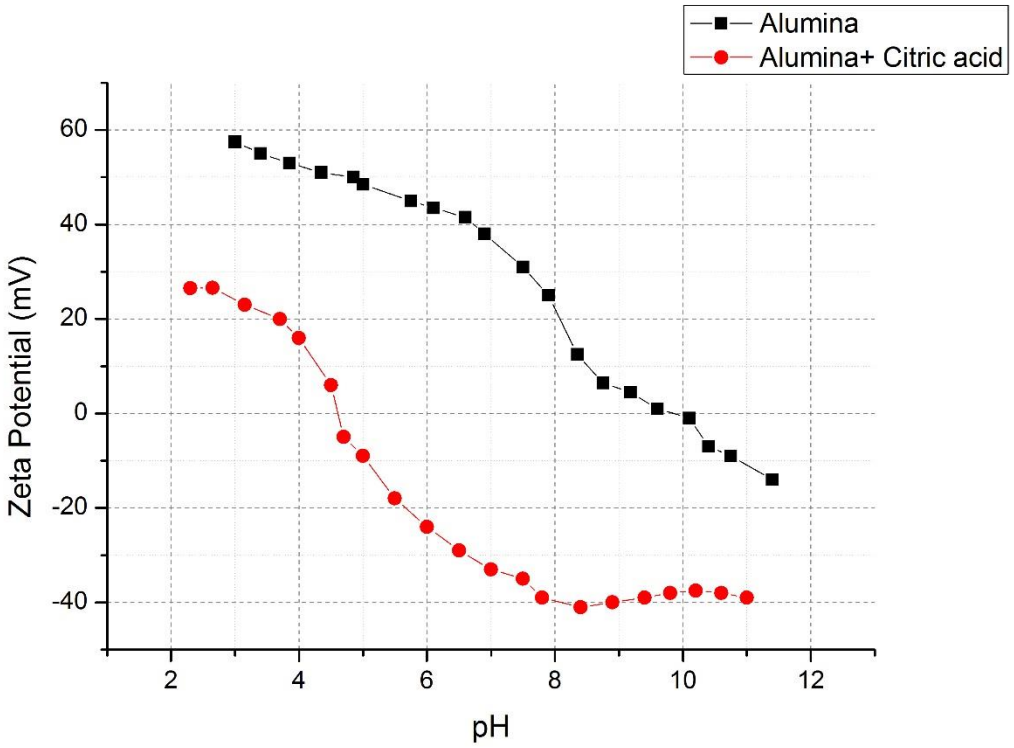

Figure 4.2 Zeta potential as a function of pH of calcined alumina without dispersant and in the presence of citric acid. Graph taken from [224]**.**

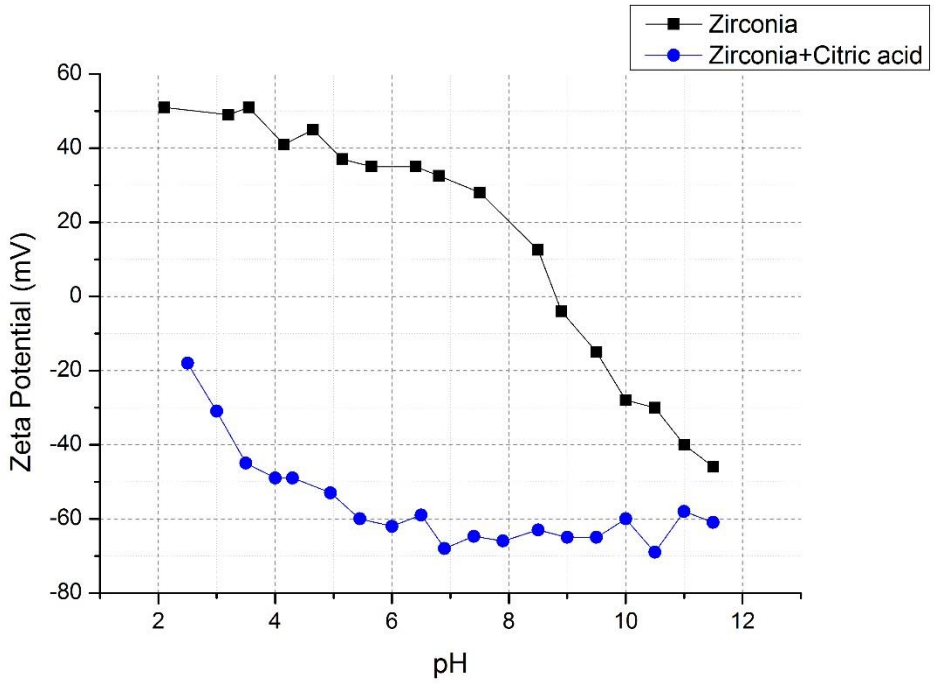

Figure 4.3 Zeta Potential of the as received, de-agglomerated Meso tetragonal zirconia as a function of the pH. Graph taken from [223]**.**

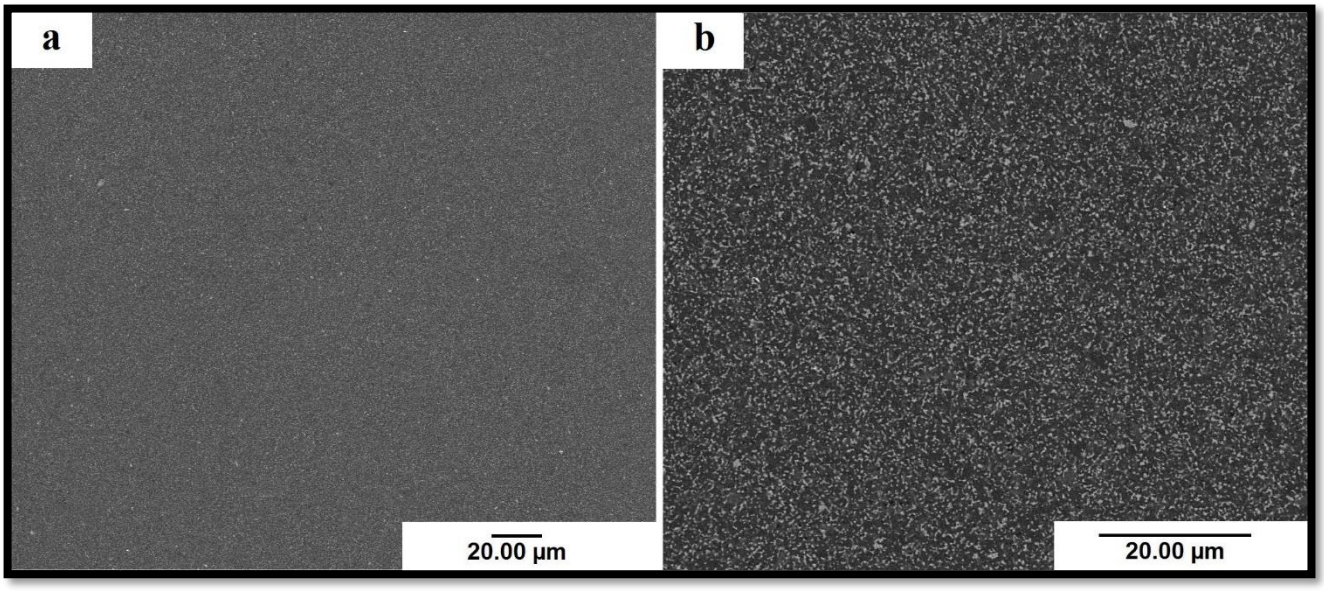

Figure 4.4 SEM micrographs of a) ZTA sintered at 1450ºC -5 min b) ZTA-additives sintered at 1500ºC-5 min.

4.2 Thermal analysis TGA/DTA

The appropriate selection of the treatment temperature and time is of a great importance as it affects the composite powder features including the amount of particle agglomeration, second phase distribution and size. Figure 4.5 gives Differential Thermal Analysis (DTA) and Thermo Gravimetric Analysis (TGA) on alumina-additives (Cr_2O_3 and $SrCO_3$) and shows few endothermic peaks in region A, and exothermic peaks in regions B and C. The corresponding mass loss for the whole process up to 1400ºC was ~ 0.55 wt.%. The TGA curve, Figure 4.5, shows a gradual and small weight loss of ~0.33 wt.% in region A between ~100ºC-720ºC. Subsequently, region B, between ~750ºC-1200ºC, exhibited a 0.08 wt.% weight loss. Finally, region C ranged at temperatures between ~ 1350ºC-1400ºC showed almost no mass loss accompanied by an exothermic peak, Figure 4.5.

Figure 4.6 shows the behaviour of pure alumina, as received, under thermal analysis and was employed as a reference to explain the data in region A. As shown in Figure 4.6, these exothermic peaks occur between ~0-450ºC and accompanied by a weight loss of ~0.85wt.%.

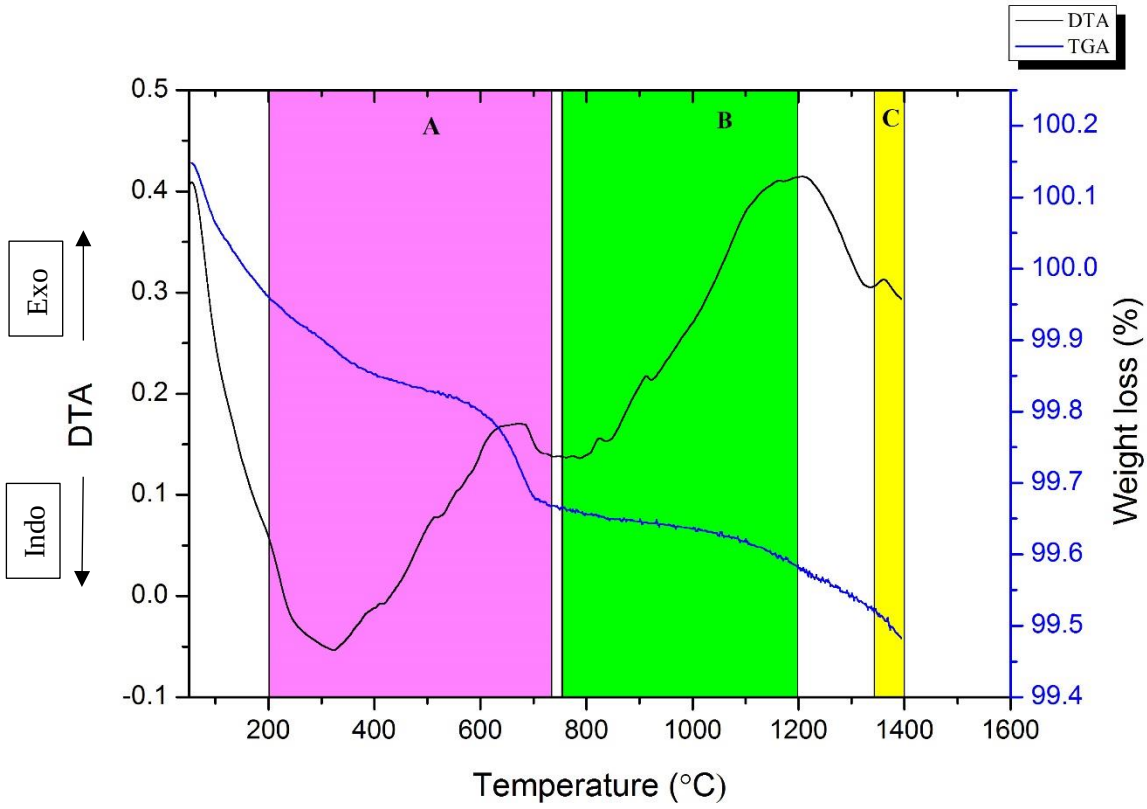

Figure 4.5. TGA/DTA of Al_2O_3 and additives.

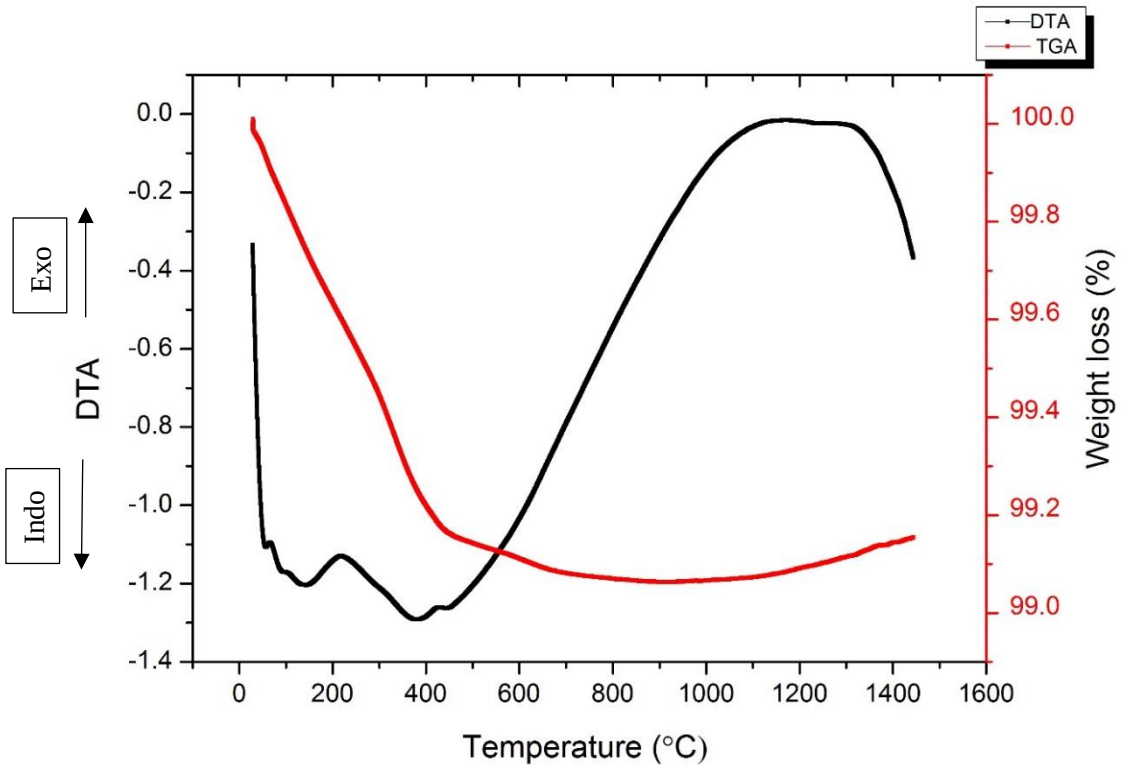

Figure 4.6. TGA/DTA of Al_2O_3.

4.3 Particle size analysis

To improve the densification of the final sample, a mixture of different particle sizes is beneficial. When fine particles are present in the green body, they can occupy the empty spaces between large particles and assist in obtaining a high density compact.

In this project, the mixture of ZTA-additives powders went through a double calcination procedure, with different temperatures and dwell times, to get rid of the unwanted gasses formed during the decomposition stages. To understand the effect of calcination temperature and time, the particle distribution analysis was run to compare the particle size of the powder, before and after calcination.

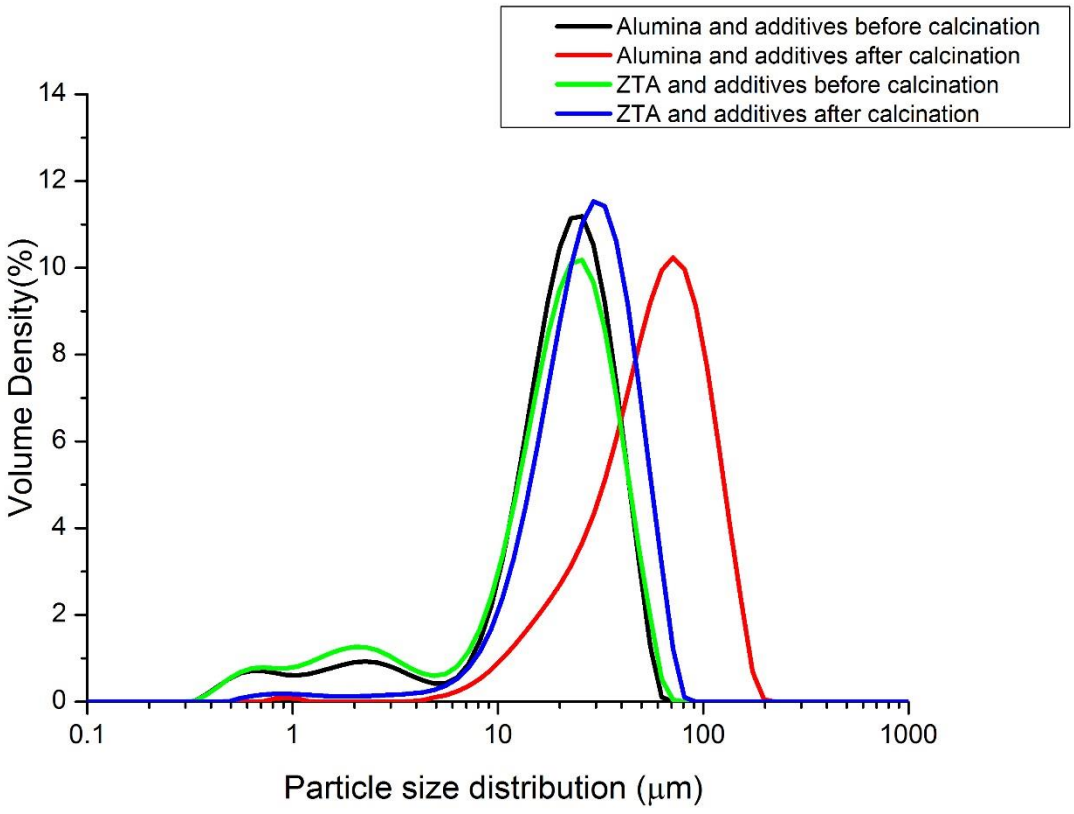

Figure 4.7. Particle size distribution of ZTA-additives in different preparation stages before SPS

In Figure 4.7, the black curve, labeled as alumina-additives before calcination represents the mixture of Al_2O_3, $SrCO_3$, and Cr_2O_3 that went through attrition milling followed by freeze drying. The alumina-additives after calcination at 1050˚C for 6 hrs is shown as the red curve. The third graph, (the green curve) tagged as ZTA-additives before calcination, represents the point at which the ZTA- additives were milled and freeze dried. The last curve, labelled as ZTA-additives after calcination (the blue curve), is after calcination at 600˚C for 2 hrs. The

cumulative statistics of particle size distribution for the powders before and after calcination are shown in Table 4.1. D_{10}, D_{50} and D_{90} are representative of the particle sizes at which 10%, 50%, and 90% of the total volume of particles were smaller than, respectively.

Table 4.1. Particle size analysis of the ingredients of the final powder mixture at different stages of production by laser diffraction method.

Composite	D_{10}	D_{50}	D_{90}
Al_2O_3 with $SrCO_3$, and Cr_2O_3 before Calcination, Size (µm)	3.39	21.0	38.6
Al_2O_3 with $SrCO_3$, and Cr_2O_3 after Calcination, Size (µm)	20.1	59.0	114.0
Al_2O_3 with $SrCO_3$, and Cr_2O_3 after Calcination, Size (µm)- Ultrasonic	1.41	18.9	54.6
ZTA with $SrCO_3$, and Cr_2O_3 before Calcination, Size (µm)	2.33	20.4	39.5
ZTA with $SrCO_3$, and Cr_2O_3 after Calcination, Size (µm)	12.3	27.3	49.6
ZTA with $SrCO_3$, and Cr_2O_3 after Calcination, Size (µm) - Ultrasonic	1.34	14.3	32.8
ZTA after Calcination, Size (µm)-Ultrasonic	1.56	15.5	37.9

All tests summarized in Figure 4.7 were obtained using the stirrer at 2000 rpm to prevent the settling of powders. For two samples, labelled as alumina-additives after calcination and ZTA-additives after calcination, another set of tests were performed under the same conditions, but with the addition of an ultrasonic agitator. As shown in Figure 4.8, the curves shifted to smaller sizes, after using ultrasonic for approximately 60s. As summarized in Table 4.1, D_{50} for alumina- additives after calcination dropped from 59.0 µm to 18.9 µm and for ZTA- additives after calcination shrank from 27.3 µm to 14.3 µm.

Figure 4.9 shows the particle size distribution comparison between ZTA and ZTA-additives, with the ultrasonic being used. Under the same condition, D_{50} for ZTA and ZTA- additives is measured at ~ 15.5 µm and ~14.3 µm, respectively.

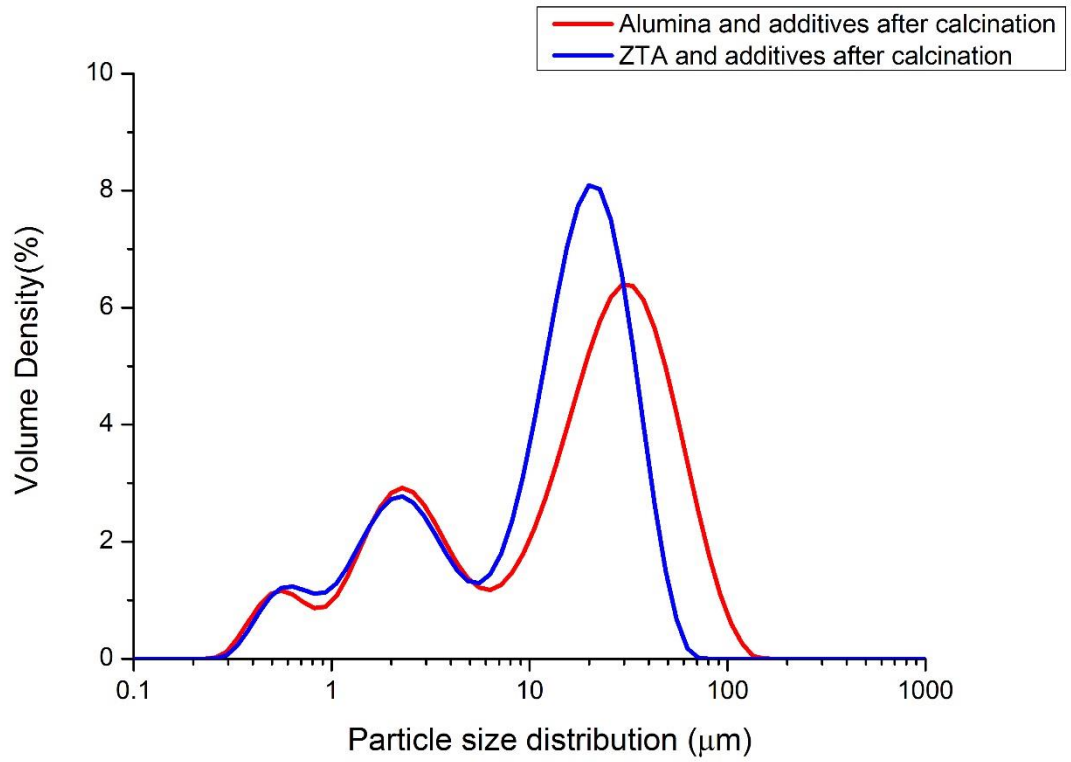

Figure 4.8. Particle size distribution of alumina-additives after calcination and ZTA- additives after calcination.

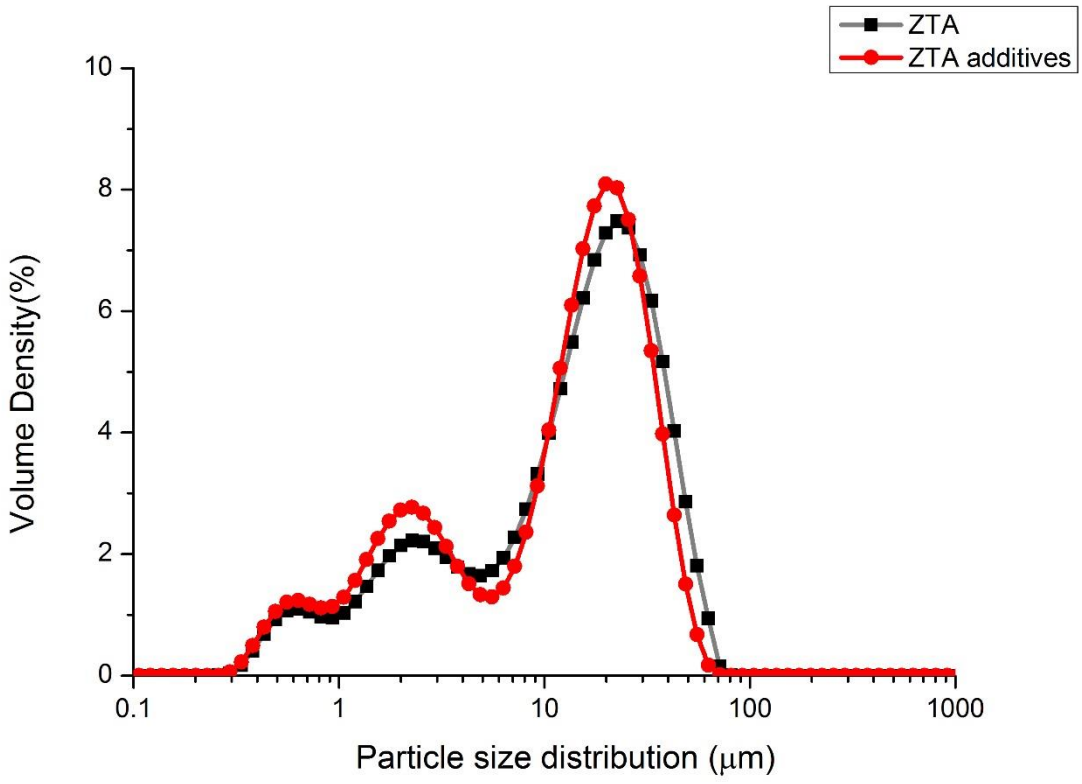

Figure 4.9. Particle size distribution of ZTA and ZTA-additives before SPS.

4.4 Properties of sintered specimens made by spark plasma sintering

4.4.1 Density

The recorded shrinkage curves for ZTA sintered at 1470ºC for 8 min holding time and ZTA with the oxide dopants sintered at 1500ºC for 5 min, are shown in Figures 4.10 and 4.11, respectively.

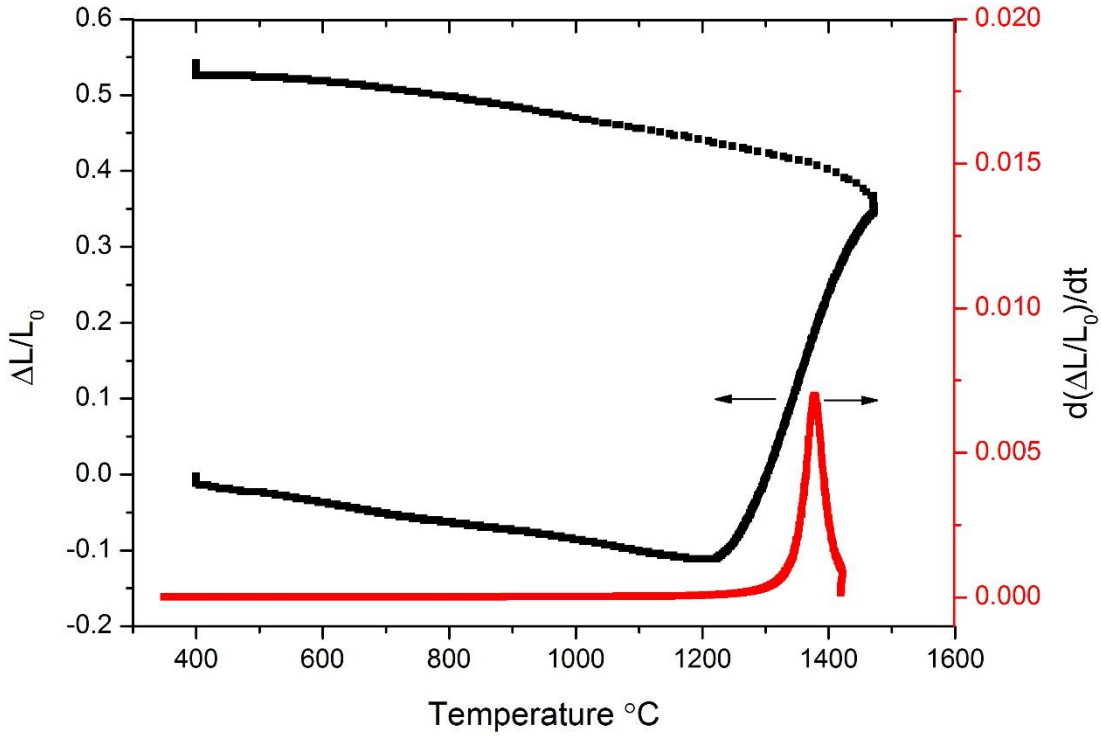

Figure 4.10. The shrinkage behaviour of ZTA during spark plasma sintering up to 1470ºC.

For both samples, the heating rate of 100 ºC min^{-1} was used up to 1200 ºC and then 50 ºC min^{-1} was used up to the final temperature. Once 1200 ºC was achieved, the pressure was increased starting from 5 KN rising to 16 KN at the final temperature. Under these sintering conditions, the ZTA shrinkage started at ~1223ºC, reached the maximum shrinkage rate at ~1345 ºC and finished at 1470 ºC (Figure 4.10). However, in the ZTA-additives specimen the shrinkage initiated at ~ 1181ºC, reached its highest value at ~1294 ºC and completed at 1405ºC (Figure 4.11). It is worth mentioning that L_0 is the thickness of the powder bed at room temperature. The results show that the main densification was completed in 2 min.

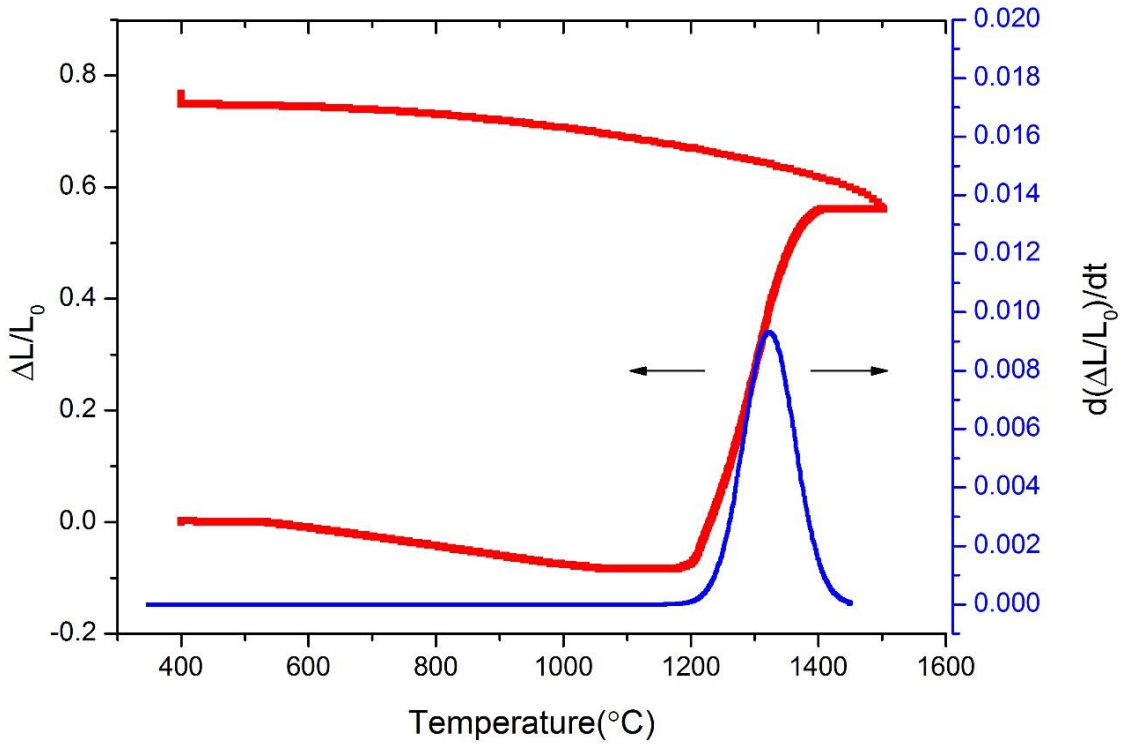

Figure 4.11. The shrinkage behaviour of ZTA -additives during spark plasma sintering up to 1500ºC.

Tables 4.2 and 4.3 show the variation of density versus temperature and holding time. The higher the temperature, the better the densification. For example, in ZTA at 1400 ºC-5 min, the relative density measured by the Archimedes method was about 95% of the theoretical density and it reached full densification at 1450 ºC-10 min. Despite the fluctuations in density as the temperature rose, the general tendency was an increase in the density with temperature. In contrast, the sample with dopants exhibited a density of ~98% TD at 1400 ºC-5 min which is about 3% more than the corresponding density in the ZTA-additives sample. The SEM micrographs in Figure 4.14 (a) and 4.15 (a), confirm the difference in densification of these two samples sintered under the same conditions. As summarized in Table 4.3, for the ZTA-additives, almost full density was obtained at 1500 ºC-5 min, although there was a minor reduction in density above this temperature on increasing the final temperature and soaking time. Figures 4.12 and 4.13 show the evolution of final density for both ZTA and ZTA-additives, respectively.

Table 4.2. Density of sintered ZTA in various temperatures/dwell time measured by Archimedes' method.

Temperature(°C)-Dwell (mins)	Density (g/cm^3) ± Std dev
1400-5	4.148± 0.041
1400-10	4.171±0.011
1450-5	4.302±0.006
1450-10	4.342±0.014
1470-8	4.340±0.016
1500-5	4.309±0.026
1500-10	4.337±0.029
1550-5	4.335±0.019
1550-10	4.328±0.0308

Table 4.3. Density of sintered ZTA-additives in various temperatures and dwell time measured by Archimedes' method.

Temperature(°C)-Dwell (mins)	Density (g/cm^3) ± Std dev
1400-5	4.272±0.002
1400-10	4.278±0.003
1450-5	4.286±0.001
1450-10	4.341±0.001
1500-5	4.341±0.046
1500-10	4.296±0.003
1550-5	4.301±0.004
1550-10	4.276±0.003
Biolox® delta	4.350±0.001

4.4.2 Grain size

The grain size was measured with the mean linear intercept method on SEM micrographs of both Al_2O_3 and ZrO_2, after being sintered by SPS. For different sintering temperatures, the measured grain size along with the calculated standard error (Equation 3.4) are presented in Table 4.4 and 4.5 for both ZTA and ZTA-additives, respectively. As expected, once the temperature and dwell time rose, the grain size of both alumina and zirconia gradually increased. However, compared with other temperatures, there seems to be a big jump in the

Al_2O_3 grain growth, particularly at 1550 ºC-10 min. At 1400ºC, the ZTA composite was still highly porous, as confirmed by the SEM micrographs 4.14 (a-b) and density measurements (Table 4.2) and hence, grain size measurement for both alumina and zirconia was impossible. At temperatures between 1450-1500ºC for holding time of 5, 7 and 10 min, alumina and zirconia grain sizes reached ~ 300 nm and ~ 200 nm, respectively. At 1500 ºC- 10 min the alumina grain size increased to ~ 500 nm. Nonetheless, a substantial change was not observed in the size of the zirconia particle.

Table 4.4. Grain size of sintered ZTA specimens in different temperatures and dwell time calculated by the linear intercept method.

Temperature(°C)-Dwell (mins)	Al_2O_3 Grain size (nm) ± Std dev	ZrO_2 Grain size (nm) ± Std dev
1400-5	Porous	Porous
1400-10	Porous	Porous
1450-5	354±68	186±34
1450-10	397±34	231±42
1470-8	363±56	226±70
1500-5	383±27	250±31
1500-10	522±35	279±31
1550-5	468±38	341±85
1550-10	805±42	489±124

Table 4.5. Grain size of sintered ZTA-additives specimens in different temperatures and dwell time calculated by the linear intercept method.

Temperature(°C)-Dwell (mins)	Al_2O_3 Grain size (nm) ± Std dev	ZrO_2 Grain size (nm) ±Std dev
1400-5	274±16	177±31
1400-10	302±17	193±27
1450-5	304±11	178±12
1450-10	306±18	180±14
1500-5	349±31	233±18
1500-10	421±28	313±25
1550-5	774±56	357±44
1550-10	920±94	465±89
Biolox® delta	520±82	453±131

At 1550°C- 5 min, there was a minor reduction in the alumina grain size compared to 1500 ºC-10 min, implying the more significant impact of time over temperature. In addition, the zirconia the particle size increased slightly at this temperature. Finally, at 1550°C- 10 min, the alumina grain size almost doubled in size compared to 1550°C- 5 min and reached ~ 800 nm. Zirconia grains, on the other hand, increased in size from 100 nm to ~500 nm. With the ZTA- additives, in contrast to the ZTA, samples were densified to ~98% TD at 1400°C- 5 and 10 min. This is in agreement with the results obtained from the shrinkage curve. Hence, the composite was dense enough to measure the grains of both alumina and zirconia. At temperatures below 1500°C- 5 min, the size of alumina and zirconia grains reached ~ 300 nm and 200 nm respectively. At 1550ºC-10 min, grain growth of alumina and zirconia accelerated faster and reached ~900 nm and ~ 450 nm, respectively.

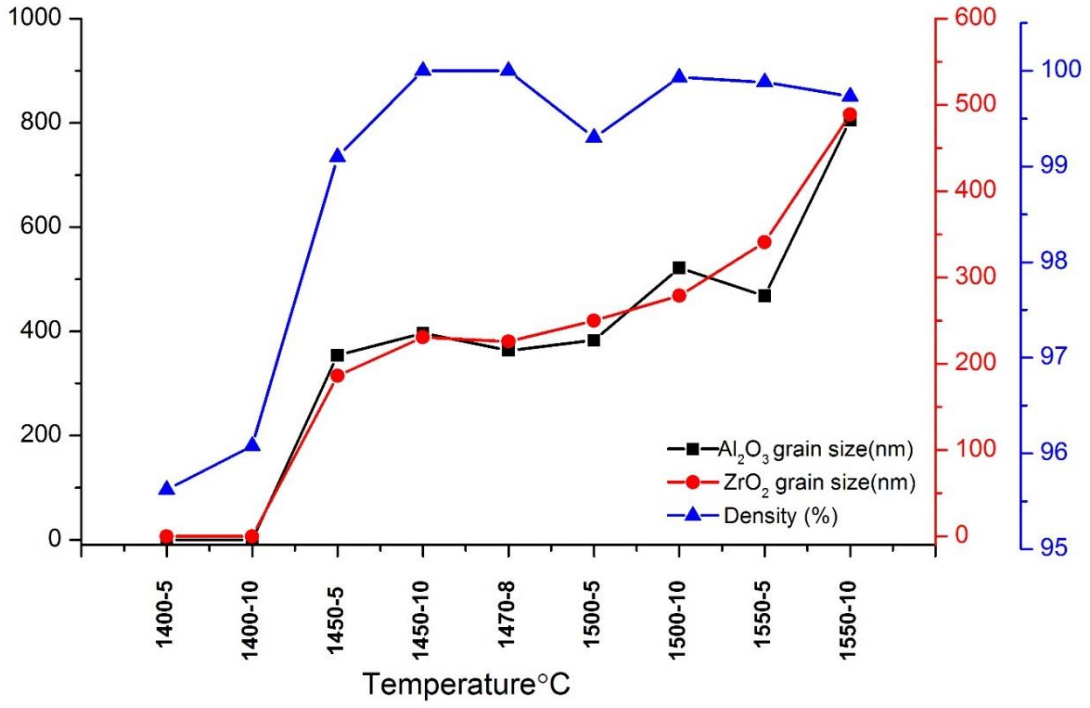

Figure 4.12. Density and grain size evolution of ZTA plotted versus sintering temperature with varied dwell time.

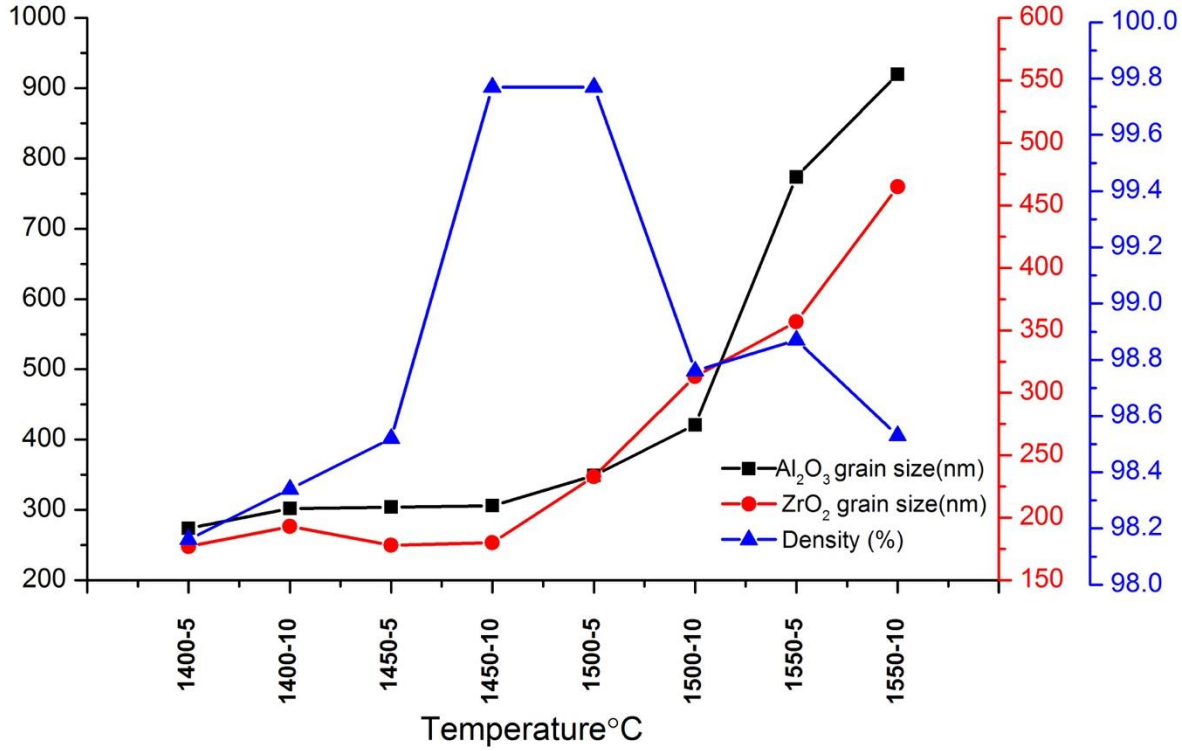

Figure 4.13. Density and grain size evolution of ZTA-additives plotted versus sintering temperature with varied dwell time.

4.4.3 Microstructural features using scanning electron microscopy (SEM)

Figure 4.14 (a-i) and Figure 4.15 (a-h) show SEM micrographs of ZTA and ZTA-additives SPSed under a pressure of 51 MPa at temperatures ranging between 1400ºC-1550ºC and soaking time of 5 and 10 min. Figure 4.15 (i), shows the microstructure of Biolox® delta. The dark grains and whitish grains are representative of Al_2O_3 and ZrO_2, respectively. Based on these micrographs, the average grain size of the ZTA, ZTA-additives and Biolox® delta was estimated by the linear intercept method at different temperatures and is tabulated in Tables 4.4 and 4.5, respectively. These SEM images also provide useful information about the densification and shape of grains.

Figures 4.14 (a-b) show microstructures of ZTA at 1400ºC-5 min and 1400ºC-10 min which contained considerable amount of voids and interconnected pores. At the higher temperature of 1550ºC-10 min (Figure 4.14(i)) more isolated pores were observed at mainly triple and four-grain junctions.

In contrast, in ZTA-additives, the absence of voids and other microstructure irregularities was evident, at 1400ºC. However, isolated pores mainly in grain boundaries, triple and four- grain junctions were observed in Figure 4.15 (g) at 1550ºC-5 min. As shown in Figures 4.14 (a-i) and 4.15 (a-i), the main difference between the microstructures of ZTA and ZTA-additives was the existence of platelet grains in ZTA-additives composites, marked by rectangles in the SEM micrograph 4.15 (a). Besides, the number of alumina grains with exaggerated grain growth was more noticeable in ZTA-additives compared to ZTA.

The red circles on Figure 4.14 (i) are indicative of intergranular pores mainly at triple junctions. It was also observed that ZrO_2 particles were either faceted-shaped or distributed between alumina particles as well as triple and four-grain junctions (intergranular) or be approximately spherical and located inside alumina grains (intragranular). ZrO_2 particles located in four-grain junctions and intragranular positions are marked by rectangles and arrows respectively, in SEM micrograph in Figure 4.14 (i).

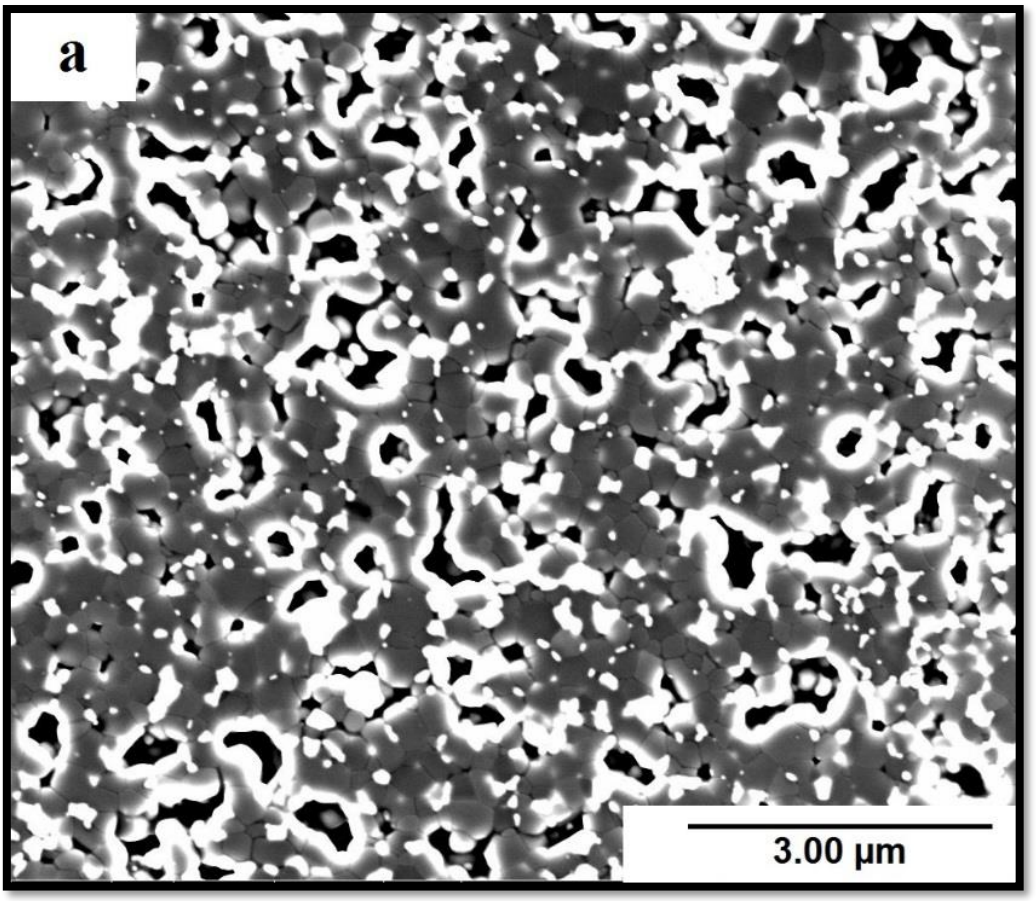
a
3.00 µm

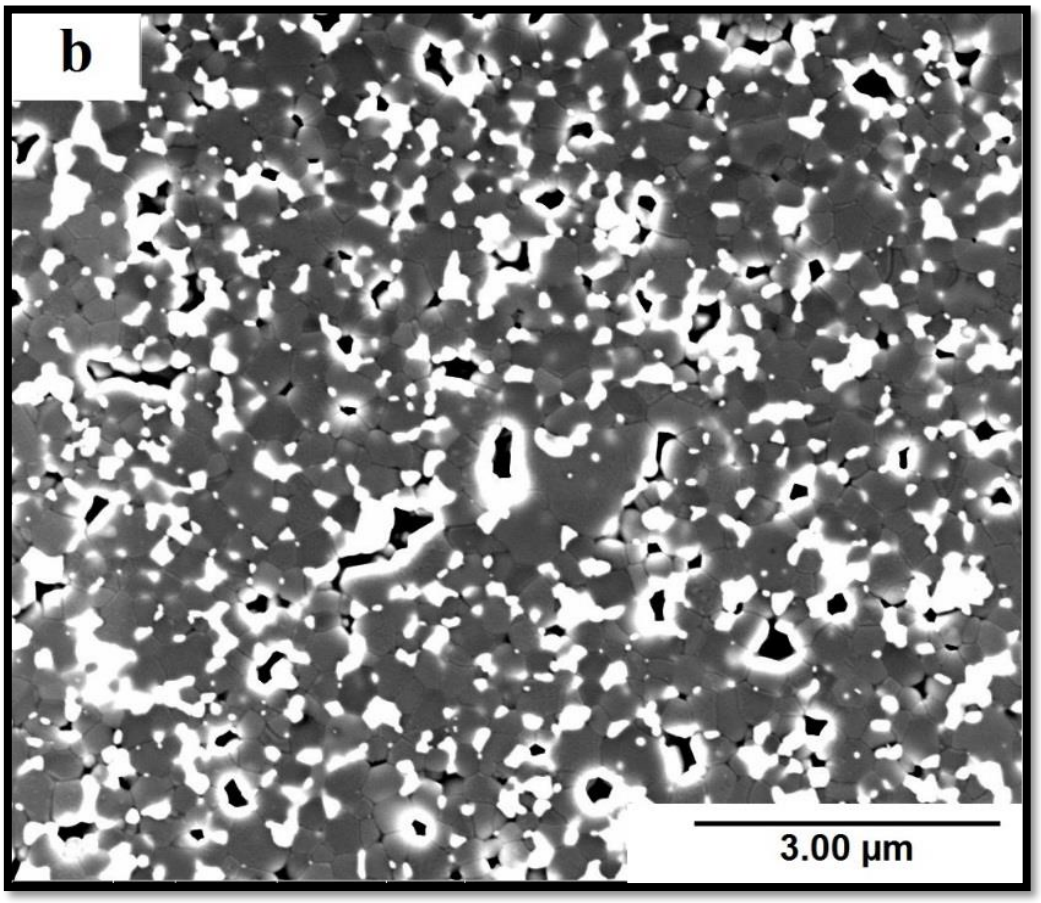
b
3.00 µm

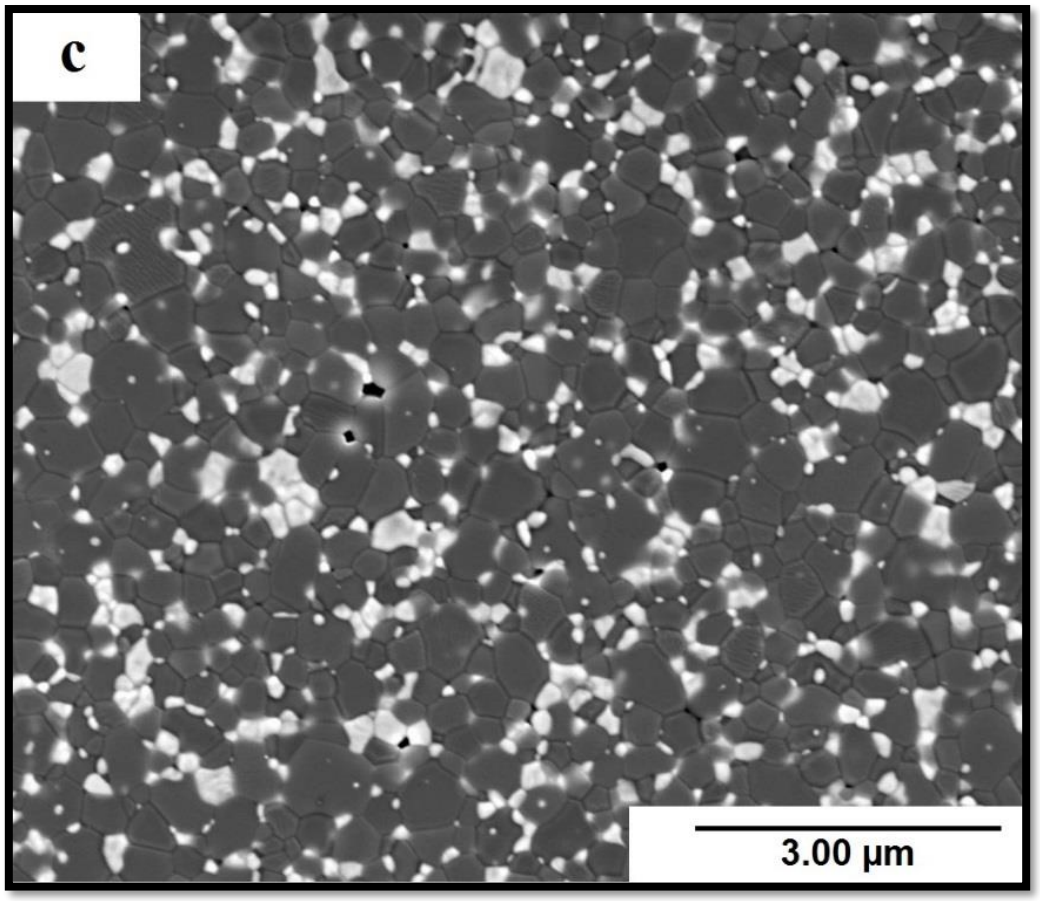
c
3.00 µm

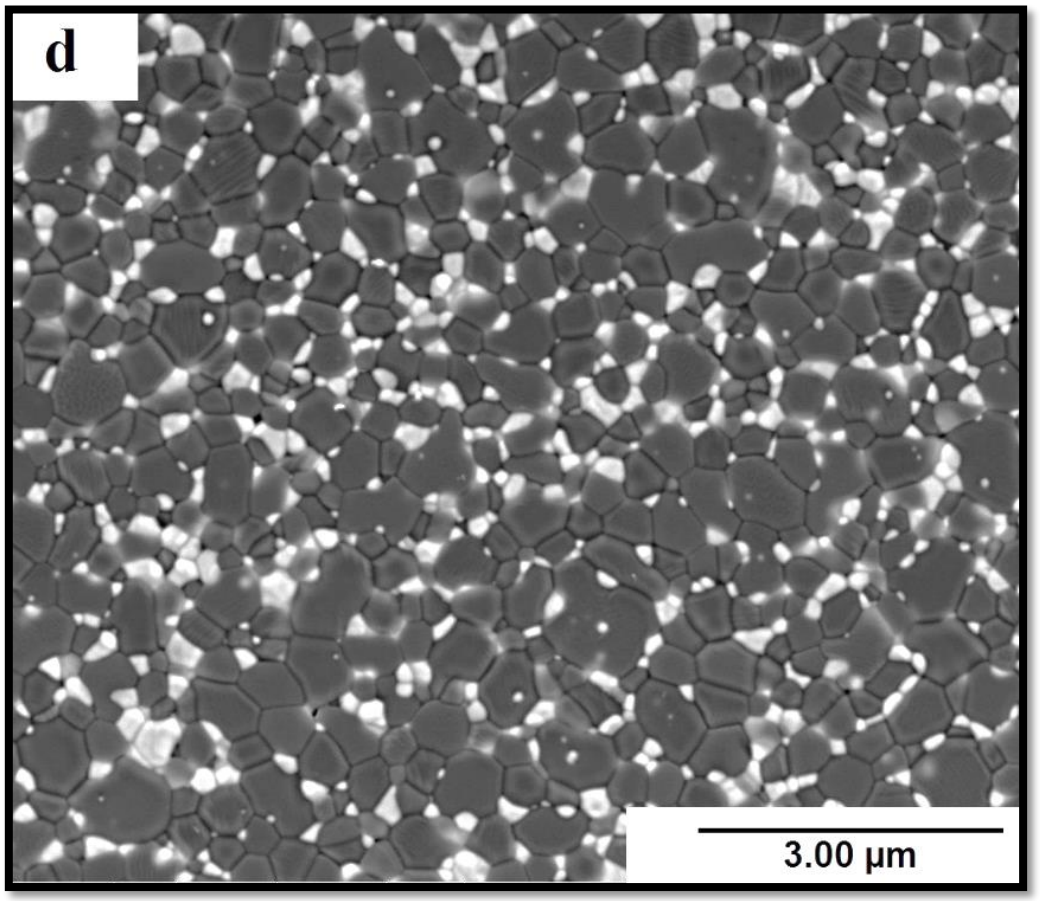
d
3.00 µm

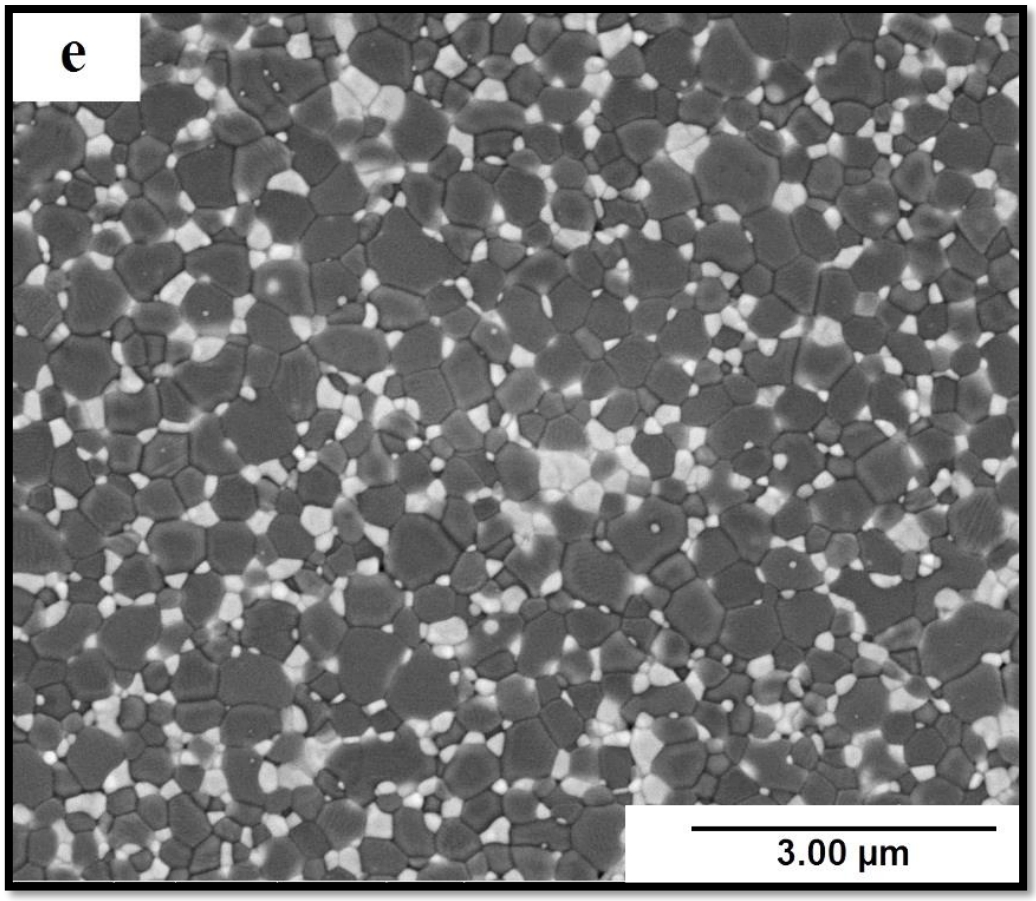
e
3.00 µm

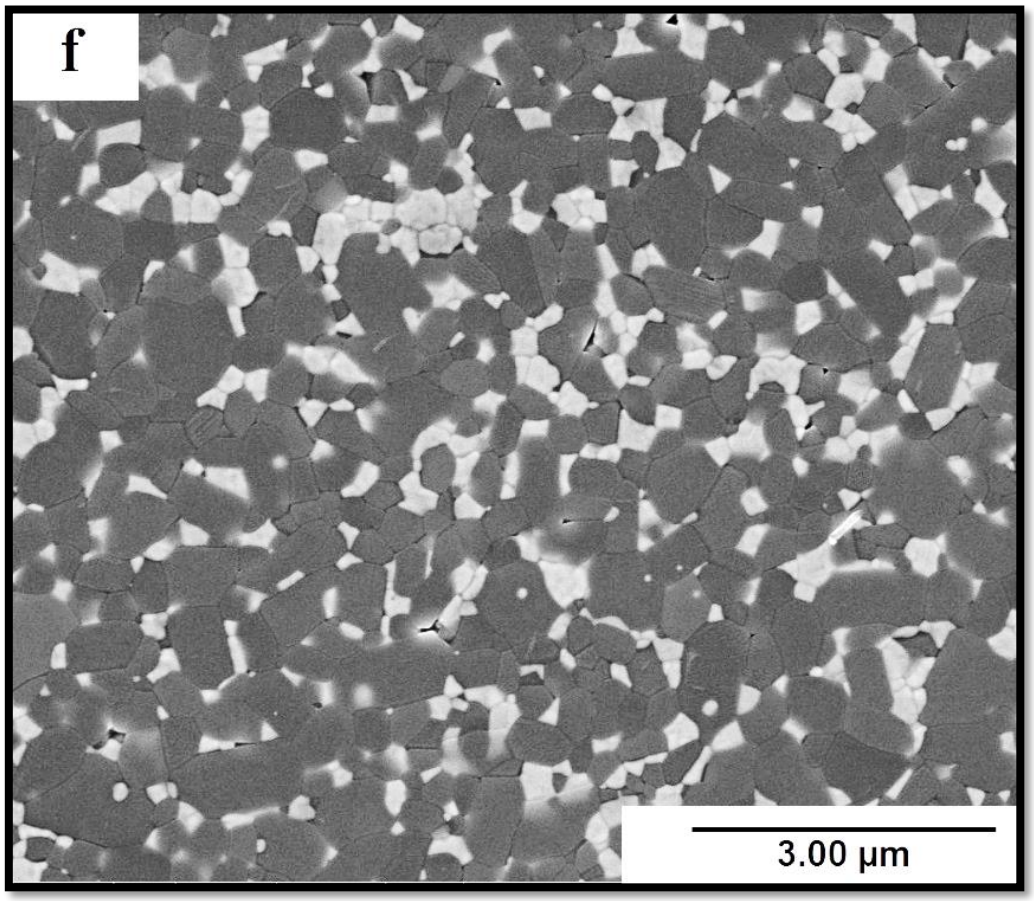
f
3.00 µm

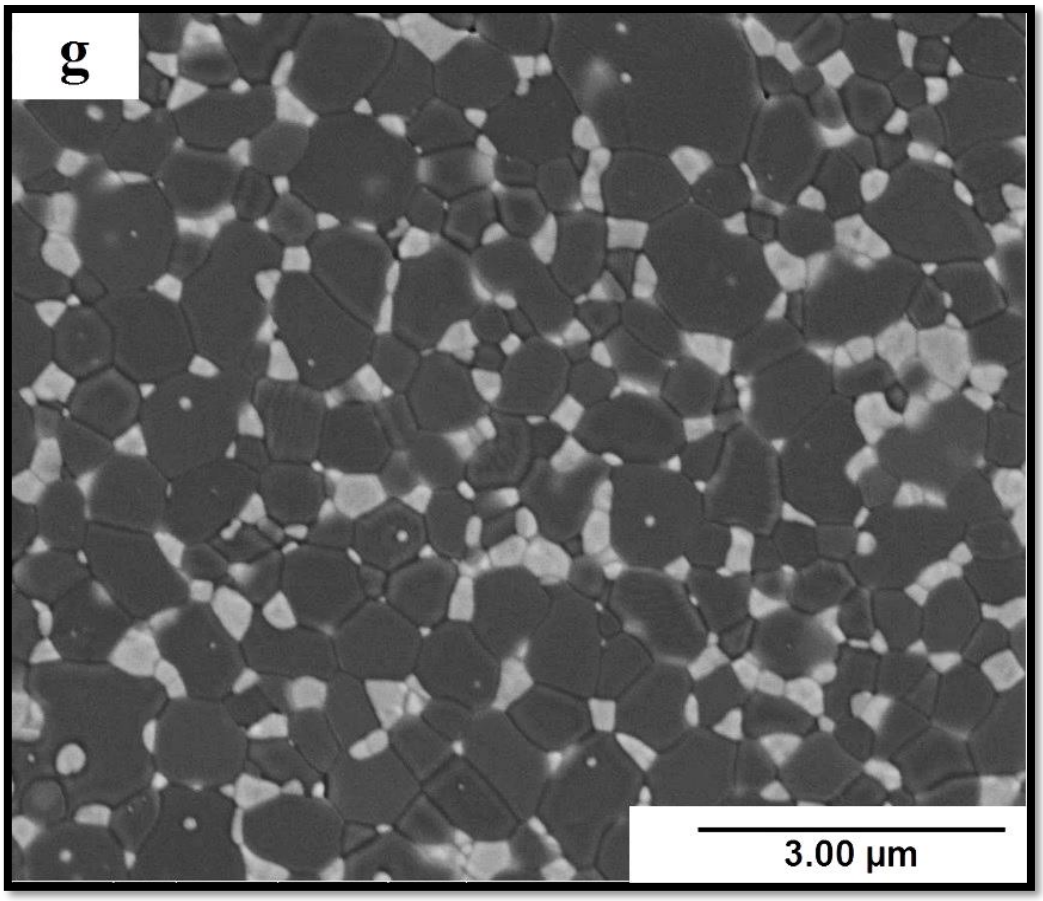
g
3.00 µm

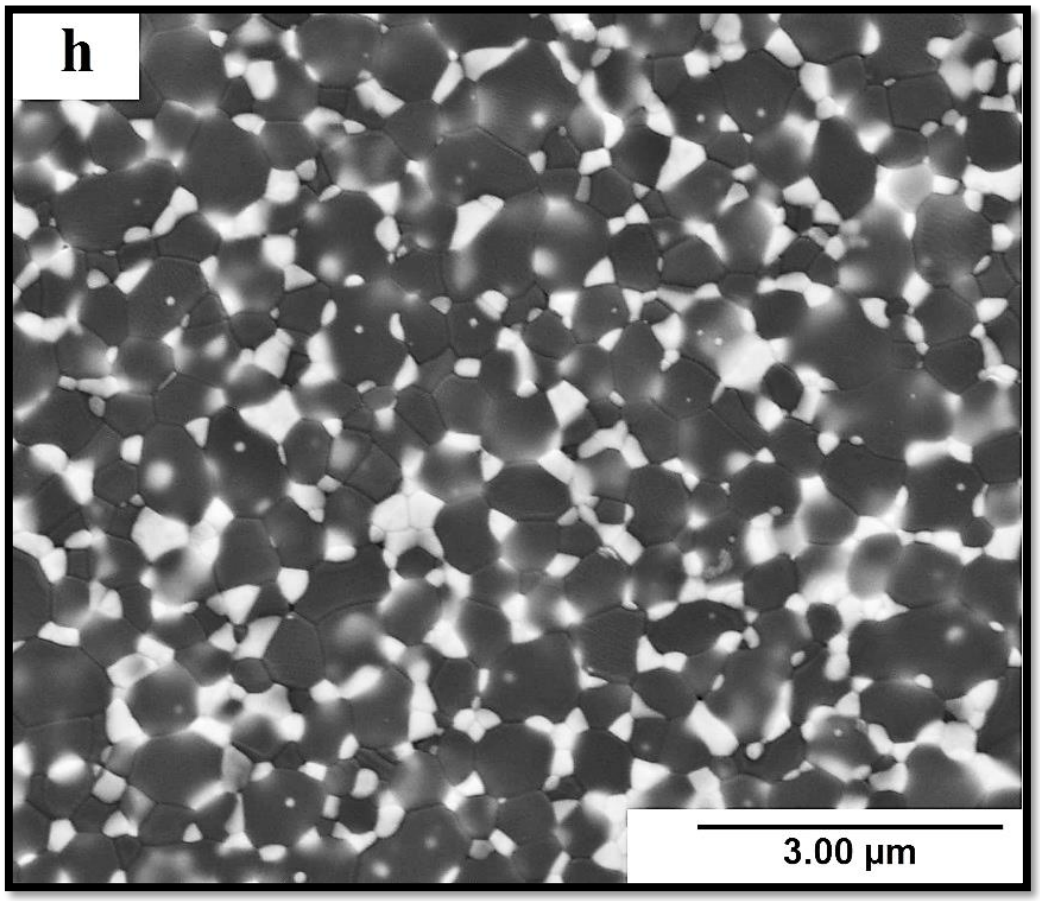
h
3.00 µm

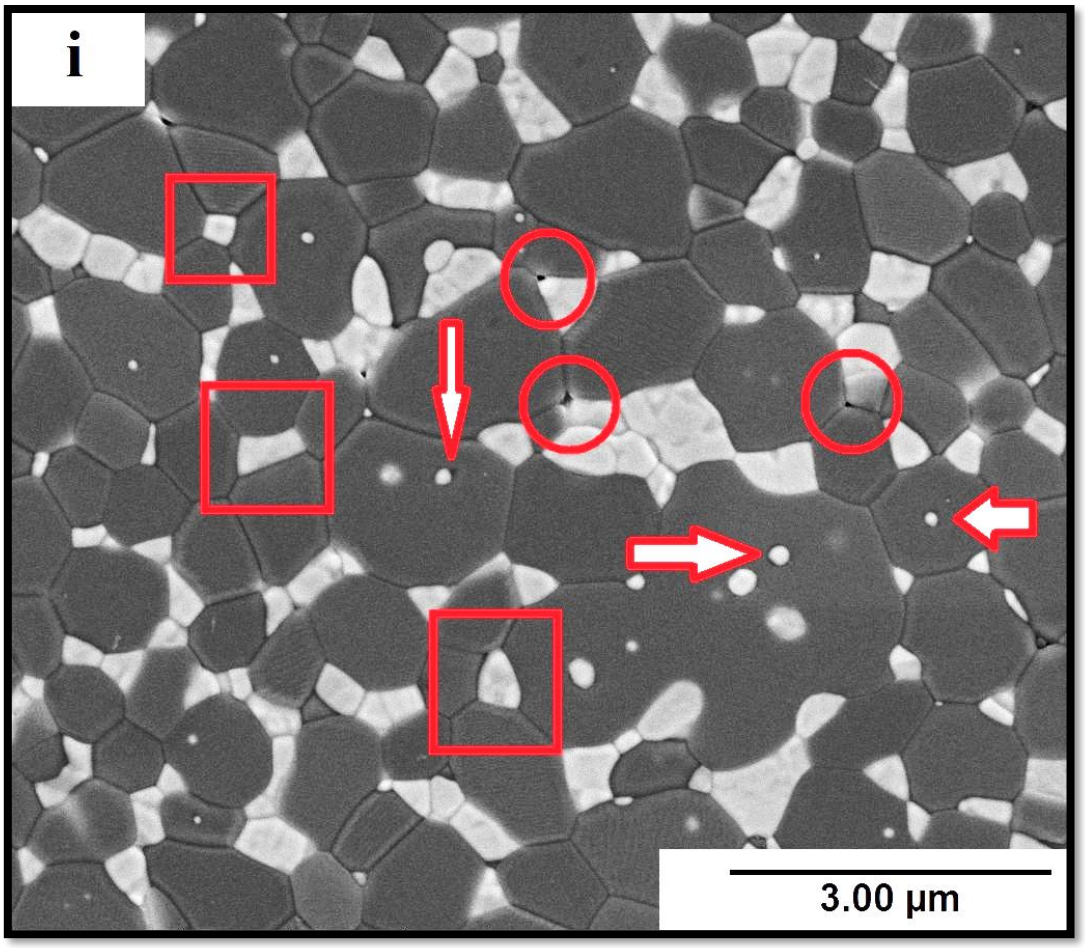

Figure 4.14. SEM micrographs of ZTA sintered at a) 1400ºC-5 min b) 1400ºC-10 min c) 1450ºC-5 min d) 1450ºC-10 min e) 1470ºC-8 min f) 1500ºC-5 min g) 1500ºC-10 min h) 1550ºC-5 min. i) 1550ºC-10 min.

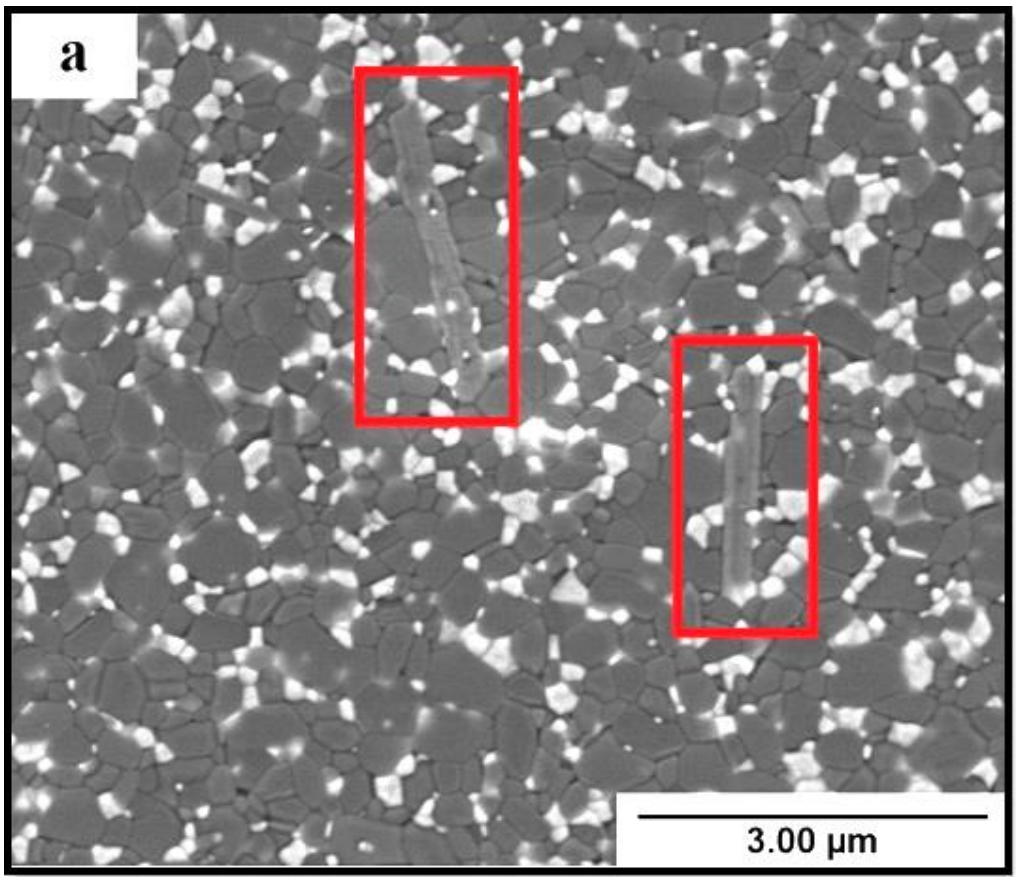
a
3.00 µm

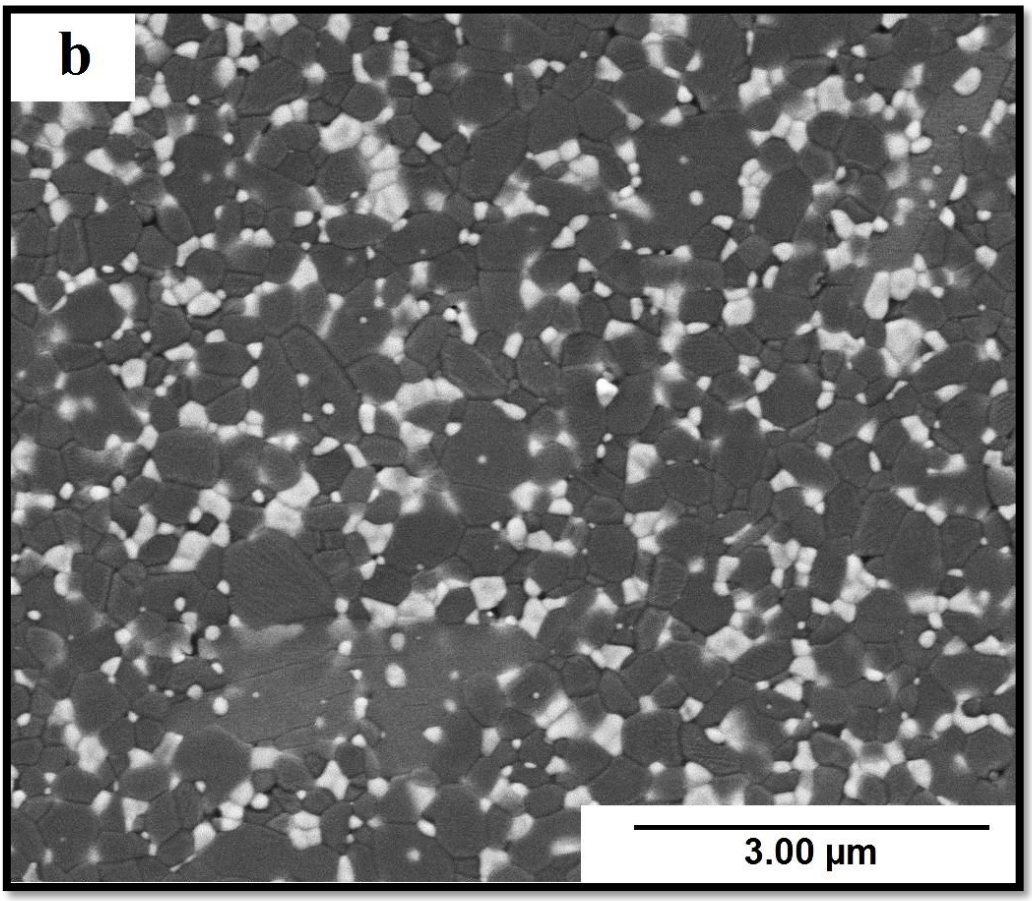
b
3.00 µm

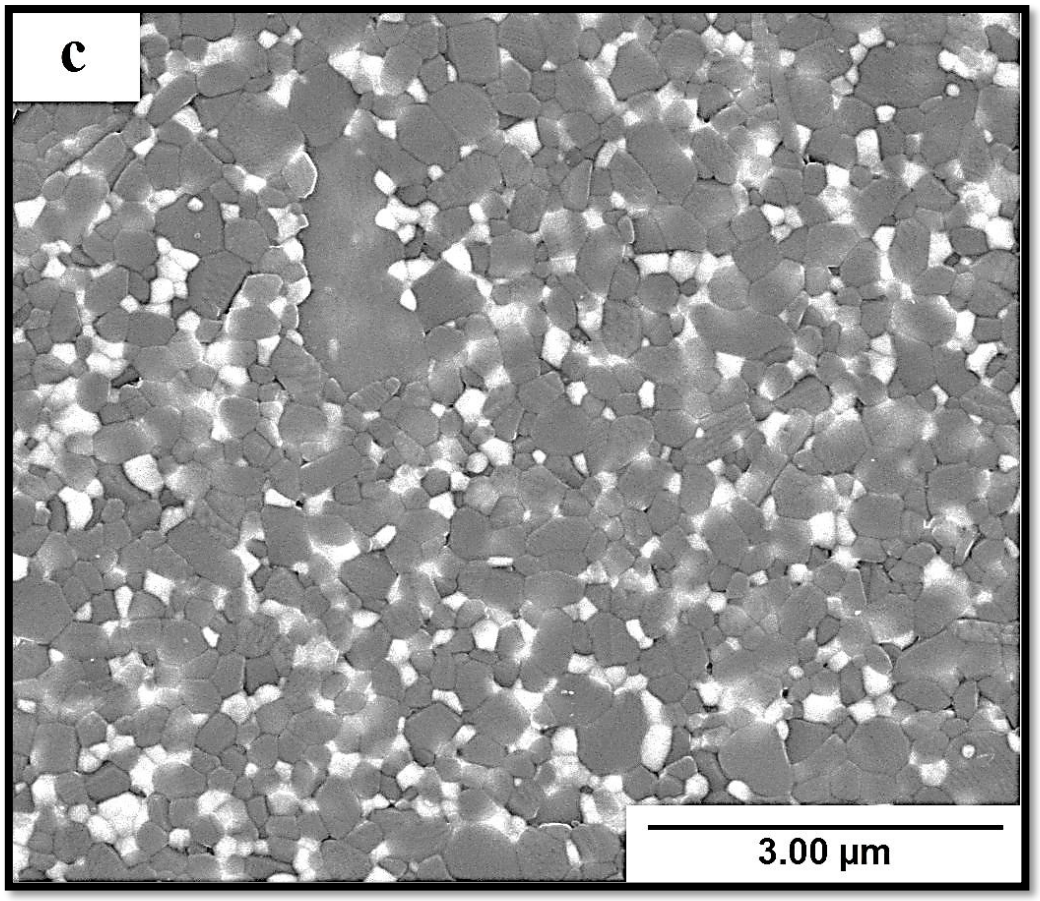
c
3.00 µm

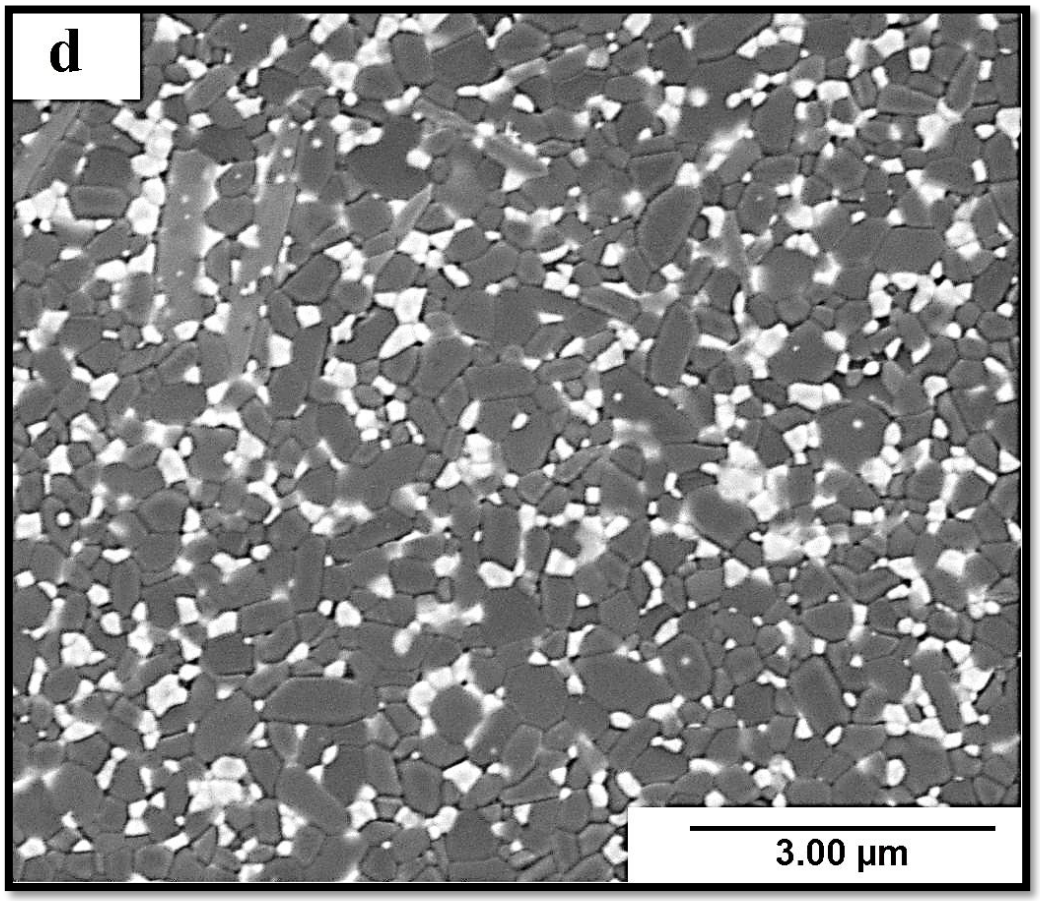
d
3.00 µm

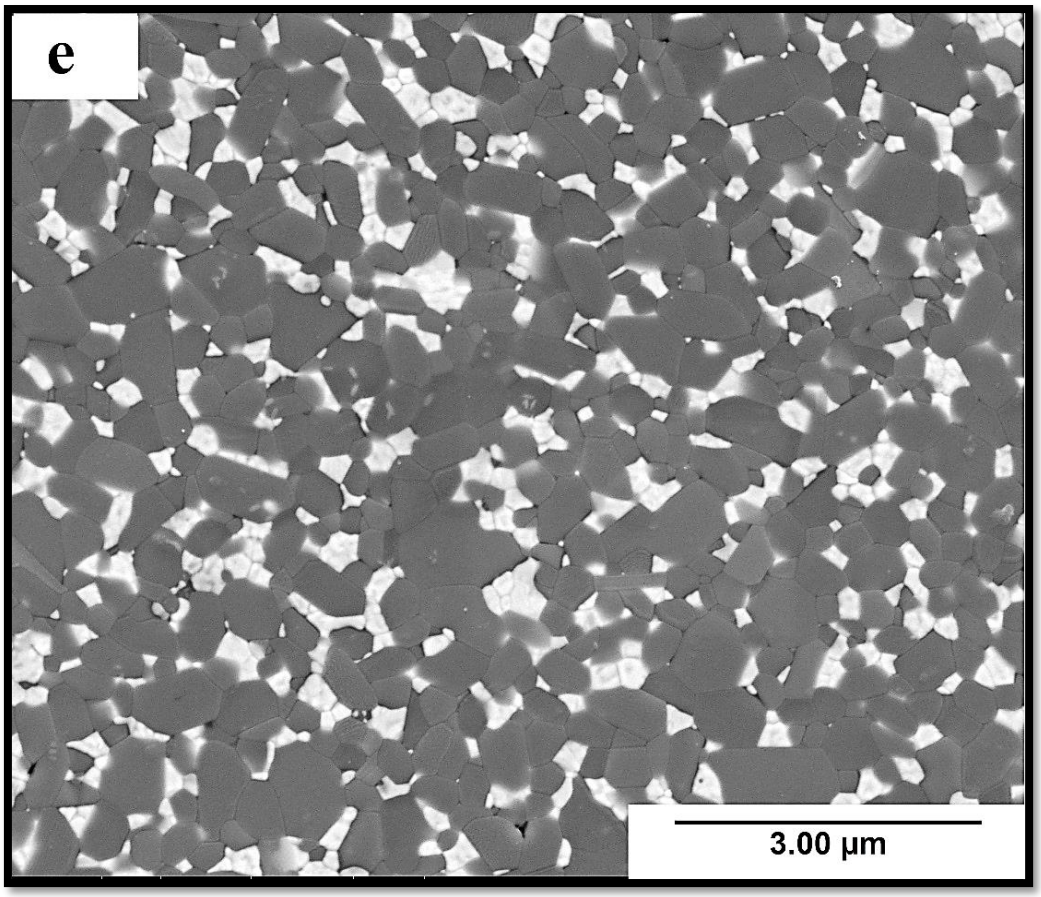
e
3.00 µm

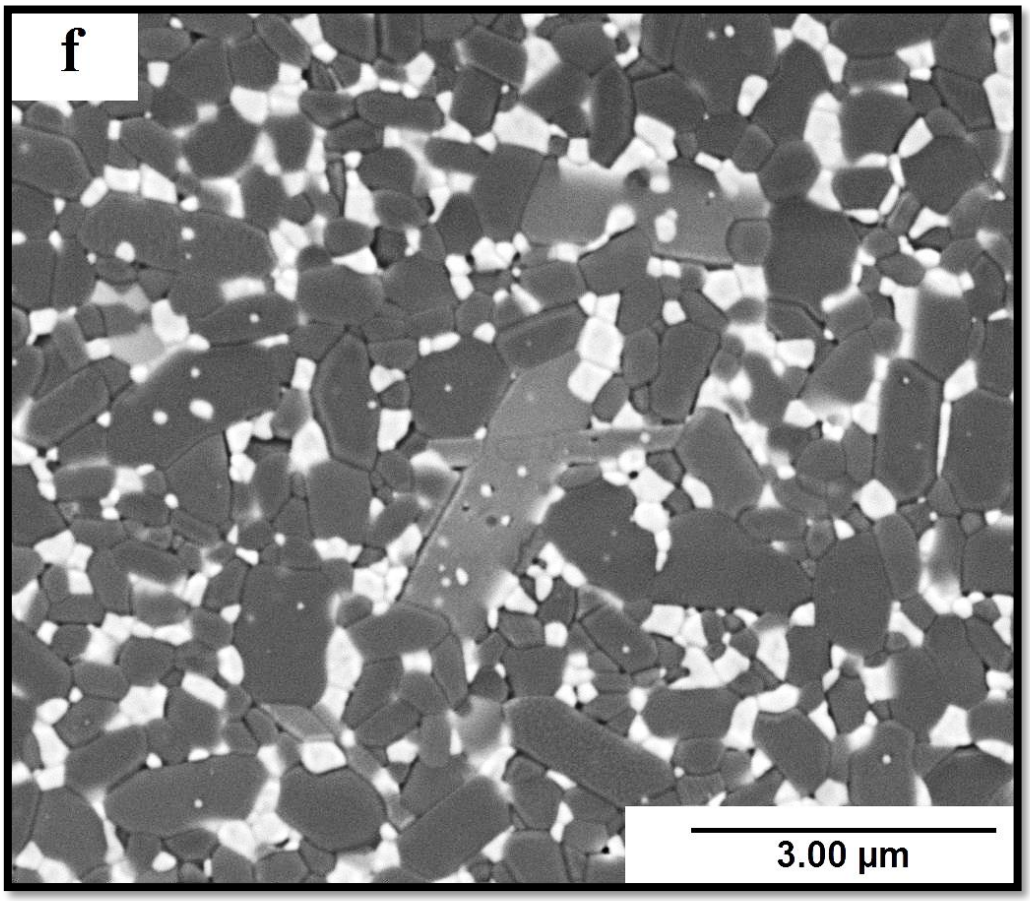
f
3.00 µm

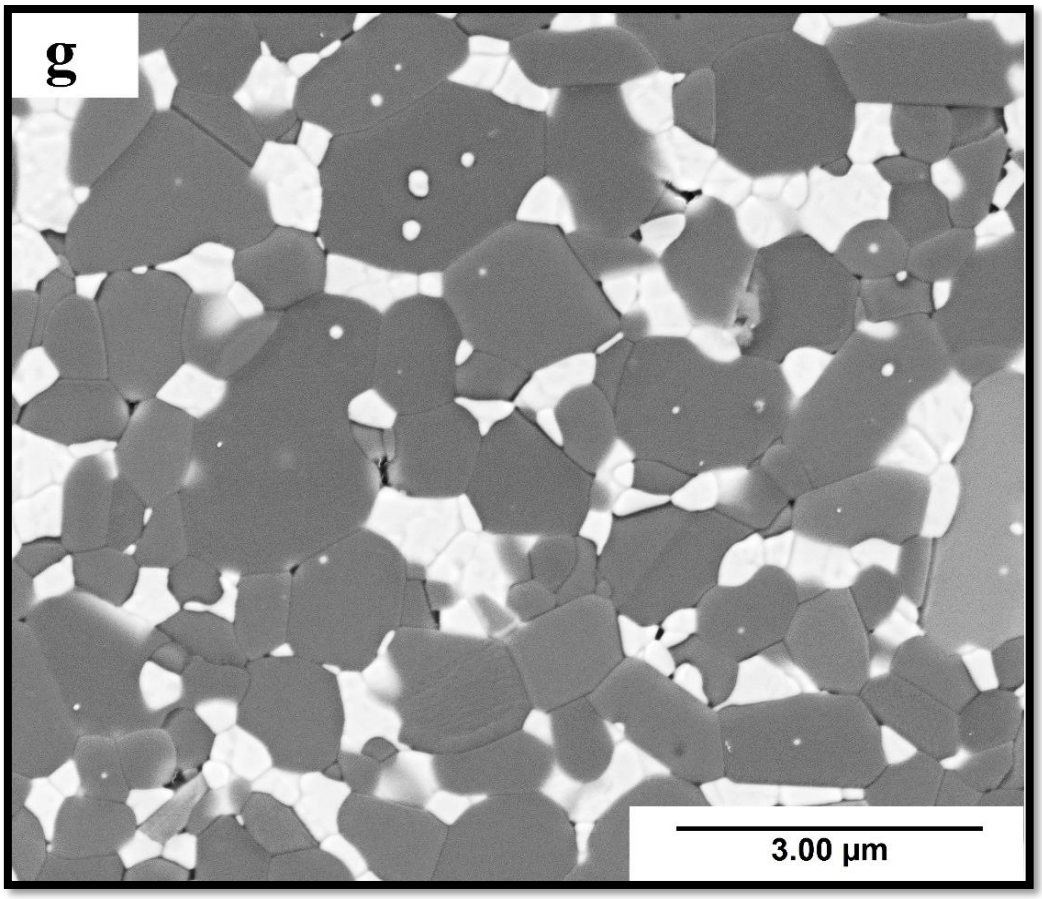
g
3.00 µm

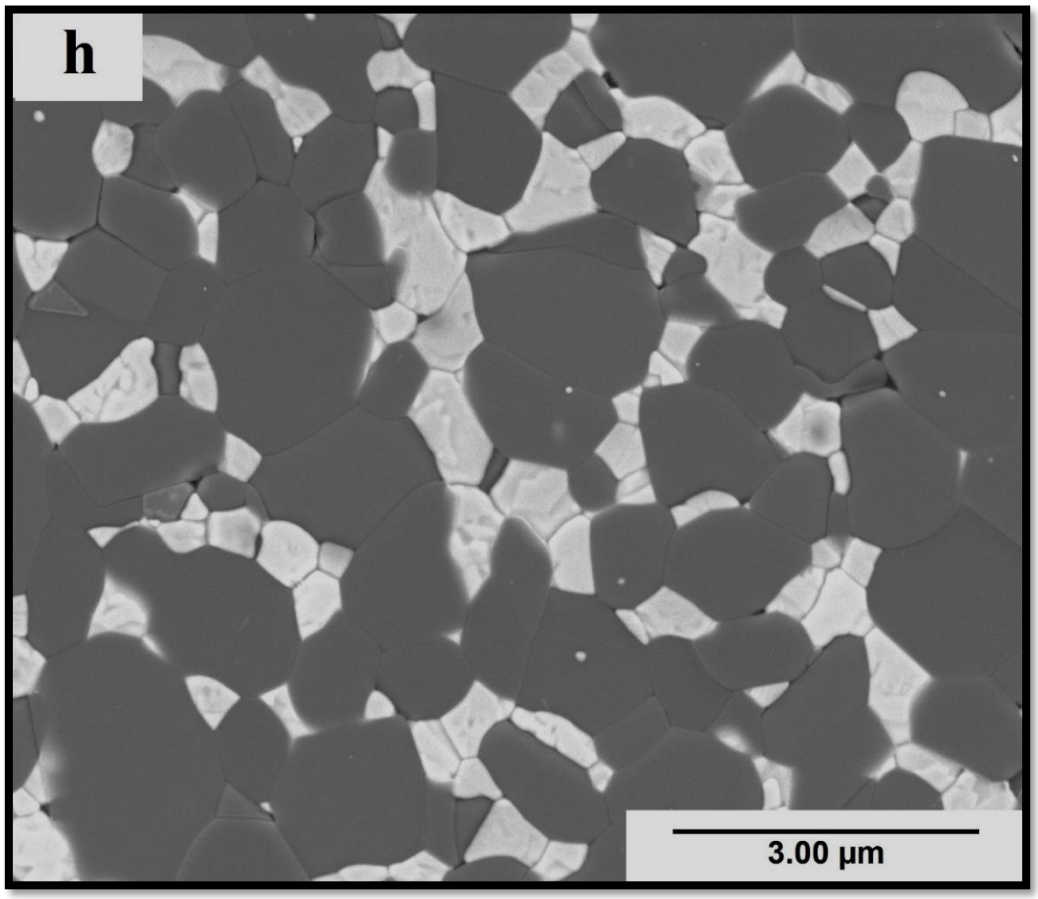
h
3.00 µm

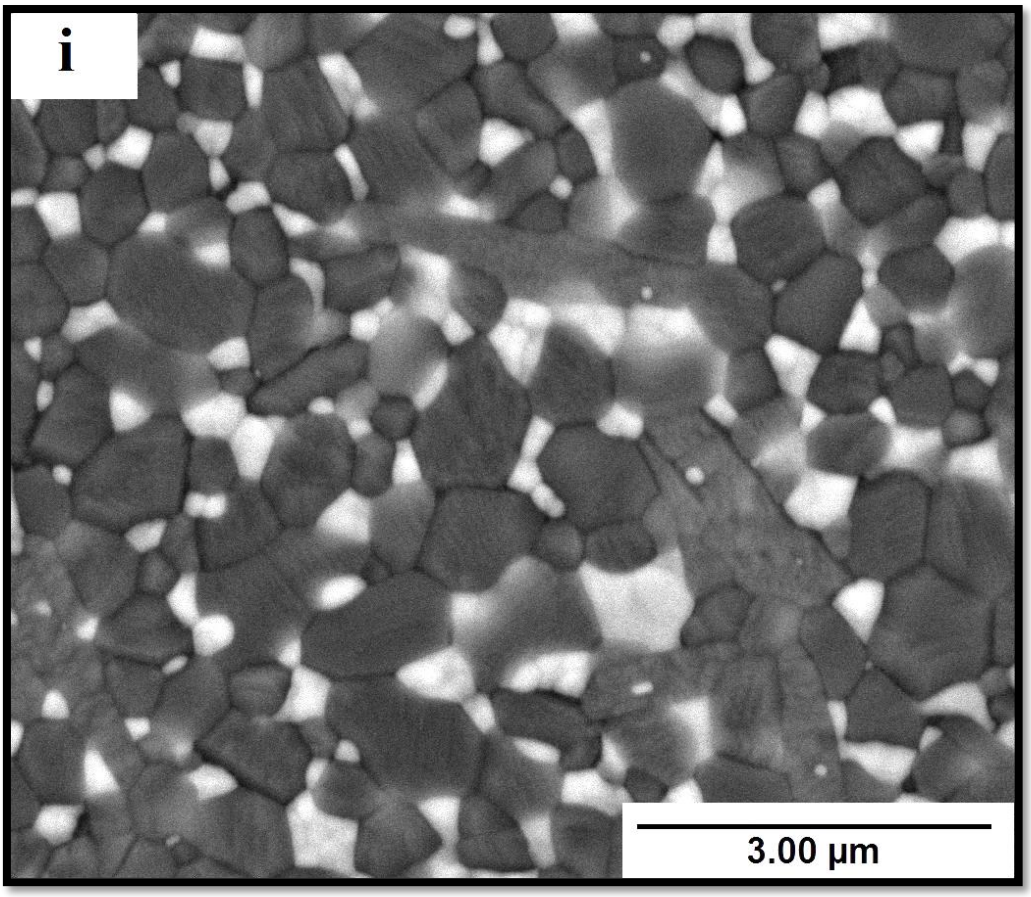

Figure 4.15. SEM micrographs of ZTA with additives sintered at a) 1400ºC-5 min. b) 1400ºC-10 min. c) 1450ºC-5 min. d) 1450ºC-10 min. e) 1500ºC-5 min. f) 1500ºC-10 min. g) 1550ºC-5 min. h) 1550ºC-10 min. i) Biolox® delta.

4.4.4 Mechanical behaviour-Vickers hardness and fracture toughness

Subsequent to optimisation of procedures to achieve the desired grain size and density, measurement of hardness and toughness is of great importance. The fracture toughness and Vickers hardness of zirconia toughened alumina (ZTA), zirconia toughened alumina with ternary and quaternary oxide dopants and Biolox® delta commercial samples were measured by Equations 3.5 and 3.6 respectively and the results were summarised in Tables 4.6 and 4.7. Vickers hardness along with fracture toughness of ZTA are presented in Table 4.6. The table shows that fracture toughness of ZTA fluctuates between 5.27-5.43 MPa.m$^{1/2}$ and the corresponding hardness changes between 17.91 and 18.62 GPa, at temperatures ranging between 1450ºC and 1550ºC. Table 4.7 shows the variation of fracture toughness and Vickers hardness for ZTA additives and Biolox® delta. Once ternary and quaternary additives are included in a composite of ZTA, the range of hardness and fracture toughness differs between

16.44 and 18.3 GPa and 5.15 and 5.66 MPa.m$^{1/2}$ respectively. As shown in Table 4.7, in the ZTA-additives specimens, the evolution of fracture toughness (5.15-5.66 MPa.m$^{1/2}$) and reduction of Vickers hardness is more noticeable compared to the ZTA as the temperature rises. As shown in Tables 4.6 and 4.7, the reduction of Vickers hardness in ZTA-additives with temperature is more evident than the ZTA, although, the enhancement of fracture toughness in ZTA-additives compared to ZTA was not appreciable. To prepare Biolox® delta as a reference specimen, the same procedure was employed for this specimen, to evaluate the corresponding Vickers hardness and fracture toughness.

Table 4.6. Fracture toughness and Vickers hardness of the sintered ZTA specimens in various temperatures and dwell time.

Temperature(°C)-Dwell (mins)	Vickers Hardness (GPa)± Std dev	Fracture Toughness (MPa.m$^{1/2}$)±Std dev
1450-5	18.48±0.21	5.32 ±0.08
1450-10	18.59±0.41	5.39±0.09
1470-8	18.62±0.39	5.43±0.07
1500-5	17.93±0.45	5.30±0.09
1500-10	18.25±0.34	5.35±0.07
1550-5	18.13±0.36	5.36±0.06
1550-10	17.91±0.35	5.27±0.06

Table 4.7. Fracture toughness and Vickers hardness of the sintered ZTA- additives in various temperatures and dwell time.

Temperature(°C)-Dwell (mins)	Vickers Hardness (GPa)± Std dev	Fracture Toughness (MPa.m$^{1/2}$)±Std dev
1400-5	18.12±0.53	5.15±018
1400-10	17.96±0.38	5.33±0.07
1450-5	17.90±0.35	5.30±0.09
1450-10	18.30±0.40	5.45±0.14
1500-5	17.65±0.3	5.66±0.12
1500-10	17.75±0.27	5.50±0.04
1550-5	16.90±0.46	5.61±0.17
1550-10	16.44±0.50	5.51±0.24
Biolox® delta	17.04±0.37	5.61±0.12

5 Tribological behaviour

5.1 Zirconia toughened alumina lubricated with 25 vol. % new-born calf serum solution

5.1.1 Lubrication regime definition

In order to assess the wear mechanisms that a real hip joint experiences in a body, the reciprocating sliding wear was employed to simulate some of the wear mechanisms observed *in vivo*. However, the reciprocating tests do not represent the full range of damage which takes place in the body. In order to understand the behaviour of materials in the reciprocating test, which is partly indicative of the hip joint motion, it is essential to understand which lubrication regime is occurring under the various test conditions. The data can then be compared with the other published literature to provide more details about the performance of these biomaterials in a body.

The first period of the sliding motion is the onset of wear between two fresh surfaces and is called the "unsteady state wear" or the "running in" state which is often only briefly commented on or is even disregarded. In this stage, the coefficient of friction (COF) shows large fluctuations and the surface experiences the highest damage. The next stage of sliding motion is called "steady state" in which coefficient of friction is relatively stable and quantitatively lower than "running in" state. Figure 5.1, 5.13, 5.14 and 5.29 show typical variations of COF versus time for ZTA, ZTA-additives (1), ZTA-additives (2), and a commercial specimen (BIOLOX ®delta), respectively. In these graphs, for the 32 N load, the corresponding sliding motion is divided into two sections by a black vertical arrow and is labelled by "R" and "S" in each side standing for "running in" and "steady" state. At other loads, the horizontal arrow points to the steady state period.

For the ZTA specimen, the fluctuation of the coefficient of friction (COF) versus time at various loads ranging between 1 N-32 N is shown in Figure 5.1. Depending on the load, the length of "running in" stage differs. For instance, at 1 N, 2 N, 4 N, 8 N, 16 N and 32 N the length of "running in" period are estimated to be ~8 min, ~19 min, ~11 min, ~10 min, ~11 min and ~54 min, respectively. As shown in Figure 5.1, 32 N represented the most extensive erratic behaviour at the start of the test. As marked by the vertical red line in Figure 5.1, the 8 N graph is divided into two sections in which the average COF of the first part is estimated to be ~0.10 ± 0.03 and after 7 hrs (the red line), it falls down to 0.06 ± 0.04.

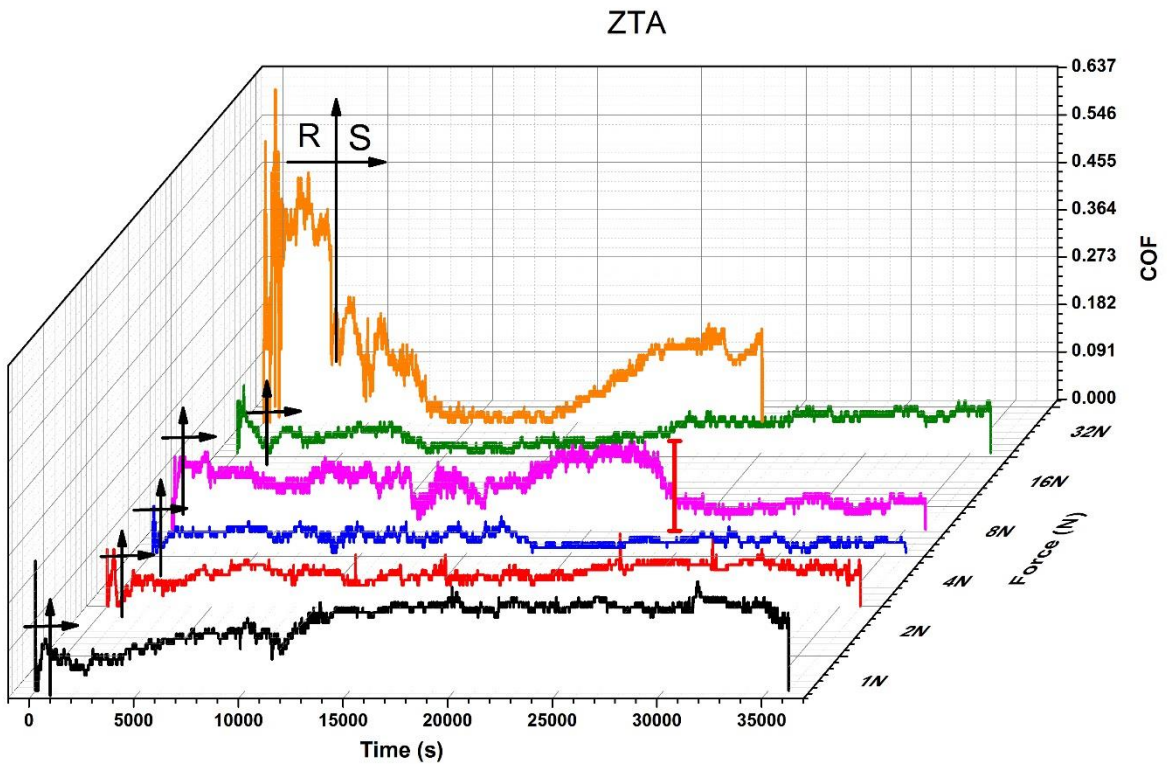

Figure 5.1. 3D illustration of the COF Vs time for the ZTA at different loads tested in 25 vol. % Bovine serum at 600 rpm for 10 hrs.

Table 5.1. Summary of the average COF corresponding to each load in ZTA.

Force (N)	Coefficient of friction	Sommerfeld (Z)
1N	0.14±0.04	2.4E-04
2N	0.07±0.02	1.2E-04
4N	0.03±0.01	6.0E-05
8N	0.10±0.03 *0.06±0.04	3.0E-05
16N	0.05±0.03	1.5E-05
32N	0.09±0.06	7.5E-06

In a lubricated reciprocating wear test, coefficient of friction is affected by the sliding speed V, lubricant viscosity η and applied load N. The combination of these three parameters yields a unique dimensionless parameter called the Sommerfeld number (Z);

$$Z = \frac{V\eta}{N}$$

The summary of the average COF values (of the lubricated reciprocating sliding test, at various loads, during ~10 hrs at 600 rpm) and the calculated Sommerfeld numbers are shown in Table 5.1, for the ZTA specimen.

The Sommerfeld number plotted against the COF is called a "Stribeck" curve. This curve provides an overall view of the behaviour of a lubricant throughout the sliding and assists in explaining the role of the wear mechanisms involved, during the motion of the counterfaces, Figure 5.2.

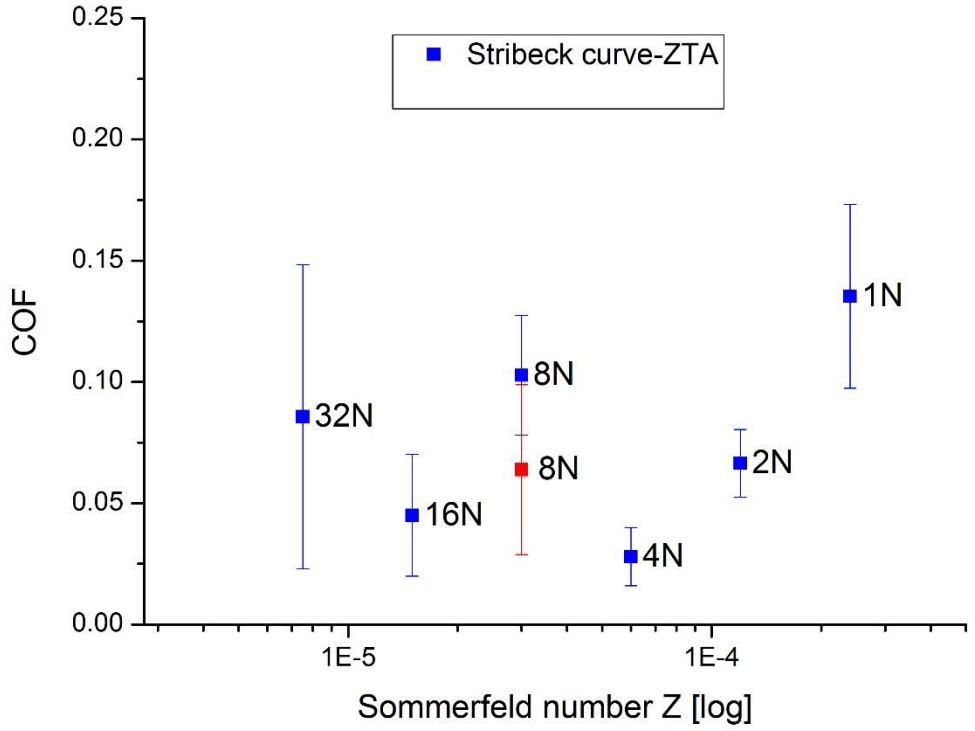

Figure 5.2. Stribeck curve for the ZTA in 25 vol. % Bovine serum lubricated wear test.

In this curve, there seems to be two dominant lubrication regimes present. In the right part of the curve, an increase in the Sommerfeld number is accompanied by an increase in COF. This is representative of the full fluid film regime and presumably the domination of the tribo-chemical mechanism at 1 N and 2 N. Section 5.1.3.2 will provide more information to determine the operating regime in this region. On the left side of the curve, a decrease of the COF was observed

when the Sommerfeld number increases, indicating the presence of a mixed lubrication regime. However, there exists an unexpected jump at 8 N making the curve slightly noisy. For the ZTA specimen, the lowest and the highest measured values of the average COF were 0.14 ± 0.04 and 0.03 ± 0.01, respectively.

5.1.2 Wear behaviour

5.1.2.1 Specific wear rate

The specific wear rates of the ZTA specimen as a function of the applied load (in Bovine serum lubricated reciprocating wear tests) are given in Figure 5.3. The general trend is an increase in the specific wear rate while each load doubles compared to the previous one. As displayed in Figure 5.3, there is an insignificant difference of the specific wear rate between 1 N and 2 N. However, there was a notable change in specific wear rate of about an order of magnitude in increasing the load to 4 N. Interestingly, the specific wear rate at 4 N, 8 N and 16 N remained at almost the same order of magnitude. Surprisingly, an abrupt and noticeable jump of about two orders of magnitude was observed as the load was increased to 32 N. Thus, for this material, the difference between the lowest and the highest values of the specific wear rate were over three orders of magnitude, namely $3.73 \pm 0.57 \times 10^{-9}$ mm^3/Nm and $6.31 \pm 1.22 \times 10^{-6}$ mm^3/Nm, which were associated with the 2 N and 32 N load, respectively.

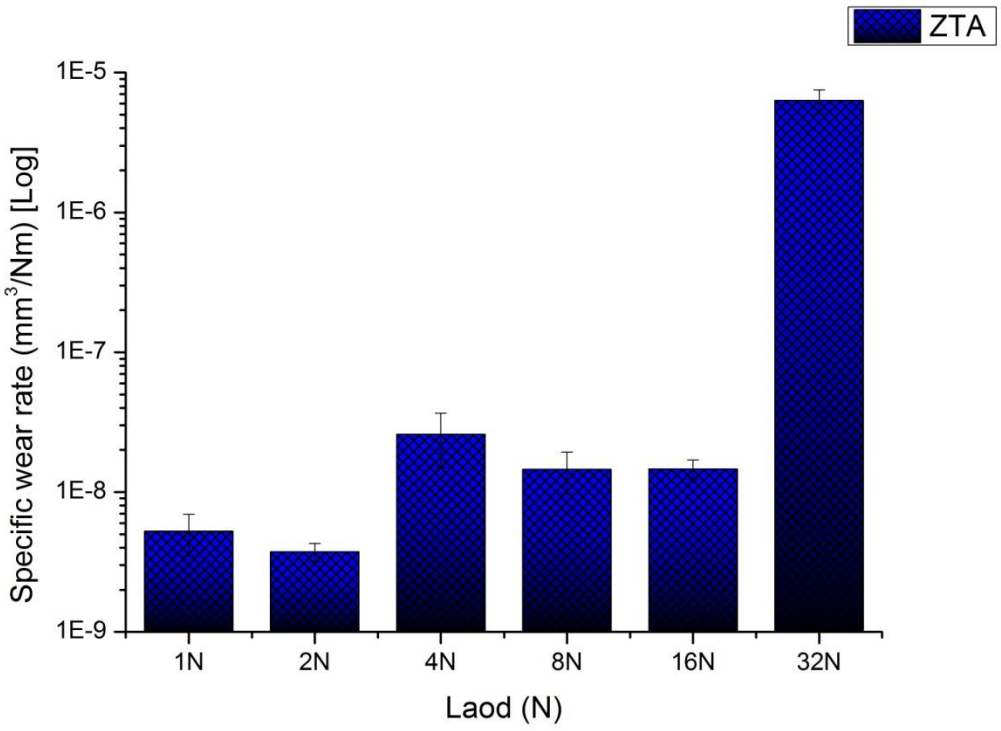

Figure 5.3. Specific wear rate of the ZTA using 25 vol.% Bovine serum solution lubrication.

5.1.2.2 Contact stress

The initial contact parameters for each individual load were calculated using the Hertzian contact theory. This theory predicts of the resulting contact area, maximum contact pressure, maximum shear stress and the depth of the maximum shear stress. As presented in Table 5.2, depending on the applied load, the maximum contact pressure varied between 1252.4MPa - 3976.2 MPa. The main deformation on the surface occurs through the initial contact stresses, though their corresponding magnitude decreases substantially in the first few minutes of the motion [226]. The difference in the wear scar widths, in various specimens, is established within the first few minutes. Subsequently, the experiment continues at much lower contact pressures, at a value that depends on the lubricant [226]. With the assumption that the elastic moduli and the Poisson's ratios of the three specimens, zirconia toughened alumina (ZTA), zirconia toughened alumina with additives (ZTA-Additives) and the commercial (BIOLOX® delta) are similar, the same initial contact stress is calculated for all three specimens.

Table 5.2. Initial contact stress for ZTA, ZTA-additives and BIOLOX® delta in the lubricated reciprocating wear tests under various loads.

Object A- High purity alumina ball					**Shape=Sphere** **Radius (Ra)=2 mm** **Elastic modulus =400 GPa** **Poisson ratio=0.25**		
Object B- BIOLOX ®delta **ZTA** **ZTA and additives**					**Shape=Flat** **Elastic modulus=358 GPa** **Poisson's ratio=0.25**		
Initial Contact	Normal Load (N)	1	2	4	8	16	32
	Calculated Contact Radius (mm)	0.0195	0.0245	0.031	0.039	0.049	0.062
	Max Hertzian Contact Pressure (MPa)	1252.4	1577.9	1988.1	2504.8	3155.9	3976.2
	Max Shear Stress (MPa)	402.9	507.6	639.5	805.8	1015.2	1279
	Depth of Max Shear Stress (mm)	0.009	0.011	0.014	0.018	0.023	0.029

5.1.3 Characterisation of worn surface

5. 1.3.1 General surface morphology by Contour GT

Reciprocating wear tests created linear wear tracks at all six loads. One of the techniques employed to image these scars was Contour GT which provided 3D images of the worn surfaces. Figures 5.4 (a-f) display images from the centre and one tail of the wear scars which are stitched together. The width of the scar for both 1 N and 2 N was ~150 µm. A few parallel grooves existed within these scars that seemed to be very shallow, for which no trace of wear debris was observed. So, it can be inferred that the full fluid film regime was operative at these loads. At 4 N, the formation of a few grooves was discernible and the depth of the deepest one inside the wear scar was less than 1 µm. In addition, extensive wear debris deposits were observed along the wear track and at the leading edges. Although the volume loss at 8 N was about two times more than at 4 N, more wear debris were observed at 4 N. Unlike 8 N and 4 N, no undulations were observed within the wear scar at 16 N, with a small intermittent distribution of wear debris evident at the edges and along the scar. Finally, at 32 N, the measured volume loss detected by VSI mode of contour GT was substantially higher compared to the lower loads, with little evidence of wear debris.

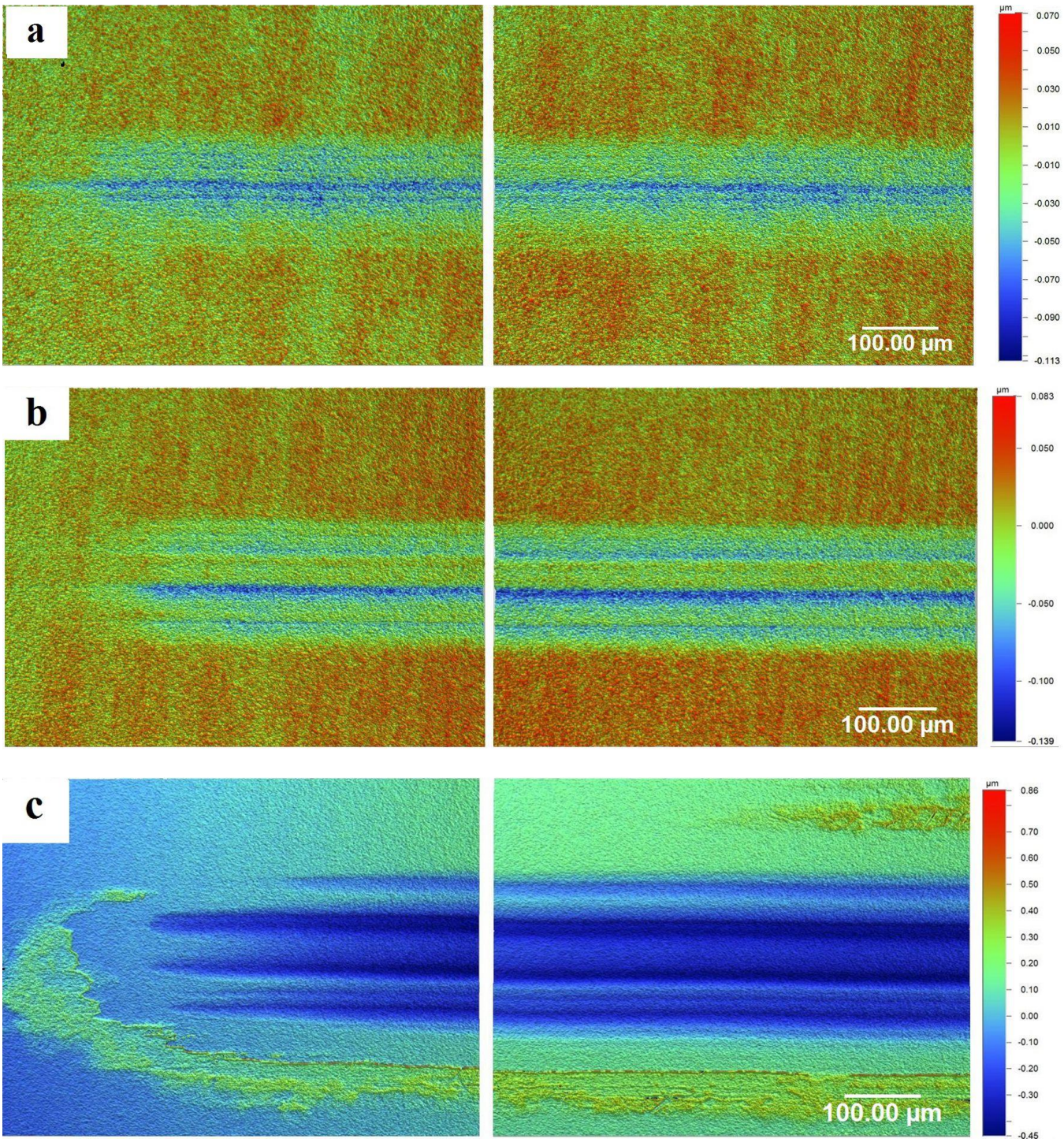
a
100.00 µm
µm
0.070
0.050
0.030
0.010
-0.010
-0.030
-0.050
-0.070
-0.090
-0.113
b
100.00 µm
µm
0.083
0.050
0.000
-0.050
-0.100
-0.139
c
100.00 µm
µm
0.86
0.70
0.60
0.50
0.40
0.30
0.20
0.10
0.00
-0.10
-0.20
-0.30
-0.45

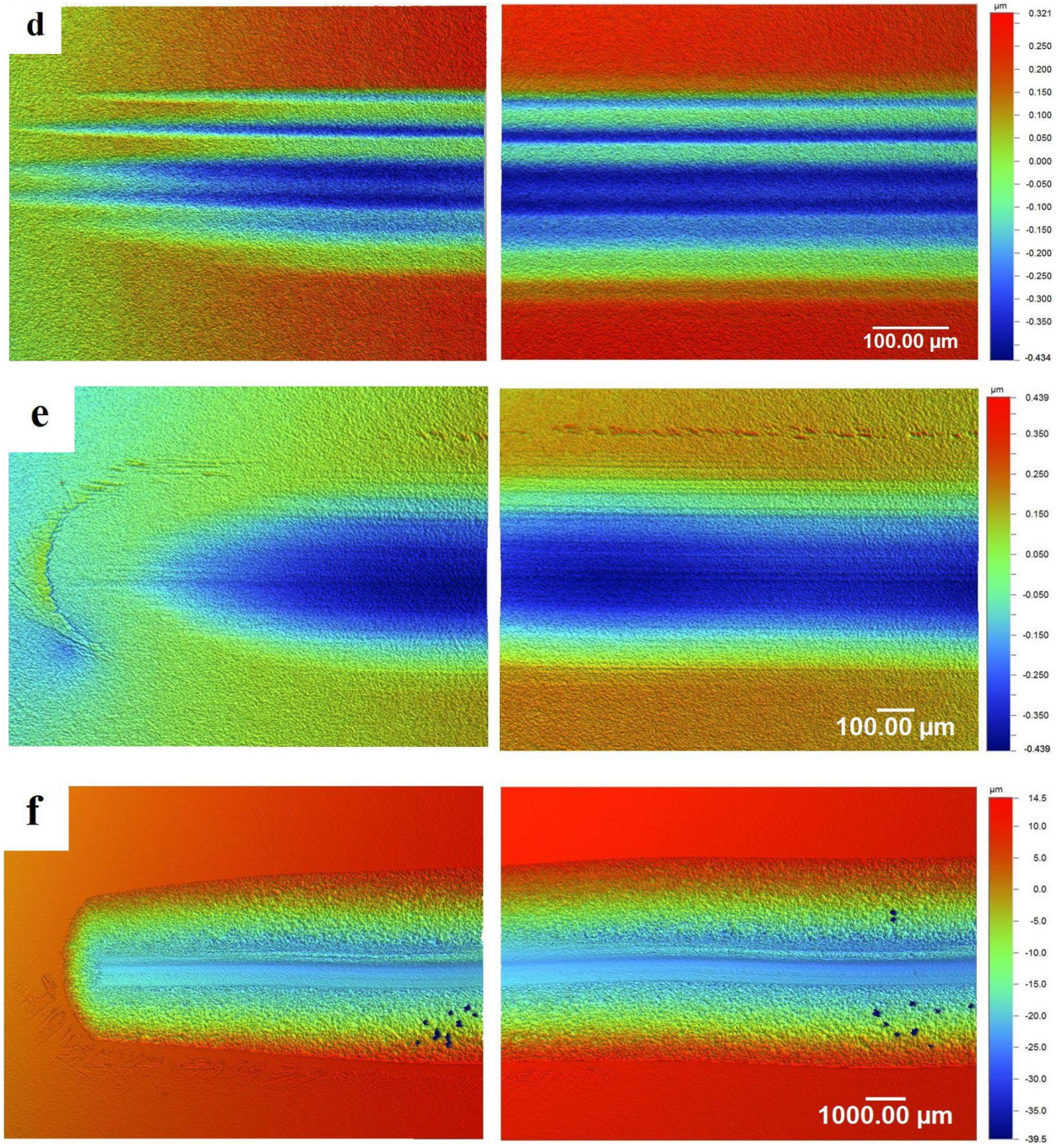

Figure 5.4. Profilometry images of the wear tracks taken by Contour GT at (a) 1 N, (b) 2 N, (c) 4 N, (d) 8 N, (e) 16 N, (f) 32 N for the ZTA specimen under lubricated reciprocating wear test during 10 hrs.

5.1.3.2 Worn surface topographic feather by SEM and AFM

Conventional SEM along with the Atomic Force Microscopy (AFM) were employed to explore the wear mechanisms involved within the wear tracks. “2D” (SEM) and “3D” (AFM) images are presented in Figures 5.6 (a-f), showing the morphology of worn surfaces under various loads ranging between 1 N - 32 N for the ZTA. The morphology of the original surface before wear test is shown in Figure 5.5.

For the ZTA composite tested at 1 N, sparsely distributed and comparatively small pits were observed which were formed as a result of grain pull out (black circle in Figure 5.6 (a)). In addition to the pits, a few parallel grooves were obvious (white arrows) in the direction of the sliding motion. The depth of these grooves reached ~10 nm in some cases and the average measured roughness of the worn scar was ~ 2.8 nm at this load, measured by AFM.

At 2 N, Figure 5.6 (b), more grain pull-out (black circle) was observed compared to 1 N. Similar to 1 N, parallel wear scars (white arrows) were evident on the direction of the sliding motion but the depth of these scars were not the same. The largest depth of the pull out, observed for this load, was ~20 nm (red arrow). The 3D AFM images for this load represent some degree of “grain relief” or “differential wear” at both 1 N and 2 N (white circle). The approximate average Ra for this wear track was ~3.4 nm.

The SEM micrograph for a load of 4 N, Figure 5.6 (c), revealed more changes in the morphology of the surface, compared to 1 N and 2 N. As shown in Figure 5.6 (c), multiple transgranular fracture or cleavage fracture in alumina grains was clearly evident, which was accompanied by the initiation of chipping in alumina grains (blue and red rectangle). Blue arrows in Figure 5.6 (c) point to the formation of a transgranular fracture within an alumina grain. The red circle in the same SEM image marks a large pit, containing a zirconia grain protruding out of the surface, while almost all of its surrounding grains no longer exist. The 3D AFM image, Figure 5.6 (c), evidenced the formation of the bigger pits (black circle) due to the connection of smaller ones. A careful observation of these pits at different angles revealed the accumulation of wear debris inside some of these pits (red circle). Also noticeable was the height difference of about 13 nm between the marked grain (red arrow) with its adjacent grains (red arrow). The comparison between the SEM micrograph and the 3D AFM image confirms the nature of the grains standing proud of the surface

to possibly be zirconia. Similar to the lower loads, an outline of the grain boundaries was still identifiable for this scar which would suggest that differential wear existed between grains. The largest depth formed by grain pull out was ~ 80 nm for this scar and the average Ra was ~ 4.6 nm.

At 8 N, Figure 5.6 (d), the SEM of the microstructure of the worn surface was almost similar to 4 N in which large pits, coupled with intergranular and transgranular fracture of alumina grains (red circle) were apparent. Unlike 4 N, the chipping of zirconia grains was more discernible at this load (red rectangle). Also, a single zirconia grain is detectable inside the large pit which was the only grain that survived in that region (blue rectangle). In the AFM image, Figure 5.6 (d), the parallel grooves were also detected, with the highest depth reaching ~12 nm, and the severity of the worn areas was similar to 4 N, with an average roughness of ~ 4.4 nm.

Under 16 N load, Figure 5.6 (e), the surface looked more featured, with an increased amount of pitting and transgranular fractures (black circle). Also, a few parallel scars with different width values were noticeable which were indicative of a third body abrasion (white arrow) resulting from third body abrasive particles with various shapes and sizes. The SEM micrograph of the same image shows the area at which the grain boundaries started to disappear (blue rectangle) under a high Hertzian contact pressure of ~ 3156 MPa. The chipping of both alumina (blue circle) and zirconia (blue arrow) are labelled in the SEM micrograph, as well as the accumulation of debris in a fairly large pit next to the elongated grain (red circle). In addition, a random spread of debris or tribo-layer over the surface was detected within the wear track in different locations (black rectangle). It is worth mentioning that the height difference between neighbouring grains, in some areas, could be due to the presence of tribo-layer on some of the grains, marked by white circle in the AFM image, Figure 5.6 (e). Interestingly, the height difference between grains was more conspicuous in the region where zirconia agglomerations are formed (black rectangle, SEM image). The 3D AFM images displayed an average roughness of ~ 4.3 nm for this load.

Figure 5.6 (f) shows a very different worn surface at 32 N, compared to the lower loads, which is in line with the specific wear rate calculated at this load. The surface is heavily pitted and the remaining grains are featured by a significant amount of transgranular fracture. As shown in the SEM micrograph, Figure 5.6 (f), the cleavage fracture and chipping (mainly on alumina grains) were the most explicit features on the surface. The blue arrow points to the grains that are ready to be liberated. In the region, labelled as “severe”, in Figure 5.6 (f) AFM, there seems to be a complete

rupture of the surface. The depth of the deepest detected pit and the roughness (Ra) of the surface were ~ 100 nm and ~ 8.7 nm, respectively. There was evidence of agglomerated wear debris scattered over the surface (red circles, AFM). The thickness of these patches was ~ 45 nm at its highest. The presence of a crack on top of the tribo-layer was also noticeable within the large voids which is marked by a blue rectangle in both SEM and AFM images, Figure 5.6 (f). The white arrow on the same image points to the survived elongated grain containing an intragranular fracture, while all its neighboring grains have almost disappeared.

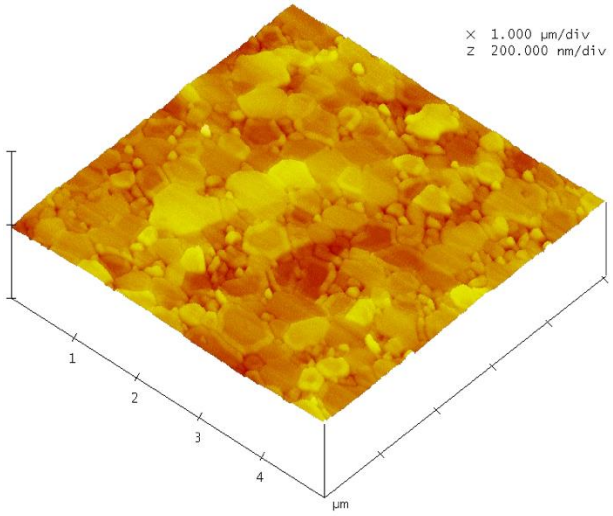

Figure 5.5. 3D AFM image of the unworn surface in the ZTA.

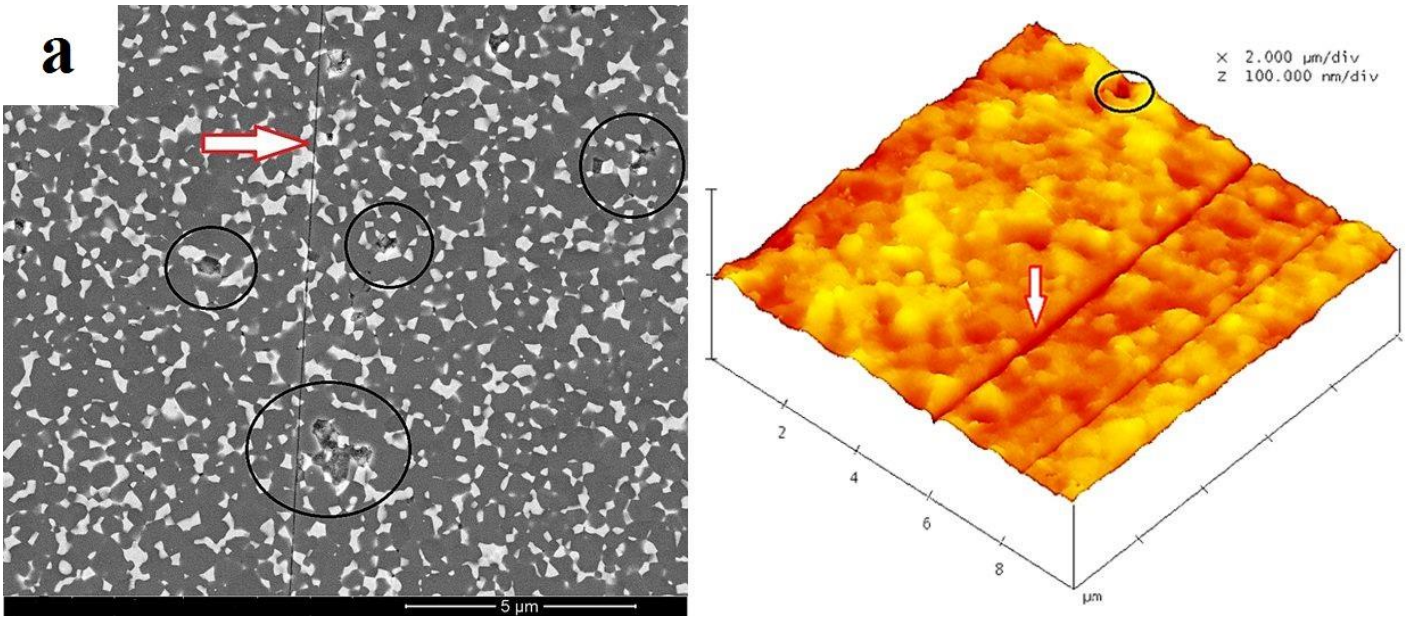

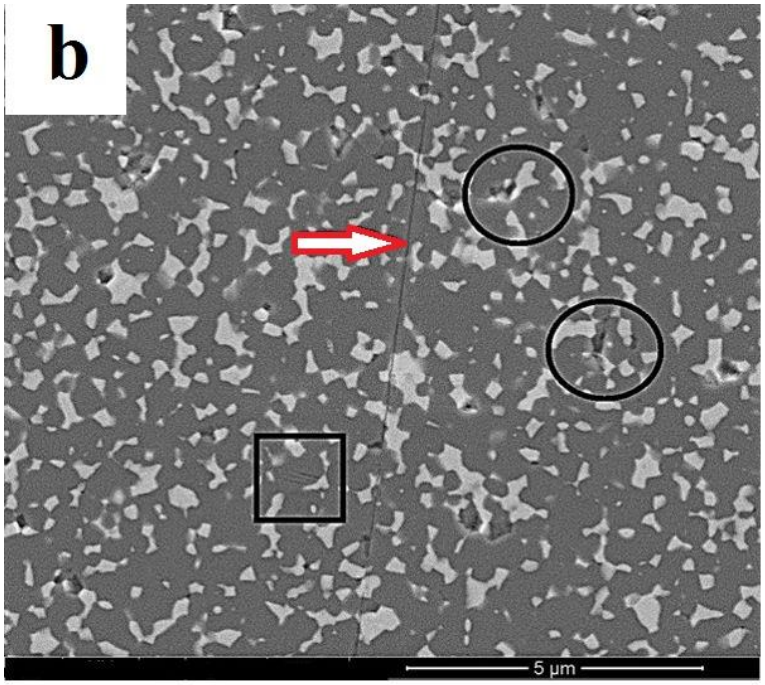
b
5 µm

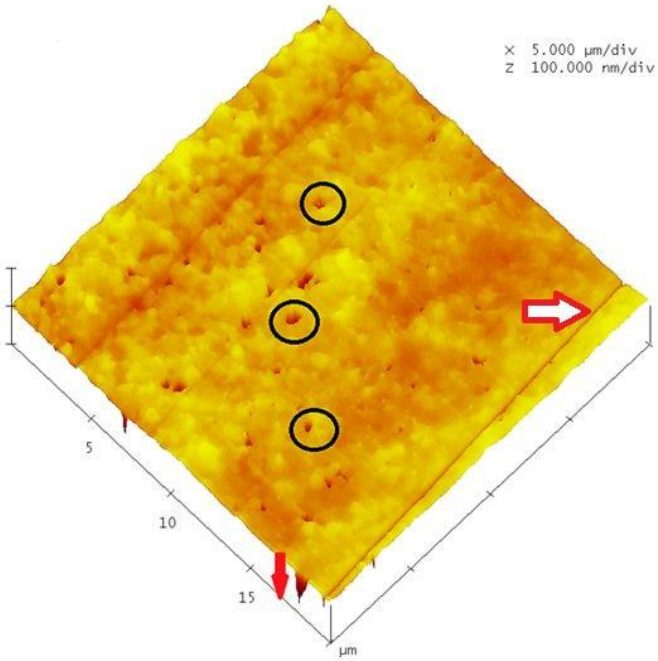
X 5.000 µm/div
Z 100.000 nm/div
5
10
15
µm

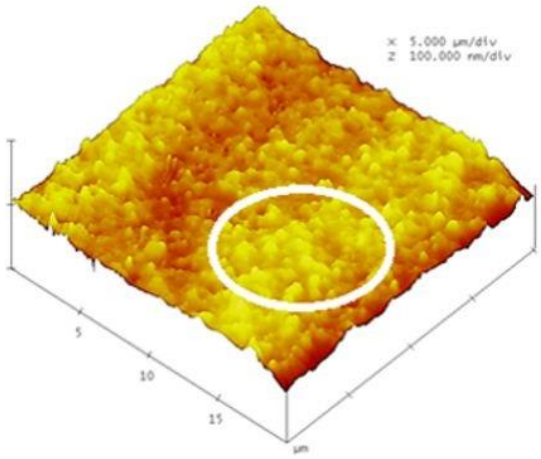
X 5.000 µm/div
Z 100.000 nm/div
5
10
15
µm

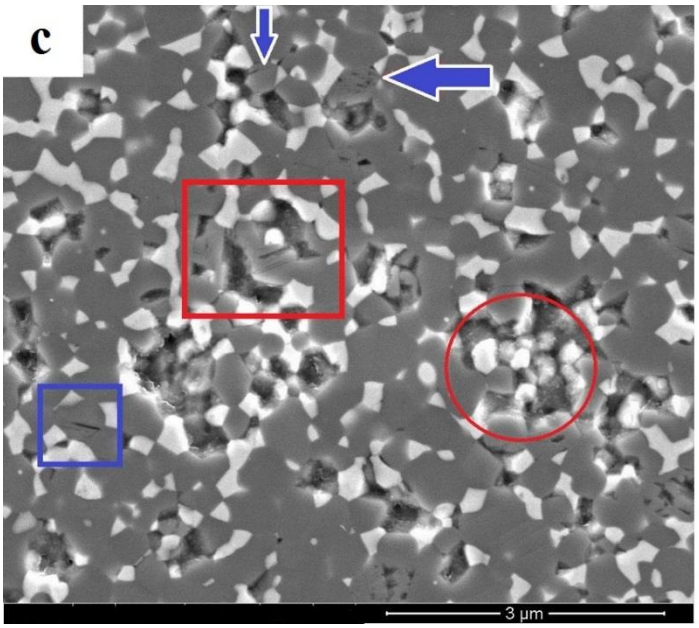
c
3 µm

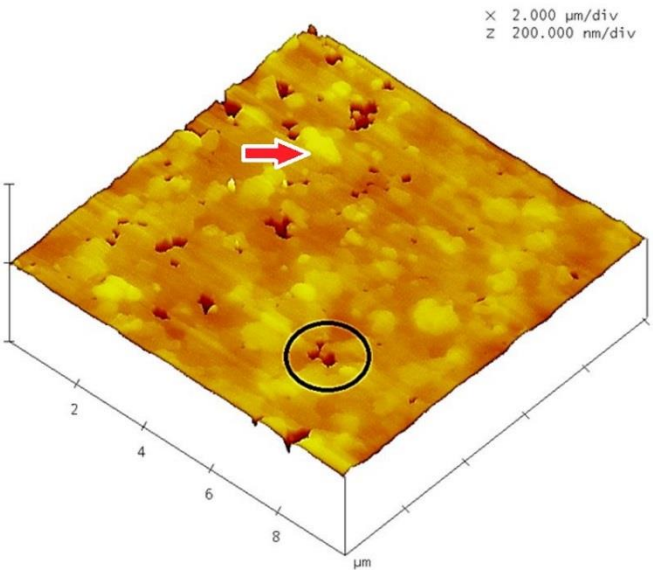
× 2.000 µm/div
z 200.000 nm/div
2
4
6
8
µm

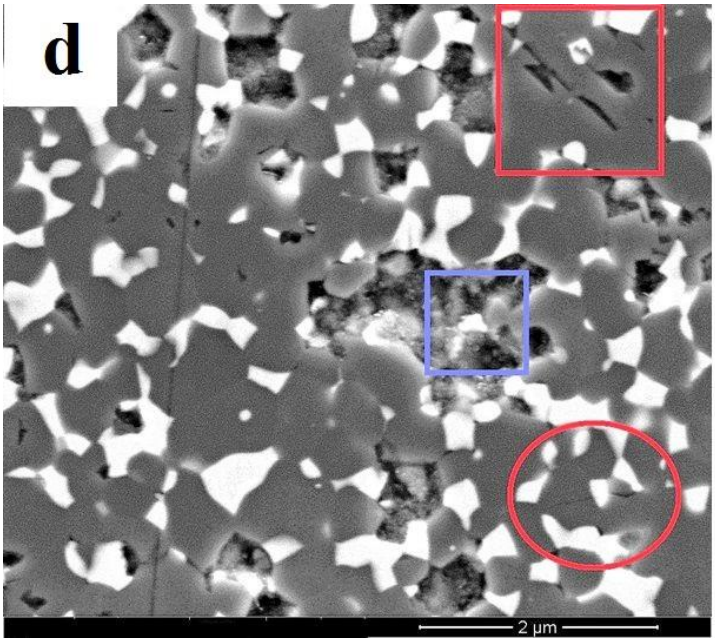
d
2 µm

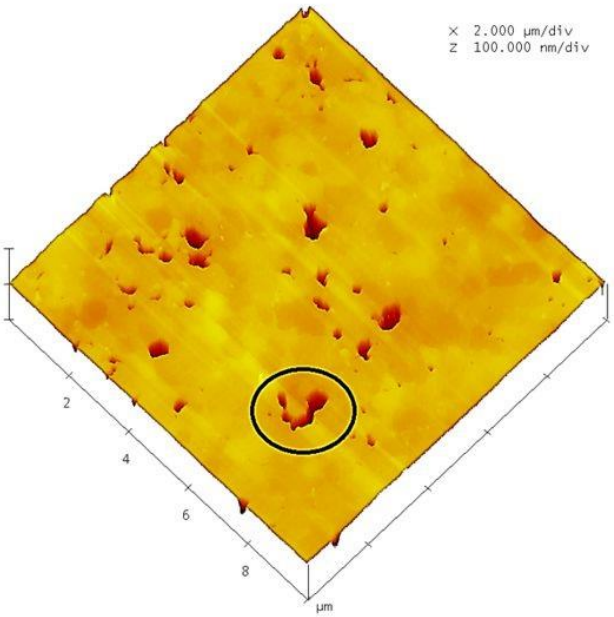
× 2.000 µm/div
z 100.000 nm/div
2
4
6
8
µm

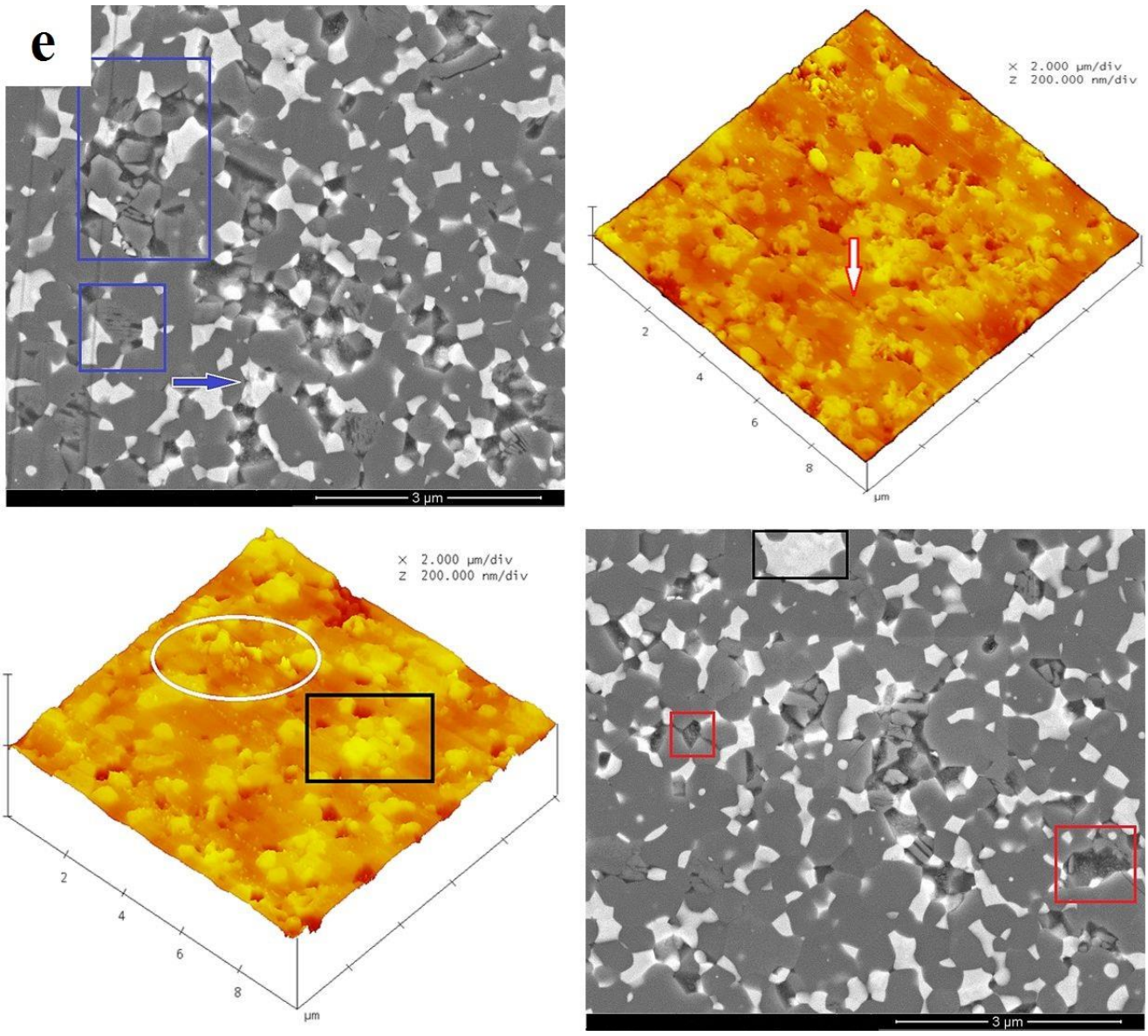
e
3 µm
× 2.000 µm/div
z 200.000 nm/div
2
4
6
8
µm
× 2.000 µm/div
z 200.000 nm/div
2
4
6
8
µm
3 µm

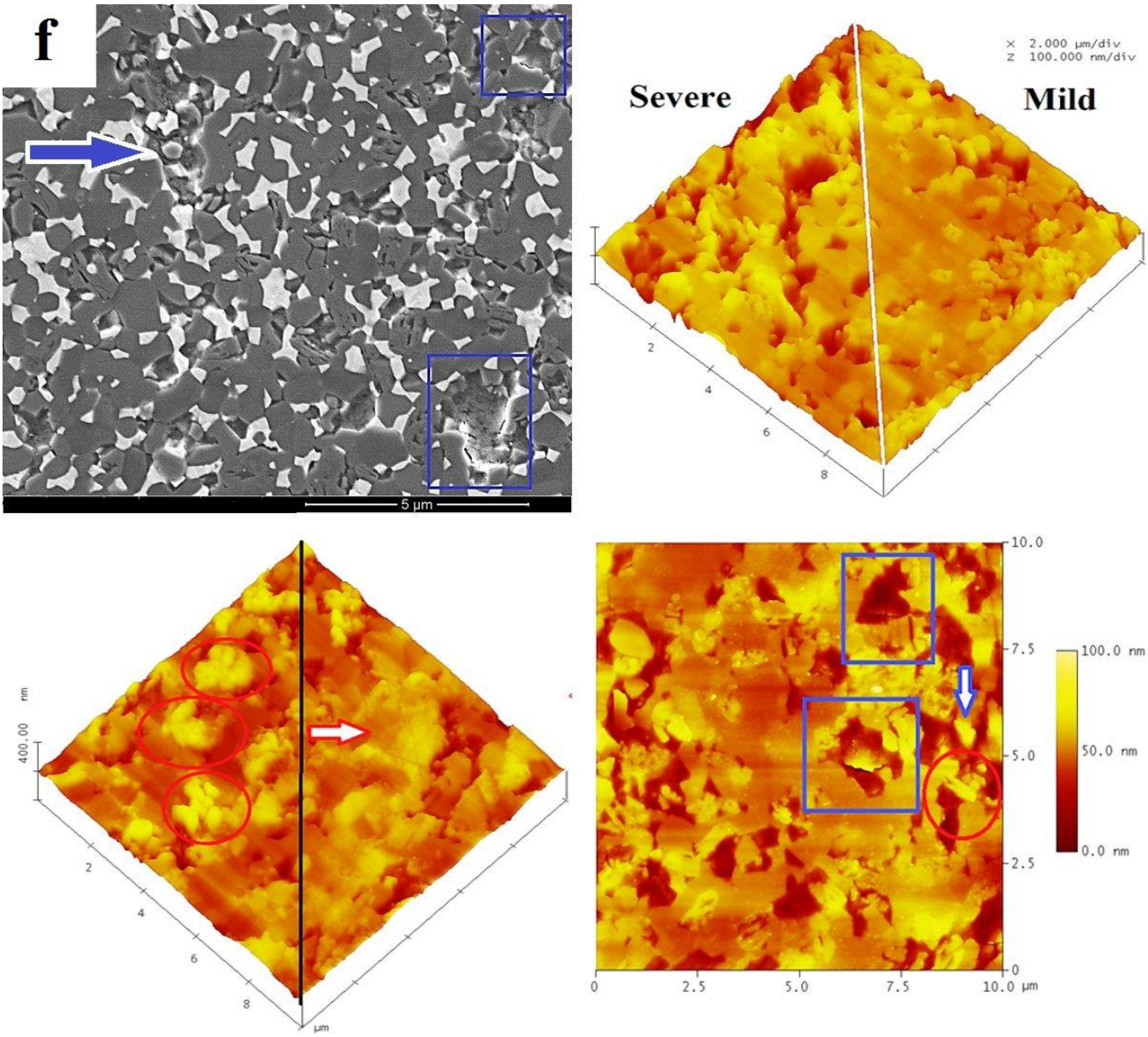

Figure 5.6. SEM and AFM images of the ZTA worn surfaces obtained from serum solution lubricated reciprocating wear test under (a) 1 N, (b) 2 N, (c) 4 N, (d) 8 N, (e) 16 N, (f) 32 N loads, at 600 rpm speed for 10 hrs.

5.1.3.3 Phase changes of the worn surface by Raman spectroscopy

The Raman spectra for the Tetragonal zirconia and ZTA specimens, under loads ranging between 1 N -32 N, are shown in Figures (5.7) and (5.8), respectively. In addition to these, the spectra of the unworn surface and the pure alumina are included for comparison. The letters "t" and "A" stand for tetragonal zirconia and alumina, respectively. For the tetragonal phase, six distinguishing bands generally exist at 148 cm^{-1}, 264 cm^{-1}, 319 cm^{-1}, 461cm^{-1}, 606 cm^{-1} and 643 cm^{-1} which are observed in this study and are confirmed by other researchers, Figure (5.7) [227,228]. Among these bands, the ones at 148 cm^{-1}, 264 cm^{-1} and 643 cm^{-1} were the most discernible ones due to their high intensity. As shown in Figure (5.8), even under a high initial Hertzian contact pressure of ~ 3976 MPa, no changes indicating the zirconia phase transformation were observed in the Raman spectrum. This is probably due to the small zirconia grain size that could not trigger the tetragonal to monoclinic phase transformation. Further explanation is provided in part 6.2.4.

In the ZTA based composite, two lines at 418 cm^{-1} and 380 cm^{-1} were associated with alumina [229]. It is worth mentioning that slightly different assignments and Raman band modes are attributed to the above lines by various authors [230, 231].

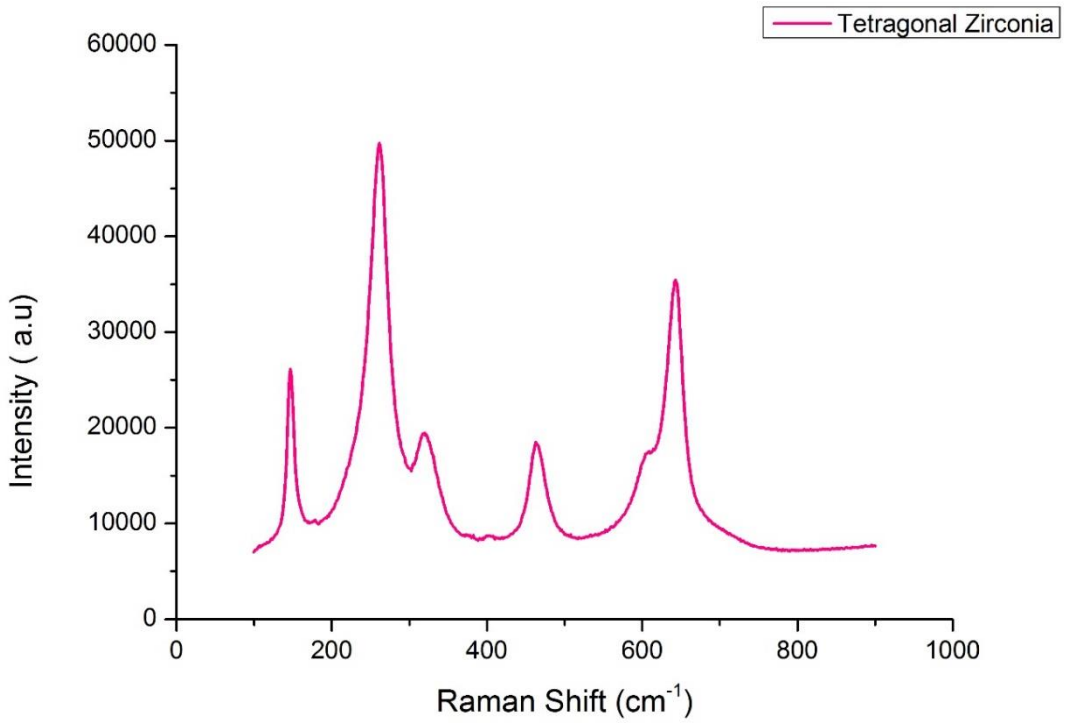

Figure 5.7. Typical Raman spectra of yttria stabilized zirconia (3Y-TZP).

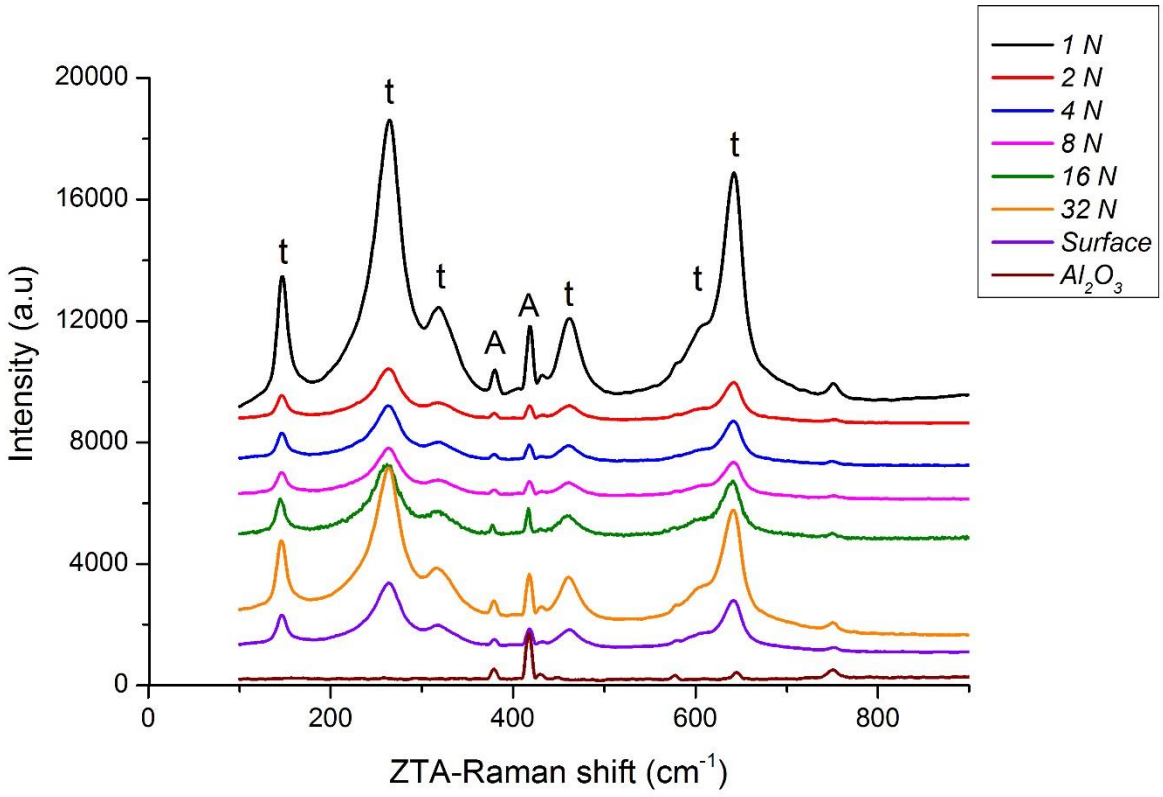

Figure 5.8. Raman spectra of the pure sintered alumina plus worn and unworn surface of the ZTA specimen under 1 N-32 N under lubricated reciprocating test.

5.1.4 Characterisation of sub-surface by TEM

Subsurface analysis of the ZTA specimen, prepared by FIB, was performed using TEM. The prepared TEM foils were removed from the specimens of the lubricated reciprocating sliding wear tests under 8 N load. The locations from which the two TEM specimens were extracted are marked in Figures 5.9 (a-b). The overviews of these cross sections are shown in Figures 5.10 (a) and 5.11 (a) in which just one single crater along each foil was obvious and the boundary between subsurface and surface appeared very smooth and flat, Figure 5.10 (b) and 5.12 (a-d). As shown in Figure 5.10 (b), the tribo-layer (red arrow) was detected inside a crater, underneath the gold layer (blue arrow). As shown in the magnified image, Figure 5.10 (b), the gold layer had almost peeled off and just a small part of it was left on top of the tribolayer. The elemental analysis demonstrated the presence of Al, Zr, O, Ca, Au and Cu in the tribo-film found in subsurface, Figure 5.10 (c). More details about the originating sources of these elements are given in part 6.2.5.

Figure 5.11 (a) shows the overview of another TEM specimen (foil 2) extracted out of the same worn track in a different area. As evidenced in Figure 5.11 (b), transgranular fracture was observed in a zirconia grain (red arrow) which also propagates along the boundary between the zirconia and the alumina and then into the alumina in a transgranular fashion. Interestingly, this subsurface fracture was located where the pitting and grain pull out were observed on the surface. As evidenced in Figure 5.11 (b) (white arrow), the presence of residual strain in an alumina grain next to the fractured zirconia grain is noticeable. If the amount of the residual strain is high enough, it can produce deformation in various forms such as dislocation.

As shown in Figure 5.12 (a-c), there were alumina grains that contained no deformation, while adjacent ones that contained significant dislocation activity. In general, a limited amount of plastic deformation was observed in alumina grains which were mainly located within the surface grain. Additionally, zirconia grains exhibited the mottled contrast in the TEM images which is known to be the characteristic of tetragonal zirconia (blue arrow), Figure 5.12 (d). As evidenced in Figure 5.12 (d), a very smooth surface was formed under ~ 2505 MPa initial Hertzian contact pressure (8 N) and the red circle highlights the deposition of four layers parallel to the surface protecting the subsurface from ion milling and are distinguishable as of their different contrast. The inner dark layer is gold and the subsequent coatings on top of the gold layer are carbon coating, Pt E-deposition and Pt deposition, respectively.

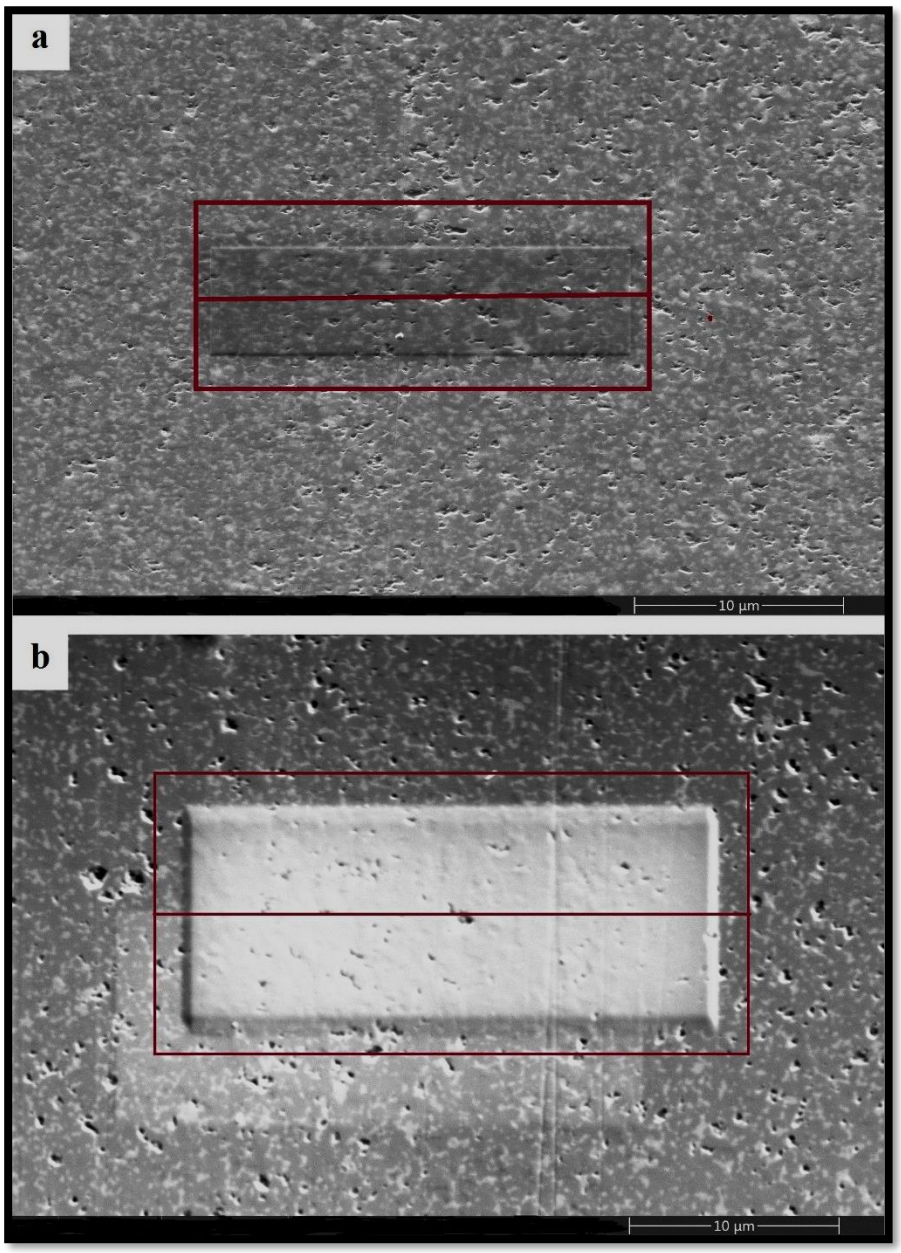

Figure 5.9 SEM images exhibit a typical damage pitting on the ZTA worn surface observed from lubricated reciprocating wear test under 8 N load for 10 hrs on which the position of two cross-sections TEM samples prepared by FIB lift-out method are marked. Foil 1 and foil 2 are extracted out of one wear scar and labelled with "a" and "b" in above images, respectively.

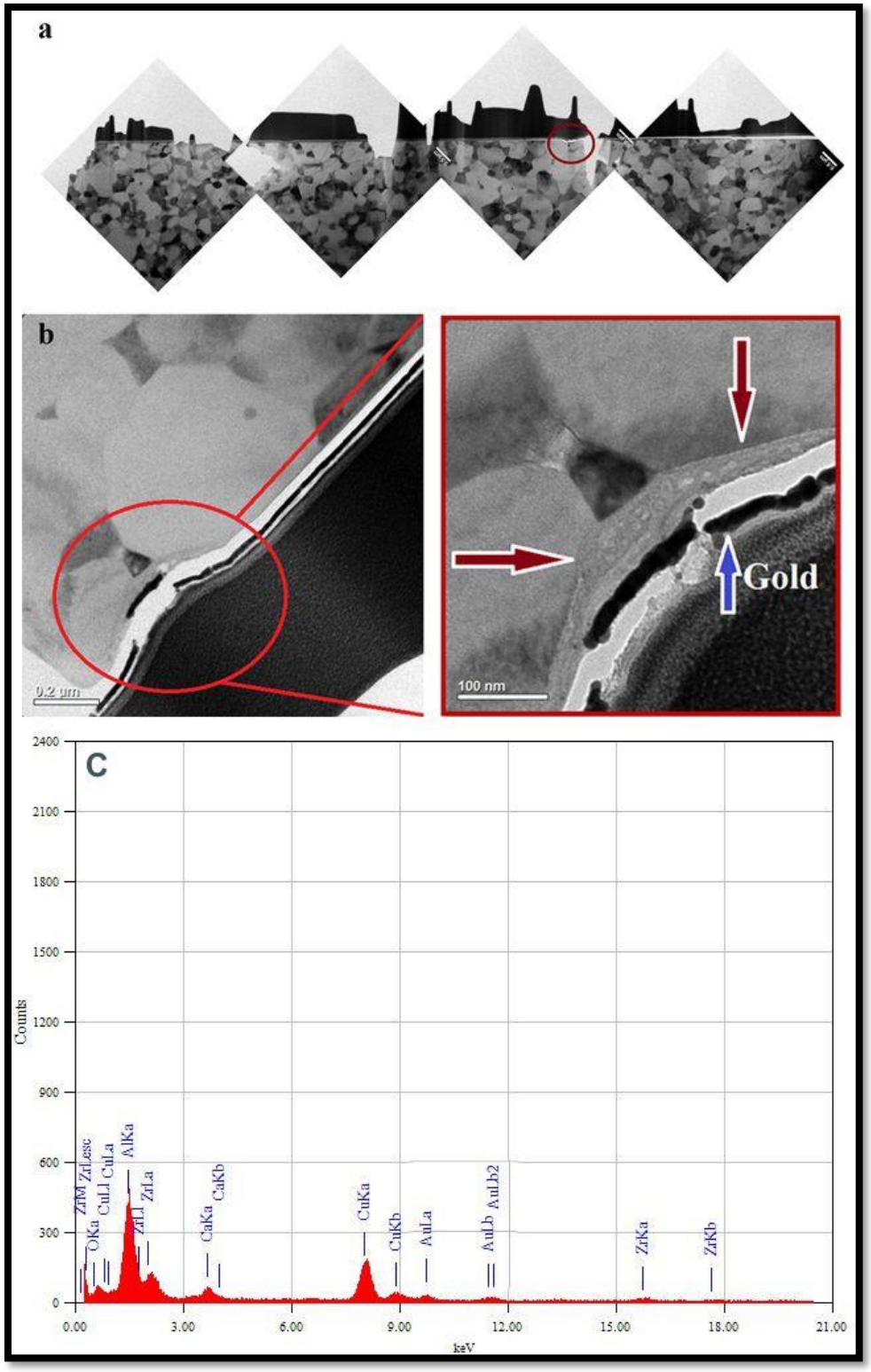

Figure 5.10. (a) Overview of the ZTA TEM cross-section specimen (Foil 1). (b). Bright field TEM image of the tribo-film in which the pitting and its corresponding tribo-layer location in nano-scale is marked. (c) Elemental analysis taken from this tribo-film.

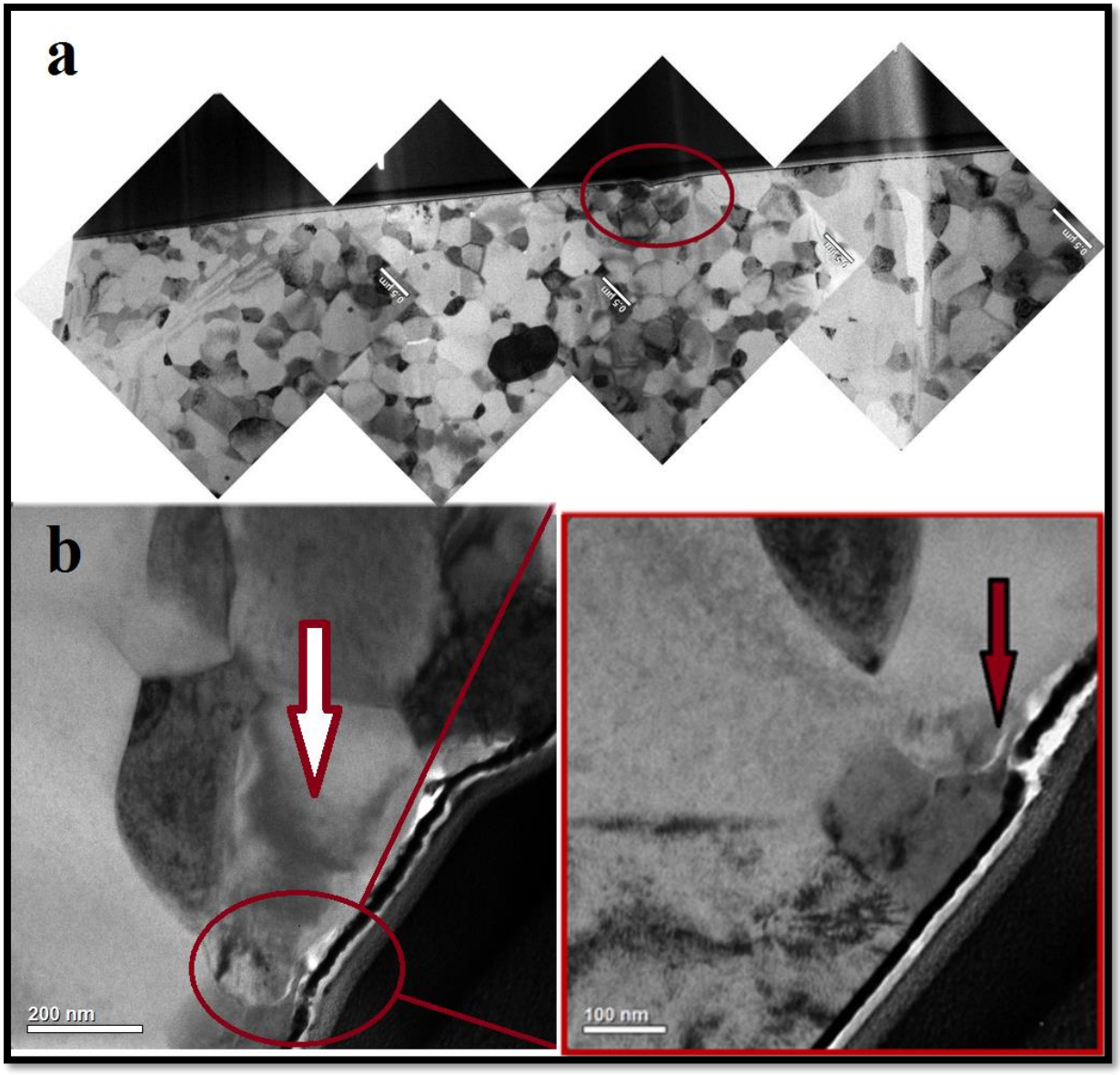

Figure 5.11. (a) The overview of the ZTA TEM cross-section specimen (Foil 2) in which the highlighted section displays (b) the bright field TEM image of the transgranular crack on a zirconia grain and the white arrow points to the residual strain on the alumina grain neighbouring to the fractured zirconia grain. The adjacent image is the magnified figure of the highlighted section.

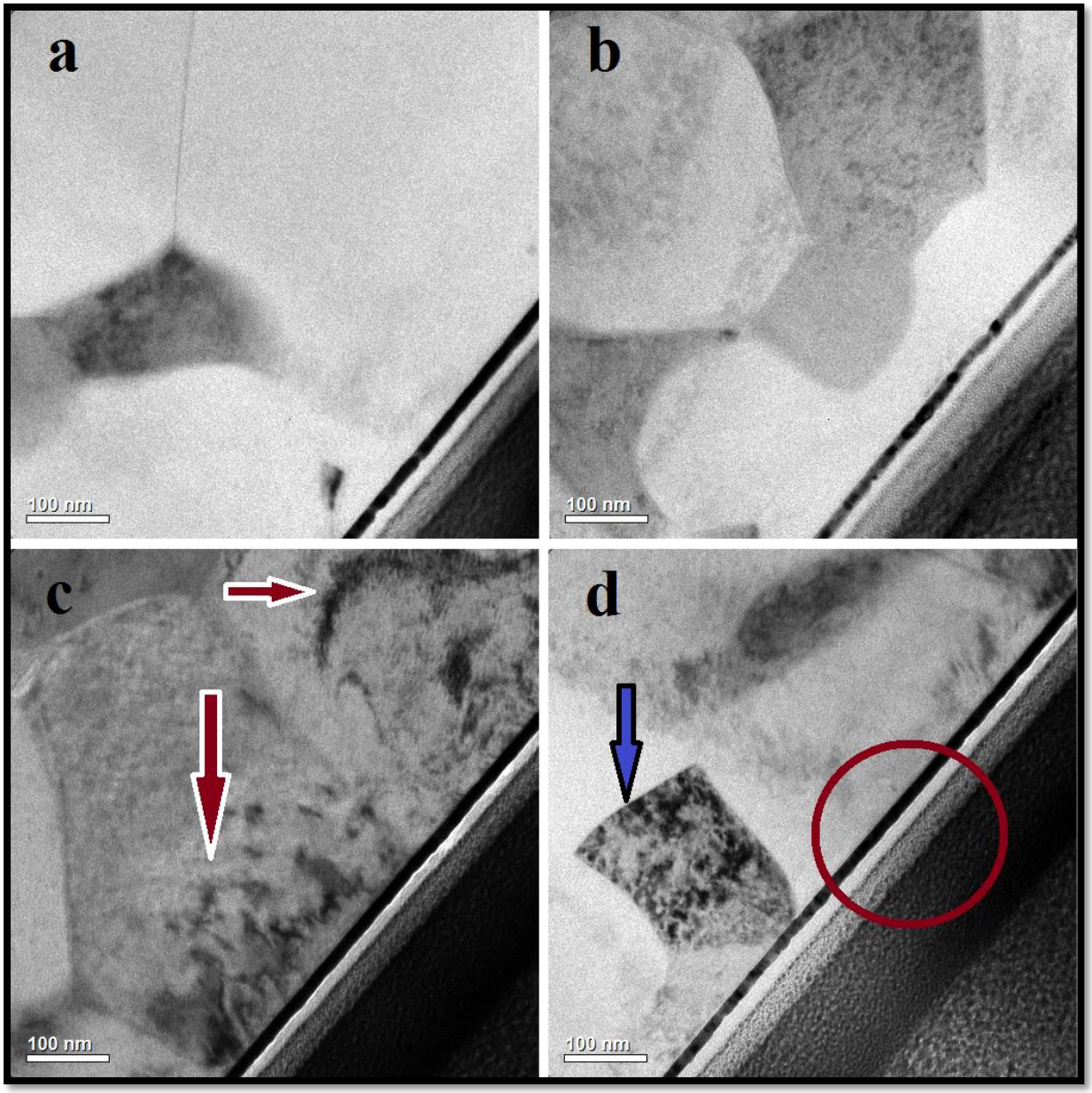

Figure 5.12. Bright field TEM images (a-b) showing alumina grains with no dislocation activity observed on the top layer of the ZTA specimen (foil 2) at 8 N load (c) exhibiting alumina grains containing occasional dislocations (d) demonstrating a very smooth coating layer between surface and subsurface; the blue arrow points to the typical tetragonal zirconia grain.

5.2 Zirconia toughened alumina-additives lubricated with 25 vol. % new-born calf serum solution

5.2.1 Lubrication regime definition

Figure 5.13 shows the trend of the COF versus time in the ZTA-Additives (1) specimen for the loads spanning 1 N to 32 N. The lowest average COF value of 0.03 ± 0.02 was measured for 2 N and the highest value of 0.20 ± 0.03 for 8 N. It is worth mentioning that the COF Vs time plot for 8 N is divided into two sections for this sample which is due to the increase of COF after about 4 hrs. The average COF of 0.06 ± 0.05 for the first part and 0.20 ± 0.03 for the second part was measured at this particular load. The estimated "running in" period for 1 N, 2 N, 4 N, 8 N, 16 N and 32 N was ~ 9 min, ~7 min, ~9 min, ~17 min, ~9 min and ~92 min, respectively.

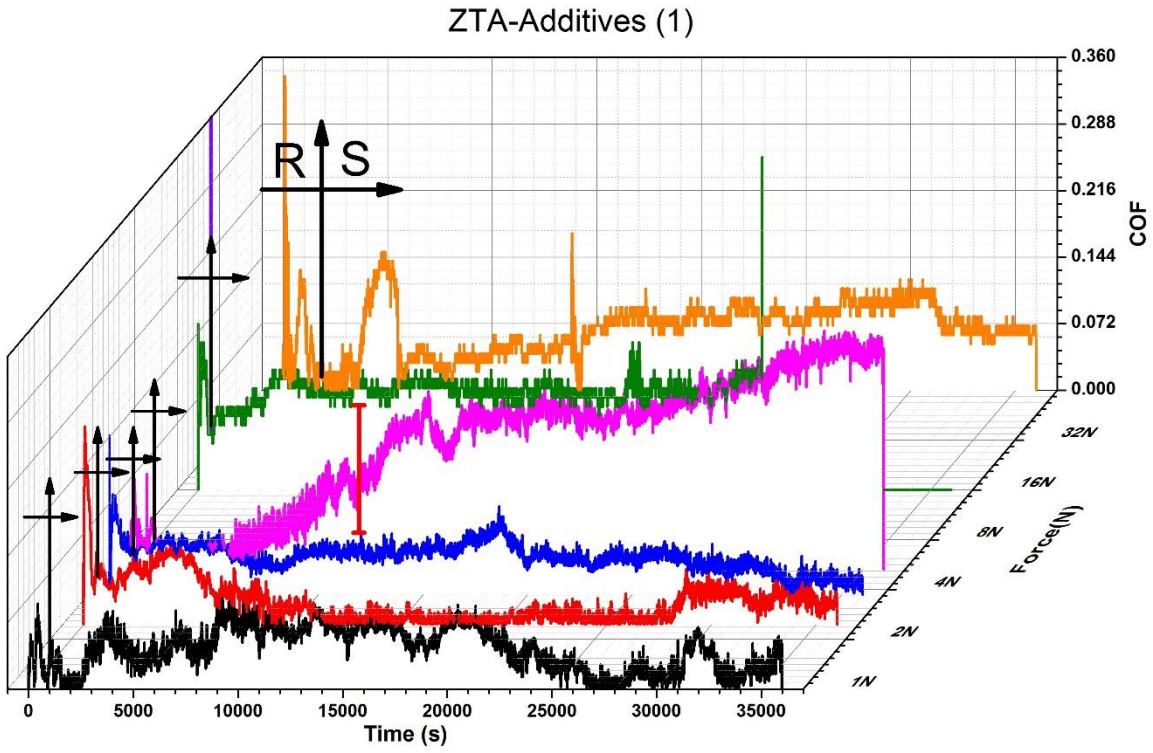

Figure 5.13. The 3D illustration of COF Vs time in the ZTA-additives (1) at different loads tested in 25 vol. % Bovine serum at 600 rpm for 10 hrs.

The COF for another specimen with the same composition, ZTA-additives (2), is shown in Figure (5.14) and is for loads spanning between 1 N - 8 N. In these graphs, the length of the "running in"

period for loads ranging between 1 N-8 N was estimated to be about 8 min, 6 min, 3 min and 8 min, respectively. As presented in Table 5.3, the highest and the lowest values for the average COF in ZTA-additives (2) are 0.08 ± 0.03 and 0.19 ± 0.02 which are corresponding to 2 N and 8 N, respectively.

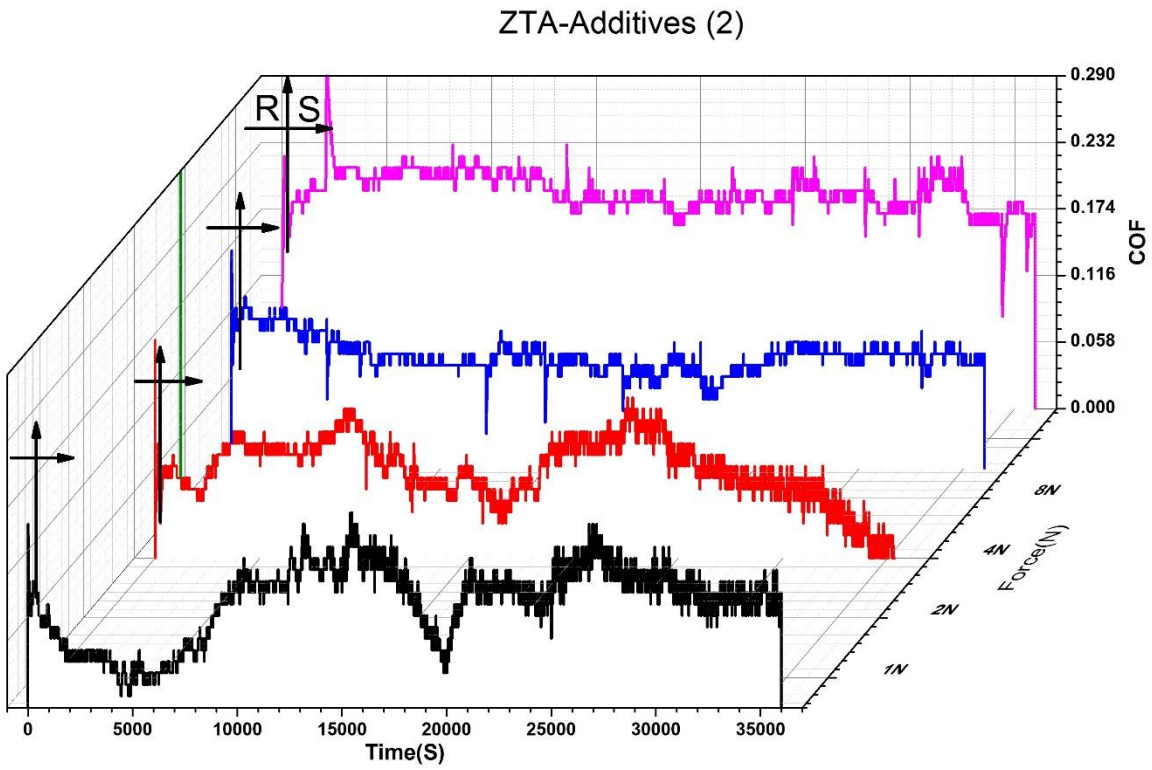

Figure 5.14. The 3D illustration of COF Vs time in ZTA-additives (2) at different loads tested in 25 vol.% Bovine serum reciprocating wear test at 600 rpm for 10 hrs.

Table 5.3. Summary of the average COF corresponding to each load in ZTA-additives.

Force (N)	Coefficient of Friction ZTA-additives (1)-Sam3	Coefficient of Friction ZTA-Additives (2)	Summerfeld (Z)
1N	0.04±0.02	0.09±0.03	2.4E-04
2N	0.03±0.02	0.08±0.03	1.2E-04
4N	0.04±0.02	0.10±0.02	6.0E-05
8N	0.06±0.05 *0.20±0.03	0.19±0.02	3.0E-05
16N	0.11±0.01		1.5E-05
32N	0.07±0.02	-	7.5E-06

The Stribeck curve for the ZTA-additives (1) does not exhibit the typical trend expected for a classic Stribeck curve, as the average COF at 32 N is less than the one at 16 N, Figure 5.15. However, the trend of this curve is indicative of the operation of the full film lubrication at 1 N and 2 N and mixed lubrication at 4 N and 8 N. It is worth mentioning that in order to determine the corresponding lubrication mode at each load more accurately, extra information is required about the morphology of the worn track for that particular load. Considering this, the results provided in part 5.1.3.2 do not confirm the operation of full fluid film mode at 1 N and 2 N. At test loads of 16 N and 32 N, although the friction decreased for the higher load, it is still believed that this was in the mixed lubrication regime. A full discussion is given in Chapter 6.

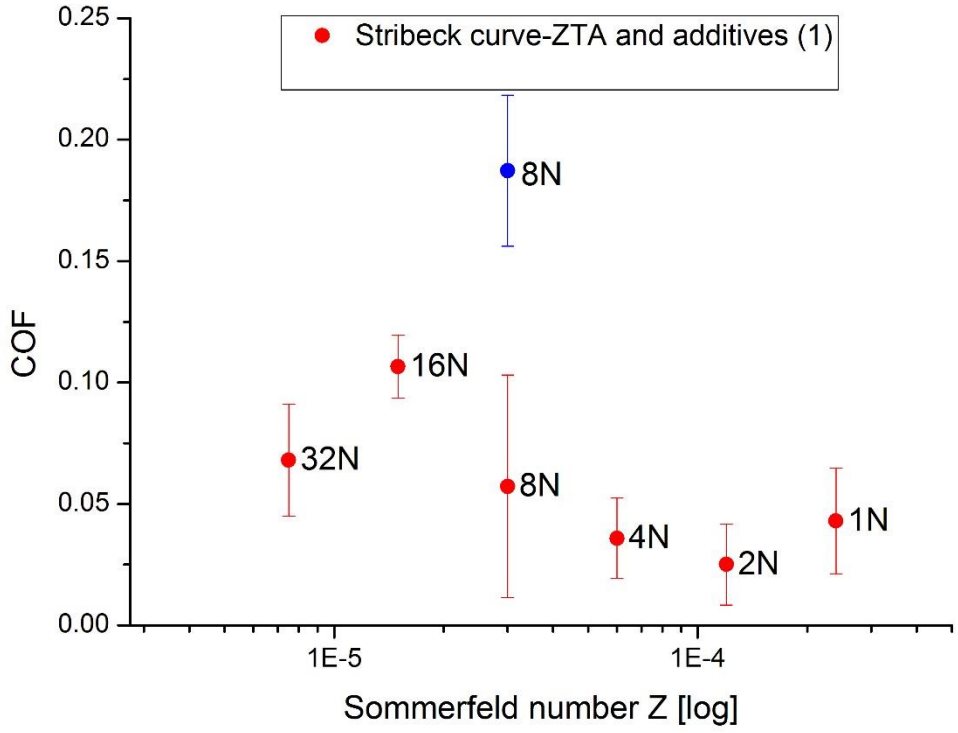

Figure 5.15. The Stribeck curve for ZTA-additives (1) in 25 vol. % Bovine serum lubricated reciprocating wear test.

For the ZTA-additives (2), the COF as a function of Summerfeld number looks more like the classic curve, Figure 5.16. The average COF value at 2 N is at its minimum which is the demarcation point between the full film and the mixed lubrication modes, Figure 5.16. With this explanation, the dominant lubrication regime at 1 N and 2 N appear to be the full fluid film. However, the mixed lubrication mode seems to operate at 4 N and 8 N.

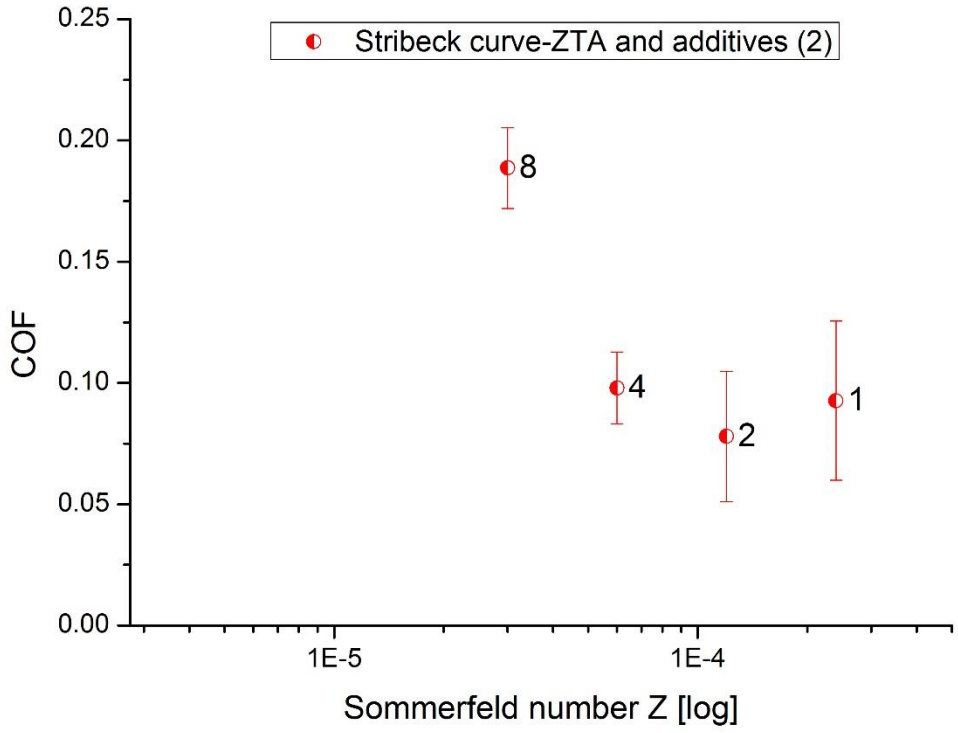

Figure 5.16. The Stribeck curve for ZTA-additives (2) in 25 vol. % Bovine serum lubricated wear test.

5.2.2 Wear behaviour

5.2.2.1 Specific wear rate

As shown in Figure 5.17, the calculated specific wear rates for ZTA- additives (1) at 1 N, 2 N and 4 N are $1.2\times10^{-8} \pm 4.68 \times10^{-9}$ mm^3/Nm, $1.79\times10^{-8} \pm 4.26 \times10^{-9}$ mm^3/Nm and $2.47\times10^{-8} \pm 2.61 \times 10^{-9}$ mm^3/Nm, respectively which are all still at the same order of magnitude. It is worth mentioning that at the lowest loads of 1 N and 2 N, the measurement of the volume loss to calculate the specific wear rate was so small that it was difficult to measure.

Almost the same specific wear rate was obtained at 8 N, $2.05\times10^{-8} \pm 4.72\times10^{-9}$ mm^3/Nm, compared to 4 N. At 16 N, the specific wear rate increased up to approximately $4.07\times10^{-8} \pm 7.94\times10^{-9}$ mm^3/Nm which was at the same order of magnitude with the lower loads. Eventually, at 32 N the specific wear rate increased to $1.69\times10^{-7} \pm 2.99\times10^{-8}$ mm^3/Nm, which is about an order of magnitude larger compared to lower loads (1 N and 2 N). However, at 32 N the specific wear rate was considerably higher, but about an order of magnitude less than the corresponding value for the ZTA at the same load.

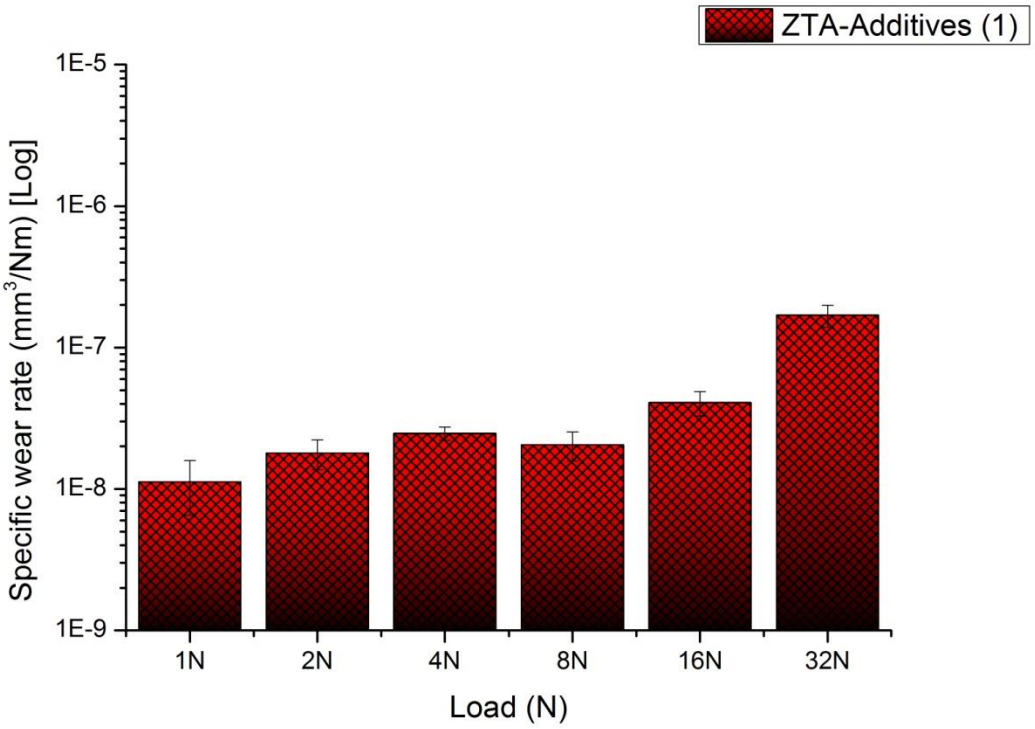

Figure 5.17. Specific wear rate of ZTA-additives (1) using 25 vol. % Bovine serum solution lubrication.

The specific wear rate for the ZTA-additives (2) for the loads between 1 N-8 N remained in the order of 10^{-8} mm^3/Nm, with a slight fluctuation, which is fairly consistent with the specific wear rates of the ZTA-additives (1). The slight change in the calculated value of the specific wear rate is linked to the fact that wear is a parameter defined by the behaviour and responses of contacting bodies in a tribo-system and should not be regarded as a material property [232].

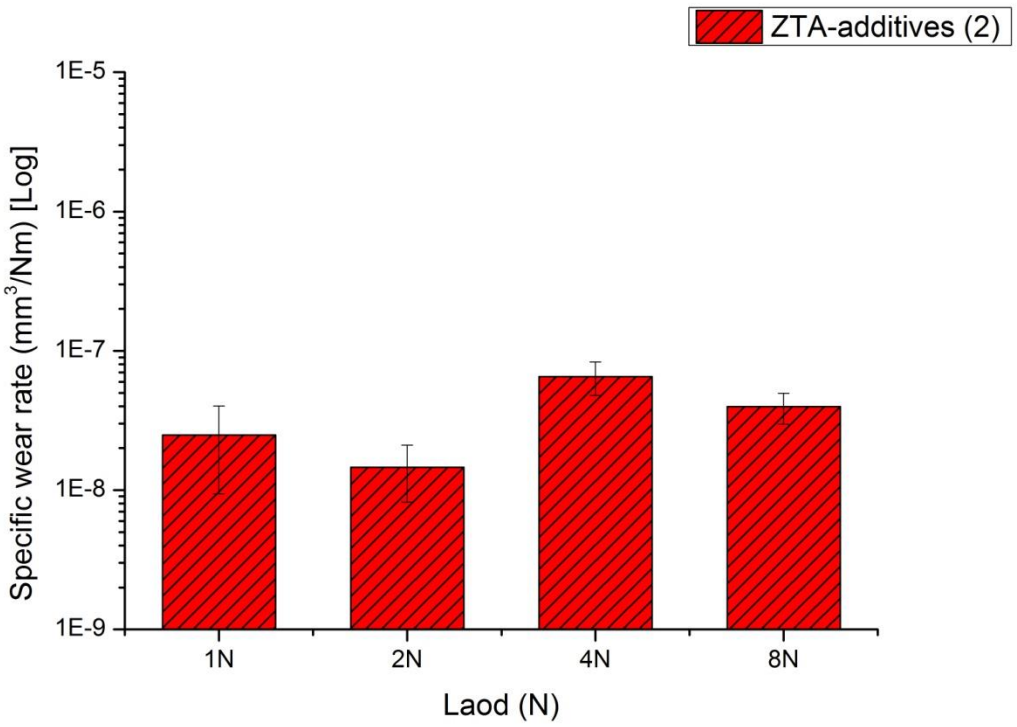

Figure 5.18. Specific wear rate of ZTA-additives (2) using 25 vol. % Bovine serum solution lubrication.

5.2.3 Characterisation of worn surface

5.2.3.1 General surface morphology by Contour GT

The Contour GT 3D optical microscopy of ZTA-additives (1) is shown in Figures 5.19 (a-f), for loads between 1 N - 32 N. These images were obtained at the centre and one edge of the wear scars. The colour scale bar next to each scar shows the depth that the microscope had detected at each point. As shown in Figures 5.19 (a-b), the depth of the scars progressively increased with increase in load. Unlike the ZTA specimen, no undulation was conspicuous inside the wear track at 1 N and 2 N. At 4 N, a well-defined wear scar was formed, although no debris was observed inside or outside of the wear track, Figure 5.19 (c). On raising the applied load to 8 N, the volume loss slightly increased, and the wear debris was apparent along the track, Figure 5.19 (d). In contrast to 8 N, debris was detected around the head of the scar at 16 N and the volume loss was about three times more than at 8 N, Figure 5.19 (e). In addition to the outer edges along the scar, a considerable accumulation of debris was evident at the trailing edges of the scar, Figure 5.19 (f).

Due to the close similarities of the morphology of the worn tracks in the ZTA-Additives (2) and ZTA-Additives (1), the Contour GT images of ZTA-additives (2) will not be presented.

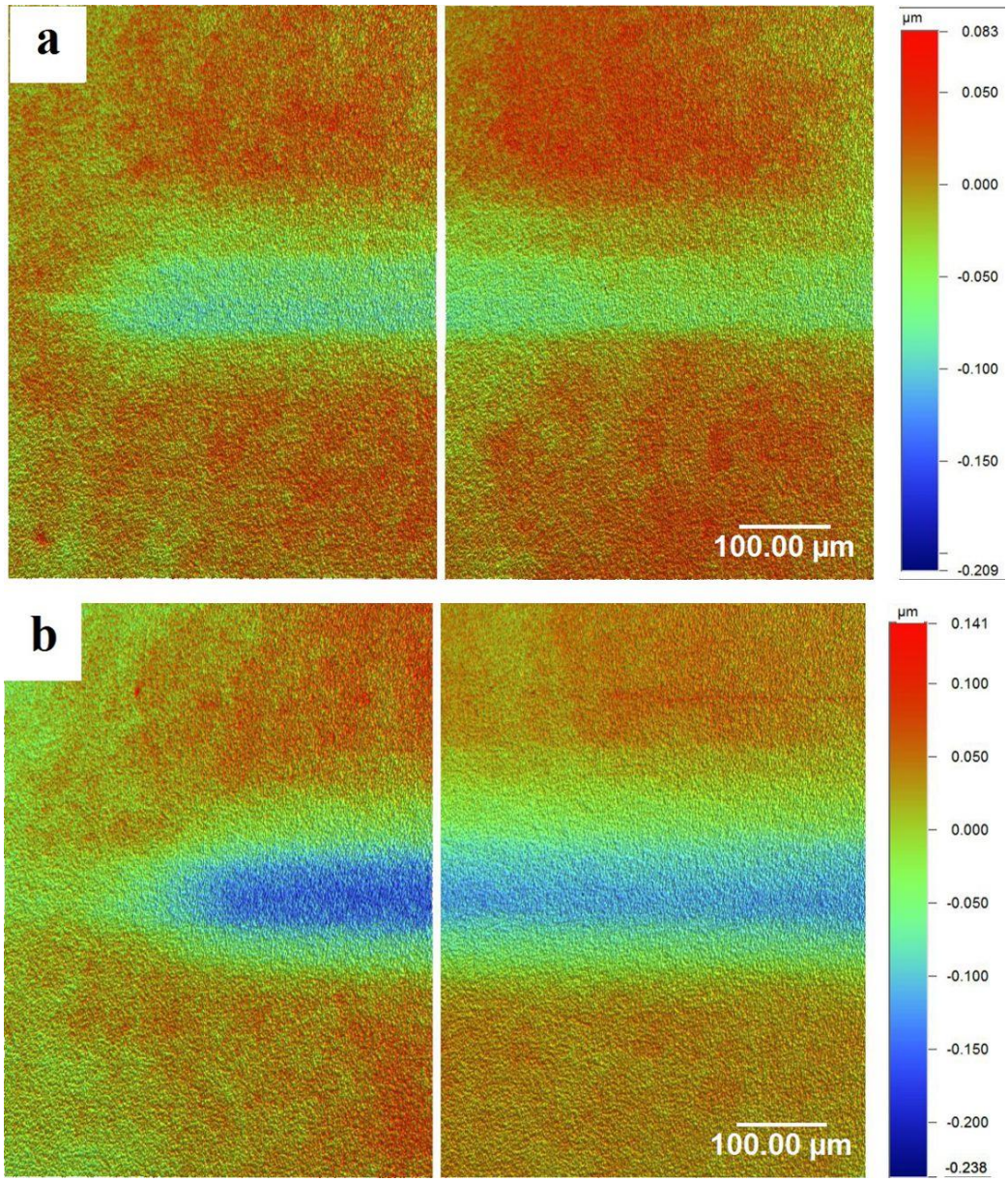

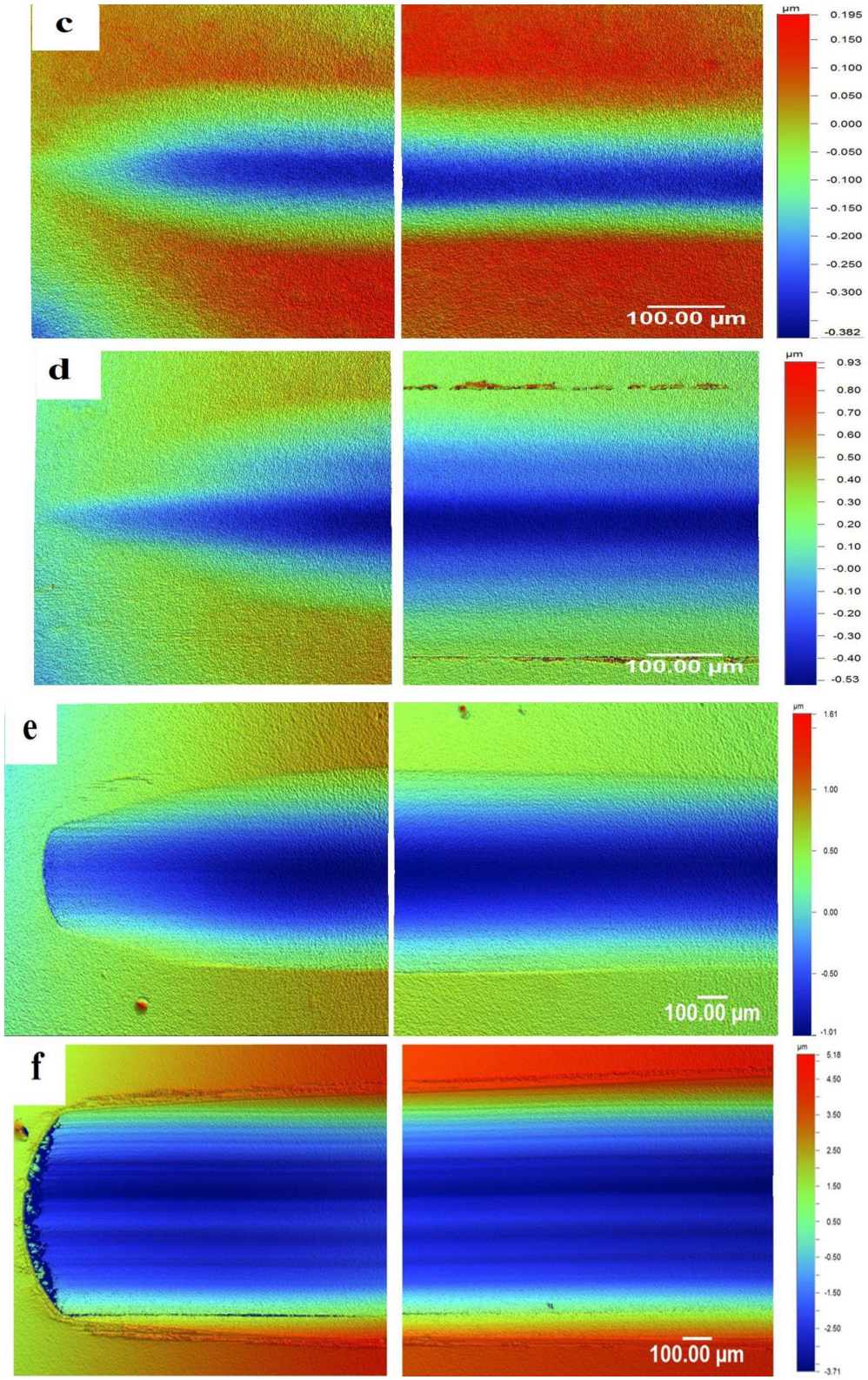

Figure 5.19. Profilometry images of the wear tracks taken by Contour GT at (a) 1 N, (b) 2 N, (c) 4 N, (d) 8 N, (e) 16 N, (f) 32 N for ZTA-additives (1) under lubricated reciprocating wear test for 10 hrs.

5.2.3.2 Worn surface topographic feature by SEM and AFM

The 3D AFM image of the unworn surface that had been immersed in the bovine serum for 10 hrs is shown in Figure 5.20. The occasional and random pitting (white circle) coupled with grooves (white arrow), were the most noticeable surface features at the 1 N and 2 N loads, detected by both SEM and AFM, Figure 5.21(a-b). At these loads, some level of differential wear seemed to exist between grains in some areas. The depth of gain pull outs reached 100 nm in some cases and the deepest observed groove was ~ 20 nm for both 1 N and 2 N. The average Ra within the wear tracks for 1 N and 2 N was ~ 4.3 nm and ~ 3 nm, respectively. In Figure 5.21 (a-b), the 3D AFM images of 1 N and 2 N, marked by a white rectangle and a red circle respectively shows the formation of a layer on the surface. SEM micrographs of the 2 N track are good examples in showing the effect of pre-existing defects (blue circle) on the initiation and propagation of a crack (white arrows), Figure 5. 21(b). Also, the formation of a groove on one side of the crack indicates the release of a particle from this region resulting in the 3rd body abrasion and formation of grooves (red arrows).

At 4 N, no trace of grooves was observed, neither by SEM nor AFM, though the spread of grain pull out was evident across the surface, Figure 5.21(c). The continuous grain pull out, which is more like the formation of a crack, is shown by black rectangles in 2D and 3D AFM images. Similar to the ZTA specimen, the presence of "cleavage fracture" and chipping mainly on alumina grains was visible. Also, the intergranular crack propagating along the outline of the elongated grain (red arrows) and the formation of the transgranular crack on its neighbouring grain (red arrow) can be observed. The presence of the pre-existing defect was also noticeable which did not display any sign of the crack initiation like the one observed at 2 N. The deepest grain pull out (red arrow) observed by AFM had a depth of ~70 nm and the average Ra in this wear scar reached ~ 2.9 nm. The 3D and 2D AFM images in Figure 5.21(c) (white rectangle) showed ~14 nm height difference of the zirconia grain with its adjacent grains. A layer that covered the surface could also be detected and its height changed between 2-5 nm.

Unlike the 4 N track, a few random grooves were observed at 8 N, Figure 5.21 (d). The pitting and chipping features of the surface were similar to 4 N. The 3D view of this wear scar exhibited the height difference between adjacent grains (red circles). The marked region (white rectangle) in Figure 5.21 (d) showed the grain relief of around 20 nm between the elongated grain and its neighbouring grains. This height difference is not necessarily due to the differential wear and might

have other origins that will be discussed in chapter 6. The schematic of the height fluctuation profile is given in Figure 5.21(d). The calculated average Ra of this scar was ~2.5 nm which displayed limited pitting in an otherwise smooth surface. In general, there was no appreciable difference in worn surface features compared to test at 4 N, which is in line with the corresponding specific wear rate obtained in part 5.2.2.1.

At 16 N, numerous shallow and random grooves were observed by SEM and AFM, Figure 5.21(e). An identifiable difference between this load and the previous one was the formation of the compacted wear debris (red rectangle) within the large pits or the loosely deposited debris (white rectangle) on top of the grains, Figure 5.21(e). The 3D AFM image showed that the height of the piled-up debris reached ~ 25 nm in some areas (red circle). As these debris accumulations were randomly spread across the surface, it was difficult to decide whether the height difference was due to the deposition of patches or the grain relief between neighbouring grains. The roll-shaped (white circle) feature, formed at this load, was noticeable in the AFM 3D view and this was also reported by other authors. The average Ra for this load was measured to be up to ~ 4 nm.

SEM micrographs of the ZTA-additives (1) specimen showed that, although the amount of pitting, inter/intra granular fracture and chipping was higher, the surface still kept its integrity, even under the 32 N load which is equivalent to ~3977 MPa of Hertzian initial contact pressure, Figure 5.21 (f). Similar to 16 N, compacted debris were noticeable on the surface or within the pits (white circle). At this load, although a large amount of grain pull out (with an average depth of ~ 100 nm) was observed, no grooves were found. The average Ra for this load was ~ 6.7 nm. It is worth mentioning that the accumulation of wear debris detected for this specimen was less than the ZTA and commercial specimens, Figure 5.21 (f).

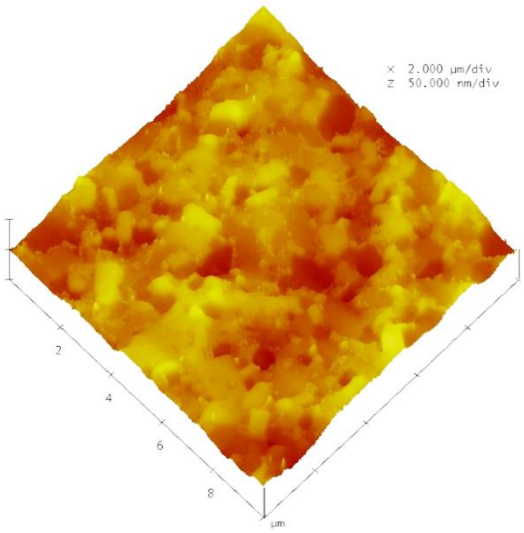

Figure 5.20. AFM image of the unworn surface of ZTA-Additives (1) soaked in 25 vol. % Bovine serum solution.

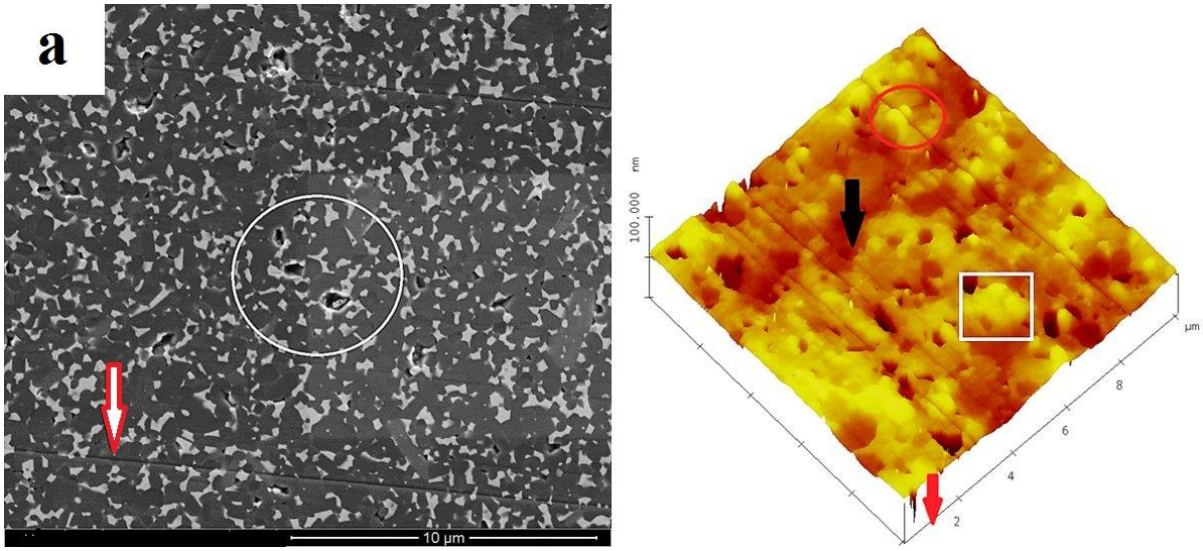

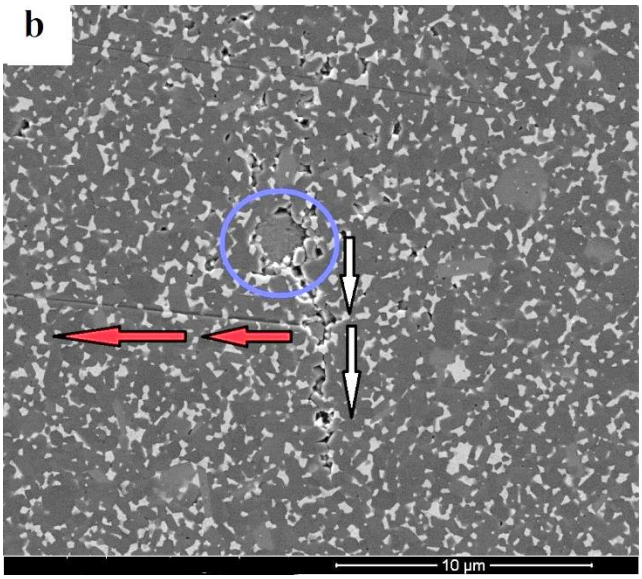
b
10 µm

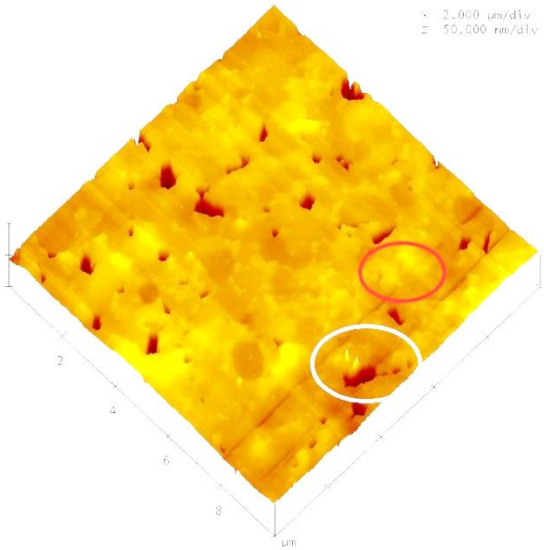
X 2.000 µm/div
Z 50.000 nm/div
µm

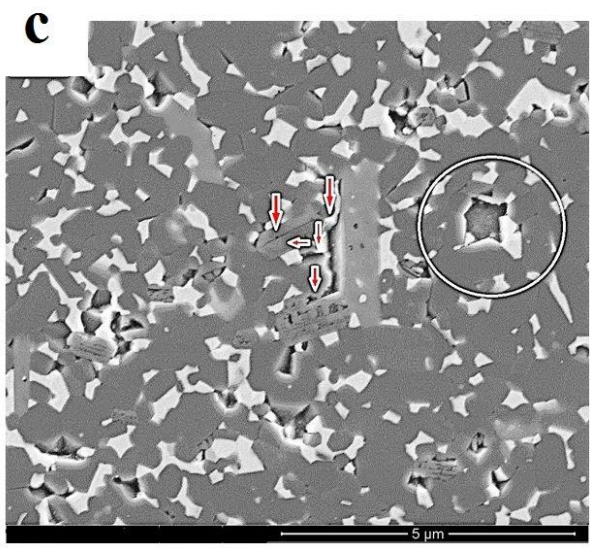
c
5 µm

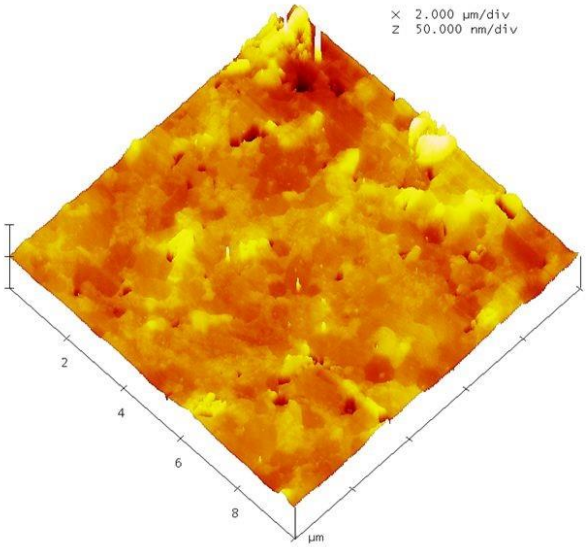
X 2.000 µm/div
Z 50.000 nm/div
µm

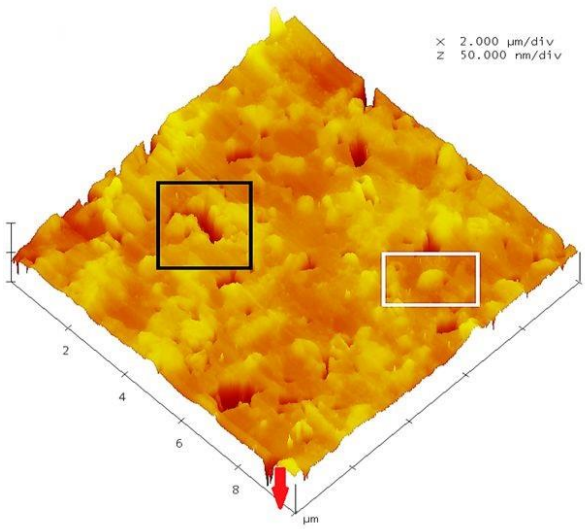
X 2.000 µm/div
Z 50.000 nm/div
µm

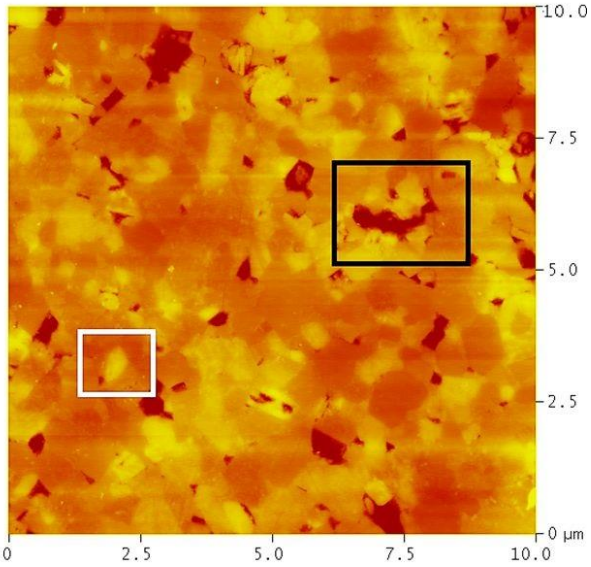
10.0
7.5
5.0
2.5
0 µm
0
2.5
5.0
7.5
10.0

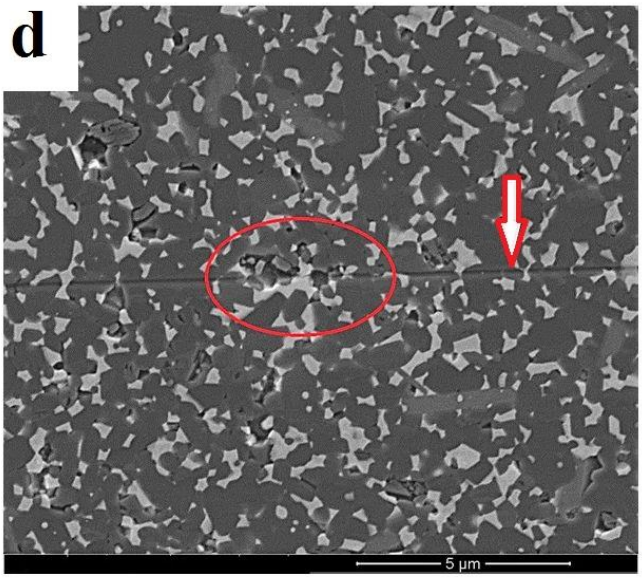

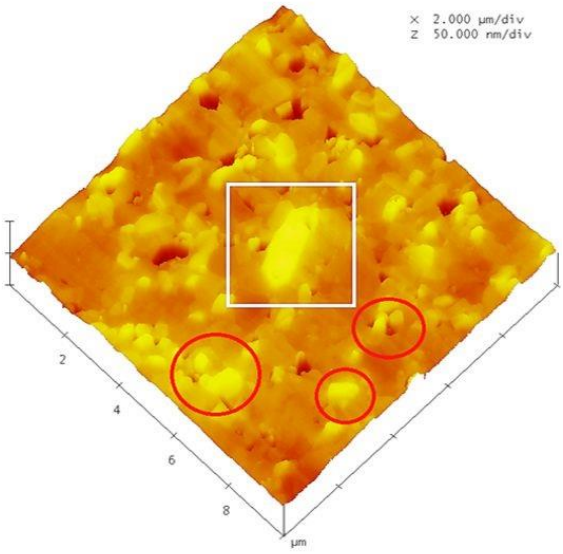

Surface distance	508.30 nm
Horiz distance(L)	507.81 nm
Vert distance	14.780 nm
Surface distance	256.61 nm
Horiz distance	253.91 nm
Vert distance	28.129 nm
Surface distance	234.77 nm
Horiz distance	234.38 nm
Vert distance	10.873 nm

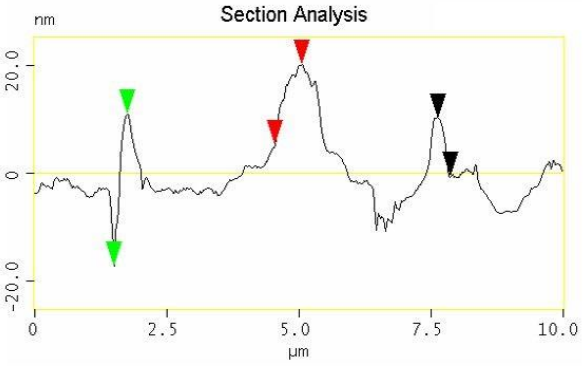

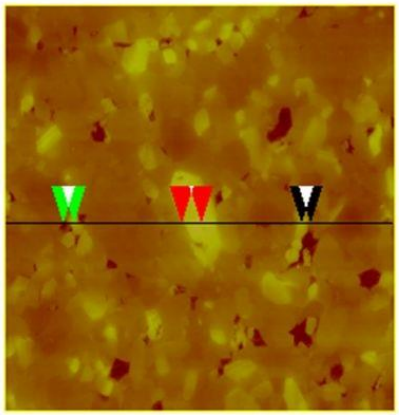

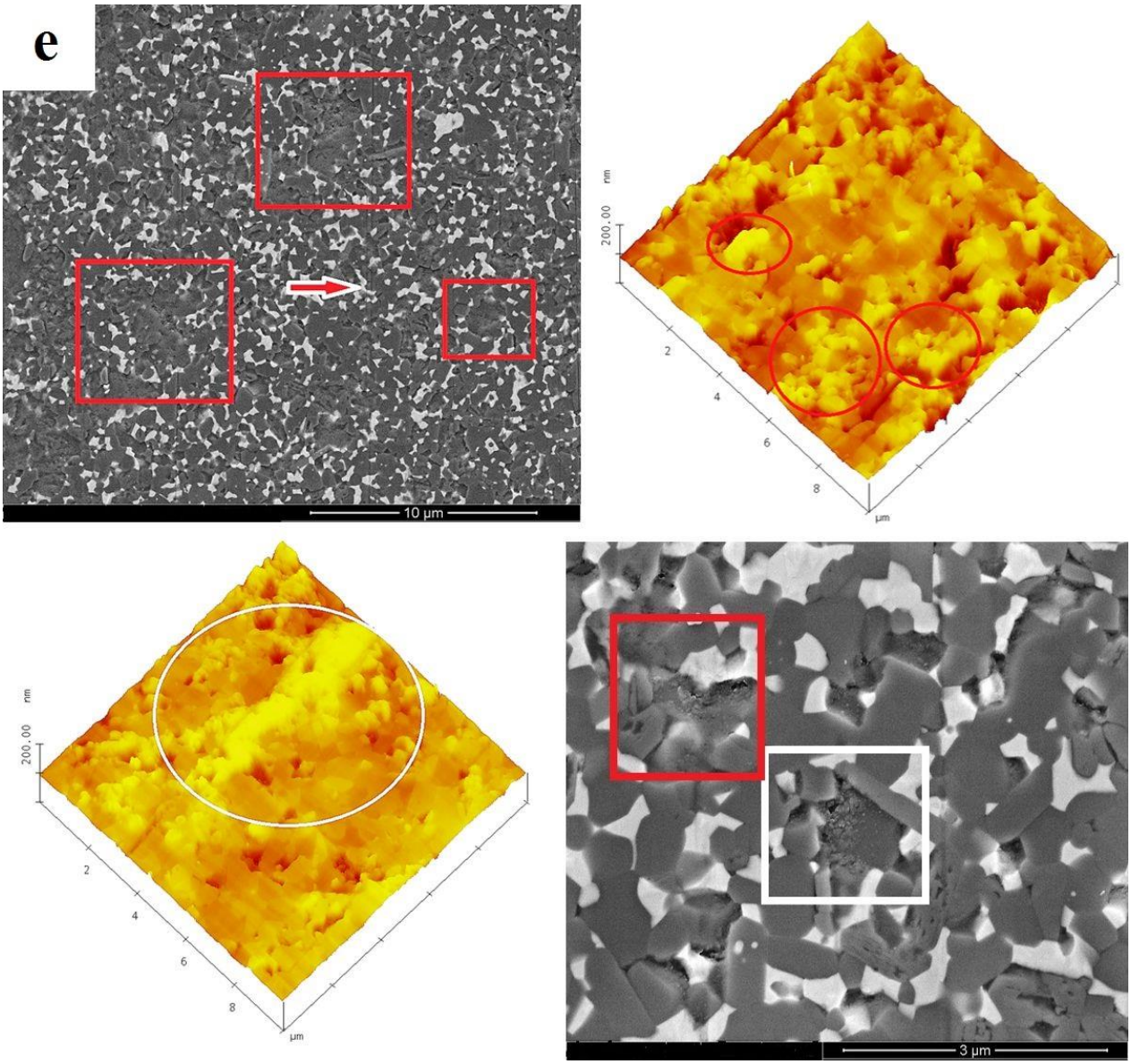
e
10 µm
200.00
nm
2
4
6
8
µm
200.00
nm
2
4
6
8
µm
3 µm

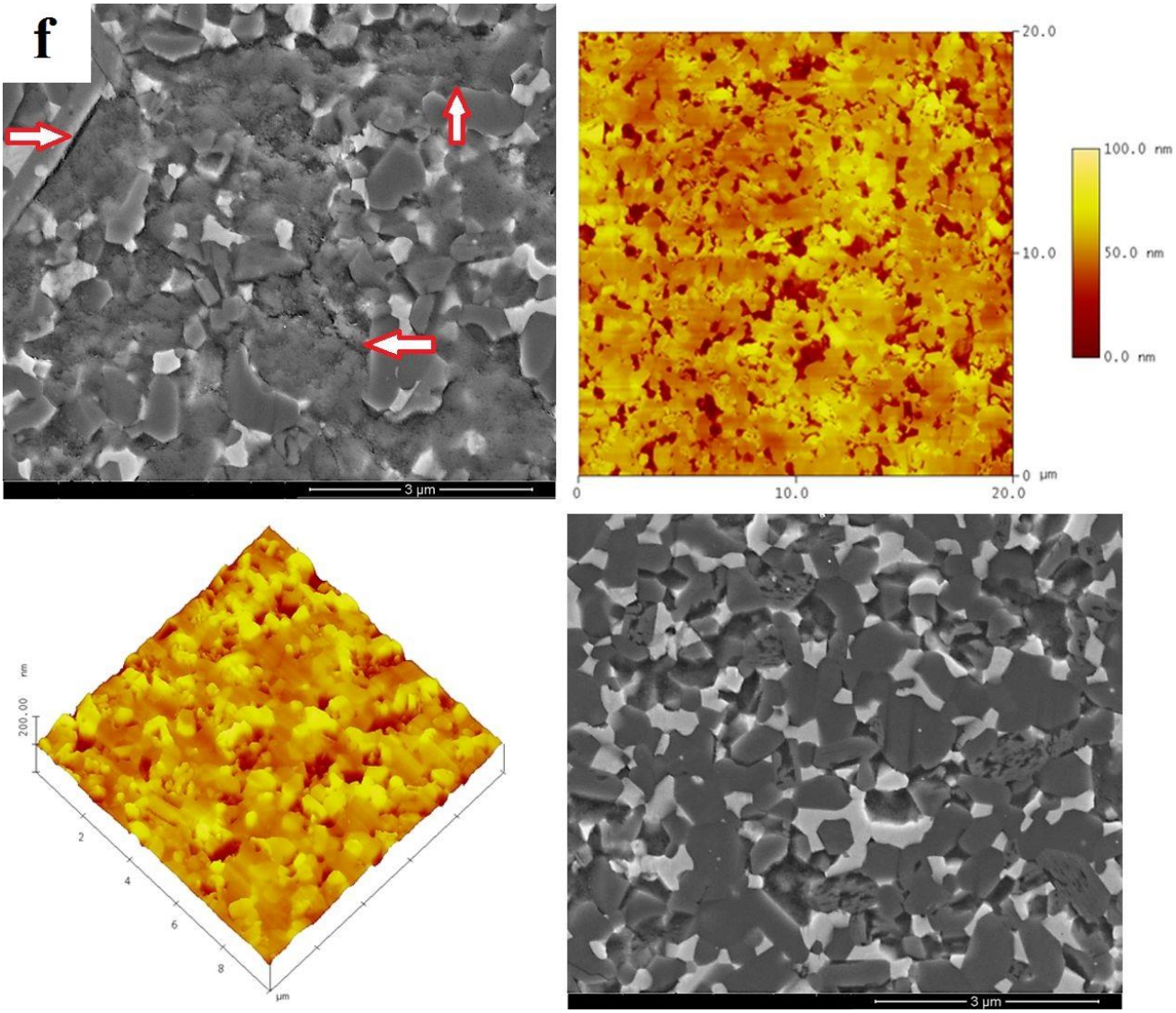

Figure 5.21. SEM and AFM images of ZTA-additives (1) worn surfaces obtained from serum solution lubricated reciprocating wear test under (a).1 N, (b).2 N, (c).4 N, (d).8 N, (e).16 N, (f). 32 N loads, at 600 rpm speed for 10 hrs.

5.2.3.3 Phase changes of the worn surface by Raman spectroscopy

For both ZTA and ZTA-additives, the Raman spectra of from worn surfaces tested at different loads did not show any appreciable difference, although the test at the highest load was the closest to the starting surface. By increasing the load, the tetragonal phase was expected to transform to the monoclinic phase. However, no sign of phase transformation was observed in any of the tests. All the detected peaks in the ZTA-additives specimen belonged to monolithic alumina and tetragonal zirconia which are labelled "t" and "A", respectively, in Figure 5.22.

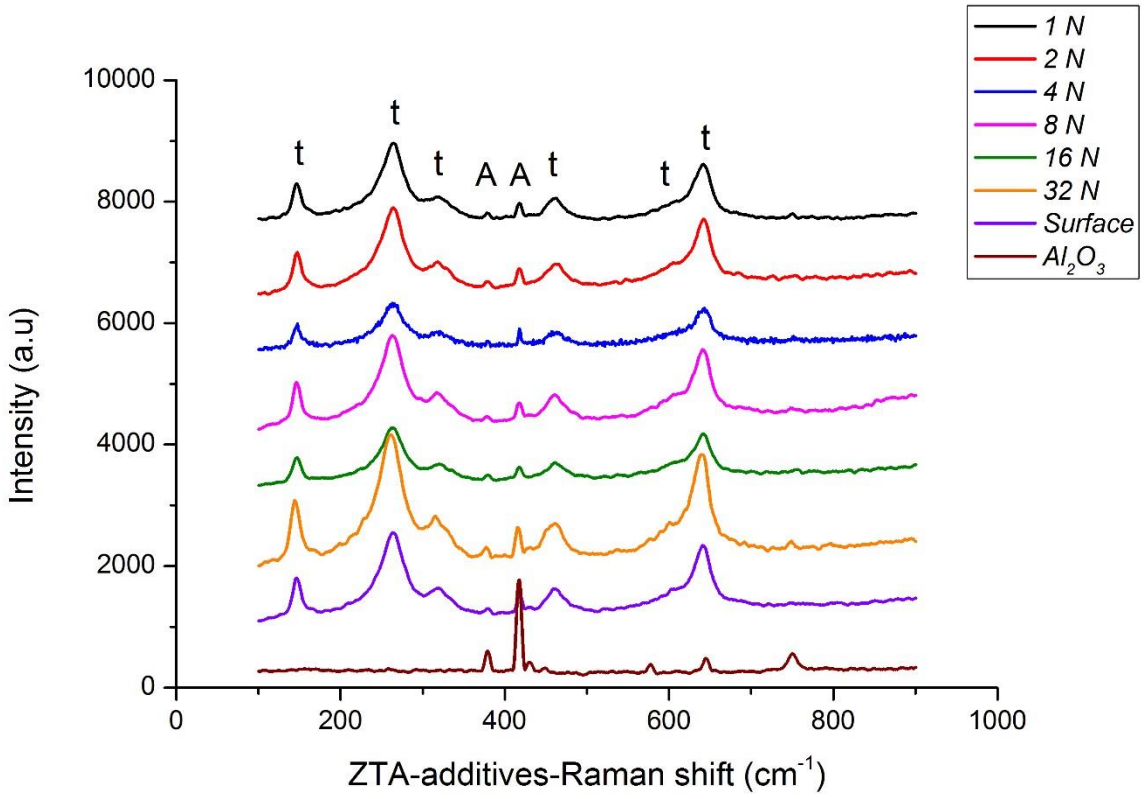

Figure 5.22. Raman spectra of the pure sintered alumina plus spectra of worn and unworn ZTA-additives (1) specimen under 1 N-32 N using lubricated reciprocating wear test.

5.2.4 Characterisation of sub-surface by TEM

The SEM micrograph in Figure 5.23 shows the location chosen to take the TEM cross section out. The TEM overview of the ZTA-additives (1) specimen (worn through lubricated reciprocating wear test, under a load of 8 N) is displayed in Figure 5.24 (a). Figure 5.24 (b) gives a bright field TEM image showing an intra-granular zirconia particle with significant residual strain around the particle in the alumina matrix (white arrow). Some dislocation activity was also observed on the neighbouring alumina grains which extended into a platelet grain below (red arrow). Figure 5.24 (c) shows the corresponding dark field TEM image of the same image. Figures 5.25 shows a few positions in which zirconia grains were standing proud of the surface. These protruding grains were also detected through AFM. The red arrow points to a zirconia grain that exhibits considerable residual strain. Figure 5.26 (a) is the only instance of the monoclinic zirconia found in this specimen. As shown in Figure 5.26 (b), this grain also protruded out of the surface, which is consistent with AFM observations. In Figure 5.26 (c) the white arrows are pointing to the transgranular fractures formed within alumina grains which were located right below the surface. The white arrow in Figure 5.26 (d) shows the grain boundary cracking around the alumina platelet. There were also some dislocations in the neighbouring alumina grain marked by the red arrow. In general, a very limited amount of dislocation activity was observed in this specimen, mainly around the intragranular zirconia, Figure 5.24 (b-c).

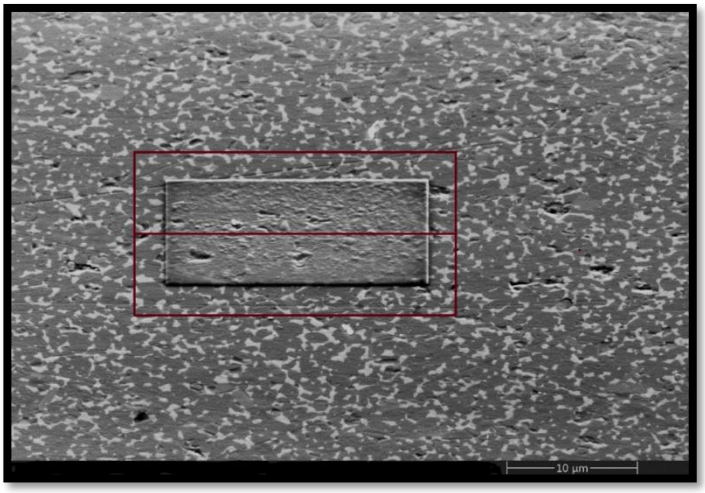

Figure 5.23. The SEM image illustrates the region worn by the lubricated reciprocating wear test under 8 N load for 10 hrs in ZTA-Additives (1). The marked area is extracted by FIB lift-out to prepare the TEM specimen.

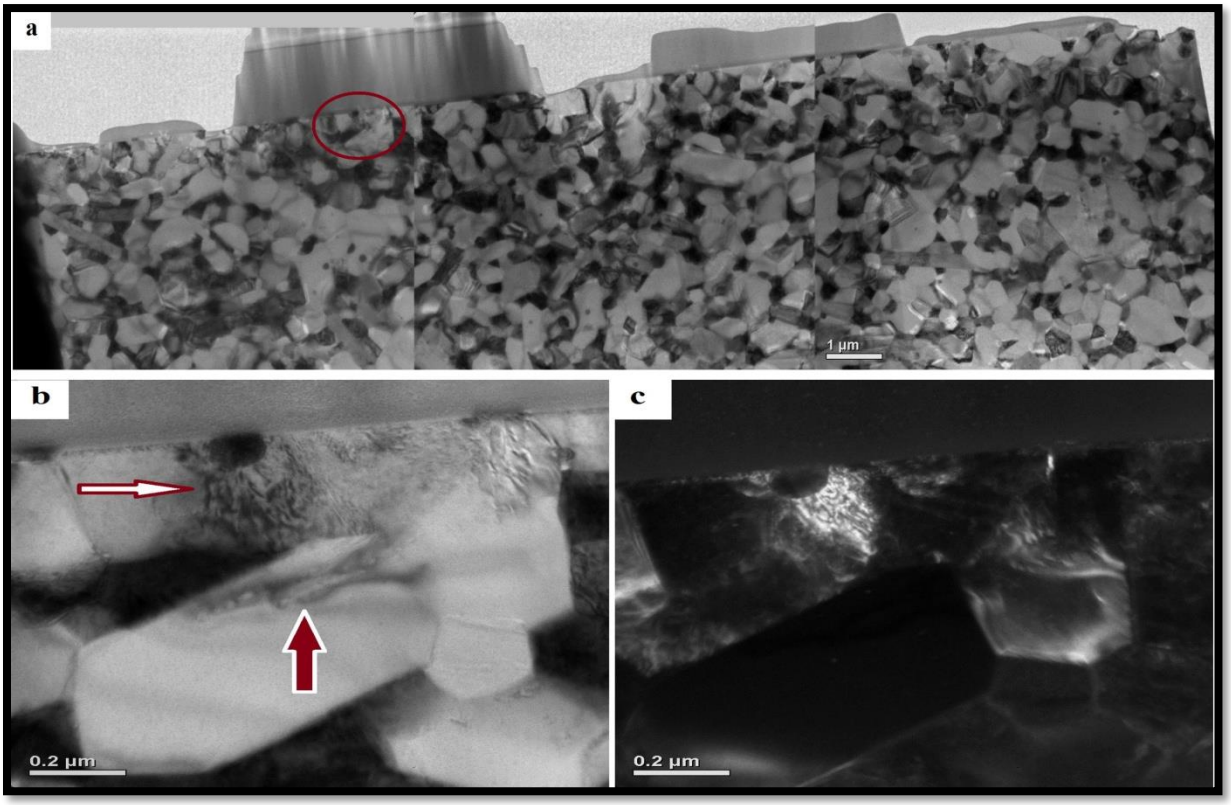

Figure 5.24. (a) Exhibits a subsurface overview of the ZTA-additives (1) (b). Bright field TEM image of the intragranular zirconia produced residual stress within alumina grain (c). The dark field TEM of part (b).

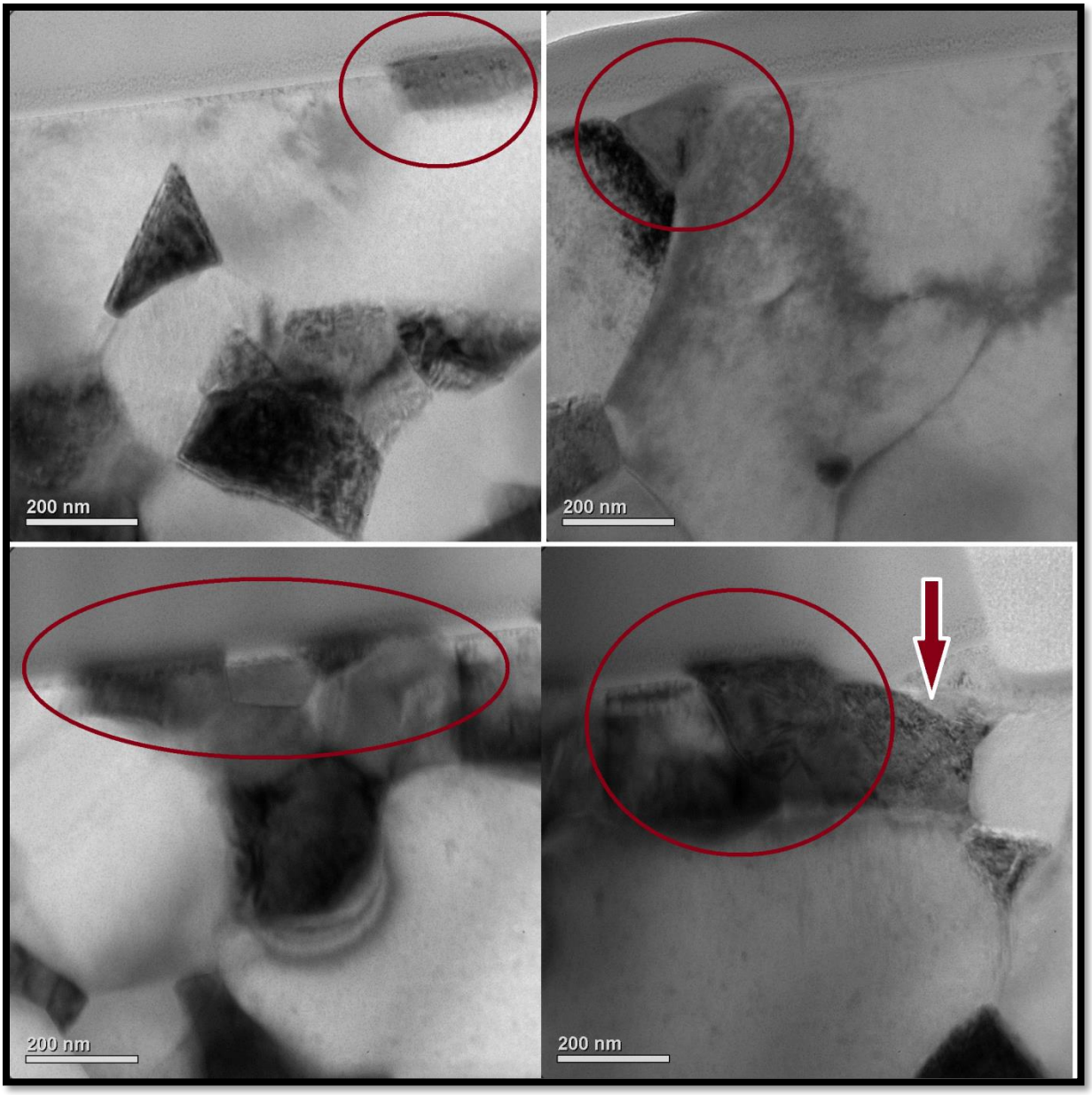

Figure 5.25. TEM images showing various locations in ZTA-Additives (1) foil cross-section in which zirconia grains standing proud of the surface. The red arrow points to the deformation on the zirconia grain.

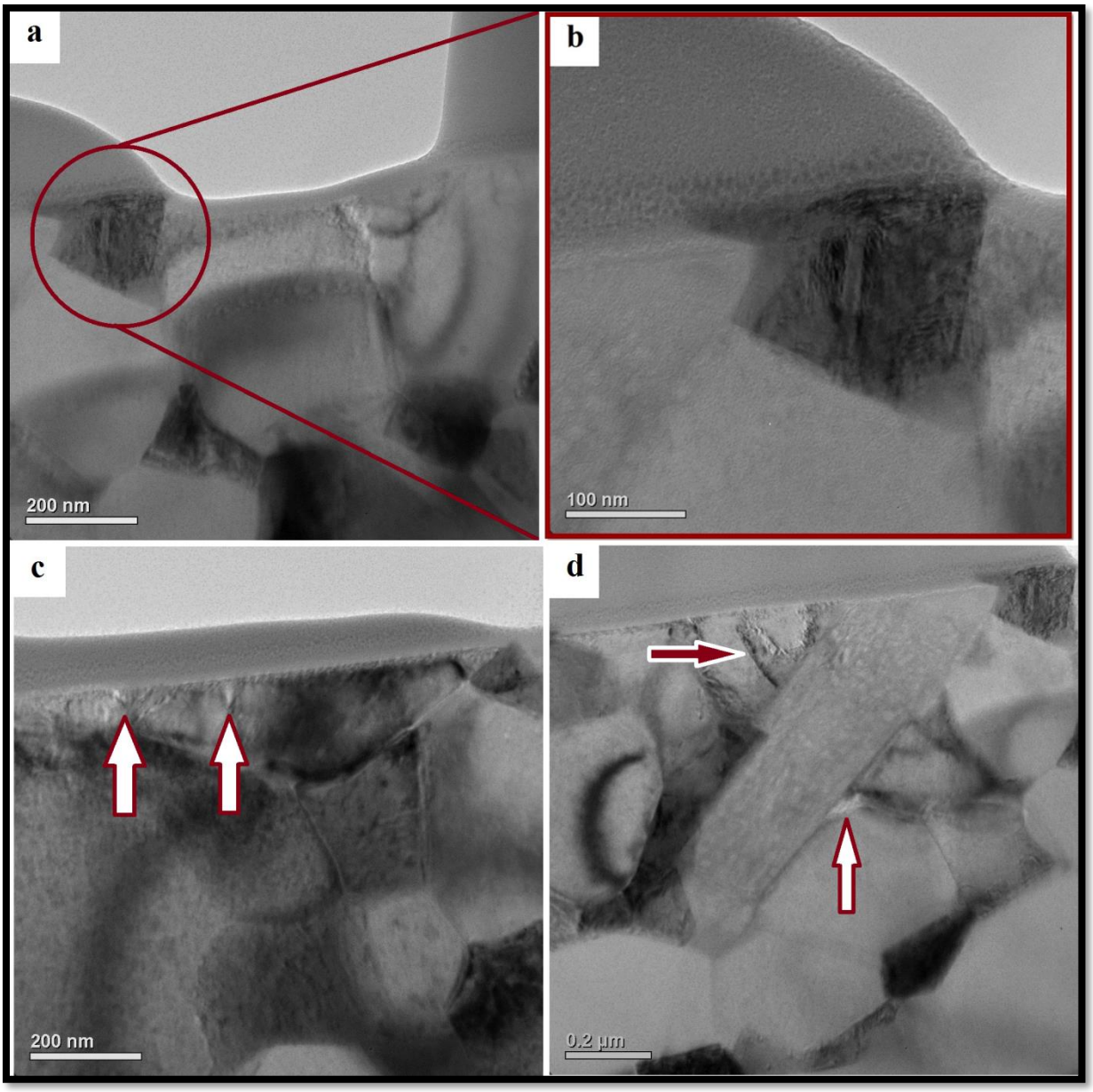

Figure 5.26. (a) Bright field TEM images of the worn surface at 8 N contact load in which (a) shows the location of the only monoclinic zirconia found in the ZTA-additives (1) and (b) gives the magnified image of the martensite transformation in a zirconia grain. (c) The white arrows point to the transgranular fracture on alumina grains. (d) The white arrow shows the grain boundary cracking and the red one points to the dislocation activities on the alumina grain.

Figure 5.27 (a) shows a low magnification bright field TEM image of the specimen extracted from the ZTA-additives (2) sample in which the exact position of the alumina grain containing the dislocation features is specified. Since the deformation caused by the residual stress during the wear test appeared mainly at the outermost grain layer (just below the coating), the appearance of the single deformed grain, marked in Figure 5.27 (b), is probably not a result of the wear process. Rather, it was most probably a result of the thermal expansion mismatch between zirconia and alumina which resulted in sufficient stress in the alumina to form a dislocation structure, as seen by Valle et al. [233]. Figure 5.27 (c) gives the corresponding dark field TEM image. As shown in Figure 5.28, formation of residual stresses around the intragranular zirconia, within the alumina matrix, is obvious, regardless of their position in the composite. However, as shown in Figure 5.24 (b-c), the residual strain was the most around intragranular zirconia, which was inevitably intensified due to the contact pressure during the sliding wear.

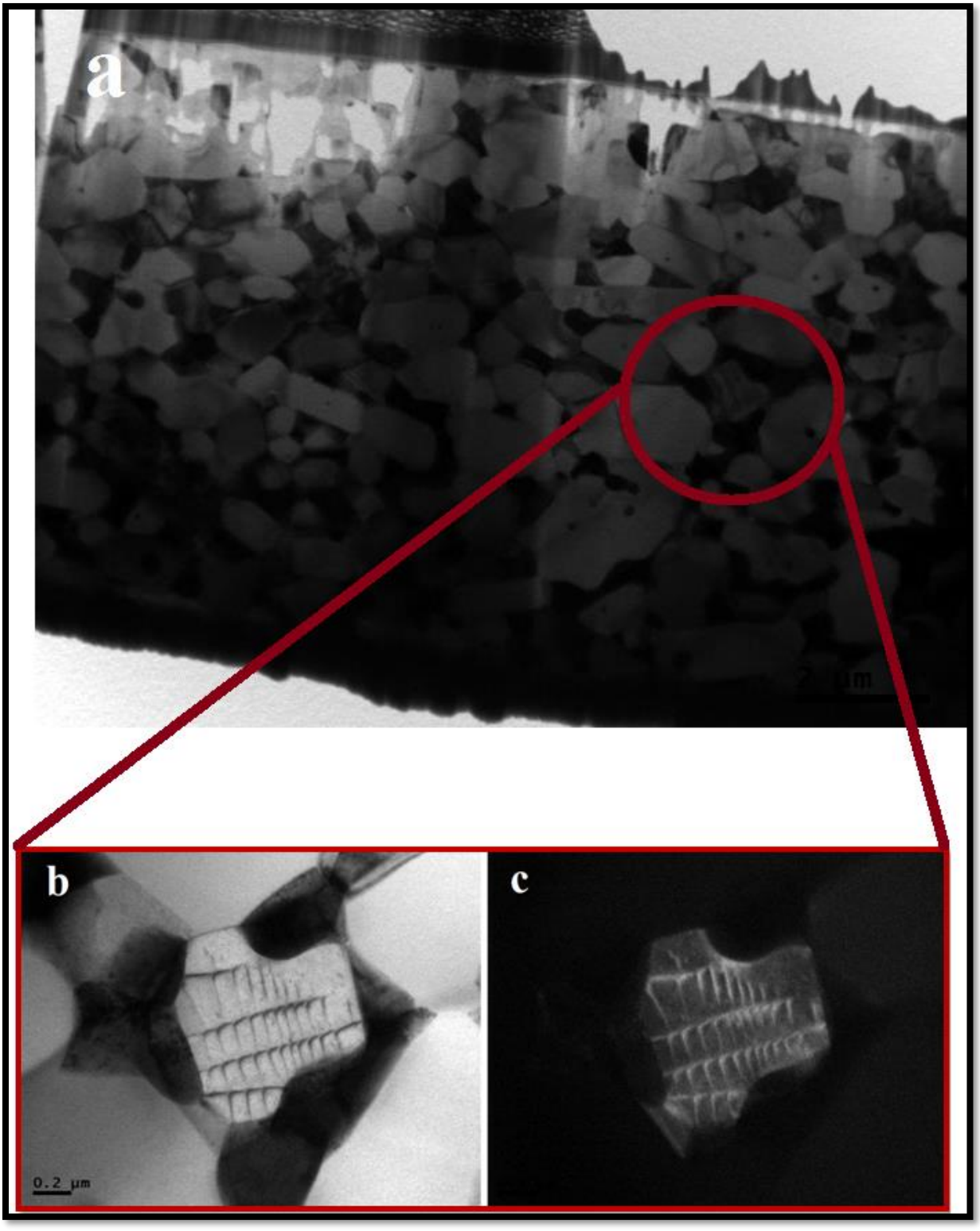

Figure 5.27. (a) Subsurface overview of the ZTA-additives (2) worn under 8 N contact stress. The marked section shows (b) the bright field TEM image of the dislocation activity on the alumina grain and (c) shows the dark field TEM image of part (b).

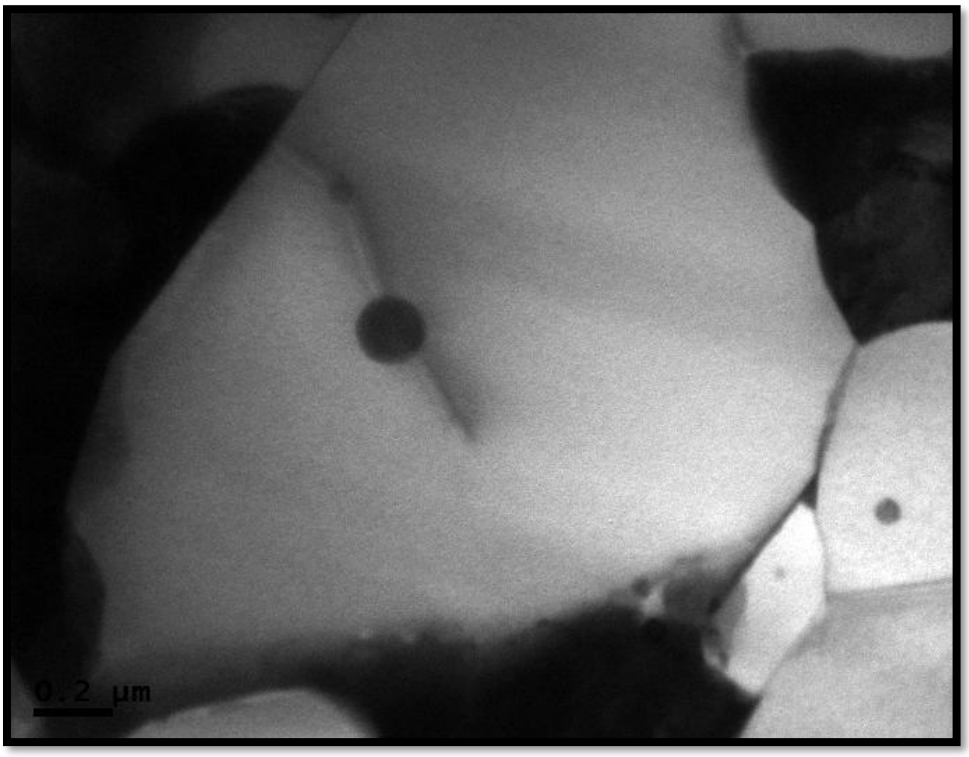

Figure 5.28. The TEM bright field image of ZTA-Additives (2) showing the residual stress around intragranular zirconia grain.

5.3 BIOLOX® delta (Commercial) lubricated with 25 vol. % new-born calf serum solution

5.3.1 Lubrication regime definition

Figure 5.29 shows the behaviour of the friction coefficient as a function of time at various loads for the commercial sample. The "running in" period for 1 N, 2 N, 4 N, 8 N, 16 N and 32 N was estimated to be ~7 min, ~9 min, ~3.5 min, ~22 min, ~21 min and ~ 42 min, respectively. Although the "running in" period for this sample was accompanied by severe fluctuations in the COF, the steady state part was reasonably stable throughout the experiment. As tabulated in Table 5.4, the average COF values obtained for 1 N and 32 N were 0.15 ± 0.04 and 0.15 ± 0.03, respectively. These are the maximum recorded average of the COF in the commercial specimen. The average COF of 0.03 ± 0.02 was the minimum value for this specimen, which was obtained at 2 N.

The Stribeck curve is given in Figure 5.30. It would appear that 1 N and 2 N were run in the full film lubrication regime, while at 8 N, 16 N and 32 N were presumably in the mixed lubrication mode, although more data points would be required to confirm this. Ignoring the average COF value at the 4 N test, the rest of the points fit fairly well into the classical Stribeck curve.

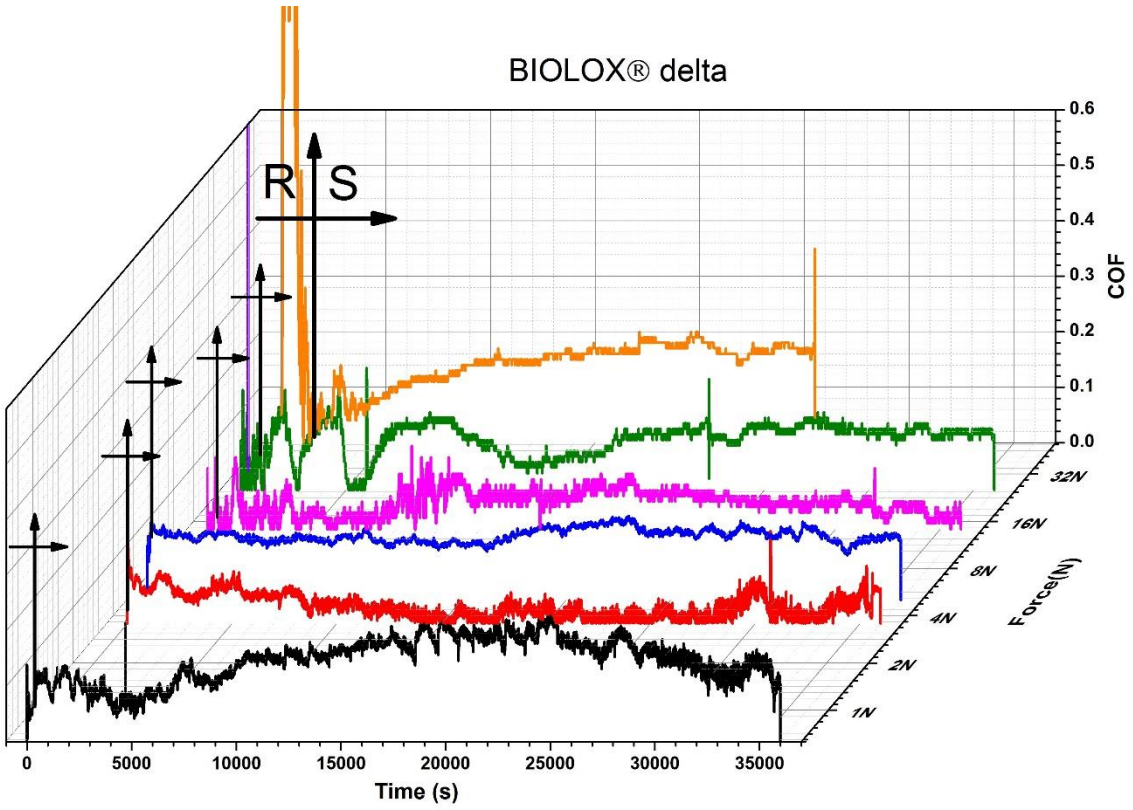

Figure 5.29. 3D illustration of COF Vs time in BIOLOX® delta at different loads tested in 25 vol.% Bovine serum at 600 rpm for 10 hrs.

Table 5.4. Summary of the average COF corresponding to the equivalent load in the commercial specimen

Force (N)	Coefficient of friction	Summerfeld (Z)
1N	0.15±0.04	2.4E-04
2N	0.03±0.02	1.2E-04
4N	0.12±0.01	6.0E-05
8N	0.05±0.02	3.0E-05
16N	0.09±0.03	1.5E-05
32N	0.15±0.03	7.5E-06

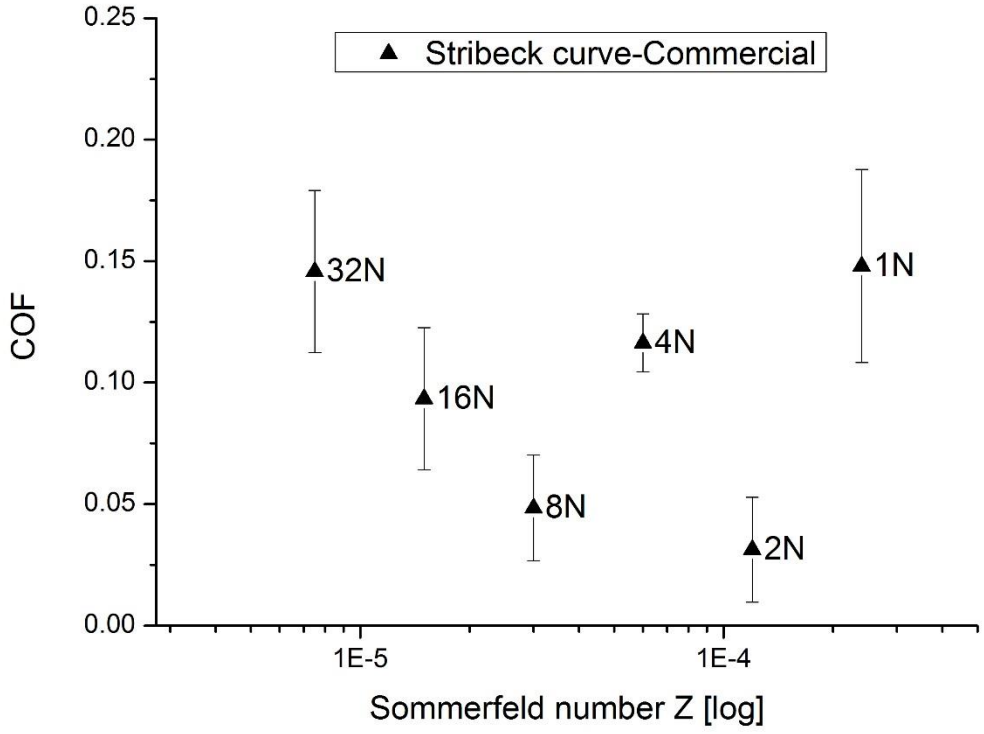

Figure 5.30. Stribeck curve for BIOLOX® delta in 25 vol. % Bovine serum lubricated wear test.

5.3.2 Wear behaviour

5.3.2.1 Specific wear rate

For the BIOLOX® delta, the calculated specific wear rates for the 1 N and 2 N loads were $4.89\times 10^{-9} \pm 1.93\times10^{-9}$ mm^3/Nm and $4.25\times10^{-9} \pm 1.28\times10^{-9}$ mm^3/Nm respectively, Figure 5.31. In contrast to the ZTA-additives and similar to the ZTA, the specific wear rates of BIOLOX® delta under 1 N and 2 N loads were in the order of 10^{-9} mm^3/Nm. As mentioned in part 5.2.2.1, measurement of the volume loss and the corresponding specific wear rate was not accurate at low loads, because of the shallow depths and undefined shape of the wear tracks.

As shown in Figure 5.31, the specific wear rates at 4 N and 8 N were almost the same, and this value was about one order of magnitude greater than 1 N and 2 N. At 16 N the specific wear rate increased to $1.53\times 10^{-7} \pm 2.85 \times 10^{-8}$ mm^3/Nm. Finally, at 32 N, equivalent to ~3976 MPa initial Hertzian contact pressure, the calculated specific wear rate was $4.68\times 10^{-7} \pm 6.01 \times 10^{-8}$ mm^3/Nm.

This was the same order of magnitude as in the case of the ZTA-additives (1) specimen, but about one order of magnitude less than ZTA.

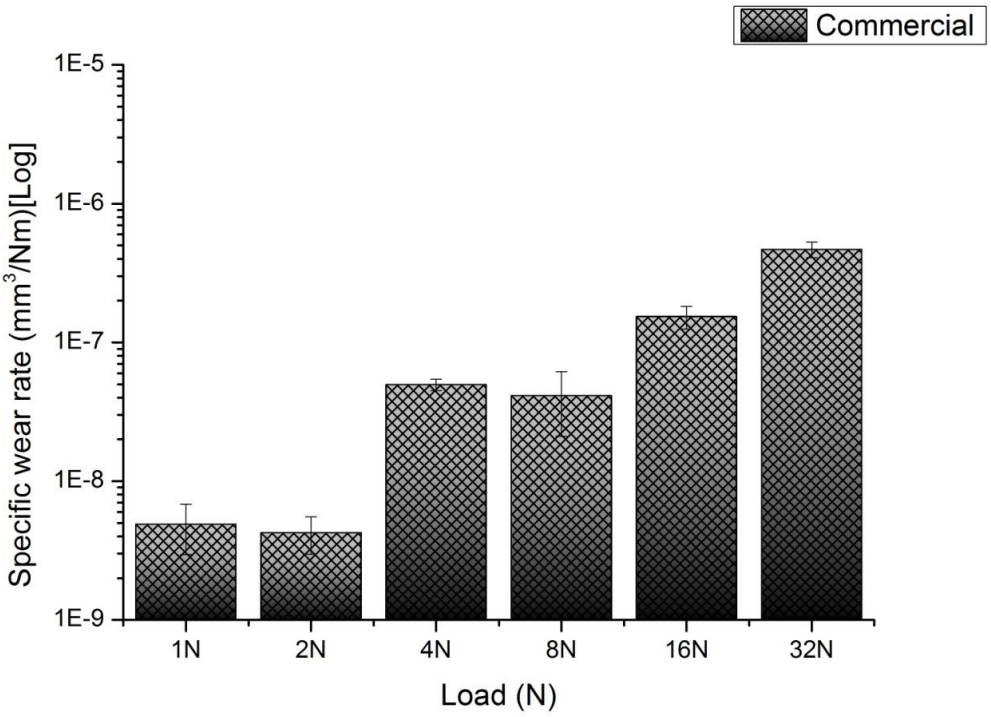

Figure 5.31. Specific wear rate of BIOLOX® delta using 25 vol. % Bovine serum solution lubrication.

5.3.3 Characterisation of worn surface

5.3.3.1 General surface morphology by Contour GT

The Contour GT optical profiles for different loads ranging between 1 N - 32 N are displayed in Figures 5.32 (a-f). It can be seen that at 1 N there was a little change in the morphology of the surface compared to the starting surface, Figure 5.32 (a). The difference between the worn surface and the neighbouring unworn area was more distinguishable at 2 N, where the amount of volume loss slightly increased, Figure 5.32 (b). The wear scars became continually deeper and wider as the contact load increased. At 4 N the wear track transformed to a more defined region compared to the 1 N and 2 N tests, though no trace of wear debris were evident, Figure 5.32 (c). At 8 N a few parallel grooves were evident inside the wear track and a small amount of debris was detected at the edges, Figure 5.32 (d). The volume loss at this load was about three times more than the 4 N track. At 16 N, the highest volume loss occurred and the presence of wear debris along the scar

and trailing edges were more apparent, Figure 5.32 (e). Under the 32 N load, the largest change in terms of the width and depth was observed. Also, the volume loss increased dramatically and reached a value about four times more than the previous load, Figure 5.32 (f).

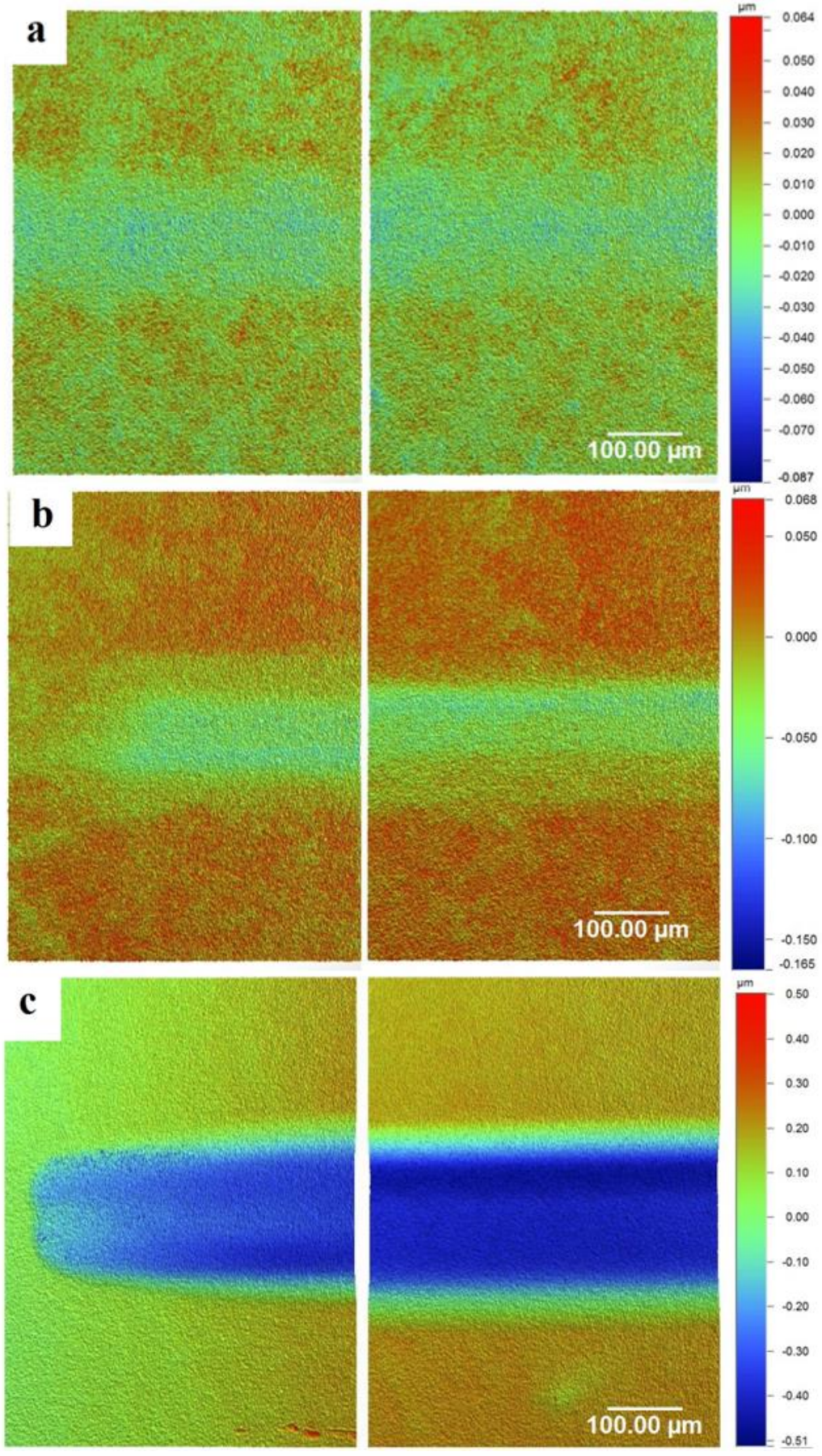
a
100.00 µm
µm
0.064
0.050
0.040
0.030
0.020
0.010
0.000
-0.010
-0.020
-0.030
-0.040
-0.050
-0.060
-0.070
-0.087
b
100.00 µm
µm
0.068
0.050
0.000
-0.050
-0.100
-0.150
-0.165
c
100.00 µm
µm
0.50
0.40
0.30
0.20
0.10
0.00
-0.10
-0.20
-0.30
-0.40
-0.51

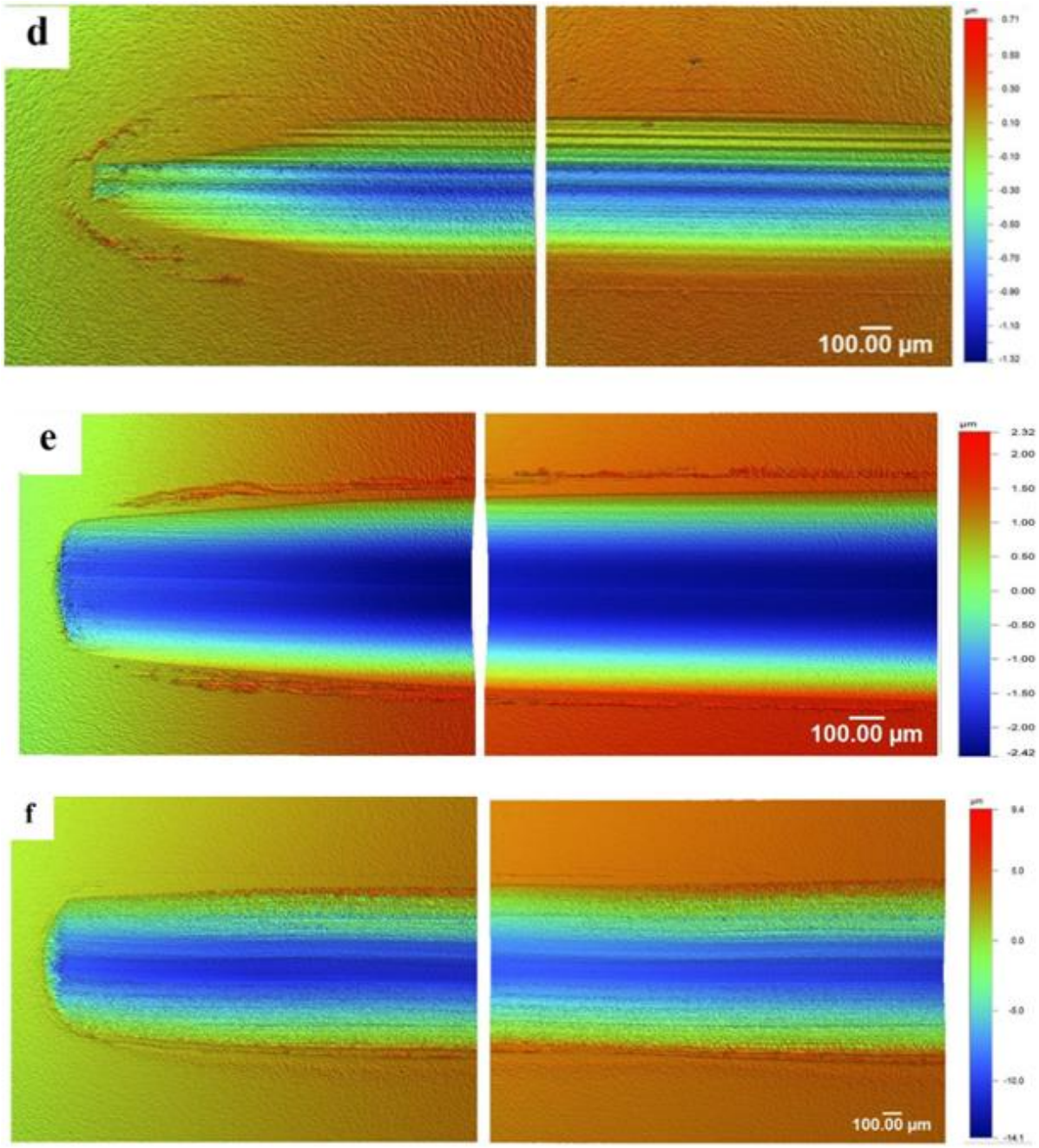

Figure 5.32. Profilometry images of the wear tracks taken by Contour GT at (a) 1 N, (b) 2 N, (c) 4 N, (d) 8 N, (e) 16 N, (f) 32 N for BIOLOX® delta under lubricated reciprocating wear test during 10 hrs.

5.3.3.2. Worn surface topographic feature by SEM and AFM

The 3D AFM image of the unworn surface is given in Figure 5.33. At 1 N, the surface was filled with grooves with various depths and widths which were located in close vicinity of each other, Figure 5.34 (a). Also noticeable was the increased number of the grooves in this specimen, compared to the ZTA and ZTA-Additives at the same load. Besides, the depth of the grooves (red arrows) and grain pull outs (white circle) reached ~100 nm and ~200 nm, respectively, which were much larger values compared to the other specimens, Figure 5.34 (a). Also evident was the trapped wear debris inside the grooves (white arrows). The average Ra for this load reached ~3.7 nm.

However, at 2 N the large pits (white rectangle) were the most predominant and noticeable features of the surface, Figure 5.34 (b). These pits were possibly the results of a few large interconnected grain pull outs, amounting to a highest observed depth of 200 nm. The 3D AFM image showed a large and deep void in which a very small fraction of the grains remained (red circle). In addition to grain pull outs, random and scattered grooves (white arrow, AFM) were observed across the surface, with a depth of 50 nm and the average Ra at this load was measured to be up ~ 5.2 nm. The SEM micrograph in Figure 5.34 (b) shows the grains that have lost their supporting neighbours and were about to be liberated (white circle). The red arrow in the same micrograph points to a groove, sourced from the large pitting, which is indicative of a 3rd body abrasion.

At 4 N, chipping was quite explicit on both alumina (white arrow) and zirconia grains (red arrow) in the SEM micrograph, Figure 5.34 (c). However, neither cleavage fracture nor chipping was observed on zirconia grains of other specimens at this load. No grooves were evident by either SEM or AFM, though the 3D view revealed grain relief next to the small void (red circle). Also evident was the intergranular crack that presumably originated from a grain pull out and was stopped after travelling along two grains (white arrow, AFM), Figure 5.34 (c). The blue arrow in the same micrograph points to the small fragments and debris trapped inside the pits. The average Ra of ~ 5.2 nm was measured for this load.

The SEM micrograph in Figure 5.34 (d) for the test at 8 N exhibited more severe chipping in the alumina grains than at 4 N (white arrow). Also visible was a transgranular crack which had propagated through an alumina grain (red circle) and also a few fragments which were confined inside the pits (white arrow). The AFM height image at the same load exposed some traces of

grooves on the grains. In some regions, grain pull out seemed quite deep, ~ 130 nm, while in other areas, it appeared that only the top layer of the surface was removed. Also, there were numerous grains that stood proud of the surface and their height reached 24 nm (white and black circles). The measured average Ra in this scar reached 14 nm, which is quite different with the Ra of the same load in the other specimens.

At 16 N, chipping and transgranular fracture on both zirconia and alumina grains were conspicuous (white arrow), Figure 5.34 (e). Also, compacted debris was detected inside the pits (red circle, SEM micrograph), as well as a grain pull out with a depth of ~ 54 nm, along with grooves with a depth of ~ 23 nm.

Under 32 N, the surface was broken and had lost integrity in some regions, Figure 5.34 (f). Also noticeable was the formation of a thick surface layer in some regions, presumably due to the accumulation of debris and possibly proteinaceous species. As marked in Figure 5.34 (f), a few cracks existed on the aforementioned layer. Similar to 16 N, the pilled-up areas of debris were evident on the worn surface, as well as inside the pitted areas. The 3D view of this track showed that the thicknesses of these layers and the average Ra were ~ 30 nm and ~10 nm, respectively.

The SEM microstructure in Figure 5.34 (f) is divided into three sections. The first section shows the boundary region of the 32 N scar and the accumulation of wear debris. Region 2 shows the part of the wear tack which appeared to be untouched, as no pitting and grooves were visible in this region. However, there was a surface layer on the unworn surface region, marked by a black rectangle, which was presumably an accumulation of wear debris. Region 3 exhibited severe wear. The height AFM image also shows the difference in the surface morphology of the adjacent regions at 32 N, Figure 5.34 (f).

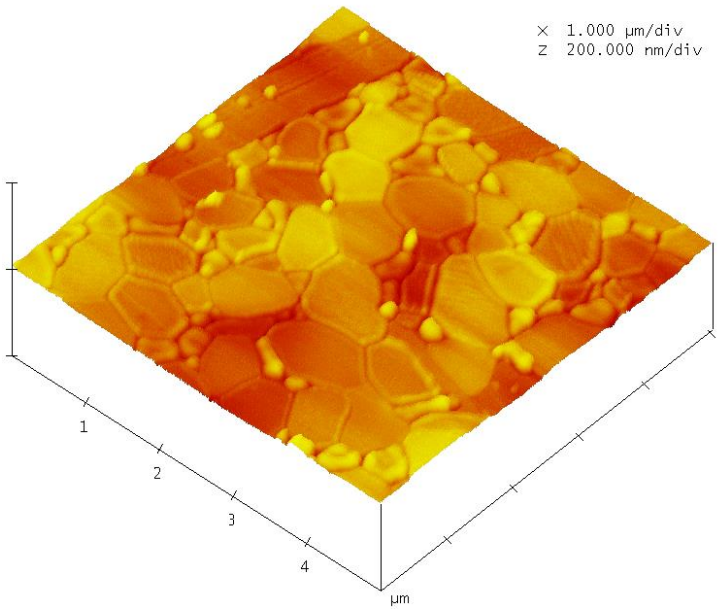

Figure 5.33. AFM image of the unworn surface in the BIOLOX® delta.

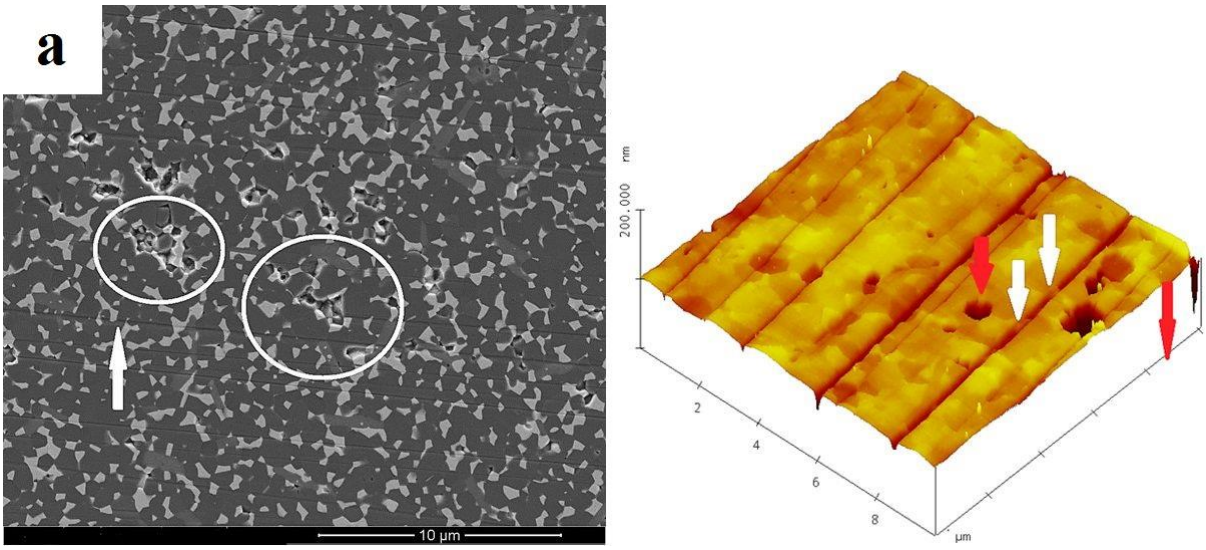

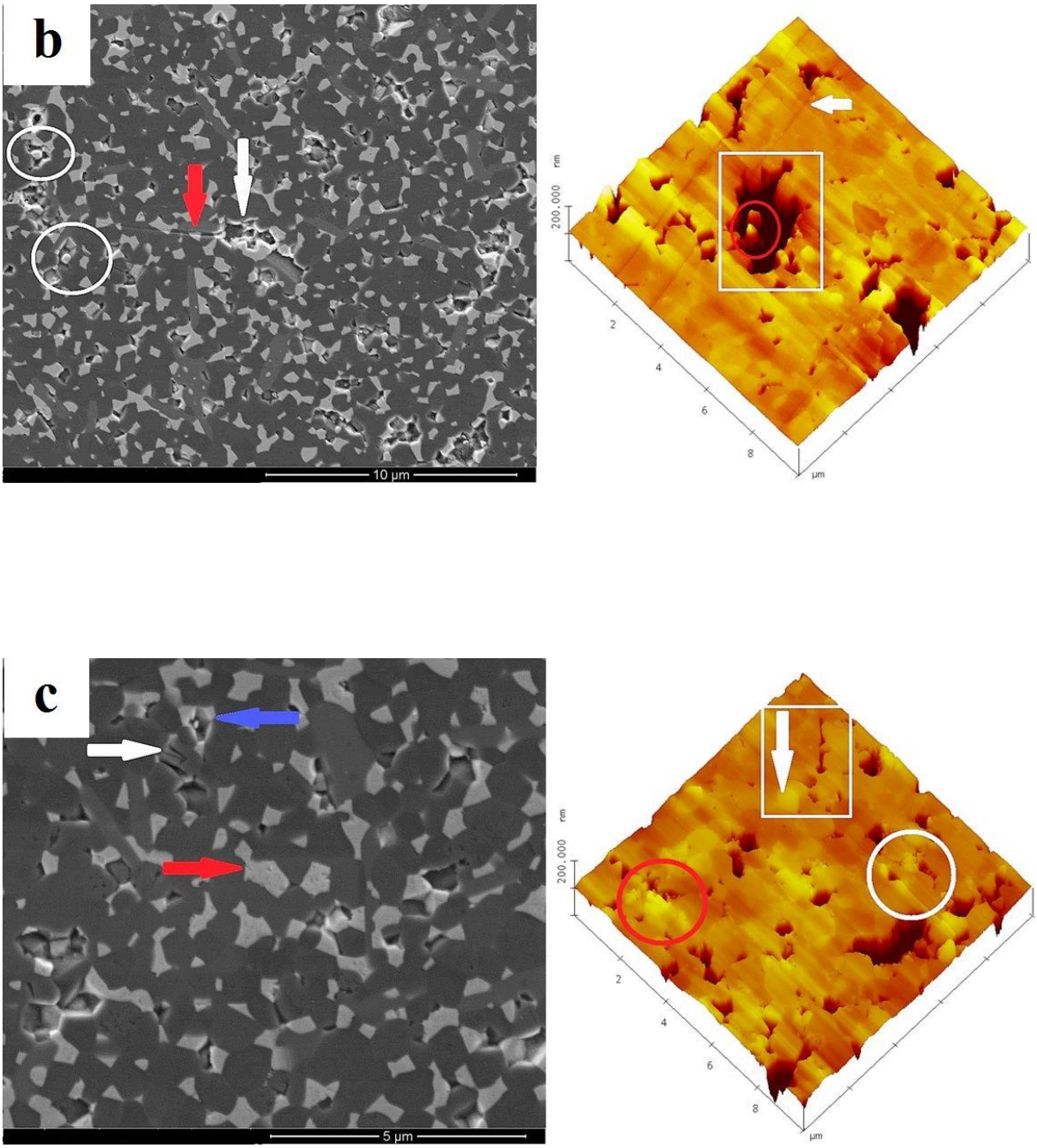
b
10 µm
200.000
nm
2
4
6
8
µm
c
5 µm
200.000
nm
2
4
6
8
µm

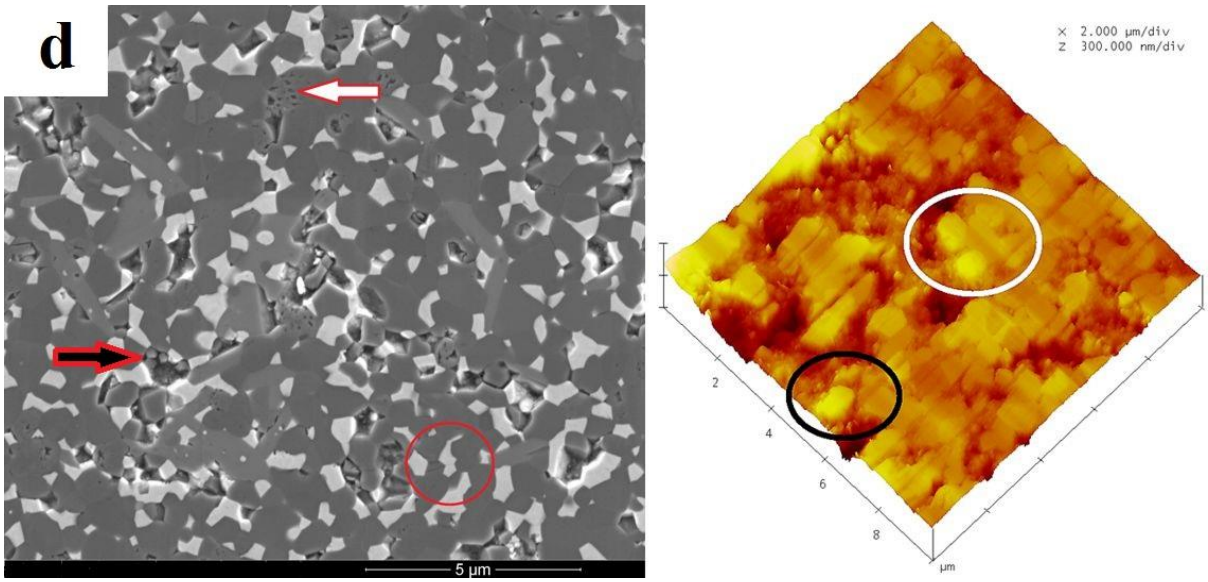
d
5 µm
X 2.000 µm/div
Z 300.000 nm/div
2
4
6
8
µm

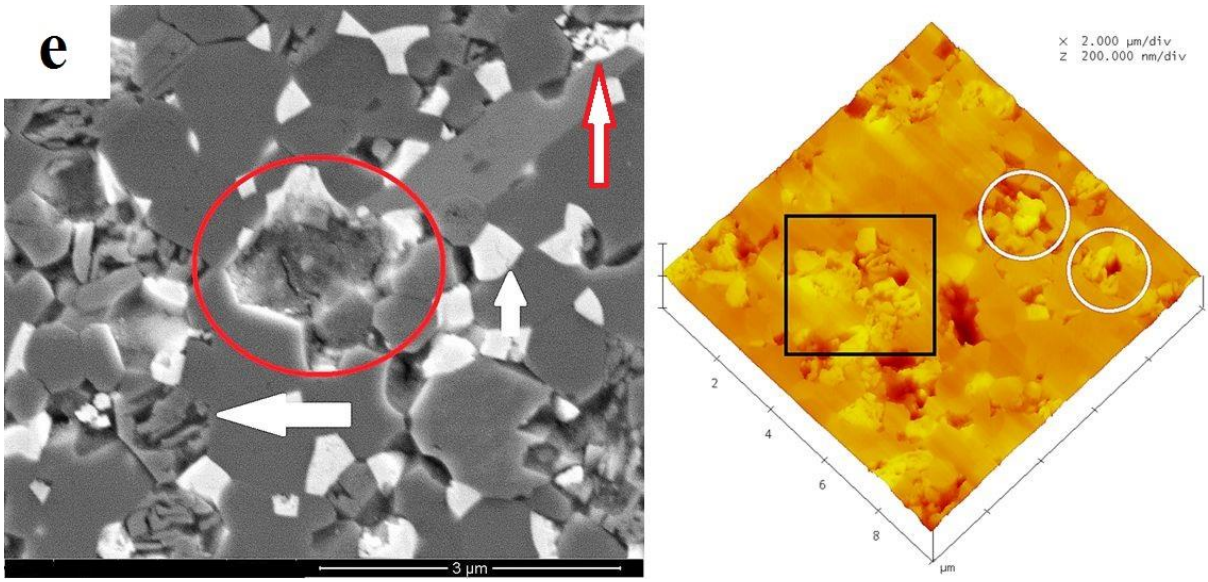
e
3 µm
X 2.000 µm/div
Z 200.000 nm/div
2
4
6
8
µm

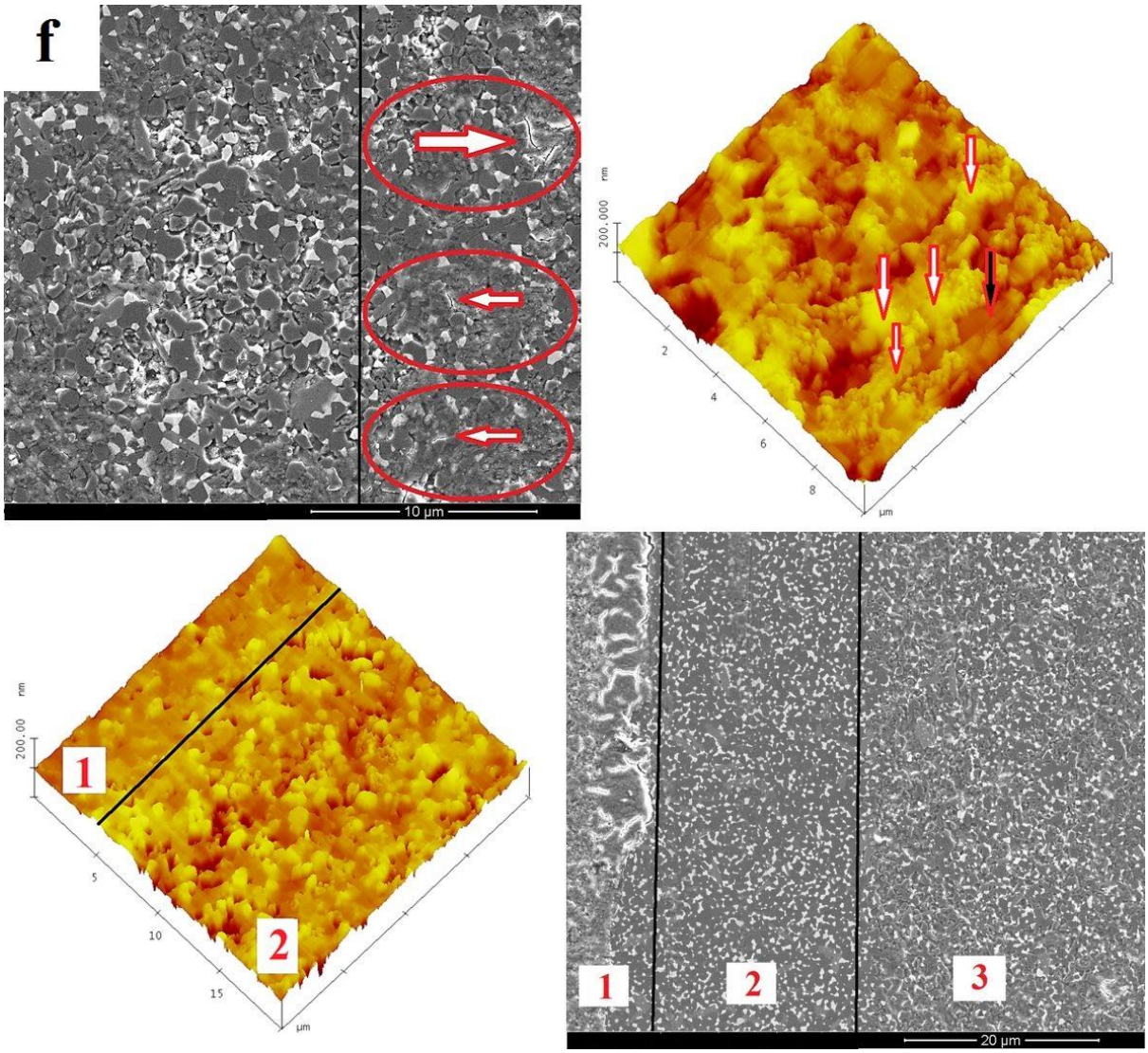

Figure 5.34. SEM and AFM images of BIOLOX® delta worn surfaces obtained from serum solution lubricated reciprocating wear test under (a). 1 N, (b). 2 N, (c). 4 N, (d). 8 N, (e). 16 N, (f). 32 N loads, at 600 rpm speed for 10 hrs.

5.3.3.3 Phase Changes of the Worn Surface by Raman Spectroscopy

The main difference in the Raman spectra of the commercial specimen and the others was the appearance of monoclinic peaks. In Figure 5.35, in addition to the six defined tetragonal peaks, four extra peaks were detected. The doublet peaks at 180 cm^{-1} and 190 cm^{-1} are the main characteristic lines of the monoclinic zirconia [228, 234]. The monoclinic peaks are marked and labelled by "m" in Figure 5.35. Besides the doublets, the line at 476 cm^{-1} was the most distinguishable peak, due to its high intensity. Under the 4 N load, which is equivalent to a 1988 MPa of initial Hertzian contact pressure, another peak for the monoclinic phase present at 335 cm^{-1}. This looks more like a shoulder and is marked by "*", in Figure 5.35. However, this peak gradually transformed into a full peak at 32 N.

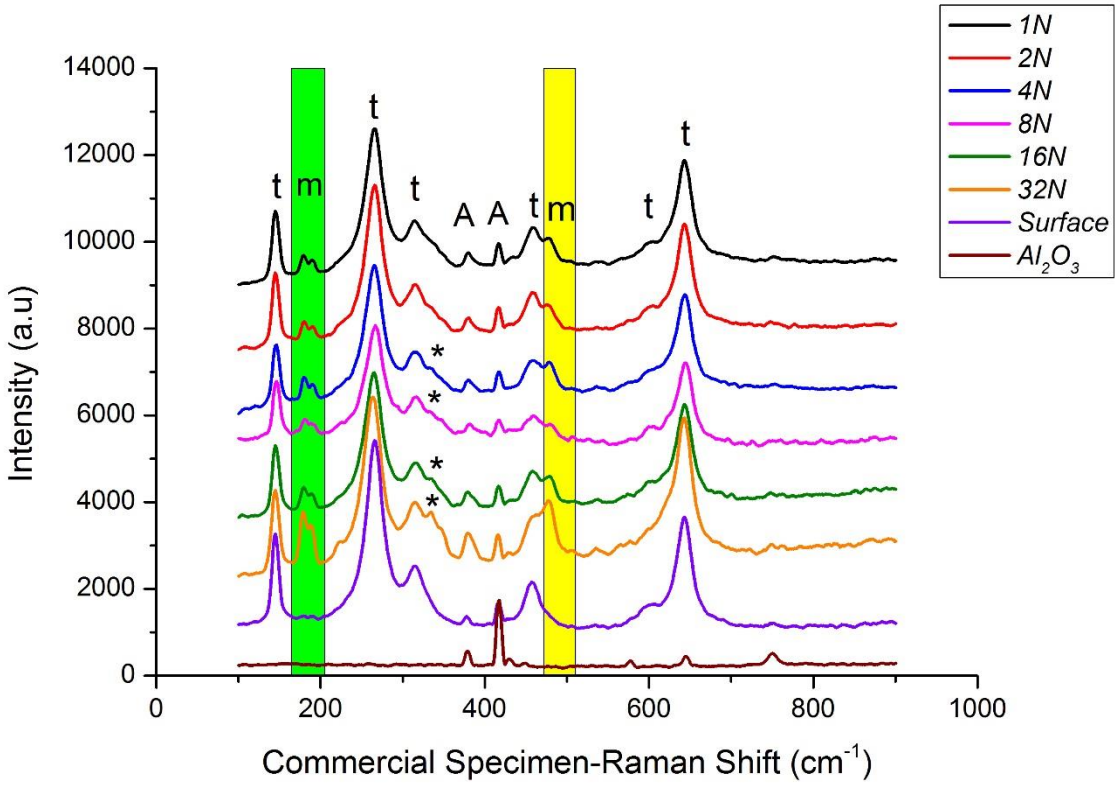

Figure 5.35. Raman spectra of the pure sintered alumina plus spectra of the worn and unworn Commercial specimen under 1 N-32 N under lubricated reciprocating test.

5.3.4 Characterisation of sub-surface by TEM

As shown in Figure 5.36, a fairly rough area was used for subsurface analysis of the commercial specimen (worn under 8 N load, through the lubricated reciprocating test). Although the selected surface was filled with extensive grain pull out, the prepared TEM foil revealed a single crater in an otherwise smooth subsurface, Figures 5.37 (a-b). Unlike the ZTA and ZTA-additives, this specimen included twining features on zirconia grains (red arrows) Figures 5.38 (a-b). Also, some minor dislocation activity was observed in alumina grains. As shown in Figures 5.37 (a-b), no tribo-layer was detected in this specimen, though a region with bright contrast existed beneath the gold coating inside a crater and seemed to be filled with wear debris.

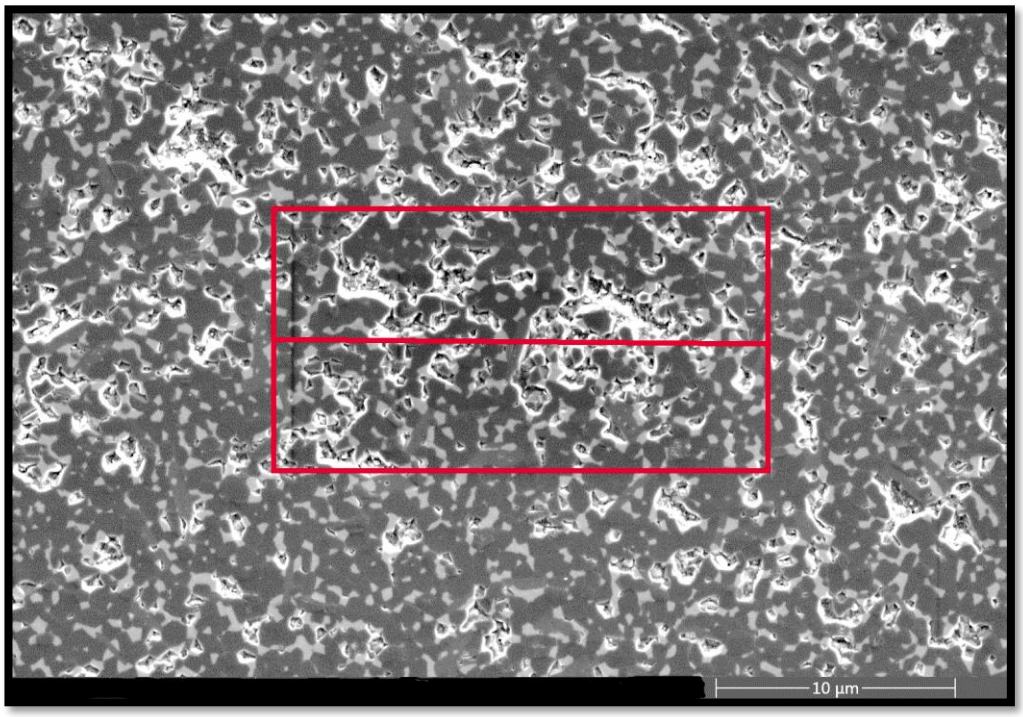

Figure 5.36. The SEM image shows the region worn by the lubricated reciprocating wear test under 8 N load for 10 hrs in the BIOLOX® delta. The marked area was extracted by FIB lift-out to prepare TEM specimen.

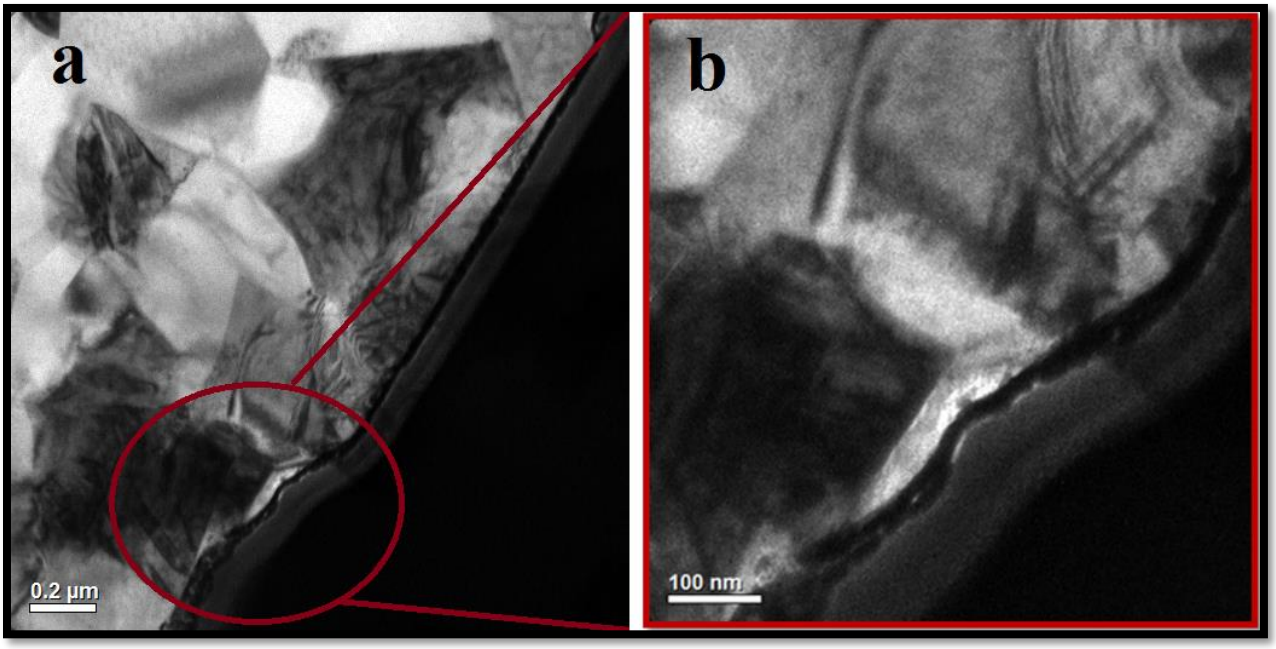

Figure 5.37 (a). The subsurface TEM image of the BIOLOX® delta showing the pitting area containing wear debris (b). The magnified image of the marked section in part (a).

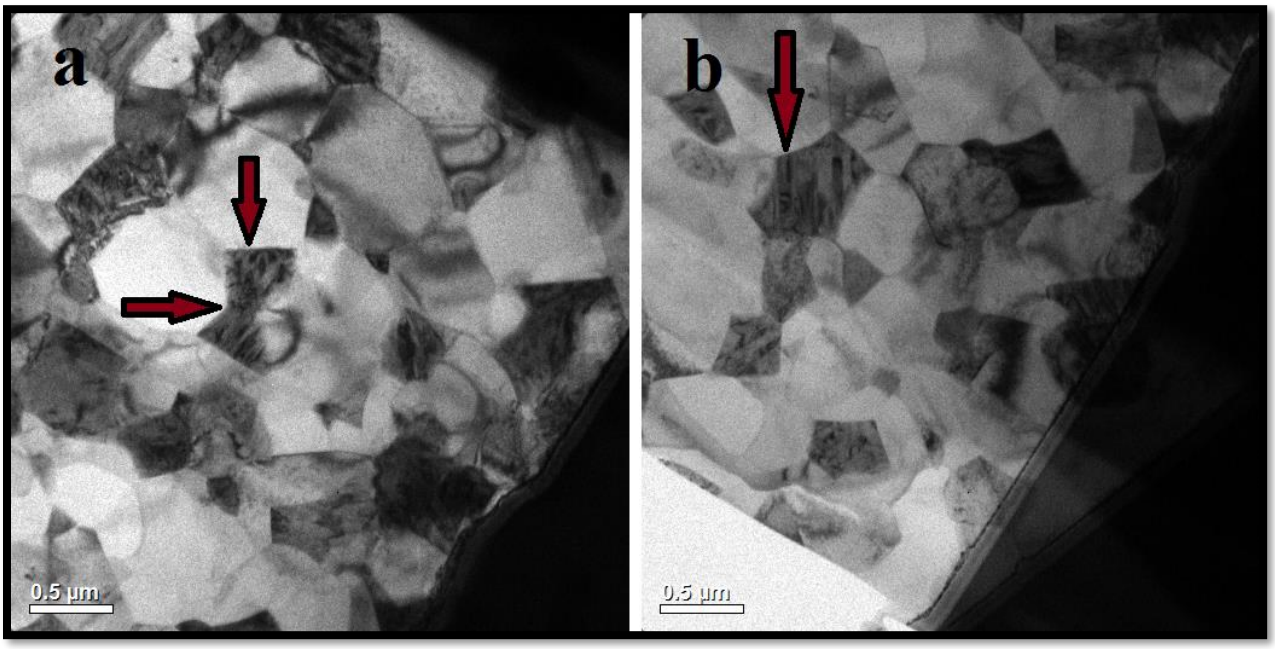

Figure 5.38 (a-b). Bright field TEM images of the worn surface in BIOLOX® delta at 8 N contact load. The red arrows point to the monoclinic zirconia grain revealing martensitic features.

6 Discussion

6.1 Ceramic processing

6.1.1 Powder dispersion

There could be three reasons for the heterogeneity of the specimens shown in Figures 4.1(a-d). One possibility is that the attrition milling method is not effective enough, leaving agglomerates originating from the starting powder intact. Therefore, at the start, the milling media, the shaft and the tank were renewed and several milling conditions (milling duration and speed) were tried.

Another possibility is that these agglomerations form during the drying stage in the oven. During drying, water evaporates resulting in a rapid increase in the ionic strength of the suspension, destabilizing the slurry and provoking agglomeration. To avoid this, the drying oven was replaced by freeze drying to help the formation of a homogenous composite.

In addition, to improve slurry stabilization, electrostatic stabilization through various chemicals such as nitric acid, ammonium citrate, citric acid and ammonium hydroxide were investigated. Through stabilization by nitric acid (pH ~4.5 as proposed by Gutknecht et al. [75]) satisfactory results were not obtained, Figures 4.1(a-b, d). This might be related to the low amount of powders in the distilled water used (~28 wt.%) and/or the fact that, at low pH values, alumina would slightly dissolve and, after drying, it would re-precipitate, connecting the particles, resulting in the formation of agglomerates [235,236]. In Figure 4.1 (c), no dispersant was used and hence due to the domination of the van der Waals attraction force, agglomerations were formed [43].

Finally, through numerous tests and considering the results taken from the literature, the optimum stabilization conditions were discovered, as explicitly explained in part 3.2, and a homogenous microstructure composite was obtained, as exhibited in Figures 4.4 (a-b).

As depicted in Figures 4.2 and 4.3, adsorption of citric acid on the oxide powder surface, shifts the isoelectric point to a lower pH range (acidic) leading to an increase in the negative zeta potential at a certain range of pH. As shown in Figures 4.2 and 4.3, by using citric acid a negative zeta potential was achieved almost in both acidic and basic range. But, an alkaline environment was chosen for this study because in an acidic environment the yttria (used as a stabilizer for the tetragonal phase in zirconia) is partially dissolved [237]. As a result, the amount of the stabilizing

dopant would decrease which might lead to a local surface change in zirconia [238] and destabilization of the tetragonal phase [239].

The investigation shows that citrate anions have strong affinity to be adsorbed on alumina and zirconia surfaces [223, 225,240]. As reported by Hidber et al., the hydroxyl group of the citric acid molecule contributes to both the adsorption ability of the citric acid molecule, particularly in the neutral and basic pH ranges, and also to the increase of a negative surface charge [225]. It is well documented that the adsorption of citric acid on the surface of alumina takes place through a ligand exchange of a hydroxyl group for a carboxylate group on the surface of the particle. In addition, the adsorption of citrate anions depends on the pH value and its effect on the deprotonation. By increasing the pH, the three carboxyl groups on the molecule would be deprotonated one by one, and when all were deprotonated, it would have the highest charge. When attached to the particle, the higher the charge of one molecule, the more negative charge on the surface of particle would be. The amount of the adsorbed citrate depends on the particle size, geometry and more importantly, the surface area. Under these circumstances, the adsorbed anions can impart electrostatic stabilization of the particles. It is worth mentioning that the presence of a large amount of unabsorbed citrate in the slurry leads to an increase of ionic strength and consequently on the suspension viscosity [225].

6.1.2 Thermal analysis (TGA and DTA)

The TGA graph, Figures 4.5 and 4.6, displayed a rising trend, up to around 50º C, meaning the weight of the powders were increasing. The reason for this behaviour is after freeze drying, the fine and fluffy powders have large and active surface areas which can absorb moisture very quickly. Hence the natural hydroscopic property of powders gets intensified after freeze drying and powers are more prone to absorb moisture from the air at the beginning of the test.

As presented in Figure 4.5, the first stage of analysis covers temperatures up to ~720˚C and involves a few steps of mass loss of ~ 0.33 wt. %. The first assumption was that the DTA peaks in this stage were related to the desorption of absorbed organics in alumina, probably added by the manufacturer. Thus, as received pure alumina was used as a reference to test this theory. As shown in Figure 4.6, a few exothermic peaks were detected, spanning between ~0-450ºC and accompanied by 0.8 wt. % loss, which might be correlated to the desorption of organic impurities

in alumina. So, by comparing Figure 4.5 Part A and Figure 4.6, it appears that these peaks are correlated to another chemical or physical reaction.

Another theory correlates these peaks to the partial dihydroxylation of alumina [241]. Alumina is known to be super hydrophilic. Therefore, during the freeze-drying process, a portion of alumina adsorbs water and can transform to $Al(OH)_3$ (Gibbsite) or AlOOH (Boehmite). The small weight loss detected by TGA indicates that a small amount of alumina had possibly gone through this transformation. Wafer et al. has shown the DTA pattern of $Al(OH)_3$ [241] which is compatible with the peak in region A around 318ºC. The complete dihydroxylation was carried out between 550-720ºC. As shown in Figure 4.5, through the entire dihydroxylation process, approximately 0.33 wt. % loss was recorded.

Subsequently, from ~750ºC-1200ºC, a very small exothermic peak was observed which is representative of the decomposition of $SrCO_3$(Figure 4.5, region B [242–244]. Beyond this region around ~1300ºC, an exothermic peak was observed which can be attributed to the solid solution formation of Al_2O_3 and Cr_2O_3 (Figure 4.5, region C) [245].

6.1.3 Particle size analysis

The particle size analysis was run after each stage of powder production, to investigate the effect of calcination time and temperature on particle size, hence it should not be considered as a representative of actual particle size (Figure 4.7). As summarized in Table 4.1, after employing an ultrasonic agitator for ~ 60 s, the D_{50} of alumina-additives and ZTA-additives after calcination (Figure 4.8) was reduced about 3 and 2 times respectively, compared to the situation in which ultrasonic had not been used (Figure 4.7). The reduction of particle size through applying ultrasonic agitation is indicative of the existence of soft and loose agglomeration that starts breaking up upon ultrasonic use.

As explained in part 3.1, the as received Al_2O_3 and ZrO_2 powders were in the nano range, so agglomeration can easily occur due to the high surface energy of this kind of nano-materials, leading to a reduction of this high surface energy. In addition, the particle size analysis was performed without using any dispersant, so the existence of soft agglomeration is unavoidable. Ultra-sonication does not change the interaction balance, it only provides energy to overcome

attraction forces in order to de-agglomerate. Therefore, the existence of soft agglomeration is still more likely to happen.

Figure 4.9 shows that under the same experimental conditions, the particle size of ZTA is about 1µm larger than ZTA-additives which can be attributed to the fact that ZTA-additives, as explained in part 3.2, have gone through milling twice. These results (smaller grain size in ZTA-additives) also demonstrate the reason behind earlier initiation of shrinkage in ZTA-additives.

6.1.4 Spark plasma sintering process

6.1.4.1 Parameters controlling density

6.1.4.1.1 Effect of temperature and time on density

The data shown in Tables 4.2 and 4.3 clearly demonstrate that with the sintering conditions employed and depending on the constituents of samples, a fully compacted composite is achievable at temperatures above 1450ºC with 8 and 10 min holding time. However, it has been reported by different authors that fully densified alumina compacts, and also zirconia specimens, are achievable at lower temperature around 1150ºC. This discrepancy can be explained through various sintering conditions including holding time, applied pressure, heating rate, pulse sequence current and also pre-sintering condition of raw powders.

It has been previously reported that a ZTA composite with submicrometer-sized alumina and zirconia powders, mixed via different procedures such as wet chemical methods (e.g. sol gel processing, pressure filtration and slip casting [246,247]) can be fully densified through pressureless sintering above 1500 ºC for several hours. This signifies the effectiveness of spark plasma sintering, which markedly lowers the holding time required. Figures 4.10 and 4.11 show that the utmost recorded shrinkage rate in ZTA- additives and ZTA reaches ~ 0.009 S^{-1}, 0.003 S^{-1}, respectively. In addition, the onset of shrinkage in ZTA-additives is observed at 1181ºC and is shifted to ~1223ºC for ZTA. The shrinkage curves show that ZTA- additives specimens experience more shrinkage (~ 0.009 S^{-1}) and occurring at ~ 42 º C lower when compared to ZTA specimens. This behaviour might be related to the smaller staring particle size of ZTA-additives compared to ZTA, and/or is due to the presence of chromia and strontia.

In theory, the density of a specimen should increase by the addition of Cr_2O_3 and SrO, because ZTA –additives has a higher calculated theoretical density compared to ZTA (~4.35 g/cm^3 and ~4.34 g/cm^3 respectively). In a recently published paper [248], it was demonstrated that, up to a temperature of about 1400ºC, increasing the amount of chromia added to alumina increases the density. Above this temperature, anomalies in the densification trend initiate, due to solid solution formation. A comparison between Tables 4.2 and 4.3 illustrates that at lower temperatures than ~1400ºC, chromia appears to contribute to the densification process [249] and results in ~ 98% TD which is higher than the density of the ZTA composite (no dopants) at similar temperatures which was ~ 95% TD. Nonetheless, at higher temperatures, chromia marginally inhibits densification [248, 250, 251]. Another explanation for this behaviour could be correlated to the particle size distribution of the starting powders. The particle size of starting ZTA–additives powder was ~1µm, smaller than ZTA due to the processing sequences explained in part 3.2 [252]. Hence, it can be deduced that finer particles have contributed to a larger amount and earlier onset of shrinkage. In addition to the soak temperature and holding time, the applied pressure, heating rate and pulse sequence play significant roles in the sintering process.

6.1.4.1.2 Effect of pressure on density

The enhanced densification at a lower soaking temperature and a smaller holding time compared to pressureless sintering could be related to the fact that as the pressure increases, more particles come into contact with each other. Besides, if the powder bed contains agglomerates, they start to break down under pressure and hence such a process improves densification [100]. As explained by Munir et al. [253], the applied pressure to reach full compaction depends on the temperature and grain size. For example, at 1200 ºC while the applied pressure was increased from 20 MPa to 141 MPa, the density of fully stabilized zirconia increased from ~ 60 % to ~ 100% [253]. Takeuchi et al. reported [254] that under a 30 MPa constant pressure, the relative density of zirconia sintered at 1200 ºC with a 5 min holding time reached 90%. Nevertheless, Wang et al. [255] reported that the maximum densification for 3Y-TZP is ~78% theoretical and no dependence on neither heating rate (50-200ºC/min) nor applied pressure (20-100 MPa) was observed. Work performed by Shen et al. showed that fully dense compacts can be obtained in SPS of alumina at 1150 ºC with an applied pressure of 200 MPa.

In this study, full density was obtained under 51MPa, at 1450 ºC for 10 min holding time. This discrepancy between the temperature required in the current study and that published in the literature might be due to the lower pressure applied in the present work compared to other studies and also the difference in the starting powder particle size. In addition, the reports in the literature were for monolithic zirconia or monolithic alumina which would have smaller particle sizes compared to the starting powder used for this study. The starting powders for this work were processed to be fully stabilized. In order to complete the required reactions, different calcination procedures were utilized which may well have resulted in an increase in the size of the starting powders. In addition to all the advantages of applying pressure during sintering, as confirmed by the literature, a high pressure allowed fully compacted samples containing sub micrometre-sized grains to be obtained, at lower temperatures at which grain boundary migration is not yet thermally activated [100].

6.1.4.1.3 Effect of heating rate on density

Sintering kinetics are greatly affected by the heating rate [256]. As reported by Shen et al. [100], a maximum normalized shrinkage would slightly shift to a lower temperature in alumina, when the heating rate is increased. They correlated this behaviour to the enhancement of grain boundary diffusion with rising current and the concomitantly heating rate. However, it has been observed that a high heating rate leads to the formation of porous alumina[256,257]. Amen et al. [258] proposed that a low SPS heating rate could favour the diffusion mechanism in alumina, including grain boundary and/or lattice diffusion, in which the centres of neighbouring particles come in contact and this would enhance the shrinkage in electrically non-conductive materials.

Mayo et al., [259] showed that a high heating rate would reduce the density of 3 mol.% yttria zirconia, due to the formation of temperature gradients. It would lead to the densification of the outer part of the specimen, while the inside section would include extensive pores. Nevertheless, Munir and Shen et al., [100,253] presented the evidence that a heating rate ranging from (50~300ºC min^{-1}) for zirconia and (50-400 ºC min^{-1}) for alumina does not influence the final density [253].

6.1.4.1.4 Effect of the current on the density

For all the tests performed the pulse pattern was kept on 1:0 (on/off) throughout the whole experiment. The pulse pattern is considered by some research groups as an important element that contributes to the densification [100, 260, 261]. On the other hand, other groups presented data implying that pulse pattern is ineffective in the densification process[100,253].

6.1.4.2 The proposed densification mechanisms

Various mechanisms of densification of alumina and zirconia are proposed by different authors, depending on the temperature, heating rate and applied pressure. It has been suggested [262] that in alumina, at temperatures ranging between 850-1200˚C, grain boundary sliding, accommodated by oxygen grain boundary diffusion are controlling the densification during a fixed heating rate of 100˚C min^{-1} and at the onset of the holding temperature. In another investigation by Langer et al., [263], it was proposed that the densification of α-Al_2O_3 was controlled by grain-boundary diffusion. Aman et al. [256], attributed the alumina densification mechanisms at low temperatures and low heating rates, to the grain boundary diffusion. However, at high heating rates, due to the large thermal gradient at interparticle contacts, surface diffusion coefficient enhances and therefore grain growth dominates. This group also suggested that regardless of the heating rate, at initial stages of sintering instantaneous densification might occur due to the plastic yield.

Wang et al. [255] studied the densification mechanism in 3Y-TZP and suggested that a few densification mechanisms are involved. They also proposed that the intensive particle rearrangement is dominant at an early sintering stage, leading to a much quicker densification compared to pressureless sintering. Besides, Bernard et al. [262] attributed the densification of stabilized zirconia, under low applied stress and temperature, to the pure diffusion (bulk?) mechanism.

Finally, some have criticized the structural homogeneity of a SPS-treated ceramic composite. Wang et al. [264] noticed that the part of an alumina sample neighbouring the graphite die densified faster than the central part. Hence, they suggested that the alumina powder had been densified only through the transfer of heat through the graphite mold and punches. However, Shen et al. [100] highlighted the importance of a fast heat transfer rate between the mold and the punches for a better sintering rate during the SPS process. This group also demonstrated that the sintering

behaviour and the densification rate depended on the reactivity of the starting powder. This means that nano powders, with a higher specific surface area, would initiate sintering and result in a well dispersed microstructure easier than coarser particles would. This conclusion is in agreement with the current observations, in which shrinkage initiated in ZTA-additives earlier, possibly due to the finer starting powders.

6.1.4.3 Parameters controlling grain growth

6.1.4.3.1 Effect of temperature on grain growth

At temperatures < 1500ºC, fairly limited grain growth was observed and at T > 1500ºC more rapid grain growth was found. All ZTA samples were almost fully dense after SPS at temperatures >1450ºC, Figures 4.12 and 4.13. Therefore, sintering at higher temperatures did not achieve greater densification, rather simply resulted in grain growth, which was particularly rapid above 1500ºC. This is broadly in agreement with Shen et al. [100] who found that the initial rate of grain growth at 1300º C was almost three times higher than that at 1200º C in alumina. Even longer holding times at 1200ºC did not result in grain sizes as large as those observed at 1300ºC with no holding time. Therefore, it is inferred that above a critical temperature the grain growth is quite rapid and that the mechanisms are thermally activated. The comparison of Tables 4.4 and 4.5 demonstrate that the alumina grain growth in a sample containing chromia and strontia at 1550ºC-10min was more rapid than ZTA for the same conditions, with a comparatively coarse grain size of ~900 nm observed. The accelerated alumina grain growth can be attributed to the presence of Cr ions [263, 265]. Since the diffusion coefficient of Cr across an alumina surface is much larger than that through the bulk, the surface of alumina grains neighbouring chromia become rich in Cr ions and grow faster [104, 266].

6.1.4.3.2 Effect of pressure on grain growth

As mentioned earlier, in the sintering regime performed for all experiments, the pressure was increased once the temperature had reached ~1200°C at which the maximum shrinkage started to occur. As confirmed by Shen et al. [100], when the pressure is applied at around the final temperature, the ultimate grain structure is finer, compared to when the pressure is applied during the whole sintering cycle. Thus, employing pressure at a high temperature, at which the grain boundary migration is kinetically favourable, leads to a reduction in the grain growth observed.

6.1.4.3.3 Effect of heating rate on grain growth

It is well documented that a high heating rate leads to the formation of a composite with a smaller grain size and a lower density [253]. Shen et al. [100] observed that the grain size of alumina sintered at 1400ºC, with a heating rate of 50°C min^{-1}, was ~ 9.5µm. However, at a rate of 370ºC min^{-1}, it dropped to ~4µm. In this work, two regimes for heating rate were proposed to make a good balance between grain growth and density; a moderate rate of 100ºC min^{-1} at temperatures below 1200°C and a low rate of 50°C min^{-1} at temperatures above 1200°C.

6.1.4.4 Effect of grain growth behaviour on density

As proposed by Bernard-Granger and Guizard [262,267], when the relative density exceeds 92-95 % (closed porosity), elimination of the residual isolated pores is difficult. Hence, grain growth is then necessary to enhance densification and reduce the surface energy remaining in the system. Therefore, grain growth might be accompanied by a minor density enhancement. In this project, as shown in the SEM micrographs in Figures 4.14 (f-i) and 4.15 (f-h), grain growth was mainly accompanied by a slight density reduction at temperatures above 1450˚C, due to abnormal grain growth and the isolated pores that were trapped mainly at triple junctions.

6.1.5 Micro structural features

6.1.5.1 Scanning electron microscopy (SEM)

The above discussion demonstrates that, for both ZTA and ZTA-additives, a fine and fully dense composite microstructure was formed at temperature ~1450ºC, and SEM micrographs shown in Figure 4.14 (a-i) and Figure 4.15 (a-i) confirm these results. SEM micrographs in Figures 4.14 (a-b) show microstructures of ZTA containing a substantial number of voids and interconnected pores at 1400ºC-5 and 10 min, which is in agreement with the density results (~95% TD, Table 4.2). At a higher temperature of 1550ºC-10 min (Figure 4.14(i)), more isolated pores were observed, mainly at triple and four grain junctions in the ZTA composite. This can be related to the abnormal grain growth of alumina. Langer et al. [268] proposed that abnormal grain growth occurs when the incorporation of the second phase does not completely fill all four grain junctions of the matrix particles and when the new phase is not homogenously dispersed throughout the matrix. As a

result, some groups of alumina grains might be formed that would behave without restraint and act as nuclei for abnormal grain growth.

In ZTA-additives and Biolox® Delta (Figure 4.15 (a-i)), elongated grains were observed which were due to the formation of platelet strontium hexaaluminate. In these series of micrographs, in contrast to the ZTA specimens, no significant number of pores and voids were observed at a temperature of ~ 1400ºC, which is in agreement with the density results (98% TD) obtained, in Table 4.3. However, at a temperature of 1550ºC-5 and 10 min (Figure 4.15 (g-h)), isolated pores were clearly noticed, mainly at triple junctions, which could be due to the accelerated grain growth rate at high temperatures. Based on their location, these pores generally shape as explained in part 2.13.1.2 and play a destructive role on the mechanical properties of the specimens.

In both types of specimen, as well as Biolox® delta, two types of ZrO_2 particles were formed in the ZTA composite. This was also reported by Kibeel and Huer [269]. The first type was intergranular zirconia, which had a faceted shape and is dispersed mainly in alumina grain boundaries or in the triple and four-grain junctions [268]. The second type was intragranular zirconia, which had a spherical shape. The intragranular zirconia was generally finer than intergranular zirconia. As proposed by Kibeel and Heuer [270,271], the larger size of the intergranular zirconia particles is the result of the quicker coarsening kinetics at the grain boundaries. This group also suggested that during sintering of ZTA, the ZrO_2 particles grow through either the Ostwald ripening or the coalescence process. Based on their observations, the coalescence process contributes to the growth of intergranular ZrO_2 particles as they are dragged together by migrating alumina grain boundaries. Subsequently, grain growth and the vanishing of fine alumina grains results in the ZrO_2 particles coming into contact as illustrated in Figure 6.1.

Although intragranular particles also went through coarsening, this would have been at a much slower rate as the coarsening would have been controlled by lattice diffusion rates. As marked by the rectangles in Figure 4.14 (i), zirconia particles can be located at four-junction grains due to their strong self-diffusion [268]. Subsequently, as marked by the red arrows in Figure 4.14 (i), a fraction of these fine particles were trapped within large alumina grains. It has been proposed that this behaviour occurs by the growth of a fraction of alumina grains which are confined by a small number of zirconia grains. They turn into an individual larger grain which later “swallow up” neighbouring alumina and zirconia particles [268].

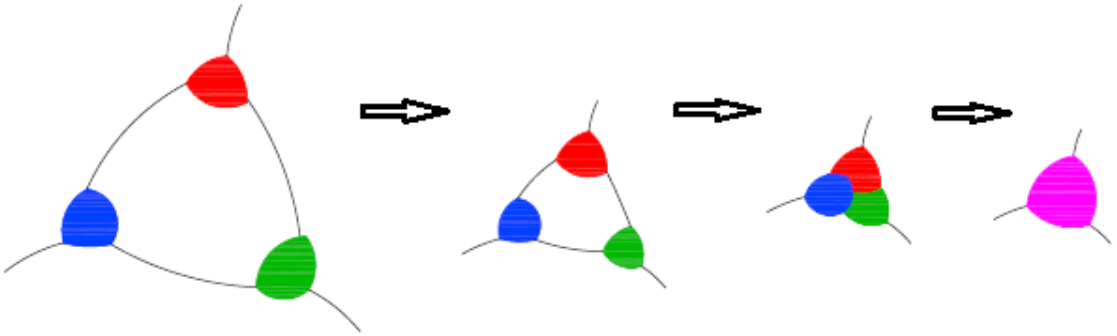

Figure 6.1.Schemiatic drawing illustrating how zirconia particles grow as a result of being dragged by migrating alumina grain boundaries during coalescence [271]**.**

6.1.6 Mechanical properties

6.1.6.1 Fracture toughness

The inclusion of zirconia in the alumina matrix enhances fracture toughness, mainly due to the tetragonal to monoclinic phase transformation of zirconia grains [272–274]. Tetragonal to monoclinic phase transformation (a stress induced phase transformation) is accompanied by a volume expansion, resulting in the introduction of compressive stresses around a crack and thus causes inhibition of crack propagation. Furthermore, through t→m transformation, micro-cracks start to form around the monoclinic zirconia grains [275–277]. These two mechanisms are known to be the most predominant in the ZTA composite. However, to trigger the phase transformation, zirconia grains need to be large enough to go through this toughening mechanism [278,279]. In addition, the amount of stabilizers added to zirconia, such as MgO and Y_2O_3, greatly affects the transformation of tetragonal particles [45]. On the other hand, the formation of pores in the microstructure lessens the fracture toughness, due to the accumulation of stress in the pores and reduces the resistant area [280].

As shown in Table 4.6, the fracture toughness of the ZTA composite fluctuated slightly between 5.27-5.43 MPa.$m^{1/2}$, which is probably a result of experimental fluctuations, and it did not considerably increase as the temperature was raised. The reason for this behaviour was attributed to the small final particle size of zirconia (186 nm – 250 nm) for samples SPSed in the temperature range of 1450°C-5 min – 1500º C- 5 min. This zirconia particle size is about two times smaller in this study than the values reported in the literature for pressureless sintered material [26, 246, 247].

Consequently, it was expected that the zirconia particles were generally too fine to go through the t→ m transformation. At temperatures (holding time) between 1500°C (10 min)-1550ºC (10 min), in which the grain size ranged between 279 nm - 489 nm, no major improvement in fracture toughness occurred. Moreover, a slight drop in toughness at 1550ºC-10 min was observed. This reduction was, however, very small, and can be correlated to the formation of pores, due to the abnormal grain growth of alumina particles, as shown in micrograph 4.14 (i). Furthermore, at 1500°C- 5 min the combination of a small grain size and the existence of pores as shown in Figure 4.14 (f) are believed to be the reasons for the lower fracture toughness.

The fracture toughness of the ZTA composite containing ternary and quaternary oxide dopants was given in Table 4.7. The largest and the smallest values of fracture toughness were 5.66 MPa.$m^{1/2}$ at 1500°C-5 min and 5.15 MPa.$m^{1/2}$ at 1400°C- 5 min, respectively. These differences are again small but are larger than the estimated experimental error. As the temperature increased, the general trend was an increase in fracture toughness, which was believed to be due to grain growth. At 1450°C- 10 min, the measured fracture toughness (5.45 MPa.$m^{1/2}$) appeared to be marginally better than the fracture toughness (5.30 MPa.$m^{1/2}$) at 1450°C-5 min, while interestingly sharing almost the same particle size (180 nm and 178 nm, respectively). Although this variation is probably a result of experimental error, it might be because a higher denser composite was formed at 1450°C- 10 min compared to 1450°C-5 min (Table 4.3). This highlights the importance of pores in leading to poor mechanical properties. At 1500°C-5 min, grain growth occurred which coincided with the maximum density (4.34 gr/cm^3), resulting in the optimum fracture toughness in this group of compositions. Subsequently, as the temperature increased, the zirconia grain size grew and reached 465 nm at 1550°C- 10 min. The fracture toughness under these conditions, 5.51 MPa.$m^{1/2}$, was within experimental error the same as observed for 1500°C- 5 min.

Tables 4.6 and 4.7 show that the ZTA-additives had superior fracture toughness compared to the ZTA samples. This enhancement in ZTA-additives might be due to the presence of an additional toughening mechanism, namely, the formation of platelet grains of strontium hexaaluminate, Figure 4.15 (a-i). This is supported by Kern et al. [281], who reported that the toughening characteristics are governed by the amount and type of hexaaluminates. He also showed [281] that these elongated grains promote strong crack deflection mechanism at their boundary with adjacent

grains. It appears, therefore, that the bonding between these interfaces is relatively weak, promoting intergranular rather than transgranular cracking.

Finally, the commercial Biolox® delta was employed as a reference specimen. In order to compare the results quantitatively, this specimen was treated and examined under similar conditions. The measured fracture toughness for the commercial sample was 5.61 MPa.m$^{1/2}$ which is very similar to the data for the ZTA-additives sintered at 1450°C- 5 min and 1500°C- 5 min. Nevertheless, the reported fracture toughness value by the company for this specimen is 6.5 MPa.m$^{1/2}$. This discrepancy can be correlated to the method used to measure fracture toughness and the equation used to calculate the toughness. In this work, the equation proposed by Shetty *et al.* for Palmqvist crack was used to evaluate the value of fracture toughness and the overall results were perfectly in agreement with the literature [211, 282].

6.1.6.2 Vickers hardness

As affirmed by the literature [283, 284], the hardness of ceramic materials is generally governed by the inherent deformability of the material, the variation of porosity, the boundary constitution and the microstructural properties including being multiphase and particle size and orientation. For ZTA based composites, most researchers [43, 283, 285, 286] have argued about the effect of grain size and porosity, as well as the contribution of the quantity of zirconia on the hardness [287–289]. As the temperature increases, the grains grow, and hardness starts to decrease which is in contrast with the increasing trend of the toughness. This is most probably a result of the well-known Hall-Petch effect, (Hall-Petch relationship) [290, 291].

Furthermore, it is well documented that a larger amount of zirconia reduces the hardness of the composite because zirconia is inherently softer than alumina. The hardness is as also correlated to the possible coarsening of zirconia and thus formation of porosity inside the composite[280, 282]. Nonetheless, fine-grain zirconia has a pinning effect on the grain boundaries of alumina, resulting in a smaller alumina grain size.

As tabulated in Table 4.6, due to grain growth as the temperature was raised, a general decreasing trend for Vickers hardness was observed in the ZTA composite. The measured values for Vickers hardness varied between 17.91-18.62 GPa. At 1470ºC-8 min, the maximum hardness of 18.62 GPa was achieved, due to the higher density. However, it is worth mentioning that this value was only

slightly larger when compared with other hardness values at lower temperatures. At 1500 ºC - 5 min, hardness slightly dropped, which is possibly due to the formation of pores as shown in the SEM images, Figure 4.14 (g, i). Subsequently, the minimum hardness occurred at 1550 ºC - 10 min, due to the detrimental impacts of grain growth and low density.

In ZTA-additives, the same decreasing trend of hardness was observed in Table 4.7. The Vickers hardness in this composite fluctuated between 16.44-18.30 GPa. At 1450 ºC - 10 min, the hardness was the largest value possible for this composite, at 18.30 GPa. This is due to the positive effects of both high density and fine grain size of alumina and zirconia (306 nm and 180 nm, respectively). On the other hand, significant grain growth and noticeable reduction in density was observed at 1550 ºC - 10 min due to the formation of pores, resulting in the lowest hardness of 16.44 GPa. This was almost 2 GPa smaller than the maximum hardness value for this composite.

As shown in Tables 4.6 and 4.7, the highest and lowest hardness values for ZTA-additives were around 2 % and 8 % smaller than the corresponding values in ZTA, respectively. This discrepancy is attributed to the formation of hexaaluminates which increase fracture toughness but adversely affect hardness. In fact, the addition of $SrCO_3$ to ZTA gives rise to the formation of pores and consequently reduces the hardness [292].

The Vickers hardness of the reference commercial sample was measured with the same method to be 17.04 MPa. This was less than the highest value obtained for ZTA-additives. Despite the fact that the commercial sample is fully dense (having been HIPed) the grains size was larger due to the pressureless sintering process used in manufacture. Thus, it was expected that this composite would possess a smaller hardness value with compared to the ZTA-additives. Nonetheless, the reported hardness by the company for this sample is 19 MPa which can be correlated to the reasons explained in section 6.1.6.1.

6.2 Tribological behaviour

6.2.1 Friction and lubrication behaviour

Various types of lubricants have been used in the reciprocating wear testing of bio-ceramic materials. Among these, bovine serum has commonly been used for wear testing. Currently, as confirmed by the International Organisation for Standardisation (ISO), bovine serum is the best lubricant to deliver clinically correlated wear rates and wear debris of a similar size and shape to

that found *in vivo* [293, 294]. The measured COF ranged between 0.03 ± 0.01 - 0.14 ± 0.04 for ZTA, 0.03 ± 0.02 -0.2 ± 0.03 for ZTA-additives (1), 0.08 ± 0.03 - 0.19 ± 0.02 for ZTA-additives (2), and 0.03 ± 0.02 - 0.15± 0.04 for BIOLOX ® delta, Tables (5.1), (5.3) and (5.4). For each specimen the lowest value of friction was not necessarily correlated to the lowest load and vice versa.

The Stribeck curve, Figure 2.17, is indicative of the lubrication regime, and is divided into three sections, namely, the full fluid film, the mixed lubrication and the boundary lubrication. On the right side of this graph, in the so-called full fluid film regime, the load is borne by the film pressure in a fluid lubricant due to the full separation of the interacting surfaces. The Elastohydrodynamic mode occurs inside this region and is the condition in which the pressure is enlarged, thus one or both contacting surfaces deform to increase the load bearing area.

At high loads, the separation between the sliding surfaces gradually decreases and they ultimately come into contact. This regime is known as the boundary lubrication in which wear, and friction are not ruled by the properties of the lubricant. Instead, the viscoelasticity and plasticity of the adsorbed lubricant films and chemistry of the contacting surfaces will define the contact area between the surfaces which are interacting [152]. The transition region between the two aforementioned regimes is termed mixed lubrication, in which the pressure is partially supported by the mechanical interaction of the surface asperities and by the fluid.

As shown in Figures 5.2, 5.15 and 5.30, the Stribeck curves seem to be slightly noisy at certain loads. For loads between 1 N - 4 N, only the commercial specimen exhibited a marked increase of the COF under the initial contact pressure of ~1988 MPa (4 N). This jump in the COF might be related to an increase in the polymorphic phase transformation, coupled with volume expansion [229]. This abrupt change in the COF value is in line with the SEM and AFM images, showing much more extensive pitting and grain pull out compared to 2 N.

The peculiar trend of the Stribeck curve at 8 N (ZTA, ZTA-Additives (1)), might be due to the presence of the protein and its adsorption onto the surface, as one of the constituents of the employed lubricant. Protein adsorption is a unique characteristic of bio-ceramics [295, 296]. Once bio-ceramics are inserted into a body, the protein from the circulating fluids will be immediately adsorbed onto their surfaces [297]. As corroborated by Ma and Rainforth [298] and Spikes [299], the adsorbed proteins can stick to the ceramic counter surfaces and operate as a “solid like” film

and increase the friction factor [300–303]. On the other hand, at larger loads, namely 16 N and 32 N, thick patches of tribo-layer with a maximum height of ~45 nm were detected through AFM and SEM. The presence of these patches would be expected to influence the coefficient of friction between the interacting bodies, although the exact role is not clear, nor the composition of these layers. Hence, the reduction of COF at 32 N in the ZTA-Additives (1) was possibly due to the presence of a tribo-layer which is believed to reduce the wear rate and the coefficient of friction [14]. It is well documented that aluminium hydroxides (AlOOH, $Al(OH)_3$) can be formed on alumina surfaces, in the water and humid air, due to the high hydrophilic property of alumina [304–306]. In the study conducted by Gee, the presence of hydroxide (OH) on the worn surface of an alumina specimen at a humidity of 50% RH was confirmed using dynamic secondary ion mass spectroscopy (SIMS)[306]. This hydroxide layer, which can be one of the constituents of the tribolayer, can then contribute to the reduction of the COF due to its lower shear strength compared to alumina. However, it is quite complicated to prove the formation and role of this hydroxide layer. It is worth mentioning that, in general, the COF values obtained for almost all loads and specimens were very small.

The above-mentioned factors might explain the irregularities of the Stribeck curves, at a few loads, which in turn make attributing specific lubrication regimes to individual loads more complex. However, as evidenced by AFM and SEM (Chapter 5), the most dominant lubrication mode in all the specimens was presumably the mixed lubrication regime, wherein the surface asperities as well as the viscoelastic properties of both, the bulk lubricant and the adsorbed film, were the ruling factors.

6.2.2 Specific wear rate

One of the main objectives of this study is evaluating the influence of grain size and the role of additives on the wear resistance of the ZTA-based composites. To achieve this goal two strategies were employed. First, grain size refinement was carried out through incorporation of zirconia in monolithic alumina, in order to form a duplex structure containing a nanoscopic phase and enhance the fracture toughness. Second, sintering of the composite was done by Spark Plasma Sintering for which the short cycle time and high pressure enhance the density and reduce the grain size.

As depicted in Figures 5.3, 5.17, 5.18 and 5.31, the graph of the specific wear rate as a function of load had a general rising trend for all the three specimens, despite their different constituents,

indicating the load dependency of the specific wear rate. Note that for no change in wear mechanism, the specific wear rate should not change with load. However, there were slight fluctuations at certain loads. The largest and the smallest specific wear rates measured for the ZTA composite were $(3.73 \pm 0.57) \times 10^{-9}$ mm^3/Nm and $(6.31 \pm 1.22) \times 10^{-6}$ mm^3/Nm, respectively. Correspondingly, these values changed between $(1.12 \pm 0.468) \times 10^{-8}$ – $(1.69 \pm 0.299) \times 10^{-7}$ mm^3/Nm for ZTA-additives (1), between $(1.46 \pm 0.663) \times 10^{-8}$ – $(6.54 \pm 1.78) \times 10^{-8}$ mm^3/Nm for ZTA-additives (2) and between $(4.25 \pm 1.28) \times 10^{-9}$ – $(4.68 \pm 0.601) \times 10^{-7}$ mm^3/Nm for the commercial specimen.

As shown in Figures 5.3, 5.17, and 5.31, the specific wear rate of the ZTA and ZTA-additives (1) were still in the range of 10^{-8} mm^3/Nm, for loads ranging between 1 N-16 N. Besides the calculated specific wear rate values for loads ranging between 1 N and 16 N, the images taken from the wear scars by SEM and AFM suggest that mild wear was the dominant mechanism, in which probably both tribochemical and mechanical wear were simultaneously operating. On the other hand, the specific wear rate for BIOLOX ®delta was of the order of 10^{-7} mm^3/Nm at 16 N. This specimen appears to be worn slightly more than ZTA and ZTA-additives (1) at this load. This was supposedly due to the detrimental impact of a large grain size on the wear resistance of materials [191, 307]. In line with Rainforth [14], the refinement in grain size yields both a reduction in thermal mismatch stresses and slip length, therefore decreasing the dislocation density in the surface grains which leads to an increase in the time to transition from mild to severe wear. As corroborated by Rainforth [14] the time dependent wear transition is influenced by a few factors including the applied stress at asperity contacts, residual thermal mismatch stress and stresses associated with dislocation accumulation at grain boundaries.

Another method for reducing the average grain size is through incorporating zirconia nano-particles in the alumina matrix and forming the ZTA composite which has a smaller average grain size compared to the monolithic alumina. He et al. [308] showed that among the 5 vol. %, 15 vol. % and 20 vol. % additions of zirconia to alumina matrix, the one with 15 vol. % zirconia exhibited the lowest pre-transition wear rate. This behaviour was attributed to at least three parameters, namely refinement of the alumina grain size as explained above, increase of the hardness and formation of a compressive stress in the wear scar [308]. In addition to the grain size reduction, the incorporation of zirconia was associated with the introduction of residual stresses

which is known to be the potential reason behind the wear reduction of ZTA-based composite compared to the monolithic alumina.

In monolithic alumina, a large alumina grain size and a strong anisotropy in thermal expansion result in local tensile stresses at some alumina/alumina grain boundaries. The accumulation of these tensile stresses increases the likelihood of the formation of the brittle and intergranular fracture under abrasive wear. As a result the role of plastic deformation is minimal [204].

On the other hand, thermal residual stresses within the ZTA composite are formed during cooling from sintering due to the mismatch in the thermal expansion of the constituting components (zirconia and alumina)[309]. Once zirconia particles are added to the monolithic alumina, the nature of the thermal stresses is predicted to be compressive in the alumina matrix when the zirconia phase is mainly present in tetragonal form. This is due to the lower thermal expansion coefficient of alumina compared to the tetragonal zirconia [309]. Therefore, the actual contact pressure in the alumina is lower in the ZTA than monolithic alumina, reducing the chance of fracture [204]. This is also in agreement with the results reported by Le et al. [158], in which the incorporation of fine zirconia grains in the BIOLOX® delta yielded a lower amount of dislocation activity at the worn surface compared to the monolithic alumina.

Two scenarios exist on the impact of the polymorphic phase transformation on the wear resistance of this composite. The first scenario occurs when contact of the counter surfaces results in a phase transformation from tetragonal to monoclinic phase and subsequently a volume expansion occurs. If this expansion happens at or near the surface it leads to the uplift of the surface. The transformation is also associated with micro cracking which weakens the surface and leads to a further increase in wear rate. The second scenario is when transformation occurs in a region below the surface where there is surrounding constraint of the zirconia particle by alumina. The volume expansion associated with the formation of monoclinic zirconia results in a compressive stress within the matrix leading to a reduction in wear rate [22, 310]. Both scenarios might occur together to an extent that depends on parameters such as the t→m expansion direction, the contact stress and the grain size. However, in this study neither scenarios worked, as no transformation in the ZTA and ZTA-additives was observed. The transformation of the zirconia is discussed further later on.

At a load of 32 N, which is equivalent to ~3976 MPa of initial Hertzian contact pressure, the specific wear rate of the ZTA-additives (1) and the commercial specimen increased compared to 16N, but not significantly, Figures 5.17 and 5.31. At this load, both mechanical and tribo-chemical wear seem to be responsible for the wear behaviour of these two specimens, so it appears that mild wear was still operating. In contrast, a substantial jump in specific wear rate of about two orders of magnitude was observed for the ZTA at 32 N. The worn surface was dominated by surface fracture (Figure 5.6 f), which demonstrates the domination of mechanical wear and therefore the transition from mild to severe wear.

The difference in grain size between the ZTA and the other materials could not explain the observation that the ZTA went through the wear transition at 32N while the other materials did not. The main difference between the ZTA and the other specimens was the presence of the Cr and Sr dopants. This suggests that one or both of these dopants plays a role in the prolongation of the pre-transition wear stage to higher loads. Pezzotti et al. [311] demonstrated that doping with Cr lowered the concentration of oxygen vacancies in alumina. This leads to a reduction of lattice constraints and thereby residual stresses. It is also known that a tensile stress field destabilizes zirconia grains and leads to the formation of intergranular cracks in alumina grains [312]. Hence, a high accumulation of oxygen vacancies is the reason for a high tensile stress concentration in the alumina monolithic and probably in the ZTA specimens where Cr dopant does not exist.

In addition to the positive role of Cr in the enhancement of wear resistance, this dopant also helps maintain the stability of zirconia, under a hydrothermal environment. As Cr dopant changes the oxygen vacany concentration it prohibits or delays moisture transfer to zirconia. As a result, oxygen vacancy annihilation and thereby polymorphic phase transformation in a hydrothermal environment is postponed. More details about this behaviour is reported elsewhere [311].

Wang et al. [15] demonstrated an equation calculating the value of the induced stress from sliding, required to initiate the wear by chipping or grain pull out. This equation (Eq. 6.1) shows that the micro-fracture resistance enhancement can be obtained through grain size refinement, prohibiting internal tensile stresses and if possible introducing compressive stresses in the composite microstructure, e.g. incorporation of zirconia grains within the alumina matrix.

$$\sigma_D = \sigma_I^* \left(\frac{d^*}{d}\right)^{1/2} - \sum_i \sigma_{Ii} \qquad \text{Eq. 6.1}$$

Where $\sum\sigma_{Ii}$ is the sum of internal stresses after the thermal process. The compressive stresses are displayed with a negative sign. σ_D is defined as the critical tensile stress induced by external sliding and needed for the propagation of micro-cracks. Hence, once the applied tensile stress, σ_{max}, reaches the critical tensile stress σ_D, the wear transition will occur. When the grain size reaches critical grain size d=d*, $\sum\sigma_{Ii}$ equates to σ_I^* and spontaneous micro fracture takes place at σ_D=0.

6.2.3 Morphology of the worn surface

The data collected through scanning electron microscopy (SEM) and atomic force microscopy (AFM) revealed similar mechanical wear mechanisms across the surface for all three materials. Differential wear between adjacent grains (grain relief) is one of the noticeable features on the pristine surfaces, (Figures 5.5, 5.20 and 5.33) and the worn surface of all the specimens at 1 N and 2 N (Figures 5.6(a-b), 5.21(a-b) and 5.34(a-b)). As evidenced by the 3D AFM images, the difference in grain heights is more conspicuous in the ZTA specimen compared to the other two materials, Figure 5.6. The presence of "grain relief" as a result of differential wear between grains is representative of mild wear in various ceramics. Grain relief is also known to be an important element for a time dependent transition to catastrophic wear, specifically in alumina [190, 191, 313]. Hence, a comprehensive knowledge of the effective mechanisms that increase grain relief is of great importance. As corroborated by Barceinas-Sanchez and Rainforth, [189] no mechanical based explanation can justify the formation of grain relief. Thus, the difference in local wear rates has been attributed to the tribochemical reaction rates, such as the dissolution rate and the properties of the amorphous film which the tribochemical wear produces. And, they are in turn dependent on the crystallographic orientation [169]. The differential wear is one of the reasons through which 3rd body abrasive are liberated from the edge of grains that have worn less. The formation of grain relief has also been reported in the monolithic alumina by a few authors, who interpreted it as relief polishing, due to the anisotropic nature of the alumina [12, 13, 314]. However, relief polishing was not observed in the series of tests performed in this study.

The other distinct features observed on the worn surfaces were pits from which grooves had originated or passed through. These mechanically induced surface features became more extensive depending on the severity of the contact pressure. The grooves have been proposed to originate from 3rd body abrasives that result from grain pop outs or the detached edges of the grains which had been standing proud of the surface [158] and they can terminate at grain boundaries [189]. The

liberated wear debris get trapped between the sliding counter bodies and are ground through the reciprocating motion of the sliding surfaces. Consequently, the 3rd body abrasion would create these deep grooves. As the trapped debris are consistently broken up during the sliding motion, the resulting grooves would become progressively finer. Interestingly, the depth of the grooves decreases as the distance from its source increases, confirming the crushing of wear debris through the 3rd body abrasion [158]. Rainforth [14] has categorized the damage resulting from these grooves into four groups; grooves that mainly create dislocation damage, grooves that chiefly produce fracture, grooves that lead to both dislocation damage and fracture and eventually the ones leaving no damage. They also found that the depth of these grooves differ from grain to grain and was basically controlled by the crystallographic orientation [189].

The wear tracks at 1 N and 2 N exhibited similar features in BIOLOX®delta, although at 2 N the grooves were much deeper, wider and in the close vicinity of each other and the pits were larger. The depth of the grooves ranged between 50-100 nm for the commercial specimen, and between 10-20 nm for the ZTA and ZTA additives. The reason for this marked difference is possibly due to the larger grain size of the commercial specimen compared to the other composites. These coarser grains would liberate larger particles through differential wear that then plough the surface. Furthermore, as confirmed by Raman spectroscopy, the zirconia phase transformation, from tetragonal to monoclinic, took place in the commercial specimen, but not in the other materials. Consequently, compared to the other two specimens, more grains protruded from the surface and had their top surface break up and act as an abrasive body.

The morphology of the worn tracks at 1 N and 2 N suggests that tribochemical wear was probably the leading wear mechanism in the ZTA specimen. This conclusion can be further supported through the presence of differential wear, the smaller numbers of grooves, the sparse grain pull outs and pitting and finally the trend in the Stribeck curve, Figure 5.2. Furthermore, there were no traces of wear debris detected in this specimen, either by Contour GT or other microscopes, probably indicating the operation of the full fluid lubrication mode.

On the other hand, the ZTA-additives (1) and particularly the commercial sample displayed more grooves and pitting, and less noticeable grain relief. Hence, it can be deduced that, for these two specimens, the mixed lubrication regime was probably operative at these loads (1 N-2 N) which contradicts with the lubrication mode inferred from the Stribeck curve, in Figures 5.15 and 5.30.

At 4 N, no grooves were observed in the ZTA and ZTA-additives, Figures 5.6 (c) and 5.21 (c), but a few hardly noticeable grooves were found in the wear track of the commercial specimen, Figure 5.34 (c). In all specimens, some level of differential wear occurred at 4 N, but was more explicit in the ZTA. The 3D AFM and SEM images affirmed that the grains protruding out of the surface were zirconia. In the ZTA-additives (1) specimen, the protuberance of zirconia grains was also demonstrated in the TEM, section 6.2.5. In addition, a layer seemed to be formed on the surface which might be the mixture of protein and wear debris. At this load the predominant wear mechanism was pitting which caused a stark difference in the morphology of the wear track, compared to the lower loads, which is in line with the observation of Le et al. [158]. This huge morphological difference was more conspicuous in the ZTA and the commercial specimen. This is in agreement with the increase in their specific wear rate by an order of magnitude. In the ZTA, this behaviour might be due to the change in the lubrication regime, from full fluid to mixed lubrication [14]. On the other hand, in the case of the commercial specimen, the abrupt COF jump was the reason, which occurred upon increasing the contact pressure from 1578 MPa (2 N) to 1988 MPa (4 N).

In addition to the intergranular fracture, formation of transgranular cleavage fracture in the alumina grains was also conspicuous at 4 N as represented in Figures 5.6 (c), 5.21 (c), 5.34 (c). The cleavage fracture takes place on certain crystal planes, leading to failure along those planes. It is also reported that transgranular cracks in alumina grains are generally formed to counteract the energy brought about during the tribo-contact [15]. As noticed in the SEM and AFM images, it appears that preferential loss first takes place in alumina grains, through this fracture along the crystal orientations which are probably more brittle [14]. This is in contrast with the observation of Le et al., who reported zirconia particles were lost preferentially to the alumina grains [158]. The SEM micrograph in Figure 5.21 (c) showed both transgranular and intergranular fractures in the platelet grains. However, it is believed that these platelet grains improve the toughening mechanism through prolongation of the crack pathway. The presence of transgranular fractures in zirconia grains was the most discernible difference in the morphology of the commercial specimen, since no evident fracture was present in the zirconia in the other two specimens. This might be due to the much smaller grain size of the zirconia in both ZTA and ZTA-additives (1) than the commercial sample that was shown to inhibit phase transformation and thereby to prohibit crack formation at 4 N load (~ 1988 MPa).

At 8 N, unlike 4 N, the presence of the grooves was clear in all specimens, indicating the operation of the 3rd body abrasion wear mechanism. As evidenced by the SEM and AFM images, ZTA and ZTA-Additives (1) exhibited similar or maybe even less pitting at this load, compared to at 4 N. This was in agreement with the specific wear rate, measured in parts 5.1.2.1 and 5.2.2.1. On the other hand, the commercial specimen exhibited a much higher degree of wear, coupled with extensive transgranular and intergranular fracture and chipping, in both zirconia and alumina grains. It is believed that chipping is the result of the cleavage type fracture.

At 16 N, the wear produced a considerable amount of wear debris in the specimens. This debris, as shown in Figure 5.21 (e), was found in two forms, called "smeared" (white square) and "compacted" (red square) and this was in agreement with what was reported by Zeng et al. [315]. The smeared wear debris was distributed randomly within the scar, on the edges and in some regions, it was presented as a rolled shape sheet of a layer (white circle), Figure 5.21 (e). This observation was in line with Nevelos et al., reporting that the appearance of this wear debris was similar to the one observed on an explanted alumina hip joints [316]. Many authors also believe that the presence of this "roll shaped debris" is beneficial, since it coincides with the low wear rate. As evidenced by Rainforth et al., these rolls are formed due to the removal of amorphous tribo-film which later roll up because of the residual stresses within the film [14]. Accordingly, 3D AFM images of the ZTA specimen, as shown in Figure 5.6 (e), represented some degree of height difference in grains, at this load.

One of the reasons that some grains appear to be higher than their neighbouring grains might be the random deposition of fairly thick patches of agglomerated wear debris. As shown in Figure 5.34 (e) for the commercial sample, some grains appear to be higher than their neighbouring grains (white circle). Differential wear is possibly not the reason for this, due to the high contact pressure at this load. So, presumably the difference in height is due to the removal and wear of their surrounding grains revealing the survived grains as higher.

At 32 N, the presence of cracks was quite obvious inside a few of the voids in Figures 5.6 (f) and 5.34 (f). These cracks were formed through sequential steps. Once the surface breaks up and losses its integrity in a particular region, the wear debris, possibly mixed with bovine serum, is displaced into the voids as these are recesses on the surface. The cracking in this material is probably a result of drying the sample after testing, which results in dehydration and the formation of cracks. The

evolution of these amorphous patches (mixture of a proteinaceous layer with wear debris) results in the formation of a more wear resistant material which often happens during wear transition. More details are given in part 6.2.5, about the constituent elements forming these types of layers. The platelet grains were also noticeable, looking mainly untouched although almost all of their neighbouring grains were totally removed. In contrast, some indications suggested that these elongated grains experienced both intergranular and transgranular fractures at 4 N. Consequently, the contradictory behaviour of these grains might be correlated to their crystal orientation, i.e. these grains are more brittle at some particular orientations, hence they get worn more [14].

6.2.4 Phase changes of the worn surface by Raman spectroscopy

For both ZTA and ZTA-additives the Raman spectra at different loads did not display any phase transformation in any spectra even at the highest applied load, Figures 5.8 and 5.22. It was expected that by increasing the contact pressure over the surface, tetragonal zirconia would transform into monoclinic. However, for these two specimens, no sign of transformation was observed by this technique, even under 32 N. The reason for this behaviour could be attributed to the small grain size of zirconia that could not trigger the induced phase transformation. The identified Raman bands described below belong to the original unworn surfaces. A recent study showed that the compressive and tensile residual stresses shift the Raman bands towards higher and lower frequencies, respectively [16].

As reported by Clarke and Adar [228], Raman spectra of tetragonal zirconia includes six characteristic bands at 148 cm^{-1}, 264 cm^{-1}, 319 cm^{-1}, 461cm^{-1}, 606 cm^{-1} and 643 cm^{-1}, Figure 5.7. The bands at 643 cm^{-1} and 606 cm^{-1} can be assigned to the Zr-O_I stretching. The lines at 319 cm^{-1} and 461 cm^{-1} belong to the coupling of O_I (or O_{II})-Zr-O_I (or O_{II}) bending and Zr-O_I and Zr-O_{II} stretching. The band at 264 cm^{-1} is related to Zr-O_{II} stretching and the one at 148 cm^{-1} is mainly linked to O_I-Zr-O_I and Zr-O_I-Zr bending [227, 317]. The coordination numbers for O_I, O_{II} and Zr in tetragonal and monoclinic zirconia are listed in Table 6.1.

Table 6. 1- The coordination number for O_I, O_{II} and Zr in tetragonal and monoclinic zirconia.

Phase	Coordination		
	Zr	O_I	O_{II}
Monoclinic	7	3	4
Tetragonal	8	4	4

In contrast to ZTA and ZTA-additives, the commercial specimen displayed well-defined bands correlated with the monoclinic phase in addition to the tetragonal phase. These locally polymorphic transformations are due to the high contact pressure [229]. As shown in Figure 5.35, the amount of the monoclinic phase increasing significant with increase in load.

In addition, the zirconia grain size was about twice as large in the commercial sample compared to the other specimens; hence, the t→m transformation was triggered and easily detected. It is worth mentioning that the presence of the monoclinic phase was also detected on the pristine surface of the commercial specimen. This observation is in line with the results reported by Pezzotti et al. [16]. Figure 6.2 shows that the amount of the monoclinic phase in BIOLOX®delta on the surface of the as-received specimens has decreased in consecutive years between 2005 - 2015. This has been because of a reduction in the zirconia grain size, which has reduced the transformability of the zirconia. The zirconia grain sizes for the ZTA-Additives and the commercial sample are superimposed on the graph in Figure 6.2. This shows that the observation of monoclinic phase for the commercial sample, but not for the ZTA-Additives is in-line with the observations of Pezzotti et al.

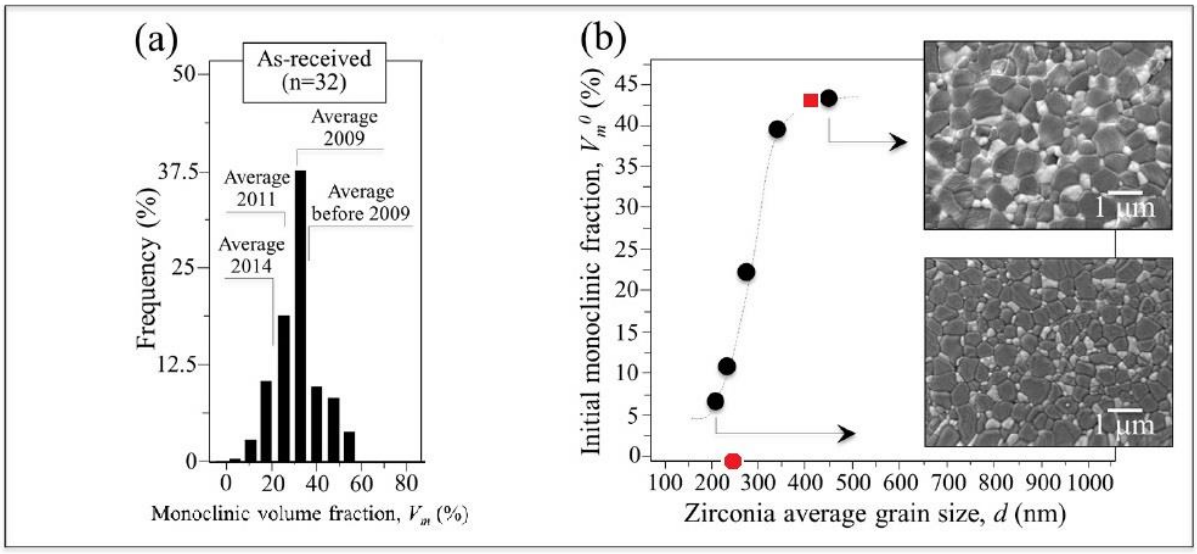

Figure 6.2. (a) Histogram exhibiting the range of the initial monoclinic volume fraction for BIOLOX®delta components released during the years (b) The graph shows the relationship between the average size of the zirconia in the BIOLOX®delta and ZTA-additives and their corresponding initial monoclinic fraction - black circles (measured by Pezzoti et al.) and the red square (measured in this study) represent the BIOLOX®delta and the red circle (measured in this study) represent the ZTA-additives [16]**.**

Although, in most of the studies, 18 characteristic bands have been attributed to monoclinic zirconia, only four bands corresponding to this phase were observed in this study, at 180 cm^{-1}, 190 cm^{-1}, 335 cm^{-1} and 476 cm^{-1}. As shown in Figure 5.35, the doublets at 180 cm^{-1} and 190 cm^{-1} and the line at 476 cm^{-1} were first obtained at small loads and they progressively intensified upon increasing the contact pressure. However, the line at 335 cm^{-1} was obtained at a contact pressure of ~1988 MPa (4 N), indicating the stress dependent nature of the polymorphic transformation in zirconia.

In agreement with Kim et al. [234], the bands at 180 cm^{-1}, 190 cm^{-1} and 335 cm^{-1} can be assigned to the $^{91.22}$Zr-$^{93.80}$Zr vibration and the line at 476 cm^{-1} can be attributed to the ^{16}O-^{18}O vibration [234]. Different assignments and more details exist about the aforementioned bands in both monoclinic and tetragonal phases, which are far beyond the scope of this study and can be found elsewhere [227, 234, 317, 318]. As displayed in Figures 5.8, 5.21 and 5.35, two additional peaks exist at 418 cm^{-1} and 380 cm^{-1} which belong to alumina. This observation is consistent with the other studies as well [229].

6.2.5 Characterisation of subsurface deformation

TEM foils were taken out of the three different specimens and were compared in order to characterise the deformation types, the polymorphic phase transformation in zirconia and the analysis of the (possible) tribolayer, formed under the 8 N load (~ 2504.8 MPa).

Among these specimens, BIOLOX®delta displayed the most significant damage on its surface, under the initial contact pressure of 2504.8 MPa, Figure 5.36. Surprisingly, despite the different morphological appearances of the worn tracks, all three specimens revealed fairly similar levels of subsurface damage and deformation in the alumina. As evidenced in Figures 5.11, 5.26 and 5.38, dislocations in alumina grains did not extend to more than a grain deep, and this is line with the observation of Le and Zeng et al. [161, 319]. In the work performed by Zeng et al. BIOLOX®forte alumina femoral heads and acetabular cups were examined in a hip-joint simulator (including micro-separation) and the damage was never further than one grain deep. On the other hand, as stated by Barceinas-Sanchez and Rainforth, a different sequence of wear behaviour exists in BIOLOX®delta and BIOLOX®forte since many more dislocations were observed at the grain boundaries of the monolithic alumina (BIOLOX®forte) compared to BIOLOX®delta [189]. The large amount of dislocations accumulated in the monolithic alumina, during the sliding wear, led to the formation of grain boundary micro cracking and subsequently the release of bits and pieces of material, leading to 3rd body abrasive wear. In contrast, Wang et al. reported the formation a higher density of dislocations and twins in the ZTA composite compared to the monolithic alumina. Such dense dislocations and twins are possibly the mechanism through which energy absorption and subsequently stress release occurs, leading to an increase in micro-fracture resistance [15]. In this research, a heterogeneous distribution of dislocations was observed in the alumina grains, i.e. some grains exhibited a small amount of dislocations while others were damage free, Figure 5.12 (a-c). This is consistent with the observation of other researchers [189]. In the ZTA specimen, formation of residual strain on the alumina next to the cracked zirconia was notable. This observation is in line with Le at al., who reported the presence of residual strain on an alumina grain next to the transformed zirconia grain. If the magnitude of the residual strain is high enough, it can produce various forms of deformation such as dislocations. Such strains are effective within a bulk material, since they can prohibit a propagating crack, but at a free surface, they can be added to contact stresses and increase the wear rate. In the ZTA-additives (1) specimen,

the main dislocation activities were observed around an intra-granular zirconia grain as depicted in Figure 5.24 (b). The incorporation of zirconia in the alumina grains (intragranular nanoparticle) is associated with the formation of residual stresses inside the alumina grain, due to the large thermal expansion mismatch between the two grains. The locally formed residual stresses are large enough, in some cases, to deform the matrix grain. As shown in Figure 5.24 (b), the residual stress appears in the form of a dislocation within the matrix, around zirconia (white arrow) and the neighbouring grains (red arrow). As reported by Bartolomé et al. [204], the nature of the residual stress in the alumina resulting from the intragranular zirconia is compressive and can reduce the rate of crack propagation or postpone the crack formation. In this regard, Palo et al. reported the compressive residual stresses formed inside the alumina grains due to the presence of intra-granular zirconia and acting as an effective factor in subcritical crack growth resistance. They also stated that a small fraction of the very fine intragranular zirconia grains was required to increase the crack resistance due to the compressive residual stresses. However, the transformation toughening mechanism would not happen, because of the small grain size of the zirconia [28]. Hence, the presence of intragranular zirconia grains might be another reason why ZTA and ZTA-additives possess fairly similar fracture toughness values as the commercial specimen, even though their zirconia grain size is about half that in the commercial material. In general, the formation of these residual stresses, due to the presence of zirconia grains, makes the predication of crack propagation pathway complicated. Another reason to justify this behaviour (the same fracture toughness value) is that the indentation could be providing enough stress on the surface to induce the phase transformation, whereas, the contact stresses exerted on the sample during the wear test might not have been high enough to activate the polymorphic transformation.

As shown in Figures 5.11-5.12 and, 5.24-5.25, almost all zirconia grains exhibited mottled contrast in the bright field mode of TEM (a characteristic of the tetragonal phase) in the ZTA and ZTA-additives (1) and (2). This was true apart from only one instance of monoclinic zirconia, which was found in the ZTA-additives (1), Figure 5.26 (a-b). Therefore, no t→m phase transformation occurred, presumably due to the small size of zirconia grains. This observation was consistent with the results obtained by the Raman spectroscopy. On the other hand, almost all zirconia grains in BIOLOX®delta exhibited twining, which is the main characteristic of the monoclinic phase, Figure 5.38 (a-b). In addition to this observation, the existence of the monoclinic phase was confirmed by the Raman spectra on an original specimen and also under various contact pressures.

The phase transformation occurring in BIOLOX®delta is due to the coarser grain size of zirconia, being twice the size of zirconia in the other two specimens. In other words, the larger grain size is more vulnerable to transforming from tetragonal to monoclinic, displaying a low phase stability [320]. Phase transformation (t→m) in zirconia grains is commonly associated with micro-cracking, but no evidence of micro-cracking was observed on the commercial specimen which was in line with Le et al. observation [158]. On the other hand, this author reported the preferential loss of zirconia in BIOLOX®delta, as a result of grain boundary cracking, originated from polymorphic transformation [321, 322] which is not consistent with this study. Principally, the possible role of zirconia phase transformation in wear resistance of composites is still debatable and needs more study.

Another observation through sub-surface characterisation was the existence of a transgranular fracture on a zirconia grain in the ZTA. Also, a transgranular fracture was observed on an alumina grain in the ZTA-Additives (1) with the grain boundary cracking around a platelet alumina. However, no trans and/or intra granular fracture was observed in the extracted foil from the commercial specimen, Figures 5.37 (a-b) and 5.38 (a-b). Further TEM specimens need to be explored to firmly confirm the presence of any type of subsurface fracture in the commercial specimen at other loads.

As shown in Figure 5.25, some zirconia grains were standing proud of the surface, possibly due to the differential wear which was discussed in part 6.2.3. These protruding grains were observed through AFM as well. However, since zirconia grains are much softer than alumina grains, it appeared odd that they were able to survive under such a high contact pressure.

The formation of a tribolayer was only observed on the subsurface of the ZTA foil 1, within the crater, Figure 5.10 (b). The elemental analysis confirmed the presence of a few elements including Al, O, Zr, Cu, Ca, and Au, Figure 5.10 (c). A common belief is that such a layer would generally be hydrated, however the hydration would not be detected by the electron microscopy. The thermal dehydration diagram for alumina displays the complexities of the chemistry of aluminum hydroxides and it also reveals the possible products that can form through the hydration reactions [306]. The work performed by Gee & Jennett, [306, 323] and Gate et al. [196] proposed that a soft tribolayer of alumina hydroxide can be formed at a low temperature. They proposed that the initial requirement for the formation of a hydroxide layer is the existence of finely scattered alumina

debris. These debris are then forced into the crater under the high pressure of the local contacts between the counter bodies. Subsequently, under the high pressure and increased temperature, the hydroxide and alumina react at the wear interfaces. Hydroxide films continue to fill the depressions until flattening of the asperities is completed and a very smooth surface is formed, Figure 6.3 [306].

Calcium was also one of the elements formed in the tribolayer, which was probably originated from the new-born calf serum solution and this is in line with Zeng et al. observation [324].

Principally, the information obtained through the TEM analysis in terms of the very smooth and flat surface and the occasional dislocation activities were consistent with the observed low specific wear rates.

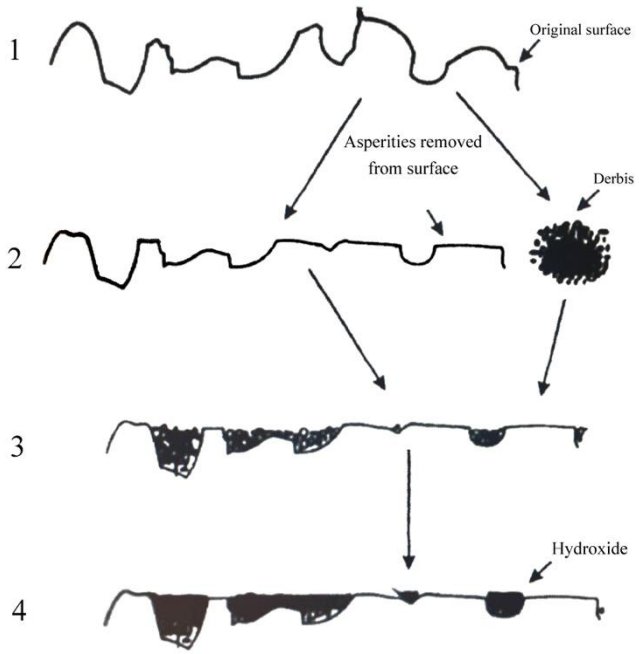

Figure 6.3. Schematic illustration of the routs proposed to form hydroxide layers [306]**.**

7 Conclusions

1. For powder processing, the combination of ammonium hydroxide, as a pH adjuster, and citric acid, as a dispersant, created electrostatic stabilization, leading to a well dispersed powder and consequently a homogeneous composite in the basic environment.
2. Freeze drying appeared to be more effective in forming a homogenous microstructure compared to oven drying. When drying in an oven, water would vaporize and subsequently the ionic strength of the suspension would greatly increase. Hence the slurry would be destabilised, which stimulates agglomeration. However, during freeze drying the particle-particle distance does not change.
3. TGA and DTA of the powder displayed endothermic peaks, correlated to the dihyrdroxylation of $Al(OH)_3$, which was accompanied by weight loss. Since alumina particles are super hydrophilic, they have a great tendency to absorb water, so presumably a few of the alumina particles would have interacted with the hydroxyl group, during the freeze drying process.
4. Thermal analysis displayed exothermic peaks and a gradual weight loss corresponding to the decomposition of $SrCO_3$, as expected, in a range of 750ºC-1200ºC. There was another exothermic peak around 1300ºC, which was presumably due to the formation of a solid solution between alumina and chromia.
5. The particle size analysis revealed the formation of possibly soft agglomerations after the calcination of Al_2O_3 and additives, conducted to release unwanted gases. However, re-milling of powders after calcination appeared to be remarkably effective in breaking up these agglomerations and in particle size reduction.
6. The onset of shrinkage for ZTA-additives specimens was about 42ºC lower than for the ZTA ones, which was probably due to the finer size of the starting particles and the constructive impact of additives on sintering mechanisms. Presumably, Cr_2O_3 effectively assists the enhancement of density, up to around ~ 1400º C but at higher temperatures prohibits the densification processes.
7. At 1550ºC, grain growth in ZTA-additives was more accelerated than in the ZTA, supposedly due to the presence of Cr ions.

8. Toughness measurements displayed a slight enhancement of fracture toughness in ZTA-additives due to the crack deflection mechanism, occurring through the formation of elongated strontium hexaluminate.
9. The optimum density, grain size and mechanical properties for ZTA and ZTA-additives, were obtained at 1470ºC-8 min and 1500ºC-5 min, respectively.
10. The enhancement of density and mechanical properties (fracture toughness/Vickers hardness) are achievable by incorporation of a specific amount of Cr_2O_3 and $SrCO_3$. In other words, the excess or lack of these additives would have a negative influence on these properties.
11. As anticipated, grain size refinement of ZTA-based composites improved the wear resistance of the specimens, by reducing both thermal mismatch stresses and slip length; hence a reduction in the dislocation density, which results in the prolongation of the transition from mild to severe wear.
12. At 32 N load, the impact of the Cr dopant appeared to delay the wear transition to higher loads. The incorporation of Cr_2O_3 introduces additional compressive stresses in the matrix by reducing the oxygen vacancy concentration in alumina. This highlights the importance of residual stresses in shifting the transition point (mild to severe), by changing the chemistry of the surface through appropriate additives. Furthermore, the presence of chromia explains the unprecedented two orders of magnitude increase in the specific wear rate of the ZTA.
13. For the ZTA specimen, the transition point from mild to severe wear was apparently between 16 N to 32 N (equivalent to ~3155.9 MPa and ~3976.2 MPa Hertzian contact pressure at the start of the test, respectively). Incorporation of the Cr_2O_3 appeared to delay the transition in BIOLOX® delta compared to the ZTA. As evidenced by the specific wear rate and topography of the surface, the commercial specimen appeared to be close to its transition point, at a 32 N load. On the other hand, due to the finer microstructure of the ZTA-additives, no evidence of transition in this specimen was observed.
14. It was inferred from the trend of the Stribeck curve and the images of the wear scars that in the ZTA specimen, full fluid film was possibly operating at 1 N and 2 N, with the mixed lubrication mode at higher loads. In contrast to the Stribeck curve behaviour, morphological images (SEM and AFM) were indicative of operation of the mixed lubrication mode in the ZTA-additives and BIOLOX® delta specimens at all loads.

15. The topography of the surfaces suggested similar wear mechanisms in the three materials at 1 N and 2 N. However, in contrast to ZTA-additives and BIOLOX®delta, tribo-chemical wear mechanism was possibly dominant in ZTA at 1 N and 2 N. This was compatible with the full fluid trend in the Stribeck curve, in which the differential wear was more conspicuous between grains.
16. At 4 N, extensive transgranular fractures were observed in the surface alumina grains, more extensively in the ZTA and BIOLOX® delta. This was consistent with the increase in the specific wear rate of these two specimens, by about an order of magnitude. Also, interestingly, the formation of microcracking was only conspicuous in the zirconia grains of the commercial specimen. This might be due to the much smaller grain size of zirconia in both ZTA and ZTA-additives, i.e. the fine zirconia grains are too small to transform to monoclinic zirconia.
17. At 16 N and 32 N, extensive patches of compacted wear debris was observed in the commercial, ZTA and ZTA-additives specimens. These layers were compacted in the voids or smeared on the surface. Also, cracks were evident inside the voids and were supposedly formed due to the dehydration of the bovine serum.
18. Although the presence of the platelet grains (strontium hexaluminate) has a positive impact on the toughening mechanism, their effect on wear mechanisms is controversial. Under a high contact pressure (32 N), some regions of alumina and zirconia were catastrophically worn, while platelet grains appeared untouched. However, in some regions, these grains experienced both intergranular and transgranular fractures. This might be due to the different crystallographic orientation of these elongated grains in the composite microstructure.
19. Despite applying a high contact pressure of ~3976 MPa (32 N), no polymorphic phase transformation was detected in zirconia grains by Raman spectroscopy, in either the ZTA and ZTA-additives, which was attributed to the fine grain size of the zirconia. However, a small amount of monoclinic phase was detected on the pristine surface of the BIOLOX® delta and increased in amount upon increasing the applied load. This was attributed to this material having a zirconia grain size about double that in the other materials.
20. Although no polymorphic transformation was observed through Raman spectroscopy in the ZTA and ZTA-additives, the value of the fracture toughness measured for these two materials was similar to the one for the commercial specimen, in which the monoclinic phase was detected. This behaviour could be explained through the fact that the indentation could be

introducing enough stress in the surface to induce the phase transformation, whereas the amount of contact stress inserted into the specimen may not have been high enough during the wear test to trigger the phase transformation. In addition, cracks were shown to have complicated interactions with zirconia grains by the local stress field, in which the propagation of a crack might be slowed down or hindered, depending on the nature of the residual stresses in the grain boundaries. For instance, introducing compressive residual stresses, associated with the presence of the intragranular zirconia, has been reported to increase crack resistance.

21. In line with the Raman spectroscopy results, cross section TEM sample of the commercial specimen exhibited the presence of the monoclinic phase. ZTA-additives, on the other hand, presented only one instance of polymorphic transformation. However, no evidence of phase transformation was observed in the ZTA cross section.
22. At 8 N, despite having different amounts of surface morphological features (mainly grain pull out and pitting which were more significant in the commercial specimen), all three specimens showed occasional, yet similar, dislocation activity levels in alumina grains, detected in TEM and within a grain's depth.
23. In the ZTA-additives, numerous dislocations were found around intragranular zirconia grains, implying that residual stresses were sufficient to produce dislocations.
24. The tribo-film was found inside a depression site in the ZTA and its constituents were detected to be Al, Zr, O, Ca, Au and Cu, through elemental analysis.

8 Future work

One of the main results obtained from this study was the impact of residual stresses on shifting of the wear transition point. To investigate the amount and the nature of the residual stresses (compressive or tensile) Cathodoluminescence Microscopy and Confocal Raman Spectroscopy would be useful. These techniques will assist in the study of the spread of residual stresses along with the formation of polymorphic transformations after the reciprocating sliding wear test under various ranges of loads. In terms of the composites to be explored, the study of ZTA-Cr_2O_3 and ZTA-SrO individually might provide further information about the contribution of these additives on both mechanical and chemical aspects of the wear. It is worth mentioning that each of these additives would be able to change the chemistry of the surface and hence alter the nature of the residual stresses. These composites with various grain size ranges are good candidates to be assessed for the distribution of residual stresses and subsequently the determination of the corresponding transformation point.

The products based on silicon nitride (Si_3N_4) are known for their good fracture toughness and have the potential to be introduced as the new generation of materials for hip joint replacement. Hence this category of materials should be explored in terms of their mechanical reliability and chemistry of the surface and be optimized in terms of mechanical properties. The optimized microstructure can then be tested under the reciprocating sliding wear test and subsequently be characterised via different techniques, including Cathodoluminescence microscopy to reveal the impact of silicon nitride on the wear resistance of the newly designed composite. FIB cross section and TEM specimens would be quite beneficial to provide complementary information about the types and amounts of deformations under the surface.

The results obtained during 10 hrs wear testing for the loads ranging between 1 N-4 N were quite similar to the ones performed by Ma [158] for 24 hrs. However, running the tests for loads between 8 N-32 N for 24 hrs are recommended. Furthermore, repeating of each test for about three times will probably provide more accurate results.

9 References

[1] N. Hinde, "Hip Replacements Increase In People Under 60," *HUFFPOST*, 2016. [Online]. Available: http://www.huffingtonpost.co.uk/2016/03/02/hip-replacement-increase-in-younger-people_n_9364420.html. [Accessed: 09-Nov-2017].

[2] J. Charnley, "Arthroplasty of the hip: a new operation," *Lancet*, vol. 277, no. 7187, pp. 1129–1132, 1961.

[3] M. A. Germain, A. Hatton, S. Williams, J. B. Matthews, M. H. Stone, J. Fisher, and E. Ingham, "Comparison of the cytotoxicity of clinically relevant cobalt–chromium and alumina ceramic wear particles in vitro," *Biomaterials*, vol. 24, no. 3, pp. 469–479, 2003.

[4] S.-A. Jacobsson, K. Djerf, and O. Wahlström, "20-Year Results of McKee-Farrar Versus Charnley Prosthesis.," *Clin. Orthop. Relat. Res.*, vol. 329, pp. S60–S68, 1996.

[5] V. Saikko, "Wear and friction properties of prosthetic joint materials evaluated on a reciprocating pin-on-flat apparatus," *Wear*, vol. 166, no. 2, pp. 169–178, 1993.

[6] J. Kusaka, K. Takashima, D. Yamane, and K. Ikeuchi, "Fundamental study for all-ceramic artificial hip joint," *Wear*, vol. 225, pp. 734–742, 1999.

[7] A. B. Joshi, M. L. Porter, I. A. Trail, L. P. Hunt, J. C. Murphy, and K. Hardinge, "Long-term results of Charnley low-friction arthroplasty in young patients," *Bone Joint J.*, vol. 75, no. 4, pp. 616–623, 1993.

[8] J. Charnley, "Post-operative Dislocation," in *Low Friction Arthroplasty of the Hip*, Springer, 1979, pp. 314–319.

[9] D. W. Howie, B. Vernon-Roberts, R. Oakeshott, and B. Manthey, "A rat model of resorption of bone at the cement-bone interface in the presence of polyethylene wear particles.," *JBJS*, vol. 70, no. 2, pp. 257–263, 1988.

[10] T. P. Schmalzried, M. Jasty, and W. H. Harris, "Periprosthetic bone loss in total hip arthroplasty. Polyethylene wear debris and the concept of the effective joint space.," *JBJS*, vol. 74, no. 6, pp. 849–863, 1992.

[11] T. Yamamoto, M. Saito, M. Ueno, T. Hananouchi, Y. Tokugawa, and K. Yonenobu, "Wear analysis of retrieved ceramic- on- ceramic articulations in total hip arthroplasty: Femoral head makes contact with the rim of the socket outside of the bearing surface," *J. Biomed. Mater. Res. Part B Appl. Biomater.*, vol. 73, no. 2, pp. 301–307, 2005.

[12] T. Shishido, K. Yamamoto, I. C. Clarke, T. Masaoka, M. Manaka, and T. Tateiwa, "Comparison of the results of a simulator study and retrieval implants in ceramic THA," in *Key Engineering Materials*, 2006, vol. 309, pp. 1277–1280.

[13] T. Shishido, K. Yamamoto, S. Tanaka, T. Masaoka, I. C. Clarke, and P. Williams, "A study for a retrieved implant of ceramic-on-ceramic total hip arthroplasty," *J. Arthroplasty*, vol. 21, no. 2, pp. 294–298, 2006.

[14] W. M. Rainforth, "The wear behaviour of oxide ceramics-A Review," *J. Mater. Sci.*, vol.

39, no. 22, pp. 6705–6721, 2004.

[15] Y. S. Wang, C. He, B. J. Hockey, P. I. Lacey, and S. M. Hsu, "Wear transitions in monolithic alumina and zirconia-alumina composites," *Wear*, vol. 181, pp. 156–164, 1995.

[16] G. Pezzotti, S. Affatato, A. Rondinella, M. Yorifuji, E. Marin, W. Zhu, B. McEntire, S. B. Bal, and K. Yamamoto, "In Vitro versus In Vivo Phase Instability of Zirconia-Toughened Alumina Femoral Heads: A Critical Comparative Assessment," *Materials (Basel).*, vol. 10, no. 5, p. 466, 2017.

[17] M. N. Rahaman, A. Yao, B. S. Bal, J. P. Garino, and M. D. Ries, "Ceramics for prosthetic hip and knee joint replacement," *J. Am. Ceram. Soc.*, vol. 90, no. 7, pp. 1965–1988, 2007.

[18] K. Knahr, *Tribology in total hip arthroplasty*. Springer Science & Business Media., 2011.

[19] A. L. Galvin, J. L. Tipper, L. M. Jennings, M. H. Stone, Z. M. Jin, E. Ingham, and I. Fisher, "Wear and biological activity of highly crosslinked polyethylene in the hip under low serum protein concentrations," *Proc Inst Mech Eng H*, vol. 221, no. 1, pp. 1–10, 2007.

[20] A. W. Schaffer, A. Pilger, C. Engelhardt, K. Zweymueller, and H. W. Ruediger, "Increased blood cobalt and chromium after total hip replacement," *J Toxicol Clin Toxicol*, vol. 37, no. 7, pp. 839–844, 1999.

[21] W. Brodner, J. G. Grohs, P. Bitzan, V. Meisinger, J. Kovarik, and R. Kotz, "Serum cobalt and serum chromium level in 2 patients with chronic renal failure after total hip prosthesis implantation with metal-metal gliding contact," *Z Orthop Ihre Grenzgeb*, vol. 138, no. 5, pp. 425–429, 2000.

[22] R. S. Nizard, L. Sedel, P. Christel, A. Meunier, M. Soudry, and J. Witvoet, "Ten-year survivorship of cemented ceramic-ceramic total hip prosthesis," *Clin Orthop Relat Res*, no. 282, pp. 53–63, 1992.

[23] M. Al-Hajjar, I. J. Leslie, J. Tipper, L. M. Jennings, S. Williams, and J. Fisher, "Delta ceramic on ceramic hip replacement," *Mater.Res. B Appl.Biomater*, vol. 81, 2007.

[24] W. E. Lee and W. M. Rainforth, *Ceramic microstructures: property control by processing*. London: Springer Science & Business Media., 1994.

[25] G. Maccauro, P. R. Iommetti, L. Raffaelli, P. F. Manicone, and R. Pignatello, *Alumina and Zirconia Ceramic for Orthopaedic and Dental Devices, Biomaterials Applications for Nanomedicine*. 2011.

[26] V. Naglieri, "Alumina-Zirconia composites:elaboration and characterization,in view of the orthopaedic application (PhD thesis)," Institut National des Sciences Appliquées de Lyon, 2010.

[27] S. Pramanik, A. K. Agarwal, and K. N. Rai, "Chronology of total hip joint replacement and materials development," *Trends Biomater. Artif. Organs*, vol. 19, no. 1, pp. 15–26, 2005.

[28] P. Palmero, L. Montanaro, H. Reveron, and J. Chevalier, "Surface Coating of Oxide Powders: A New Synthesis Method to Process Biomedical Grade Nano-Composites," *Materials (Basel).*, vol. 7, no. 7, pp. 5012–5037, 2014.

[29] C. Piconi, S. C. Condo, T. Kosmač, and J. Shen, "Alumina and zirconia-based ceramics for load-bearing applications. In Advanced Ceramic for Dentistry," in *Advanced Ceramics for Dentistry*, Elsevier Inc, 2014, pp. 219–253.

[30] C. Piconi and G. Maccauro, "Zirconia as a ceramic biomaterial," *Biomaterials*, vol. 20, no. 1, pp. 1–25, 1999.

[31] R. H. J. Hannink, P. M. Kelly, and B. C. Muddle, "Transformation toughening in zirconia-containing ceramics," *J. Am. Ceram. Soc.*, vol. 77, 2000.

[32] x. J. Jin, "Martensitic transformation in zirconia containing ceramics and its applications," 2005.

[33] J. Chevalier, C. Olagnon, and G. Fantozzi, "Crack propagation and fatigue in zirconia-based composites," *Composites*, pp. 525–530, 1999.

[34] P. Li, I. W. Chen, and J. E. Penner-Hahn, "Effect of dopants on zirconia stabilization—an X-ray absorption study:1, trivalent dopants.," 1994.

[35] A. A. Nogiwa Valdez, "Effect of ternary oxide additions on the hydrothermal degradation resistance of 3Y-TZP (PhD thesis)," The University of Sheffield, 2009.

[36] A. G. Evans, "Perspective on the Development of High-Toughness Ceramics," *J. Am. Ceram. Soc.*, 1990.

[37] R. C. Garvie, "The Occurrence of Metastable Tetragonal Zirconia as a Crystallite Size Effect," *J. Phys. Chem.*, vol. 69, no. 4, pp. 1238–1243, 1965.

[38] S. Shukla and S. Seal, "Mechanisms of room temperature metastable tetragonal phase stabilisation in zirconia," *Int. Mater. Rev.*, vol. 50, no. 1, pp. 45–64, 2005.

[39] J. F. Shackelford, *Bioceramics. Advanced ceramics*. Gordon and Breach science, 1999.

[40] H. McKellop and B. Lu, "Friction, lubrication and wear of polyethylene/metal and polyethylene/ceramic hip prostheses on a joint simulator," 1992.

[41] P. Kumar, M. Oka, K. Ikeuchi, K. Shimizu, T. Yamamuro, H. Okumura, and Y. Kotoura, "Low wear rate of UHMWPE against zirconia ceramic (Y-PSZ) in comparison to alumina ceramic and SUS 316L alloy," *J. Biomed. Mater. Res.*, vol. 25, no. 7, pp. 813–828, 1991.

[42] C. D. Hummer, R. H. Rothman, and W. J. Hozack, "Catastrophic failure of modular zirconia-ceramic femoral head components after total hip arthroplasty," *J Arthroplast.*, vol. 10, no. 6, pp. 848–850, 1995.

[43] A. H. De Aza, J. Chevalier, G. Fantozzi, M. Schehl, and R. Torrecillas, "Crack growth resistance of alumina, zirconia and zirconia toughened alumina ceramics for joint prostheses," *Biomaterials*, vol. 23, no. 3, pp. 937–945, 2002.

[44] R. C. Garvie, R. H. Hannink, and R. T. Pascoe, "Ceramic steel?," *Nature*, vol. 258, no. 5537, pp. 703–704, 1975.

[45] T. K. Gupta, F. F. Lange, and J. H. Bechtold, "Effect of stress-induced phase transformation on the properties of polycrystalline zirconia containing metastable tetragonal phase," *J.*

Mater. Sci., vol. 13, no. 7, pp. 1464–1470, 1978.

[46] P. Palmero, "Structural Ceramic Nanocomposites: A Review of Properties and Powders' Synthesis Methods," *Nanomaterials* , vol. 5, no. 2. 2015.

[47] E. Tsalouchou, M. J. Cattell, J. C. Knowles, P. Pittayachawan, and A. McDonald, "Fatigue and fracture properties of yttria partially stabilized zirconia crown systems," *Dent Mater*, vol. 24, no. 3, pp. 308–318, 2008.

[48] S. M. Kurtz, S. Kocagöz, C. Arnholt, R. Huet, M. Ueno, and W. L. Walter, "Advances in zirconia toughened alumina biomaterials for total joint replacement," *J. Mech. Behav. Biomed. Mater.*, vol. 31, pp. 107–116, 2014.

[49] P. F. Becher, K. B. Alexander, A. Bleier, S. B. Waters, and W. H. Warwick, "Influence of ZrO2 Grain Size and Content on the Transformation Response in the Al2O3─ZrO2 (12 mol% CeO2) System," *J. Am. Ceram. Soc.*, vol. 76, no. 3, pp. 657–663, 1993.

[50] N. Claussen, "Fracture Toughness of Al2O3 with an Unstabilized ZrO2Dispersed Phase," *J. Am. Ceram. Soc.*, vol. 59, no. 1–2, pp. 49–51, 1976.

[51] N. Claussen and M. Ruhle, "Design of transformation-toughened ceramics," in *"Science and Technology of Zirconia". Proc. 1 st. Int. Conf. held at Cleveland, Ohio, June 16-18, 1980. Advances in Ceramics*, 1980, vol. 3, p. 137.

[52] M. Ruhle, N.Claussen, and A. H. Heuer, "Transformation and Microcrack Toughening as Complementary Processes in Zr02-Toughened A1203," *Jounrnal Am. Ceram. Soc.*, vol. 69, no. 3, pp. 195–197, 1986.

[53] H.-G. Pfaff, R. Rack, and G. Willmann, "Long-term performance of a transformation toughened platelet reinforced alumina matrix composite," in *Key Engineering Materials*, 2001, vol. 218, pp. 541–542.

[54] C. Pecharromán, J. F. Bartolomé, J. Requena, J. S. Moya, S. Deville, J. Chevalier, G. Fantozzi, and R. Torrecillas, "Percolative mechanism of aging in zirconia-containing ceramics for medical applications," *Adv. Mater.*, vol. 15, no. 6, pp. 507–511, 2003.

[55] J. Chevalier and L. Gremillard, "Ceramics for medical applications: A picture for the next 20 years," *J. Eur. Ceram. Soc.*, vol. 29, no. 7, pp. 1245–1255, 2009.

[56] Z. Chen, K. K. Chawla, and M. Koopman, "Microstructure and mechanical properties of in situ synthesized alumina/Ba-β-alumina/zirconia composites," *Mater. Sci. Eng. A*, vol. 367, no. 1, pp. 24–32, 2004.

[57] N. Claussen, J. Steeb, and R. F. Pabst, "Effect on induced microcracking on the fracture toughness of ceramics," *Am. Ceram. Soc. Bull.*, vol. 56, no. 6, pp. 559–562, 1977.

[58] T. Kosmač, M. V Swain, and N. Claussen, "The role of tetragonal and monoclinic ZrO 2 particles in the fracture toughness of Al 2 O 3 ZrO 2 composites," *Mater. Sci. Eng.*, vol. 71, pp. 57–64, 1985.

[59] G. H. Campbell, M. Rühle, B. J. Dalgleish, and A. G. Evans, "Whisker toughening: a comparison between aluminum oxide and silicon nitride toughened with silicon carbide,"

J. Am. Ceram. Soc., vol. 73, no. 3, pp. 521–530, 1990.

[60] C. O. McHugh, T. J. Whalen, and M. Humenik, "Dispersion-Strengthened Aluminum Oxide," *J. Am. Ceram. Soc.*, vol. 49, no. 9, pp. 486–491, 1966.

[61] R. P. Wahi and B. Ilschner, "Fracture behaviour of composites based on Al2O3-TiC," *J. Mater. Sci.*, vol. 15, no. 4, pp. 875–885, 1980.

[62] M. Yoshimura, "Phase stability of zirconia," *Am. Ceram. Soc. Bull.;(United States)*, vol. 67, no. 12, 1988.

[63] N. Claussen, M. Ruhle, and A. H. Heuer, "Advances in Ceramics, vol. 12," *Sci. Technol. zirconia II*, 1984.

[64] R. A. Cutler, R. J. Mayhew, K. M. Prettyman, and A. V Virkar, "High-Toughness Ce-TZP/Al2O3 Ceramics with Improved Hardness and Strength," *J. Am. Ceram. Soc.*, vol. 74, no. 1, pp. 179–186, 1991.

[65] C. Schmid, E. Lucchini, O. Sbaizero, and S. Maschio, "The synthesis of calcium or strontium hexaluminate added ZTA composite ceramics," *J. Eur. Ceram. Soc.*, vol. 19, no. 9, pp. 1741–1746, 1999.

[66] M. Belmonte, A. J. Sanchez-Herencia, R. Moreno, P. Miranzo, J. S. Moya, and A. P. Tomsia, "In situ formation of CA6 platelets in Al2O3 and Al2O3/ZrO2 matrices," *Le J. Phys. IV*, vol. 3, no. C7, pp. C7-1443-C7-1447, 1993.

[67] S. Maity, S. Catterjee, and M. K. Basu, "Improvement of mechanical properties of zirconia-toughened alumina in presence of SrAl sub 1 sub 2 O sub 1 sub 9," *Third Euro-Ceram.*, vol. 3, pp. 731–736, 1993.

[68] A. R. West, *Solid state chemistry and its applications*. John Wiley & Sons, 2007.

[69] T. J. Davies, H. G. Emblem, C. S. Nwobodo, A. A. Ogwu, and V. Tsantzalou, "Preparation and properties of some alumina-chrome refractories," *J. Mater. Sci.*, vol. 26, no. 4, pp. 1061–1068, 1991.

[70] T. Hirata, K. Akiyama, and H. Yamamoto, "Sintering behavior of Cr 2 O 3–Al 2 O 3 ceramics," *J. Eur. Ceram. Soc.*, vol. 20, no. 2, pp. 195–199, 2000.

[71] G. Pezzotti, T. Saito, G. Padeletti, P. Cossari, and K. Yamamoto, "Nano-scale topography of bearing surface in advanced alumina/zirconia hip joint before and after severe exposure in water vapor environment," *J. Orthop. Res.*, vol. 28, no. 6, pp. 762–766, 2010.

[72] M. Jayaratna, M. Yoshimura, and S. Sōmiya, "Hot pressing 0f Y2O3-stabilized ZrO2 with Cr2O3 additions," *J. Mater. Sci.*, vol. 21, no. 2, pp. 591–596, 1986.

[73] H.-T. Lin, B.-Z. Liu, W. Chen, J.-L. Huang, and P. K. Nayak, "Study of color change and microstructure development of Al 2 O 3–Cr 2 O 3/Cr 3 C 2 nanocomposites prepared by spark plasma sintering," *Ceram. Int.*, vol. 37, no. 7, pp. 2081–2087, 2011.

[74] A. Z. A. Azhar, L. C. Choong, H. Mohamed, M. M. Ratnam, and Z. A. Ahmad, "Effects of Cr 2 O 3 addition on the mechanical properties, microstructure and wear performance of zirconia-toughened-alumina (ZTA) cutting inserts," *J. Alloys Compd.*, vol. 513, pp. 91–96,

2012.

[75] D. Gutknecht, J. Chevalier, V. Garnier, and G. Fantozzi, “Key role of processing to avoid low temperature ageing in alumina zirconia composites for orthopaedic application,” *J. Eur. Ceram. Soc.*, vol. 27, no. 2, pp. 1547–1552, 2007.

[76] S. Deville, J. Chevalier, G. Fantozzi, J. F. Bartolomé, J. Requena, J. S. Moya, R. Torrecillas, and L. A. Díaz, “Low-temperature ageing of zirconia-toughened alumina ceramics and its implication in biomedical implants,” *J. Eur. Ceram. Soc.*, vol. 23, no. 15, pp. 2975–2982, 2003.

[77] W. H. Tuan, R. Z. Chen, T. C. Wang, C. H. Cheng, and P. S. Kuo, “Mechanical properties of Al 2 O 3/ZrO 2 composites,” *J. Eur. Ceram. Soc.*, vol. 22, no. 16, pp. 2827–2833, 2002.

[78] D. Sarkar, D. Mohapatra, S. Ray, S. Bhattacharyya, S. Adak, and N. Mitra, “Nanostructured Al2O3–ZrO2 composite synthesized by sol–gel technique: powder processing and microstructure,” *J. Mater. Sci.*, vol. 42, no. 5, pp. 1847–1855, 2007.

[79] D. D. Jayaseelan, D. A. Rani, T. Nishikawa, H. Awaji, and F. D. Gnanam, “Powder characteristics, sintering behavior and microstructure of sol–gel derived ZTA composites,” *J. Eur. Ceram. Soc.*, vol. 20, no. 3, pp. 267–275, 2000.

[80] B.-T. Lee, J.-K. Han, and F. Saito, “Microstructure of sol–gel synthesized Al 2 O 3–ZrO 2 (Y 2 O 3) nano-composites studied by transmission electron microscopy,” *Mater. Lett.*, vol. 59, no. 2, pp. 355–360, 2005.

[81] Y. Matsumoto, K. Hirota, O. Yamaguchi, S. Inamura, H. Miyamoto, N. Shiokawa, and K. Tsuji, “Mechanical Properties of Hot Isostatically Pressed Zirconia-Toughened Alumina Ceramics Prepared from Coprecipitated Powders,” *J. Am. Ceram. Soc.*, vol. 76, no. 10, pp. 2677–2680, 1993.

[82] R. P. Rana, S. K. Pratihar, and S. Bhattacharyya, “Powder processing and densification behaviour of alumina–high zirconia nanocomposites using chloride precursors,” *J. Mater. Process. Technol.*, vol. 190, no. 1, pp. 350–357, 2007.

[83] F. Prete, A. Rizzuti, L. Esposito, A. Tucci, and C. Leonelli, “Highly Homogeneous Al2O3–ZrO2 Nanopowder via Microwave-Assisted Hydro-and SolvoThermal Synthesis,” *J. Am. Ceram. Soc.*, vol. 94, no. 10, pp. 3587–3590, 2011.

[84] J. R. Groza, “Nanosintering,” *Nanostructured Mater.*, vol. 12, no. 5, pp. 987–992, 1999.

[85] F. F. Lange, “Sinterability of Agglomerated Powders,” *MRS Proc.*, vol. 24, pp. 83–89, 1983.

[86] J. R. Groza and R. J. Dowding, “Nanoparticulate materials densification,” *Nanostructured Mater.*, vol. 7, no. 7, pp. 749–768, 1996.

[87] H. K. Christenson, “DLVO (Derjaguin-Landau-Verwey-Overbeek) theory and solvation forces between mica surfaces in polar and hydrogen-bonding liquids,” *J. Chem. Soc. Faraday Trans. 1*, vol. 80, no. 7, p. 1933, 1984.

[88] D. Kopeliovich, “Stabilization of colloid,” 2013. [Online]. Available: http://www.substech.com/dokuwiki/doku.php?id=stabilization_of_colloids. [Accessed: 09-

Nov-2017].

[89] J. Shi, "Steric Stabilization," Columbus, 2002.

[90] A. . Gurumoorthy and K. . Khan, "Polymers at interfaces: biological and non-biological Applications," *Recent Res. Sci. Technol.*, vol. 3, no. 2, pp. 80–86, 2011.

[91] Z. Zhou, P. J. Scales, and D. V Boger, "Chemical and physical control of the rheology of concentrated metal oxide suspensions," *Chem. Eng. Sci.*, vol. 56, no. 9, pp. 2901–2920, 2001.

[92] V. Ramakrishnan, Pradip, and S. G. Malghan, "The stability of alumina-zirconia suspensions," *Colloids Surfaces A Physicochem. Eng. Asp.*, vol. 133, no. 1–2, pp. 135–142, Feb. 1998.

[93] S. Novak, T. Kosmač, and V. Ribitsch, "Investigation of the powder characteristics and microstructures of alumina-zirconia composites," *Mater. Sci. Eng. A*, vol. 194, no. 2, pp. 235–241, May 1995.

[94] A. Leriche, G. Moortgat, F. Cambier, P. Homerin, F. Thevenot, G. Orange, and G. Fantozzi, "Preparation and characterization of a dispersion toughened ceramic for thermomechanical uses (ZTA). Part I: Material preparation. Characterization of microstructure," *J. Eur. Ceram. Soc.*, vol. 9, no. 3, pp. 169–176, 1992.

[95] G. Orange, G. Fantozzi, P. Homerin, F. Thevenot, A. Leriche, and F. Cambier, "Preparation and characterization of a dispersion toughened ceramic for thermomechanical uses (ZTA). Part II: Thermomechanical characterization. Effect of microstructure and temperature on toughening mechanisms," *J. Eur. Ceram. Soc.*, vol. 9, no. 3, pp. 177–185, Jan. 1992.

[96] Z. A. Munir, U. Anselmi-Tamburini, and M. Ohyanagi, "The effect of electric field and pressure on the synthesis and consolidation of materials: A review of the spark plasma sintering method," *J. Mater. Sci.*, vol. 41, no. 3, pp. 763–777, 2006.

[97] M. Suárez, A. Fernández, H. U. Kessel, J. Hennicke, J. L. Menéndez, R. Kirchner, R. Torrecillas, and T. Kessel, "Challenges and opportunities for spark plasma sintering: a key technology for a new generation of materials," in *sintering application.*, InTech, 2013.

[98] O. Guillon, J. Gonzalez-Julian, B. Dargatz, T. Kessel, G. Schierning, J. Räthel, and M. Herrmann, "Field-assisted sintering technology/spark plasma sintering: Mechanisms, materials, and technology developments," *Adv. Eng. Mater.*, vol. 16, no. 7, pp. 830–849, 2014.

[99] D. V. Quach, H. Avila-Paredes, S. Kim, M. Martin, and Z. A. Munir, "Pressure effects and grain growth kinetics in the consolidation of nanostructured fully stabilized zirconia by pulsed electric current sintering," *Acta Mater.*, vol. 58, no. 15, pp. 5022–5030, 2010.

[100] Z. Shen, M. Johnsson, Z. Zhao, and M. Nygren, "Spark Plasma Sintering of Alumina," *J. Am. Ceram. Soc.*, vol. 85, no. 8, pp. 1921–1927, Aug. 2002.

[101] Y. Zhou, K. Hirao, Y. Yamauchi, and S. Kanzaki, "Densification and grain growth in pulse electric current sintering of alumina," *J. Eur. Ceram. Soc.*, vol. 24, no. 12, pp. 3465–3470, 2004.

[102] S. Schwarz, A. M. Thron, J. Rufner, K. Benthem, and O. Guillon, "Low Temperature Sintering of Nanocrystalline Zinc Oxide: Effect of Heating Rate Achieved by Field Assisted Sintering/Spark Plasma Sintering," *J. Am. Ceram. Soc.*, vol. 95, no. 8, pp. 2451–2457, Aug. 2012.

[103] T. B. Holland, T. B. Tran, D. V. Quach, U. Anselmi-Tamburini, J. R. Groza, and A. K. Mukherjee, "Athermal and thermal mechanisms of sintering at high heating rates in the presence and absence of an externally applied field," *J. Eur. Ceram. Soc.*, vol. 32, no. 14, pp. 3675–3683, 2012.

[104] C. G. Goetzel and V. S. De Marchi, "ELECTRICALLY ACTIVATED PRESSURE-SINTERING (SPARK SINTERING) OF TITANIUM--ALUMINUM--VANADIUM ALLOY POWDERS.," Lockheed Palo Alto Research Lab., Calif., 1971.

[105] Y. Zhou, K. Hirao, Y. Yamauchi, and S. Kanzaki, "Effects of heating rate and particle size on pulse electric current sintering of alumina," *Scr. Mater.*, vol. 48, no. 12, pp. 1631–1636, 2003.

[106] E. A. Olevsky and L. Froyen, "Impact of Thermal Diffusion on Densification During SPS," *J. Am. Ceram. Soc.*, vol. 92, pp. S122–S132, Jan. 2009.

[107] T. B. Holland, U. Anselmi-Tamburini, D. V Quach, T. B. Tran, and A. K. Mukherjee, "Effects of local Joule heating during the field assisted sintering of ionic ceramics," *J. Eur. Ceram. Soc.*, vol. 32, no. 14, pp. 3667–3674, 2012.

[108] B. McWilliams and A. Zavaliangos, "Multi-phenomena simulation of electric field assisted sintering," *J. Mater. Sci.*, vol. 43, no. 14, pp. 5031–5035, 2008.

[109] D. S. and G. S. and R. T. and N. S. and N. P. and H. W. and R. S. and D. E. Wolf, "From nanoparticles to nanocrystalline bulk: percolation effects in field assisted sintering of silicon nanoparticles," *Nanotechnology*, vol. 22, no. 13, p. 135601, 2011.

[110] A. Becker, S. Angst, A. Schmitz, M. Engenhorst, J. Stoetzel, D. Gautam, H. Wiggers, D. E. Wolf, G. Schierning, and R. Schmechel, "The effect of Peltier heat during current activated densification," *Appl. Phys. Lett.*, vol. 101, no. 1, p. 13113, 2012.

[111] S. D. Antolovich and H. Conrad, "The effects of electric currents and fields on deformation in metals, ceramics, and ionic materials: An interpretive survey," *Mater. Manuf. Process.*, vol. 19, no. 4, pp. 587–610, 2004.

[112] R. Raj, M. Cologna, and J. S. C. Francis, "Influence of Externally Imposed and Internally Generated Electrical Fields on Grain Growth, Diffusional Creep, Sintering and Related Phenomena in Ceramics," *J. Am. Ceram. Soc.*, vol. 94, no. 7, pp. 1941–1965, Jul. 2011.

[113] Y. Makino, "Characteristics of sintering process based on pulsed high current," *New Ceram.*, vol. 10, no. 10, pp. 39–42, 1997.

[114] H. Tomino, H. Watanabe, and Y. Kondo, "Electric current path and temperature distribution for spark sintering," *J Jap Soc Powder Powder Met.*, vol. 44, no. 10, pp. 974–979, 1997.

[115] B. Yoon, E. Chin, and S. L. Kang, "Dedensification During Sintering of BaTiO3 Caused by the Decomposition of Residual BaCO3," *J. Am. Ceram. Soc.*, vol. 91, no. 12, pp. 4121–

4124, 2008.

[116] D. Jiang and A. K. Mukherjee, "The influence of oxygen vacancy on the optical transmission of an yttria–magnesia nanocomposite," *Scr. Mater.*, vol. 64, no. 12, pp. 1095–1097, 2011.

[117] A. Rečnik, J. Bruley, W. Mader, D. Kolar, and M. Rühle, "Structural and spectroscopic investigation of (111) twins in barium titanate," *Philos. Mag. B*, vol. 70, no. 5, pp. 1021–1034, 1994.

[118] F. Di Puccio and L. Mattei, "Biotribology of artificial hip joints.," *World J. Orthop.*, vol. 6, no. 1, pp. 77–94, 2015.

[119] D. F. Amanatullah, J. Landa, E. J. Strauss, J. P. Garino, S. H. Kim, and P. E. Di Cesare, "Comparison of surgical outcomes and implant wear between ceramic-ceramic and ceramic-polyethylene articulations in total hip arthroplasty," *J. Arthroplasty*, vol. 26, no. 6, pp. 72–77, 2011.

[120] G. H. Stafford, S. U. Islam, and J. D. Witt, "Early to mid-term results of ceramic-on-ceramic total hip replacement," *J Bone Jt. Surg Br*, vol. 93, no. 8, pp. 1017–1020, 2011.

[121] P. Damm, J. Dymke, R. Ackermann, A. Bender, F. Graichen, A. Halder, A. Beier, and G. Bergmann, "Friction in total hip joint prosthesis measured in vivo during walking," *PLoS One*, vol. 8, no. 11, pp. 1–8, 2013.

[122] Z. Bascarevic, Z. Vukasinovic, N. Slavkovic, B. Dulic, G. Trajkovic, V. Bascarevic, and S. Timotijevic, "Alumina-on-alumina ceramic versus metal-on-highly cross-linked polyethylene bearings in total hip arthroplasty: a comparative study," *Int. Orthop.*, vol. 34, no. 8, pp. 1129–1135, 2010.

[123] J. W. Mesko, J. A. D'Antonio, W. N. Capello, B. E. Bierbaum, and M. Naughton, "Ceramic-on-ceramic hip outcome at a 5-to 10-year interval: has it lived up to its expectations?," *J. Arthroplasty*, vol. 26, no. 2, pp. 172–177, 2011.

[124] N. Sugano, M. Takao, T. Sakai, T. Nishii, H. Miki, and K. Ohzono, "Eleven- to 14-year Follow-up Results of Cementless Total Hip Arthroplasty Using a Third-generation Alumina Ceramic-on-ceramic Bearing," *J. Arthroplasty*, vol. 27, no. 5, pp. 736–741, May 2012.

[125] K. Mai, M. E. Hardwick, R. H. Walker, S. N. Copp, K. A. Ezzet, and C. W. Colwell, "Early Dislocation Rate in Ceramic-on-Ceramic Total Hip Arthroplasty," *HSS J.*, vol. 4, no. 1, pp. 10–13, 2008.

[126] E. Garcia-Cimbrelo, E. Garcia-Rey, A. Murcia-Mazón, A. Blanco-Pozo, and E. Martí, "Alumina-on-Alumina in THA," *Clin. Orthop. Relat. Res.*, vol. 466, no. 2, pp. 309–316, 2008.

[127] Y.-H. Kim, Y. Choi, and J.-S. Kim, "Cementless total hip arthroplasty with ceramic-on-ceramic bearing in patients younger than 45 years with femoral-head osteonecrosis," *Int. Orthop.*, vol. 34, no. 8, pp. 1123–1127, Dec. 2010.

[128] G. E. Petsatodis, P. P. Papadopoulos, K. A. Papavasiliou, I. G. Hatzokos, F. G. Agathangelidis, and A. G. Christodoulou, "Primary cementless total hip arthroplasty with

an alumina ceramic-on-ceramic bearing," *J Bone Jt. Surg Am*, vol. 92, no. 3, pp. 639–644, 2010.

[129] Y.-K. Lee, Y.-C. Ha, J. J. Yoo, K.-H. Koo, K. S. Yoon, and H. J. Kim, "Alumina-on-Alumina Total Hip Arthroplasty," *J Bone Jt. Surg Am*, vol. 92, no. 8, pp. 1715–1719, 2010.

[130] E. Yeung, P. T. Bott, R. Chana, M. P. Jackson, I. Holloway, W. L. Walter, B. A. Zicat, and W. K. Walter, "Mid-Term Results of Third-Generation Alumina-on-Alumina Ceramic Bearings in Cementless Total Hip Arthroplasty," *J. Bone Jt. Surg.*, vol. 94, no. 2, pp. 138–144, 2012.

[131] W. N. Capello, J. A. D'Antonio, J. R. Feinberg, M. T. Manley, and M. Naughton, "Ceramic-on-ceramic total hip arthroplasty: update," *J. Arthroplasty*, vol. 23, no. 7, pp. 39–43, 2008.

[132] S.-H. Baek and S.-Y. Kim, "Cementless total hip arthroplasty with alumina bearings in patients younger than fifty with femoral head osteonecrosis," *J Bone Jt. Surg Am*, vol. 90, no. 6, pp. 1314–1320, 2008.

[133] J. J. Yoo, Y.-M. Kim, K. S. Yoon, K.-H. Koo, W. S. Song, and H. J. Kim, "Alumina-on-alumina total hip arthroplasty," *J Bone Jt. Surg Am*, vol. 87, no. 3, pp. 530–535, 2005.

[134] L. Savarino, N. Baldini, G. Ciapetti, A. Pellacani, and A. Giunti, "Is wear debris responsible for failure in alumina-on-alumina implants? Clinical, histological, and laboratory investigations of 30 revision cases with a median follow-up time of 8 years," *Acta Orthop.*, vol. 80, no. 2, pp. 162–167, 2009.

[135] A. J. Lipowitz and C. . Newton, *Degenerative joint disease and traumatic arthritis. Textbook of small animal orthopaedics*. International Veterinary Information Service, Ithaca., 1985.

[136] G. Bergmann, F. Graichen, A. Rohlmann, N. Verdonschot, and G. H. van Lenthe, "Frictional heating of total hip implants, Part 1: measurements in patients," *J. Biomech.*, vol. 34, no. 4, pp. 421–428, 2001.

[137] A. Rana, "Wear resistant alumina for artificial hip replacements (PhD thesis)," University of Sheffield, 2013.

[138] J. E. Nevelos, F. Prudhommeaux, M. Hamadouche, C. Doyle, E. Ingham, A. Meunier, A. B. Nevelos, L. Sedel, and J. Fisher, "Comparative analysis of two different types of alumina-alumina hip prosthesis retrieved for aseptic loosening," *Bone Joint J.*, vol. 83, no. 4, pp. 598–603, 2001.

[139] W. L. Walter, G. M. Insley, W. K. Walter, and M. A. Tuke, "Edge loading in third generation alumina ceramic-on-ceramic bearings: Stripe wear," *J. Arthroplasty*, vol. 19, no. 4, pp. 402–413, 2004.

[140] J. Nevelos, E. Ingham, C. Doyle, R. Streicher, A. Nevelos, W. Walter, and J. Fisher, "Microseparation of the centers of alumina-alumina artificial hip joints during simulator testing produces clinically relevant wear rates and patterns," *J. Arthroplasty*, vol. 15, no. 6, pp. 793–795, Jun. 2000.

[141] A. Hatton, E. Ingham, J. B. Matthews, and J. Fisher, "Cytokine release by human peripheral

blood macrophages after stimulation with alumina ceramic particles in vitro," in *Sixth World Congress of Biomaterials, Hawaii, USA*, 2000, p. 1186.

[142] M. J. Nine, D. Choudhury, A. C. Hee, R. Mootanah, and N. A. A. Osman, "Wear debris characterization and corresponding biological response: Artificial hip and knee joints," *Materials (Basel).*, vol. 7, no. 2, pp. 980–1016, 2014.

[143] N. S. Bonnaig, R. A. Freiberg, and A. A. Freiberg, "Total hip arthroplasty with ceramic-on-ceramic bearing failure from third-body wear," *Orthopedics*, vol. 34, no. 2, p. 132, 2011.

[144] S. C. Scholes and T. J. Joyce, "Ceramic-On-Ceramic Joints: A Suitable Alternative Material Combination?," *Adv. Biomater. Sci. Biomed. Appl.*, pp. 539–558, 2013.

[145] Z. M. Jin, M. Stone, E. Ingham, and J. Fisher, "(v) Biotribology," *Curr. Orthop.*, vol. 20, no. 1, pp. 32–40, 2006.

[146] I. M. Hutchings, "Tribology: friction and wear of engineering materials: Edward Arnold,1992, 352pp, ε19. 95 paperback, ISBN 0 340 56184," *Mater. Des.*, vol. 13, no. 3, p. 187, 1992.

[147] J. Fisher and D. Dowson, "Tribology of total artificial joints," *Proc. Inst. Mech. Eng. Part H J. Eng. Med.*, vol. 205, no. 2, pp. 73–79, 1991.

[148] K. J. Brown, J. R. Atkinson, D. Dowson, and V. Wright, "The wear of ultrahigh molecular weight polyethylene and a preliminary study of its relation to the in vivo behaviour of replacement hip joints," *Wear*, vol. 40, no. 2, pp. 255–264, Nov. 1976.

[149] R. . . Rose and E. L. Radin, "Wear of polyethylene in the total hip prosthesis.," *Clin. Orthop. Relat. Res.*, vol. 170, pp. 107–115, 1982.

[150] E. von Recum, A. F, *Handbook Of Biomaterials Evaluation: Scientific,Technical And Clinical Testing Of Implant Materials*. CRC Press, 1998.

[151] J. B. Medley, J. J. Krygier, J. D. Bobyn, F. W. Chan, and M. Tanzer, "Metal-metal bearing surfaces in the hip: investigation of factors influencing wear," *Trans Orthop Res Soc*, vol. 20, no. 2, p. 765, 1995.

[152] J. Sotres and T. Arnebrant, "Experimental Investigations of biological lubrication at the nanoscale: the cases of synovial joints and the oral cavity," *Lubricants*, vol. 1, no. 4, pp. 102–131, 2013.

[153] M. P. Gispert, A. P. Serro, R. Colaco, and B. Saramago, "Friction and wear mechanisms in hip prosthesis: Comparison of joint materials behaviour in several lubricants," *Wear*, vol. 260, no. 1, pp. 149–158, 2006.

[154] Z. JIN, S. WILLIAMS, J. TIPPER, E. INGHAM, and J. FISHER, "Tribology of hip joints from natural hip joints, cartilage substitution, artificial replacements to cartilage tissue engineering," *J. Biomech. Sci. Eng.*, vol. 1, no. 1, pp. 69–81, 2006.

[155] S. Affatato, M. Spinelli, M. Zavalloni, C. Mazzega-Fabbro, and M. Viceconti, "Tribology and total hip joint replacement: current concepts in mechanical simulation," *Med. Eng. Phys.*, vol. 30, no. 10, pp. 1305–1317, 2008.

[156] S. Begin-Colin, A. Mocellin, J. Von Stebut, K. Bordji, and D. Mainard, "Al2O3 and Al2O3--TiN wear resistance in a simulated biological environment," *J. Mater. Sci.*, vol. 33, no. 11, pp. 2837–2843, 1998.

[157] H. J. Früh, G. Willmann, and H. G. Pfaff, "Wear characteristics of ceramic-on-ceramic for hip endoprostheses," *Biomaterials*, vol. 18, no. 12, pp. 873–876, 1997.

[158] L. Ma, "Wear Behaviour of Biolox ® delta ceramic Composite for Joint Replacements (PhD thesis)," University of Sheffield, 2010.

[159] M. Manaka, I. C. Clarke, K. Yamamoto, T. Shishido, A. Gustafson, and A. Imakiire, "Stripe wear rates in alumina THR—comparison of microseparation simulator study with retrieved implants," *J. Biomed. Mater. Res. Part B Appl. Biomater.*, vol. 69, no. 2, pp. 149–157, 2004.

[160] I. C. Clarke, D. D. Green, P. A. Williams, K. Kubo, G. Pezzotti, A. Lombardi, A. Turnbull, and T. K. Donaldson, "Hip-simulator wear studies of an alumina-matrix composite (AMC) ceramic compared to retrieval studies of AMC balls with 1–7 years follow-up," *Wear*, vol. 267, no. 5, pp. 702–709, 2009.

[161] P. Zeng, B. J. Inkson, and W. M. Rainforth, "Characterisation of alumina hip-joint wear by FIB microscopy," in *Journal of Physics: Conference Series*, 2006, vol. 26, no. 1, p. 343.

[162] J. E. Nevelos, E. Ingham, C. Doyle, J. Fisher, and A. B. Nevelos, "Analysis of retrieved alumina ceramic components from Mittelmeier total hip prostheses," *Biomaterials*, vol. 20, no. 19, pp. 1833–1840, 1999.

[163] J. Fisher, Z. Jin, J. Tipper, M. Stone, and E. Ingham, "PRESIDENTIAL GUEST LECTURE: Tribology of Alternative Bearings.," *Clin. Orthop. Relat. Res.*, vol. 453, pp. 25–34, 2006.

[164] J. T. Burwell, "Survey of possible wear mechanisms," *Wear*, vol. 1, no. 2, pp. 119–141, 1957.

[165] B. Gueroult and K. Cherif, "State of the art review on friction and wear mechanisms of ceramics," *J. Can. Ceram. Soc.*, vol. 63, no. 2, pp. 132–142, 1994.

[166] J. C. Walker, "Lubricated sliding wear of some aluminium alloy composites (PhD thesis)," University of Sheffield, 2006.

[167] J. A. Williams, "Engineering tribology Oxford University Press," *New York*, 1994.

[168] K. C. Ludema, *Friction, wear, lubrication: a textbook in tribology*. CRC press, 1996.

[169] W. M. Rainforth, "The sliding wear of ceramics," *Ceram. Int.*, vol. 22, no. 5, pp. 365–372, 1996.

[170] R. W. Rice, "Micromechanics of microstructural aspects of ceramic wear," in *Proceedings of the 9th Annual Conference on Composites and Advanced Ceramic Materials: Ceramic Engineering and Science Proceedings, Volume 6, Issue 7/8*, 1985, pp. 940–958.

[171] C. S. Yust and R. G. Bayer, *Selection and use of wear tests for ceramics*. Philadelphia: STP-1010, American Society for Testing and Materials, 1988.

[172] R. Narayanan Manibharathi, "Study on Hertzian cone crack in brittle materials and experimental investigation of fretting wear in bearings using bearing fretting test rig (Doctoral dissertation)," Purdue University, 2011.

[173] G. Biresaw and K. L. Mittal, *Surfactants in tribology*, vol. 4. CRC Press, 2014.

[174] D. Kopeliovich, "Mechanisms of wear," 2015. [Online]. Available: http://www.substech.com/dokuwiki/doku.php?id=mechanisms_of_wear. [Accessed: 01-Jan-2017].

[175] R. G. Bayer, *Engineering Design for Wear, Revised and Expanded*. CRC Press, 2004.

[176] B. R. Lawn and M. V Swain, "Microfracture beneath point indentations in brittle solids," *J. Mater. Sci.*, vol. 10, no. 1, pp. 113–122, 1975.

[177] G. D. Quinn and J. A. Salem, "Effect of Lateral Cracks on Fracture Toughness Determined by the Surface-Crack-in-Flexure Method," *J. Am. Ceram. Soc.*, vol. 85, no. 4, pp. 873–880, 2002.

[178] Q. An, W. Ming, and M. Chen, "Experimental Investigation on Cutting Characteristics in Nanometric Plunge-Cutting of BK7 and Fused Silica Glasses," *Materials (Basel).*, vol. 8, no. 4, pp. 1428–1441, 2015.

[179] H. S. C. Metselaar, "Thermally induced wear transition in ceramics," *Univ. Twente, Enschede*, 2001.

[180] B. Kerkwijk, "Wear and friction of nanostructured zirconia and alumina ceramics and composites," 1971.

[181] H. Czichos, D. Klaffke, E. Santner, and M. Woydt, "Advances in tribology: the materials point of view," *Wear*, vol. 190, no. 2, pp. 155–161, 1995.

[182] G. W. Stachowiak and G. B. Stachowiak, "Environmental effects on wear and friction of toughened zirconia ceramics," *Wear*, vol. 160, no. 1, pp. 153–162, 1993.

[183] K.-H. Zum Gahr, "Modeling and microstructural modification of alumina ceramic for improved tribological properties," *Wear*, vol. 200, no. 1, pp. 215–224, 1996.

[184] P. Zeng, "Biocompatible alumina ceramic for total hip replacements," *Tribol. Surfaces Interfaces*, 2013.

[185] K. H. Z. Gahr, *Microstructure and Wear of Materials*. Elsevier Science, 1987.

[186] B. Basu and M. Kalin, *Tribology of ceramics and composites: materials science perspective*. John Wiley & Sons, 2011.

[187] M. Miranda-Martinez, R. W. Davidge, and F. L. Riley, "Grain size effects on the wet erosive wear of high-purity polycrystalline alumina," *Wear*, vol. 172, no. 1, pp. 41–48, 1994.

[188] R. W. Davidge and F. L. Riley, "Grain-size dependence of the wear of alumina," *Wear*, vol. 186, pp. 45–49, 1995.

[189] J. D. O. Barceinas-Sanchez and W. M. Rainforth, "On the role of plastic deformation during

the mild wear of alumina," *Acta Mater.*, vol. 46, no. 18, pp. 6475–6483, 1998.

[190] H. Liu and M. E. Fine, "Modeling of Grain-Size-Dependent Microfracture-Controlled Sliding Wear in Polycrystalline Alumina," *J. Am. Ceram. Soc.*, vol. 76, no. 9, pp. 2393–2396, 1993.

[191] S. Cho, B. J. Hockey, B. R. Lawn, and S. J. Bennison, "Grain-Size and R-Curve Effects in the Abrasive Wear of Alumina," *J. Am. Ceram. Soc.*, vol. 72, no. 7, pp. 1249–1252, 1989.

[192] L. Zhang, X. Qu, B. Duan, X. He, and M. Qin, "Effect of porosity on wear resistance of SiC p / Cu composites prepared by pressureless infiltration," *Trans. Nonferrous Met. Soc. China*, vol. 18, no. 5, pp. 1076–1082, 2008.

[193] Y. Wang and S. M. Hsu, "Wear and wear transition mechanisms of ceramics," *Wear*, vol. 195, no. 1, pp. 112–122, 1996.

[194] K. Adachi and K. Kato, "Formation of smooth wear surfaces on alumina ceramics by embedding and tribo-sintering of fine wear particles," *Wear*, vol. 245, no. 1, pp. 84–91, 2000.

[195] P. L. Menezes, S. P. Ingole, M. Nosonovsky, S. V Kailas, and M. R. Lovell, *Tribology for scientists and engineers*. New York: Springer, 2013.

[196] R. S. Gates, M. Hsu, and E. E. Klaus, "Tribochemical mechanism of alumina with water," *Tribol. Trans.*, vol. 32, no. 3, pp. 357–363, 1989.

[197] S. Jahanmir, "Wear transitions and tribochemical reactions in ceramics," *Proc. Inst. Mech. Eng. Part J J. Eng. Tribol.*, vol. 216, no. 6, pp. 371–385, 2002.

[198] M. Kalin, S. Novak, and J. Vižintin, "Wear and friction behavior of alumina ceramics in aqueous solutions with different pH," *Wear*, vol. 254, no. 11, pp. 1141–1146, 2003.

[199] X. Dong, S. Jahanmir, and S. M. Hsu, "Tribological Characteristics of α-Alumina at Elevated Temperatures," *J. Am. Ceram. Soc.*, vol. 74, no. 5, pp. 1036–1044, 1991.

[200] M. Woydt and K.-H. Habig, "High temperature tribology of ceramics," *Tribol. Int.*, vol. 22, no. 2, pp. 75–88, 1989.

[201] F. Kern, P. Palmero, F. G. Marro, and A. Mestra, "Processing of alumina-zirconia composites by surface modification route with enhanced hardness and wear resistance," *Ceram. Int.*, vol. 41, no. 1, pp. 889–898, 2015.

[202] A. K. Pandey, U. R. Jena, and K. Biswas, "In vitro ageing and wear behaviour of ceria stabilized zirconia toughened alumina (CSZ-TA) bio-ceramic," *Mater. Chem. Phys.*, vol. 146, no. 3, pp. 456–463, 2014.

[203] A. K. Dey and K. Biswas, "Dry sliding wear of zirconia-toughened alumina with different metal oxide additives," *Ceram. Int.*, vol. 35, no. 3, pp. 997–1002, 2009.

[204] J. F. Bartolomé, A. H. De Aza, A. Martin, J. Y. Pastor, J. Llorca, R. Torrecillas, and G. Bruno, "Alumina/zirconia micro/nanocomposites: A new material for biomedical applications with superior sliding wear resistance," *J. Am. Ceram. Soc.*, vol. 90, no. 10, pp. 3177–3184, 2007.

[205] J. F. Bartolomé, C. Pecharromán, J. S. Moya, A. Martín, J. Y. Pastor, and J. Llorca, "Percolative mechanism of sliding wear in alumina/zirconia composites," *J. Eur. Ceram. Soc.*, vol. 26, no. 13, pp. 2619–2625, 2006.

[206] Y. J. He, A. J. A. Winnubst, A. J. Burggraaf, H. Verweij, P. G. T. van der Varst, and G. de With, "Sliding wear of ZrO 2-Al 2 O 3 composite ceramics," *J. Eur. Ceram. Soc.*, vol. 17, no. 11, pp. 1371–1380, 1997.

[207] B. Kerkwijk, L. Winnubst, E. J. Mulder, and H. Verweij, "Processing of Homogeneous Zirconia-Toughened Alumina Ceramics with High Dry-Sliding Wear Resistance," *J. Am. Ceram. Soc.*, vol. 82, no. 8, pp. 2087–2093, 1999.

[208] M. Instruments, "INFORM WHITE PAPER A Basic Guide to Particle Characterization," 2012. .

[209] R. L. Higginson and C. M. Sellars, *Worked examples in quantitative metallography*, vol. 788. Maney Pub, 2003.

[210] L. IMR TEST, "Hardness testing of ceramic materials." [Online]. Available: https://www.imrtest.com/tests/hardness-testing. [Accessed: 01-Jan-2017].

[211] D. K. Shetty, I. G. Wright, P. N. Mincer, and A. H. Clauer, "Indentation fracture of WC-Co cermets," *J. Mater. Sci.*, vol. 20, no. 5, pp. 1873–1882, 1985.

[212] C. B. Ponton and R. D. Rawlings, "Vickers indentation fracture toughness test Part 1 Review of literature and formulation of standardised indentation toughness equations," *Mater. Sci. Technol.*, vol. 5, no. 9, pp. 865–872, 1989.

[213] J. H. Dumbleton, *Tribology of natural and artificial joints*, vol. 3. Elsevier, 1981.

[214] C. Lentner, *Geigy scientific tables*, vol. Vol 1: Uni. Basle, Switzerland: Ciba-Geigy limited, 1981.

[215] S. L. Smith, D. Dowson, A. A. J. Goldsmith, R. Valizadeh, and J. S. Colligon, "Direct evidence of lubrication in ceramic-on-ceramic total hip replacements," *Proc. Inst. Mech. Eng. Part C J. Mech. Eng. Sci.*, vol. 215, no. 3, pp. 265–268, 2001.

[216] J. L. Tipper, A. Hatton, J. E. Nevelos, E. Ingham, C. Doyle, R. Streicher, A. B. Nevelos, and J. Fisher, "Alumina–alumina artificial hip joints. Part II: characterisation of the wear debris from in vitro hip joint simulations," *Biomaterials*, vol. 23, no. 16, pp. 3441–3448, 2002.

[217] J. Palacios-Carvajal, J. Palacios-Cabezas, and P. Palacios-Cabezas, "The reason for failures of hip prostheses," *Orthop. Int. Ed.*, vol. 4, pp. 11–16, 1996.

[218] H. Kiefer, "Differences and opportunities of THA in the USA, Asia and Europe," *Bioceram. Altern. Bear. Jt. Arthroplast.*, pp. 3–8, 2007.

[219] I. Instruments Veeco, "New Product: Veeco's Surface Metrology System," 2010. [Online]. Available: https://www.qualitydigest.com/inside/twitter-ed/new-product-veeco-s-surface-metrology-system.html#. [Accessed: 01-Jan-2017].

[220] I. technologies Nanoworld, "CONTACT MODE AFM PROBES." [Online]. Available:

http://afm-probes.windsorscientific.co.uk/AFM-Probe-PNP-TRS.html.

[221] E. Casero, L. Vázquez, A. . Parra-Alfambra, and E. Lorenzo, "AFM , SECM and QCM as useful analytical tools in the characterization of enzyme-based bioanalytical platforms.," *Analyst*, vol. 135, no. 8, pp. 1878–1903, 2010.

[222] H. Bender, A. Franquet, C. Drijbooms, B. Parmentier, T. Clarysse, W. Vandervorst, and L. Kwakman, "Surface contamination and electrical damage by focused ion beam: conditions applicable to the extraction of TEM lamellae from nanoelectronic devices," *Semicond. Sci. Technol.*, vol. 30, no. 11, p. 114015, 2015.

[223] Z. Shen, "Colloidal processing and partial sintering of high-performance porous zirconia nanoceramics with hierarchical heterogeneities," vol. 33, pp. 3165–3176, 2013.

[224] A. R. Studart, V. C. Pandolfelli, E. Tervoort, and L. J. Gauckler, "Selection of dispersants for high-alumina zero-cement refractory castables," *J. Eur. Ceram. Soc.*, vol. 23, no. 7, pp. 997–1004, 2003.

[225] P. C. Hidber, T. J. Graule, and L. J. Gauckler, "Citric Acid-A Dispersant for Aqueous Alumina Suspensions," *J. Am. Ceram. Soc.*, vol. 79, no. 7, pp. 1857–1867, Jul. 1996.

[226] G. Plint, "The Sliding Hertzian Point Contact in Tribotesting: Understanding its Limitations as a Model of Real Systems." Phoenix Tribology Ltd, Kingsclere, United Kingdom, 2015.

[227] X. Wang, "Phase transformation in TZP-ZrO2 under local stress and numerical simulation," Tübingen, 2010.

[228] D. R. Clarke and F. Adar, "Measurement of the crystallographically transformed zone produced by fracture in ceramics containing tetragonal zirconia," *J. Am. Ceram. Soc.*, vol. 65, no. 6, pp. 284–288, 1982.

[229] L. Puppulin, A. Leto, Z. Wenliang, N. Sugano, and G. Pezzotti, "Innovative tribometer for in situ spectroscopic analyses of wear mechanisms and phase transformation in ceramic femoral heads," *J. Mech. Behav. Biomed. Mater.*, vol. 31, pp. 45–54, 2014.

[230] P. E. Quintard, P. Barbéris, A. P. Mirgorodsky, and T. Merle-Méjean, "Comparative Lattice-Dynamical Study of the Raman Spectra of Monoclinic and Tetragonal Phases of Zirconia and Hafnia," *J. Am. Ceram. Soc.*, vol. 85, no. 7, pp. 1745–1749, 2002.

[231] T. Merle, R. Guinebretiere, A. Mirgorodsky, and P. Quintard, "Polarized Raman spectra of tetragonal pure ZrO 2 measured on epitaxial films," *Phys. Rev. B*, vol. 65, no. 14, p. 144302, 2002.

[232] K. Kato, "Wear in relation to friction - A review," *Wear*, vol. 241, no. 2, pp. 151–157, 2000.

[233] J. Valle, M. Anglada, B. Ferrari, and C. Baudín, "Processing, nanoindentation and scratch testing of alumina-coated YTZP," *Boletín la Soc. Española Cerámica y Vidr.*, vol. 54, no. 4, pp. 133–141, 2015.

[234] B.-K. Kim and H. Hamaguchi, "Mode Assignments of the Raman Spectrum of Monoclinic Zirconia by Isotopic Exchange Technique," *Phys. status solidi*, vol. 203, no. 2, pp. 557–563, 1997.

[235] P. A. Dowben and A. Miller, *Surface Segregationphenomena*. CRC Press, 1990.

[236] E. Tombácz and M. Szekeres, "Interfacial acid-base reactions of aluminum oxide dispersed in aqueous electrolyte solutions. 1. Potentiometric study on the effect of impurity and dissolution of solid phase," *Langmuir*, vol. 17, no. 5, pp. 1411–1419, 2001.

[237] F. Shojai and T. A. Mäntylä, "Chemical stability of yttria doped zirconia membranes in acid and basic aqueous solutions: chemical properties, effect of annealing and ageing time," *Ceram. Int.*, vol. 27, no. 3, pp. 299–307, 2001.

[238] D. Kim, "Effect of Ta2O5, Nb2O5, and HfO2 Alloying on the Transformability of Y2O3-Stabilized Tetragonal ZrO2," *J. Am. Ceram. Soc.*, vol. 73, no. 1, pp. 115–120, 1990.

[239] H. Schubert, "Anisotropic Thermal Expansion Coefficients of Y2O3-Stabilized Tetragonal Zirconia," *J. Am. Ceram. Soc.*, vol. 69, no. 3, pp. 270–271, 1986.

[240] S. Biggs, P. J. Scales, Y.-K. Leong, and T. W. Healy, "Effects of citrate adsorption on the interactions between zirconia surfaces," *J. Chem. Soc. Faraday Trans.*, vol. 91, no. 17, pp. 2921–2928, 1995.

[241] K. Wefers and C. Misra, "Oxides and Hydroxides of Aluminum 1987," *Alco Lab.*, p. 92, 1987.

[242] M. I. Zaki, G. A. M. Hussien, and R. B. Fahim, "A thermogravimetric study of the solid-state reaction between alumina and strontium carbonate," vol. 30, pp. 129–134, 1985.

[243] Y.-L. Chang, H.-I. Hsiang, M.-T. Liang, and F.-S. Yen, "Phase evolution and thermal behaviors of the solid-state reaction between SrCO3 and Al2O3 to form SrAl2O4 under air and CO2-air atmospheres," *Ceram. Int.*, vol. 38, no. 3, pp. 2269–2276, 2012.

[244] P. Ptáček, F. Šoukal, T. Opravil, E. Bartoníčková, M. Zmrzlý, and R. Novotný, "Synthesis, hydration and thermal stability of hydrates in strontium-aluminate cement," *Ceram. Int.*, vol. 40, no. 7 PART A, pp. 9971–9979, 2014.

[245] F. Bondioli, a M. Ferrari, C. Leonelli, T. Manfredini, L. Linati, and P. Mustarelli, "Reaction mechanism in alumina/chromia (Al2O3-Cr2O3) solid solutions obtained by coprecipitation," *J. Am. Ceram. Soc.*, vol. 83, no. 8, pp. 2036–2040, 2000.

[246] D. Sarkar, "Synthesis and thermo-mechanical properties of sol-gel derived zirconia toughened alumina nanocomposite (Doctoral dissertation).," National institute of technology Rourkela, 2007.

[247] R. P. Rana, "Powder processing, densification behaviour, microstructure and mechanical properties of AL2O3- 50 Vol% ZrO2 composites (PhD thesis)," National institute of technology Rourkela, 2009.

[248] M. Nath, P. Kumar, A. V. Maldhure, S. Sinhamahapatra, K. Dana, A. Ghosh, and H. S. Tripathi, "Anomalous densification behavior of Al2O3-Cr2O3 system," *Mater. Charact.*, vol. 111, pp. 8–13, 2016.

[249] D. H. Riu, Y. M. Kong, and H. E. Kim, "Effect of Cr2O3 addition on microstructural evolution and mechanical properties of Al2O3," *J. Eur. Ceram. Soc.*, vol. 20, no. 10, pp.

1475–1481, 2000.

[250] A. Harabi and T. J. Davies, “Densification and grain growth in sintered alumina-chromia powder mixtures,” *Br. Ceram. Trans.*, vol. 94, no. 3, pp. 97–102, 1995.

[251] A. Harabi and T. J. Davies, “Mechanical properties of sintered alumina-chromia refractories,” *Br. Ceram. Trans.*, vol. 94, no. 2, pp. 79–84, 1995.

[252] S. Maschio and G. Pezzotti, “Microstructural Development and Mechanical Properties of Alumina-Hexaluminate Composites As-Sintered and after Aging in Aqueous and Physiological Solution,” *J. Ceram. Soc. Japan*, vol. 107, no. 1243, pp. 270–274, 1999.

[253] U. Anselmi-Tamburini, J. E. Garay, Z. a. Munir, A. Tacca, F. Maglia, and G. Spinolo, “Spark plasma sintering and characterization of bulk nanostructured fully stabilized zirconia: Part I. Densification Studies,” *J. Mater. Res.*, vol. 19, no. 11, pp. 3263–3269, 2004.

[254] T. Takeuchi, I. Kondoh, N. Tamari, N. Balakrishnan, K. Nomura, H. Kageyama, and Y. Takeda, “Improvement of mechanical strength of 8 mol% Yttria-stabilized zirconia ceramics by spark-plasma sintering,” *J. Electrochem. Soc.*, vol. 149, no. 4, pp. A455–A461, 2002.

[255] L. Wang, V. Pouchly, K. Maca, Z. Shen, and Y. Xiong, “Intensive particle rearrangement in the early stage of spark plasma sintering process,” *J. Asian Ceram. Soc.*, vol. 3, no. 2, pp. 183–187, 2015.

[256] Y. Aman, V. Garnier, and E. Djurado, “Spark plasma sintering kinetics of pure alpha-alumina,” *J. Am. Ceram. Soc.*, vol. 94, no. 9, pp. 2825–2833, 2011.

[257] O. Guillon and J. Langer, “Master sintering curve applied to the field-assisted sintering technique,” *J. Mater. Sci.*, vol. 45, no. 19, pp. 5191–5195, 2010.

[258] Y. Aman, V. Garnier, and E. Djurado, “A screening design approach for the understanding of spark plasma sintering parameters: a case of translucent polycrystalline undoped alumina,” *Int. J. Appl. Ceram. Technol.*, vol. 7, no. 5, pp. 574–586, 2010.

[259] D. Chen and M. J. Mayo, “Rapid Rate Sintering of Nanocrystalline ZrO2− 3 mol% Y2O3,” *J. Am. Ceram. Soc.*, vol. 79, no. 4, pp. 906–912, 1996.

[260] J. Kanters, U. Eisele, H. Böder, and J. Rödel, “Continuum mechanical description of sintering nanocrystalline zirconia,” *Adv. Eng. Mater.*, vol. 3, no. 3, pp. 158–162, 2001.

[261] M. Cain and R. Morrell, “Nanostructured ceramics: a review of their potential,” *Appl. Organomet. Chem.*, vol. 15, no. 5, pp. 321–330, 2001.

[262] G. Bernard-Granger and C. Guizard, “Spark plasma sintering of a commercially available granulated zirconia powder: I. Sintering path and hypotheses about the mechanism(s) controlling densification,” *Acta Mater.*, vol. 55, no. 10, pp. 3493–3504, 2007.

[263] J. Langer, M. J. Hoffmann, and O. Guillon, “Direct comparison between hot pressing and electric field-assisted sintering of submicron alumina,” *Acta Mater.*, vol. 57, no. 18, pp. 5454–5465, 2009.

[264] S. W. Wang, L. D. Chen, and T. Hirai, “Densification of Al 2 O 3 powder using spark

plasma sintering," *J. Mater. Res.*, vol. 15, no. 4, pp. 982–987, 2000.

[265] J. Langer, M. J. Hoffmann, and O. Guillon, "Electric Field-Assisted Sintering in Comparison with the Hot Pressing of Yttria-Stabilized Zirconia," *J. Am. Ceram. Soc.*, vol. 94, no. 1, pp. 24–31, 2011.

[266] C. G. Goetzel, "TENSILE PROPERTIES OF TITANIUM ALLOY FORGINGS MADE FROM SPARK-SINTERED PREFORMS.," Lockheed Missiles and Space Co., Sunnyvale, Calif., 1971.

[267] G. Bernard-Granger and C. Guizard, "Densification mechanism involved during spark plasma sintering of a codoped α-alumina material: Part I. Formal sintering analysis," *J. Mater. Res.*, vol. 24, no. 1, pp. 179–186, 2009.

[268] F. F. Lange and M. M. Hirlinger, "Hindrance of Grain Growth in Al2O3 by ZrO2 Inclusions.," *J. Am. Ceram. Soc.*, vol. 67, no. 3, pp. 164–168, 1984.

[269] J. Wang and R. Stevens, "Zirconia-toughened alumina (ZTA) ceramics," *J. Mater. Sci.*, vol. 24, no. 10, pp. 3421–3440, 1989.

[270] B. W. Kibbel and A. H. Heuer, "Advances in Ceramics, Vol. by N," *Claussen, M. Riihle AH Heuer, Am. Ceram. Soc., Columbus*, pp. 415–424, 1984.

[271] B. Kibbel and A. H. Heuer, "Exaggerated Grain Growth in ZrO2-Toughened Al2O3," *J. Am. Ceram. Soc.*, vol. 69, no. 3, pp. 231–236, 1986.

[272] S. Hori, M. Yoshimura, and S. Somiya, "Strength-Toughness Relations in Sintered and Isostatically Hot-Pressed ZrO2-Toughened Al2O3," *J. Am. Ceram. Soc.*, vol. 69, no. 3, pp. 169–172, 1986.

[273] G. L. Messing and M. Kumagai, "Low-Temperature Sintering of Seeded Sol—Gel-Derived, ZrO2-Toughened Al2O3 Composites," *J. Am. Ceram. Soc.*, vol. 72, no. 1, pp. 40–44, 1989.

[274] S. Hori, R. Kurita, M. Yoshimura, and S. Sōmiya, "Suppressed grain growth in final-stage sintering of Al2O3 with dispersed ZrO2 particles," *J. Mater. Sci. Lett.*, vol. 4, no. 9, pp. 1067–1070, 1985.

[275] K. Tsukuma, K. Ueda, K. Matsushita, and M. Shimada, "High-Temperature Strength and Fracture Toughness of Y2O3-Partially-Stabilized ZrO2/Al2O3 Composites," *J. Am. Ceram. Soc.*, vol. 68, no. 2, 1985.

[276] V. V Srdi and L. Radonji, "Transformation Toughening in Sol–Gel-Derived Alumina-Zirconia Composites," *J. Am. Ceram. Soc.*, vol. 80, no. 8, pp. 2056–2060, 1997.

[277] B. Lawn, *Fracture of brittle solids*. Cambridge university press, 1993.

[278] A. H. Heuer, N. Claussen, W. M. Kriven, and M. Ruhle, "Stability of tetragonal ZrO2 particles in ceramic matrices," *J. Am. Ceram. Soc.*, vol. 65, no. 12, pp. 642–650, 1982.

[279] D. J. Green, "Critical Microstructures for Microcracking in Al2O3-ZrO2 Composites," *J. Am. Ceram. Soc.*, vol. 65, no. 12, pp. 610–614, 1982.

[280] M. Moraes and C. Elias, "Mechanical properties of alumina-zirconia composites for

ceramic abutments," *Mater. Res.*, vol. 7, no. 4, pp. 643–649, 2004.

[281] F. Kern, "A comparison of microstructure and mechanical properties of 12Ce-TZP reinforced with alumina and in situ formed strontium- or lanthanum hexaaluminate precipitates," *J. Eur. Ceram. Soc.*, vol. 34, no. 2, pp. 413–423, 2014.

[282] D. Sarkar, S. Adak, M. C. Chu, S. J. Cho, and N. K. Mitra, "Influence of ZrO 2 on the thermo-mechanical response of nano-ZTA," vol. 33, no. Accepted, pp. 255–261, 2007.

[283] S. Tekeli, "Fracture toughness (KIC), hardness, sintering and grain growth behaviour of 8YSCZ/Al2O3 composites produced by colloidal processing," *J. Alloys Compd.*, vol. 391, no. 1–2, pp. 217–224, Apr. 2005.

[284] O. Fakolujo, A. Merati, M. Bielawski, M. Bolduc, and M. Nganbe, "Role of Microstructural Features in Toughness Improvement of Zirconia Toughened Alumina," no. January, pp. 87–102, 2016.

[285] J. Echeberria, J. Tarazona, J. . He, T. Butler, and F. Castro, "Sinter-HIP of α-alumina powders with sub-micron grain sizes," *J. Eur. Ceram. Soc.*, vol. 22, no. 11, pp. 1801–1809, 2002.

[286] J. Daguano, C. Santos, R. C. Souza, R. M. Balestra, K. Strecker, and C. N. Elias, "Properties of ZrO 2–Al 2 O 3 composite as a function of isothermal holding time," *Int. J. Refract. Met. Hard Mater.*, vol. 25, no. 5, pp. 374–379, 2007.

[287] F. F. Lange, "Transformation toughening," *J. Mater. Sci.*, vol. 17, no. 1, pp. 225–234, 1982.

[288] V. Srdic and L. Radonjic, "Processing of the alumina-zircônia composite and its mechanical properties," in *Third ECers. Proc. 3 rd European Ceramic Society Conf.*, 1993, vol. 3, pp. 701–706.

[289] A. Nevarez-Rascon, A. Aguilar-Elguezabal, E. Orrantia, and M. H. Bocanegra-Bernal, "On the wide range of mechanical properties of ZTA and ATZ based dental ceramic composites by varying the Al2O3 and ZrO2 content," *Int. J. Refract. Met. Hard Mater.*, vol. 27, no. 6, pp. 962–970, 2009.

[290] E. O. Hall, "The deformation and ageing of mild steel: III discussion of results," *Proc. Phys. Soc. Sect. B*, vol. 64, no. 9, p. 747, 1951.

[291] C. Suryanarayana, "Nanocrystalline materials," *Int. Mater. Rev.*, vol. 40, no. 2, pp. 41–64, 1995.

[292] C. Exare, J.-M. Kiat, N. Guiblin, and V. Petricek, "Mechanical Properties of ZTA: Correlation with Structural Properties and Influence of Ageing," *J. Ceram.*, vol. 2016, 2016.

[293] T. J. Joyce, *Biopolymer tribology*. Imperial College Press: London, 2009.

[294] A. P. Harsha and T. J. Joyce, "Challenges associated with using bovine serum in wear testing orthopaedic biopolymers," *Proc. Inst. Mech. Eng. Part H J. Eng. Med.*, vol. 225, no. 10, pp. 948–958, 2011.

[295] P. Ducheyne and Q. Qiu, "Bioactive ceramics: the effect of surface reactivity on bone formation and bone cell function," *Biomaterials*, vol. 20, no. 23, pp. 2287–2303, 1999.

[296] W. Yan, M. Oka, and T. Nakamura, "Bone bonding in bioactive glass ceramics combined with bone matrix gelatin," *J. Biomed. Mater. Res. Part A*, vol. 42, no. 2, pp. 258–265, 1998.

[297] K. Wang, C. Zhou, Y. Hong, and X. Zhang, "A review of protein adsorption on bioceramics," *Interface Focus*, vol. 2, no. 3, pp. 259–277, 2012.

[298] L. Ma and W. M. Rainforth, "A study of Biolox® delta subject to water lubricated reciprocating wear," *Tribol. Int.*, vol. 43, no. 10, pp. 1872–1881, 2010.

[299] H. Spikes, "Mechanisms of boundary lubrication," in *Proceedings of the Tenth International Colloquium on Tribology–solving friction and wear problems, Esslingen, Germany*, 1996, pp. 9–11.

[300] S. C. Scholes, A. Unsworth, R. M. Hall, and R. Scott, "The effects of material combination and lubricant on the friction of total hip prostheses," *Wear*, vol. 241, no. 2, pp. 209–213, 2000.

[301] M. P. Heuberger, M. R. Widmer, E. Zobeley, R. Glockshuber, and N. D. Spencer, "Protein-mediated boundary lubrication in arthroplasty," *Biomaterials*, vol. 26, no. 10, pp. 1165–1173, 2005.

[302] E. Beurer, N. V Venkataraman, M. Sommer, and N. D. Spencer, "Protein and nanoparticle adsorption on orthogonal, charge-density-versus-net-charge surface-chemical gradients," *Langmuir*, vol. 28, no. 6, pp. 3159–3166, 2012.

[303] P. A. Wierenga, M. B. J. Meinders, M. R. Egmond, A. G. J. Voragen, and H. H. J. de Jongh, "Quantitative description of the relation between protein net charge and protein adsorption to air− water interfaces," *J. Phys. Chem. B*, vol. 109, no. 35, pp. 16946–16952, 2005.

[304] T. E. Fischer, Z. Zhu, H. Kim, and D. S. Shin, "Genesis and role of wear debris in sliding wear of ceramics," *Wear*, vol. 245, no. 1, pp. 53–60, 2000.

[305] S. Chaiwan, M. Hoffman, and P. Munroe, "Investigation of sliding wear surfaces in alumina using transmission electron microscopy," *Sci. Technol. Adv. Mater.*, vol. 7, no. 8, pp. 826–833, 2006.

[306] M. G. Gee, "The formation of aluminium hydroxide in the sliding wear of alumina," *Wear*, vol. 153, no. 1, pp. 201–227, 1992.

[307] S.-J. Cho, H. Moon, B. J. Hockey, and S. M. Hsu, "The transition from mild to severe wear in alumina during sliding," *Acta Metall. Mater.*, vol. 40, no. 1, pp. 185–192, 1992.

[308] C. He, Y. S. Wang, J. S. Wallace, and S. M. Hsu, "Effect of microstructure on the wear transition of zirconia-toughened alumina," *Wear*, vol. 162, pp. 314–321, 1993.

[309] G. Pezzotti, "Bioceramics for hip joints: the physical chemistry viewpoint," *Materials (Basel).*, vol. 7, no. 6, pp. 4367–4410, 2014.

[310] S. H. Teoh, "Fatigue of biomaterials: a review," *Int. J. Fatigue*, vol. 22, no. 10, pp. 825–837, 2000.

[311] G. Pezzotti, M. C. Munisso, A. A. Porporati, and K. Lessnau, "On the role of oxygen vacancies and lattice strain in the tetragonal to monoclinic transformation in

alumina/zirconia composites and improved environmental stability," *Biomaterials*, vol. 31, no. 27, pp. 6901–6908, 2010.

[312] F. C. Linn, "Lubrication of Animal Joints: I. THE ARTHROTRIPSOMETER.," *JBJS*, vol. 49, no. 6, pp. 1079–1098, 1967.

[313] J. D. O. Barceinas-Sanchez, "On the role of plastic deformation during the mild wear of alumina (PhD thesis)," University of Sheffield, 1997.

[314] J.-M. Dorlot, "Long-term effects of alumina components in total hip prostheses.," *Clin. Orthop. Relat. Res.*, vol. 282, pp. 47–52, 1992.

[315] P. Zeng, "Biocompatible alumina ceramic for total hip replacements," *Mater. Sci. Technol.*, vol. 24, no. 5, pp. 505–516, 2008.

[316] A. B. Nevelös, P. A. Evans, P. Harrison, and M. Rainforth, "Examination of alumina ceramic components from total hip arthroplasties," *Proc. Inst. Mech. Eng. Part H J. Eng. Med.*, vol. 207, no. 3, pp. 155–162, 1993.

[317] E. Fernández López, V. Sánchez Escribano, M. Panizza, M. M. Carnasciali, and G. Busca, "Vibrational and electronic spectroscopic properties of zirconia powders," *J. Mater. Chem.*, vol. 11, no. 7, pp. 1891–1897, 2001.

[318] A. Feinberg and C. H. Perry, "Structural disorder and phase transitions in ZrO2-Y2O3 system," *J. Phys. Chem. Solids*, vol. 42, no. 6, pp. 513–518, 1981.

[319] P. Zeng, B. J. Inkson, W. M. Rainforth, and T. Stewart, "3D surface reconstruction and FIB microscopy of worn alumina hip prostheses," in *Journal of Physics: Conference Series*, 2008, vol. 126, no. 1, p. 12044.

[320] N. F. Amat, A. Muchtar, N. Yahaya, and M. J. Ghazali, "A review of zirconia as a dental restorative material," *Aust. J. Basic Appl. Sci.*, vol. 6, no. 12, pp. 9–13, 2012.

[321] P. M. Kelly and L. R. Francis Rose, "The martensitic transformation in ceramics — its role in transformation toughening," *Prog. Mater. Sci.*, vol. 47, no. 5, pp. 463–557, 2002.

[322] B. C. Muddle and R. H. J. Hannink, "Crystallography of the Tetragonal to Monoclinic Transformation in MgO-Partially-Stabilized Zirconia," *J. Am. Ceram. Soc.*, vol. 69, no. 7, pp. 547–555, 1986.

[323] M. G. Gee and N. M. Jennett, "High resolution characterisation of tribochemical films on alumina," *Wear*, vol. 193, no. 2, pp. 133–145, 1996.

[324] P. Zeng, W. M. Rainforth, and R. B. Cook, "Characterisation of the oxide film on the taper interface from retrieved large diameter metal on polymer modular total hip replacements," *Tribol. Int.*, vol. 89, pp. 86–96, 2015.